Technische Universität München
Physik Department
Lehrstuhl für Funktionelle Materialien

Co-Re Alloys for Ultra-high Temperature Applications – Investigated by In-situ Neutron Scattering and Complementary Methods

Lukas Karge

Vollständiger Abdruck der von der
Fakultät für Physik der Technischen Universität München
zur Erlangung des akademischen Grades eines

Doktors der Naturwissenschaften (Dr. rer. nat.)

genehmigten Dissertation.

Vorsitzender:		Prof. Dr. Frank Pollmann
Prüfer der Dissertation:	1.	Prof. Dr. Winfried Petry
	2.	Prof. Dr. Joachim Rösler
	3.	Prof. Dr. Andreas Meyer (schriftliche Beurteilung)

Die Dissertation wurde am 04.10.2017 an der Technischen Universität München eingereicht und durch die Fakultät für Physik am 16.01.2018 angenommen.

Co-Re Alloys for Ultra-high Temperature Applications – Investigated by In-situ Neutron Scattering and Complementary Methods

Abstract

Co-Re alloys are a future candidate for high-temperature applications. The alloys are hardened by a dispersion of nano-scaled TaC precipitates. In-situ small-angle neutron scattering (SANS) was used to comprehensively study the precipitate nucleation and coarsening kinetics at high temperatures. Thereby, the activation energies for nucleation, growth and coarsening of the TaC precipitates could be determined. It is shown that they can be used to effectively strengthen the Co-Re alloys up to 1473 K. Neutron diffraction experiments reveal that the Co-Re matrix undergoes an allotropic phase transformation from ϵ-Co (hcp) $\rightarrow$ γ-Co (fcc) at $T \approx 1500$ K that results in an instability of the nano-scaled TaC precipitates. Cr and B are important for the alloy performance at high temperatures and their influence on this Co-Re phase transformation and the precipitate stability was studied. It is shown that Cr stabilizes the ϵ-Co phase, while B lowers the matrix transformation temperature. In addition, the creep behavior of the Co-Re alloy was investigated during an in-situ diffraction experiment with synchrotron radiation at 1373 K. X-ray diffraction and microscopy yielded complementary results on the high-temperature behavior of the Co-Re microstructure.

Co-Re Legierungen für Anwendungen bei ultra-hohen Temperaturen – Untersucht mit in-situ Neutronenstreuung und komplementären Methoden

Zusammenfassung

Co-Re Legierungen sind ein zukünftiger Kandidat für Hochtemperaturanwendungen. Die Legierungen werden durch fein verteilte, nanoskalige TaC Ausscheidungen gehärtet. In-situ Kleinwinkelneutronenstreuung (SANS) wurde verwendet um die Keimbildung und Vergröberung der Ausscheidungen bei Temperaturen bis zu 1770 K umfangreich zu charakterisieren. Damit konnten die Aktivierungsenergien für Keimbildung, Wachstum und Vergröberung der TaC Ausscheidungen bestimmt werden. Es wird gezeigt, dass diese bis zu Temperaturen von 1473 K verwendet werden können um die Festigkeit von Co-Re Legierungen effiktiv zu erhöhen. Experimente mit Neutronendiffraktion zeigen, dass die Co-Re Matrix bei $T \approx 1500$ K eine allotrope Phasentransformation von ϵ-Co (hcp) $\rightarrow$ γ-Co (fcc) durchläuft was zu einer Instabilität der nanoskaligen TaC Ausscheidungen führt. Cr und B Zusätze sind wichtig für die Leistungsfähigkeit der Legierung bei hohen Temperaturen

und ihr Einfluss auf die Co-Re Phasentransformation und die Stabilität der Ausscheidungen wurde charakterisiert. Es wird gezeigt, dass Cr die ϵ-Co phase stabilisiert, während B die Transformationstemperatur der Matrix senkt. Außerdem wurde das Kriechverhalten der Legierung bei 1373 K während eines in-situ Beugungsexperiments mit Synchrotronstrahlung untersucht. Röntgendiffraktion und Mikroskopie lieferten ergänzende Ergebnisse zum Hochtemperaturverhalten der Co-Re Mikrostruktur.

Contents

Für Meike

Chapter 1

Introduction

1.1 Service temperature of gas turbines – the hotter the better

The steady increase of world population, industry and means of transport is accompanied by an increased energy demand. Although there is a variety of new power generation possibilities – especially in the field of renewable energies – fossil fuel and its combustion will keep the center role in the growing economies over the world in the upcoming decades. Therefore, it is crucial to run power generating heat engines as efficient as possible.

The Carnot cycle gives an upper limit for the theoretical best efficiency of a heat engine

$$\eta \leq 1 - \frac{T_{\text{min}}}{T_{\text{max}}} \quad . \tag{1.1}$$

Therefore, the efficiency is limited by the maximum and minimum temperature during the process of converting heat to mechanical energy [1, 2]. Gas turbines are an important class of such engines, since they are used in aircrafts, trains, ships, pumps, gas compressors and electrical generators [3]. In such heat engines, T_{min} is the gas outlet temperature and T_{max} the rotor inlet temperature where the fuel combustion occurs. It is generally unpractical to lower the gas outlet temperature T_{min}, but the fuel can be combusted at a higher temperature T_{max}. Therefore, there is a general interest in the development of high temperature alloys for the hottest parts of the turbine.

Fig. 1.1.1 depicts a turbojet engine. The compressor consists of compressor blades and discs that compresses the incoming air. The compressed air is mixed with fuel and ignited in the combustor. Energy is released of the hot, expanding air-fuel mixture and extracted by the turbine to drive the compressor. The fan and compressor sections demand a good specific strength and fatigue resistance accompanied with a low material density. The hottest temperatures are reached in the combustor and the turbine inlet temperature determines the turbine's efficiency. Modern turbines operate with gas entry temperatures in the range of 1800 K and the externally cooled materials have to be heat-resistant up to 1300 K [4]. Therefore, components in this section must withstand loading under static, fatigue and creep conditions at high temperatures (HT).

Especially in the scope of aircraft engineering and the development of jet aircraft, the operating temperatures were steadily increased to run the turbine engines more efficient. Fig. 1.1.2 shows the produced power as a function of the inlet temperature. On the one hand,

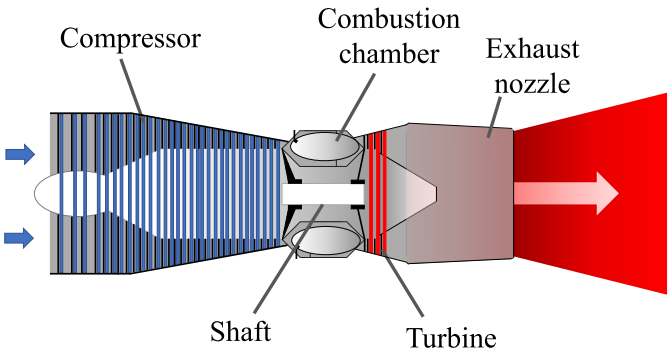

FIGURE 1.1.1: Schematic of the basic features of a gas turbine. The area in the turbine and the red turbine blades are exposed to the highest temperatures and are nowadays dominated by Ni-base superalloys.

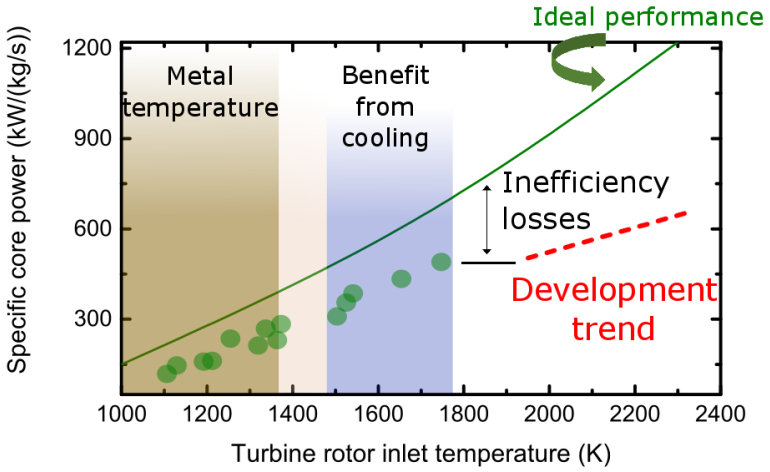

FIGURE 1.1.2: The specific core power of a turbine in dependence of rotor inlet temperature. The green dots schematically represent used high temperature materials. At higher inlet temperatures, the material has to be externally cooled. This results in a loss of efficiency, caused by the needed extra work to provide cooling for the turbine blades. Since nowadays materials reach inherent temperature limits, this trend is likely to increase in the future. Tha graphic was adapted from [2].

the created power is steadily rising, while on the other the relative efficiency is worsening. This is a consequence from the need for extra work to provide enough flow of cooling air for the turbines blades to prevent melting. Therefore, materials that withstand higher temperatures could significantly increase the output power. In addition, the turbine would highly benefit of a simplified manufacturing and reduced weight as a result of eliminating the complexity of auxiliary cooling requirements.

Potential materials for such applications, must have high tensile strength, a high ductility for their mechanical shaping, and they must withstand oxidation and fatigue at HT. Nickel-base superalloys fulfill many of these requirements and are currently the dominating turbine blade material. They benefit from decades of development which steadily increased their application temperature. Fig. 1.1.3 depicts the development of the Ni-base superalloy application temperature in the last half century. Directional solidification (1^{st} generation) and single crystal growth (2^{nd} generation) techniques allowed to produce single crystal (SX)

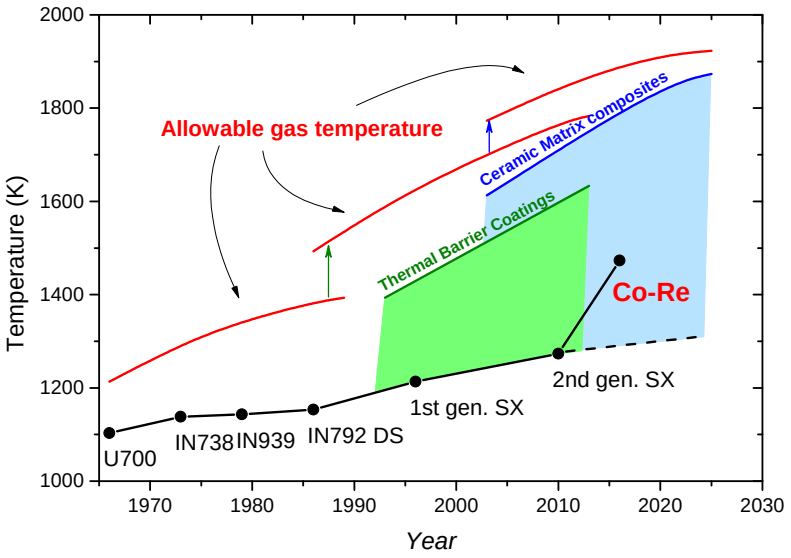

Figure 1.1.3: History of superalloys in the last 50 years and the maximum material and allowable gas temperature of state of the art superalloys. The maximum allowable temperature of the basic materials (black dots and line) is considerably lower than the gas inlet temperature (red line). In order to reduce the temperature of the basic material, protective coatings and cooling mechanisms are applied. State of the art single-crystal (SX) superalloys reach inherent temperature limits since they operate at $\sim 90\%$ of their melting temperature. The Co-Re alloy aims to increase the application temperature of the material.

and significantly improved the alloy's properties. However, the Ni-base superalloys are reaching inherent temperature limits, since they already operate at more than $80-90\%$ of their melting range near 1630 K [4].

Cobalt-base alloys have a melting-point advantage over the Ni-base superalloys and have found minor usage as combustor parts in gas turbines at temperatures > 1400 K [5]. However, as their temperature advantage is not large, their lower strength compared with that of Ni-base alloys prevented widespread application [6]. In this context, the development of a new high temperature material, the Cobalt-Rhenium-base alloy was started [7].

Co-Re-base alloys are mainly attractive for their high melting range. Addition of 17 at. % of Re to Co increases the melting range of the Co-Re-base alloys above 1780 K, which is more than 150 K higher than current Ni-base superalloys. Re shows complete miscibility in the Co-matrix and the alloys benefit from a solid solution strengthening effect due to the different atomic radii of Co and Re. Additionally, they can be hardened by precipitates, in particular by the mono-carbide of Ta. Although the density of Co-Re alloys is higher ($\rho \approx 11.5\,\mathrm{g\,cm^{-3}}$), their specific strength (strength/ρ) at room temperature (RT) is comparable to the much lighter single crystal Ni-base superalloys. In addition, further alloying additions (e.g. Cr, Si, Ni) impart an excellent oxidation resistance of the alloy. Therefore, the alloy is an excellent candidate in the hottest sections of stationary gas turbines.

1.2 Neutron scattering experiments in alloy development

Neutron and X-ray scattering experiments were extensively used in the development of Co-Re alloys to investigate their microstructure and kinetics [8–10]. Such experiments have the advantage of being non-destructive and yield physical quantities, averaged over large

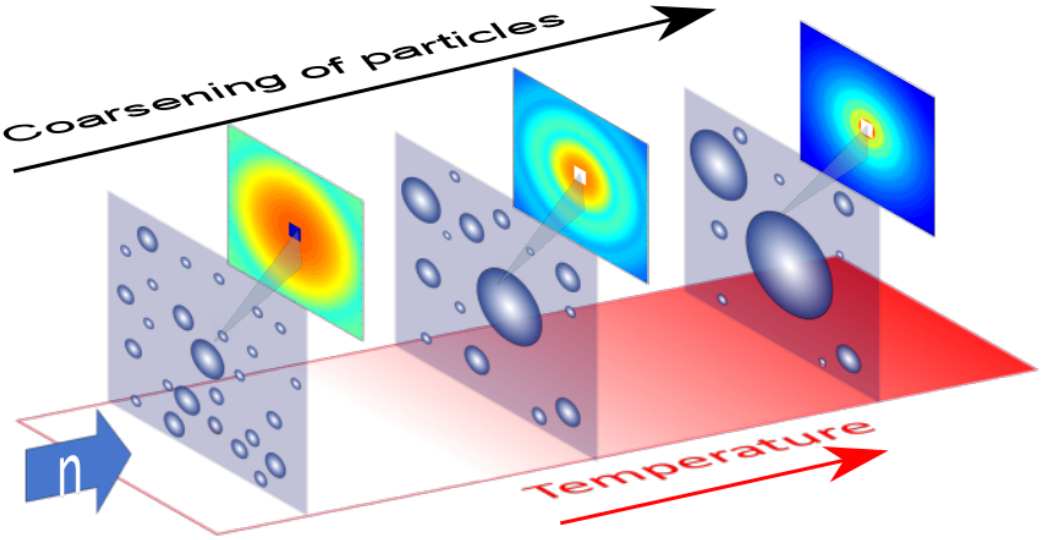

FIGURE 1.2.1: In-situ small-angle neutron scattering experiments at HT can monitor precipitate coarsening in an alloy. A certain precipitate size distribution results in a characteristic scattering pattern at small angle around the transmitted primary beam.

sample volumes. Small-angle scattering (SAS) is a technique to investigate kinetic properties and the size of particles in materials. Elastic small-angle neutron scattering (SANS) typically probes the *mesoscopic* length scale of roughly $1 - 300$ nm [11, 12]. Structures on this length scale are critical to the performance of advanced engineering materials that content secondary phases such as strengthening precipitates. Although they are well visible by microscopy, only local information can be found on the micrographs and it is only applicable *ex-situ* before and after the application of heat treatments. It is crucial to get statistical knowledge of the microstructure for the sample bulk in order to understand the material's macroscopic behavior. SANS yields statistical information on the bulk sample. Additionally, the investigations can be performed *in-situ* which is especially difficult with other methods. Fig. 1.2.1 schematically shows an in-situ SAS experiment at HT. The presence of nano scaled precipitates of a secondary phase yields a scattering signal and a change in their size gives rise to a characteristic change of the scattering pattern. In addition, in-situ neutron diffraction (ND) methods are used to investigate the presence, atomic structure and stability of phases.

1.3 Scope of the thesis

Pure Co has two allotropic forms: hexagonal close-packed (hcp) ϵ-Co and face-centered cubic (fcc) γ-Co. The HT γ-Co phase is often metastably retained at RT. Re addition stabilizes the low temperature ϵ-Co structure in Co-Re alloys. Depending on the exact alloy composition, the Co-Re matrix exhibits a hcp $\leftrightarrow$ fcc transformation in the interval $1450 - 1770$ K. The influence of individual additions to the Co-Re system is studied in this thesis, in order to get an understanding of their interplay with the matrix transformation.

This thesis focuses on the finely dispersed mono-carbide phase of nano-sized TaC precipitates, used for strengthening of the alloys. They interact with dislocations during HT creep

name	type	Co	Re	Cr	Ta	C	B
TaC05	low C content alloy	81.20	17	0	1.20	0.60	0
TaC07	low C content alloy	80.96	17	0	1.20	0.84	0
TaC09	high C content alloy	80.72	17	0	1.20	1.08	0
TaC10	high C content alloy	80.60	17	0	1.20	1.20	0
5Cr	low Cr content alloy	75.72	17	5	1.20	1.08	0
15Cr	high Cr content alloy	70.72	17	15	1.20	1.08	0
01B	low B content alloy	80.71	17	0	1.20	1.08	0.1
04B	high B content alloy	80.68	17	0	1.20	1.08	0.4

Table 1.3.1: Co-Re alloy types that are investigated in this thesis. The influence of varying C/Ta ratio on TaC precipitates is studied in TaC05-TaC10 alloys, the influence of Cr addition in the 5Cr, 15Cr alloys and the influence of B addition in the 01B, 04B alloys.

deformation and their characterization, depending on C/Ta ratio with varying Cr and B addition. Neutron and X-ray scattering, as well as complementary microscopy experiments were performed to study the stability of the TaC precipitate at HT up to 1770 K. Several innovative tools were developed to extract information about their nucleation, growth and coarsening kinetics in Co-Re alloys.

In summary, this thesis gives answers to the following questions:

- How is the (long term) stability of the cubic TaC-precipitates affected by the C/Ta ratio?
- How is the lattice parameter of the cubic TaC-phase affected by the C/Ta ratio and does this influence the coherency between matrix and precipitate?
- Is the precipitate morphology, e.g. Chinese script versus fine precipitates, affected by the C/Ta ratio?
- Are other Ta_xC_y-phases occurring at low C/Ta ratios?
- If so, how does the stability of these Ta_xC_y-phases compare with that of the cubic TaC-phase?
- How are the volume fraction and/or C/Ta-ratio of the tantalum carbides affected by Cr addition?
- Is there a precipitation of $Cr_{23}C_6$ and does it influence the stability of the tantalum carbides, e.g. due to an altered C/Ta ratio?
- Is boron segregating to the phase boundaries of the tantalum carbides?
- If so, does this affect the stability of the tantalum carbides?

Table 1.3.1 summarizes the investigated Co-Re alloy compositions. In the TaC05-10 alloys the C content was varied to investigate the influence of C/Ta stoichiometry. The 5Cr and 15Cr alloys have a fixed ratio C/Ta= 0.9 and were studied for the influence of Cr addition on the TaC precipitates and the Co-Re matrix. Finally, the 01B and 04B alloys were produced with C/Ta= 0.9 to explore the effect of B addition on the Co-Re matrix phase and TaC precipitate stability.

Chapter 2

Cobalt Rhenium Alloys

Cobalt-base alloys are commonly used for static parts in gas turbines at temperatures $\sim$ 1300 K [1, 5]. Usually they have a cubic fcc matrix structure, referred to as γ phase. Currently, there is considerable effort to reproduce the γ/γ' structure (known as L_{12}) of Nickel-base superalloys to improve their mechanical properties with γ' precipitates [6, 13, 14]. Co-Re-base alloys, however, aim to significantly increase the application temperature of the alloy. The refractory metal Re has a melting point of 3455 K and shows complete miscibility in the binary Co-Re system. Therefore, the melting range of the Co-Re alloy can be continuously raised by increasing the Re content. 17 at.% of Re raises the liquidus temperature to $\sim$ 1970 K in the Co-17Re binary system (Fig. 2.0.1). Although Re is rather expensive, its addition is affordable since the highest costs of gas turbine blades arise due to their manufacturing (precision casting and coating).

The microstructure of Co-Re alloys was studied in detail for its high-temperature properties throughout the last decade [7, 9, 15–21]. This chapter aims to give an overview about the

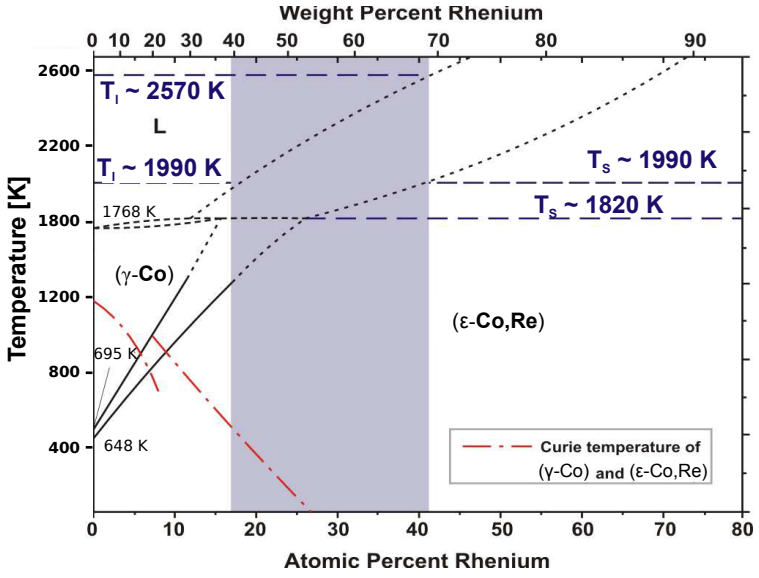

Figure 2.0.1: Binary Co-Re phase diagram. Increase of Re content stabilizes the ϵ-Co phase (hcp). The gray underlaid area represents the interesting Co-Re stoichiometry that was investigated in the past years. Alloys within the current thesis deal with a Re content of 17 at.% Re. Adapted from [15].

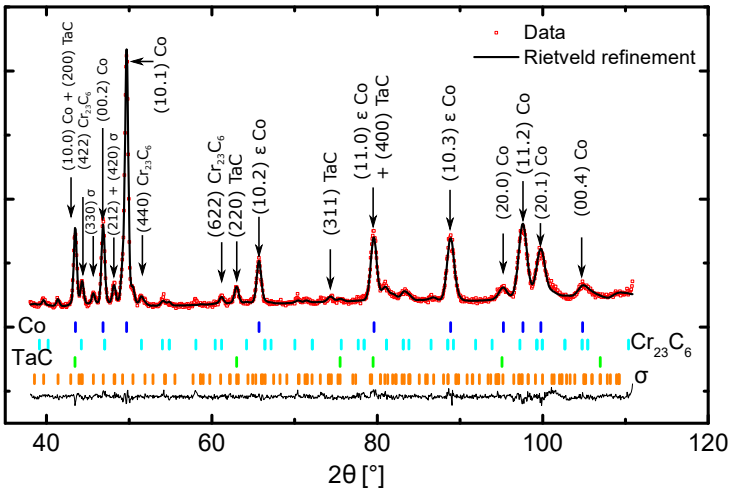

FIGURE 2.0.2: Diffractogram of Co-Re-Cr-Ta-C alloy, measured with neutrons. The ϵ-Co phase, Cr- and Ta-carbides, as well as a σ-phase are observed.

Phase	Typical composition	Crystal structure	Space group	Lattice parameter(s) [Å]
ϵ-Co	(Co,Re)	hcp	P 63/m m c	$a = 2.567723, c = 4.145375$
γ-Co	(Co,Re)	fcc	F m $\bar{3}$ m	$a = 3.640$
MC	TaC	NaCl	F m $\bar{3}$ m	$a = 4.454$
σ-phase	Cr_2Re_3	tetragonal	P 42/m n m	$a = 9.007, c = 4.664$
$M_{23}C_6$	$Cr_{23}C_6$	NaCl-type packing of cubo-octahedra [22]	F m $\bar{3}$ m	$a = 10.724436$

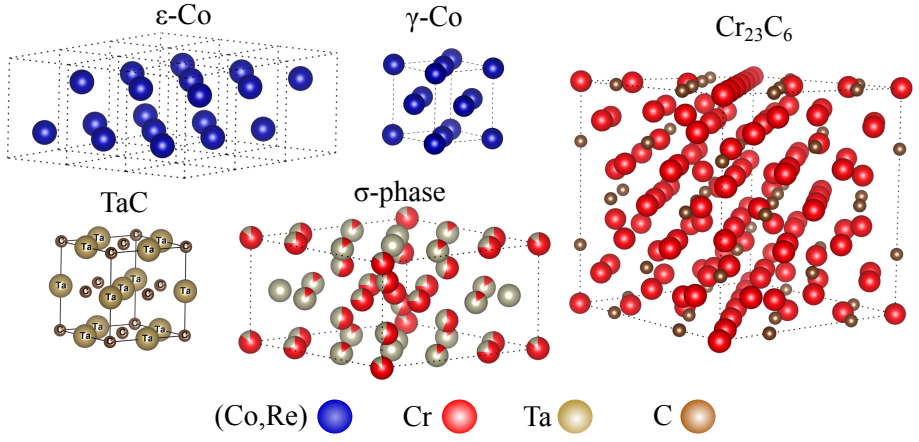

FIGURE 2.0.3: (Top) Crystal structures of the phases in Co-17Re-23Cr-1.2Ta-2.6C alloy. γ-Co is the high temperature phase of the alloy and the lattice constants are very sensitive on the exact composition and temperature. (Bottom) Unit cells of the various phases.

basic properties, the present phases and their behavior near the application temperature of the material at $\sim 1470\,\mathrm{K}$.

2.1 Phases in the Co-Re system

The microstructure of Co-Re alloys is rather complex. The alloys contain multiple phases with different morphologies on different length scales. Fig. 2.0.2 shows a ND pattern of a Co-Re-Cr-Ta-C sample and reveals the general microstructure of the alloy at RT. The low temperature ϵ-Co phase, Cr- and Ta-carbides, as well as a Cr-rich σ phase can directly be

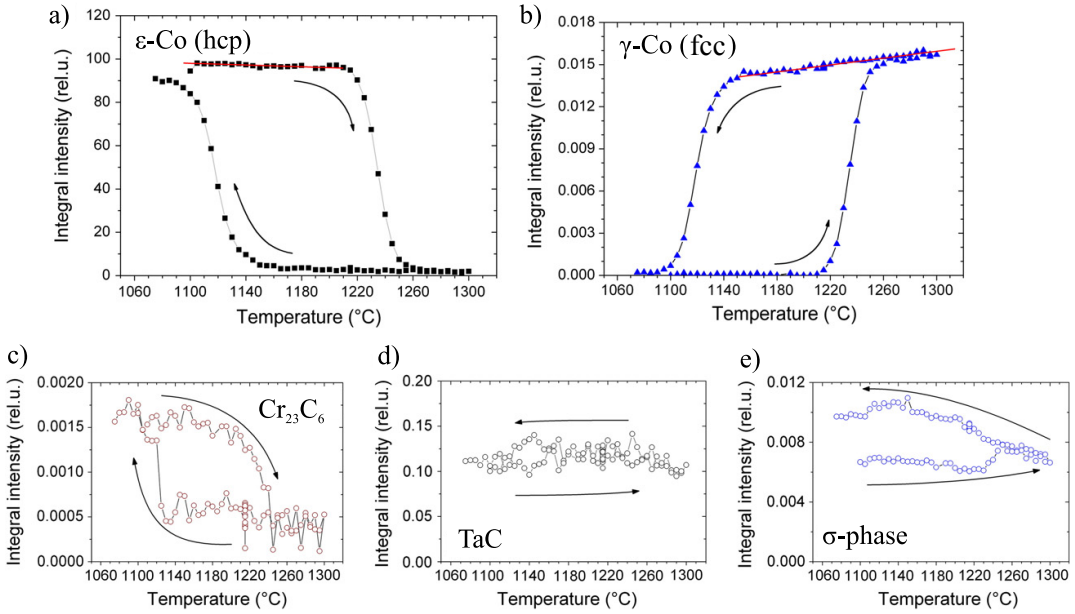

FIGURE 2.1.1: Phase transformations in Co-17Re-23Cr-1.2Ta-2.6C alloy. (a,b) The allotropic phase transformation of the Co-Re matrix $\gamma \leftrightarrow \epsilon$ shows a large hysteresis on cooling. (c) Cr carbides dissolve upon heating $> 1473\,\mathrm{K}$. (d,e) The TaC and σ phase are stable up to very high temperatures. Adapted from [17].

identified. In the following, an overview over previous experiments on these phases and their function in the Co-Re system is presented.

2.1.1 The allotropic $\epsilon \leftrightarrow \gamma$ Co-Re phase transformation

Pure Co is stable in two allotropic forms. The low temperature ϵ-Co phase hexagonal close-packed (hcp) martensitically transforms to the high temperature γ-Co face centered cubic (fcc) phase at about $\sim 690\,\mathrm{K}$ during heating [23, 24]. The ABABAB... stacking of the close-packed planes of hcp phase transforms into the ABCABC... stacking sequence of fcc phase by movements of Shockley partial dislocations on alternate close-packed planes. Alloying additions either increases or decreases the transformation temperature depending on whether they are hcp or fcc stabilizer in Co. Therefore, the Re content can be used to tune the transformation temperature (Fig. 2.0.1). Additionally, the exact temperature is very sensitive on minor additions of B, Cr, C and Ta to the alloy [8, 10, 20]. These elements can form (among others) MC-type Ta-carbide precipitates, $M_{23}C_6$-type Cr carbides or Cr_2Re_3 σ-phase, that interplay with the Co-Re matrix transformation.

Commonly, some of the high temperature γ-Co phase is metastably retained, when cooling Co to RT. The metastable γ-Co phase can exhibit a strain induced martensitic $\gamma \rightarrow \epsilon$ transformation upon deformation [25]. A similar behavior was found in the Co-Re-Ta-C system when cooling to RT with rates of $\leq 10\,\mathrm{K\,min^{-1}}$ in vacuum [20]. However, when adding 23 at.% Cr to the Co-Re-Ta-C system, the high temperature γ-Co phase completely transformed to ϵ-Co phase during cooling at $\sim 1400\,\mathrm{K}$ (Fig. 2.1.1). It is essential to prevent any phase transformation while operating the Co-Re alloys at their envisaged temperature, since is could result in fatal microstructural instabilities and density changes of sensitive

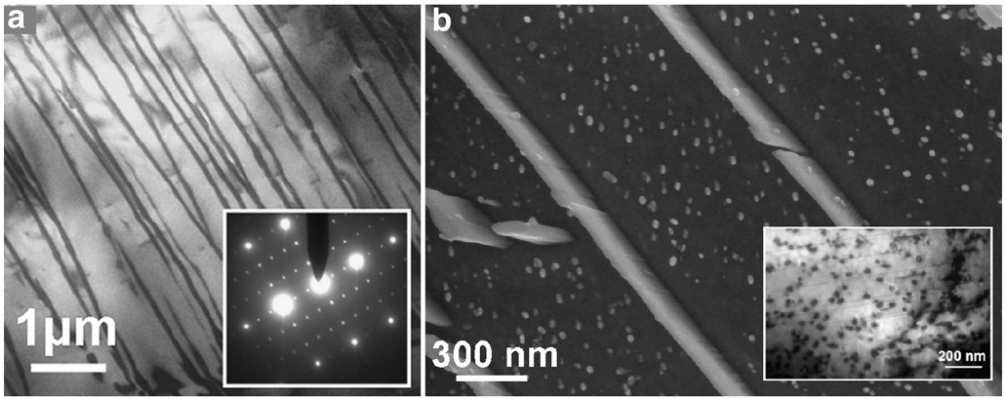

Figure 2.1.2: Micrograph from Co-Re-Cr-Ta-C alloy showing various carbide morphologies. (a) The lamellar $Cr_{23}C_6$ type carbides are present with their orientation relationship to the matrix. Inset: Area diffraction pattern. (b) Fine dispersion of TaC, embedded in ϵ-Co matrix, between the $Cr_{23}C_6$ lamellae. The inset shows a TEM image of the TaC precipitates. Adapted from [17]

parts. Due to the high transformation temperature, the goal is stabilizing the ϵ-Co phase above the application temperature range.

The influence of elemental additions C, Cr and B on the allotropic phase transformation is comprehensively investigated in this thesis.

2.1.2 Carbides

Carbon in small amounts combines with reactive elements, such as titanium, tantalum, hafnium, and niobium, to form metal carbides. Nearly all polycrystalline superalloys contain a small amount of carbon as they can stabilize the alloy matrix. In order to effectively strengthen the alloy, such carbides need to be finely dispersed in the microstructure. Then, the particles impede the movement of dislocations through the lattice during creep deformation at high temperatures.

The formation and stability of carbides in Co-Re alloys were extensively studied over the last years [9, 10, 26, 27]. Electron microscopy, SANS, X-ray, synchrotron and ND showed the general good properties in a sample alloy with composition Co-17Re-23Cr-1.2Ta-2.6C. After a solution heat treatment (1673 K / 7.5 h+1723 K / 7.5 h + quenching in argon atmosphere), two types of carbides were found, namely the $M_{23}C_6$ type Cr-carbides and MC type Ta-carbides [9, 26]. The latter are commonly used for precipitation hardening in high temperature alloys [1]. The transmission electron microscopy (TEM) image in Fig. 2.1.2 shows typical morphologies of both carbides. The TaC phase is present in form of fine precipitates ($\sim$ 20 nm), while $Cr_{23}C_6$ form lamellae with a thickness of ($\sim$ 40 nm). EDX shows the elemental partitioning in γ-Co and ϵ-Co phase. In addition, the method can identify σ phase and TaC precipitates. A typical result of elemental distribution maps from the sample alloy Co-17Re-23Cr-1.2Ta-2.6C is presented in Fig. 2.1.3. The method can clearly resolve the Ta- and Cr-carbides in the matrix.

The mono-carbide of Ta is a strongly non-stoichiometric interstitial compound that exists over a wide composition range as binary system. The phase diagram in Fig. 2.1.4 shows that (i) TaC is stable over a wide range of C/Ta ratios and (ii) there exist various other stable Ta_xC_y-type phases (e.g. ζ-Ta_4C_3, α-Ta_2C). ND and SANS revealed TaC volume fractions

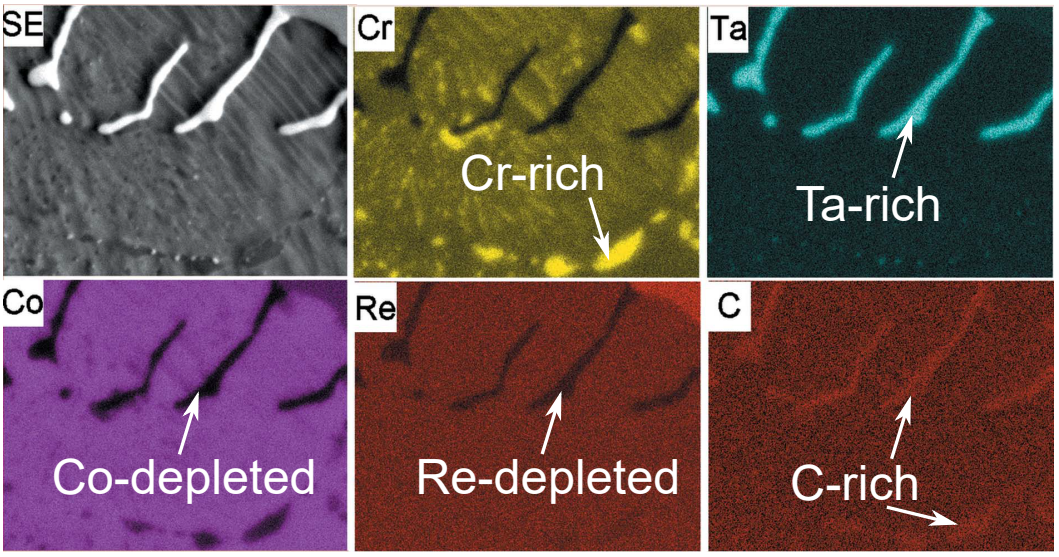

Figure 2.1.3: SE and EDX elemental maps of the elements Cr, Ta, Co, Re and C. The various types of carbides can be identified as TaC and $Cr_{23}C_6$. Adapted from [9]

of $\sim 2-3\%$ for precipitation hardening within the microstructure of a Co-Re-Cr-Ta-C alloy. Their morphology, distribution and size are crucial for effective strengthening. Further, their stability at high temperatures in the Co-Re microstructure is of key interest. Rather than forming a global secondary phase, they preserve a nano scaled, spherical morphology up to temperatures of 1473 K. An *in-situ* SANS shows that the coarsening due to diffusion of these nano particles is moderate and the mean precipitate size is < 100 nm after 15 h of holding at the temperature (Fig. 2.1.5). When heating to higher temperatures, ND shows on the one hand that the TaC phase is still present (Fig. 2.1.1), while on the other hand SANS shows that fine TaC precipitates dissolve or grow out of the method's resolution maximum (> 300 nm).

The lamellar Cr-carbides were studied by in-situ neutron and synchrotron experiments. The Cr-carbide laths follow the standard hcp/fcc orientation relationship $[100]_{hcp}||[112]_{fcc}$, $(002)_{hcp}||(111)_{fcc}$ [18]. However, *in-situ* ND showed that they start dissolving at ~1473 K during an experiment that step-wise ramped up the temperature (Figure 2.1.1). In addition, it was found that Cr carbides increasingly start breaking up when holding for > 3 h at 1273 K and Cr recombines with Re [26], forming the topologically close packed (TCP) σ phase (cf. section 2.1.4). For that reason, Cr-carbides are unsuited for strengthening the Co-Re alloys at very high temperatures and the TaC phase in form of fine precipitates is used as the main hardening mechanism.

The influence of carbon content on the TaC precipitate stability is discussed in chapter 5 and their kinetics are studied *in-situ* at high temperature in chapter 7.

2.1.3 Borides

Modern single crystal (SX) solidification techniques allow to essentially eliminate the grain boundaries in superalloys [1]. At this early stage of development, no such technique exists for Co-Re alloys and they are only available with a polycrystalline structure. Therefore, the problems of grain boundary embrittlement and cohesion are important issues and boundary

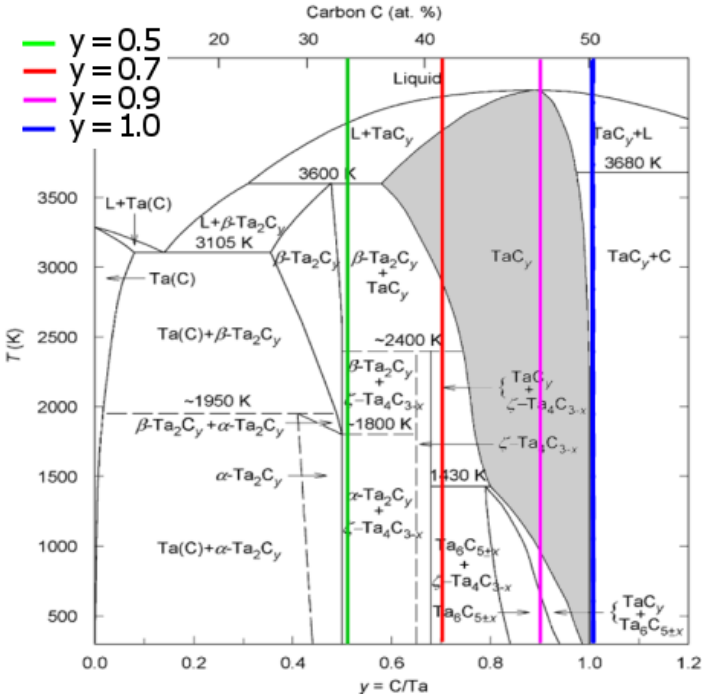

FIGURE 2.1.4: The binary TaC phase diagram showing the various stable phases. The mono-carbide phase of TaC is highlighted in gray. The vertical bars represent the C/Ta ratios, investigated in the present study. Adapted from [28].

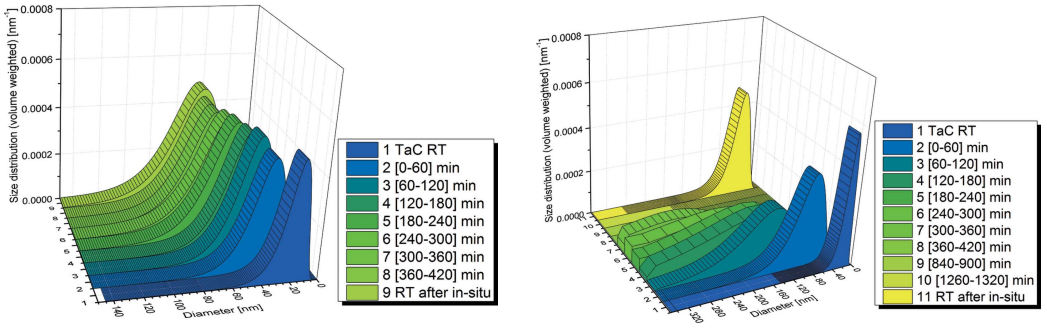

FIGURE 2.1.5: Size distribution of fine TaC precipitates, measured during in-situ SANS at 1473 K (left) and 1533 K (right). While the size distribution is essentially unchanged at 1473 K, the TaC precipitates in form of nano scaled precipitates vanish at 1533 K. Adapted from [9].

migration effects can cause stability problems of the material. Bend tests at RT with a reference Co-Re alloy (Co-17Re-23Cr) failed with brittle inter-granular fracture [29]. However, the cohesion could be significantly improved by addition of boron. Borides preferably deposit on grain boundaries and can suppress continuous carbide films around grains, increasing the creep resistance [1, 30]. Even for the small addition of 500 ppm of B, the strength and ductility of Co-Re alloys were shown to improve strongly [31] and to be comparable with SX Ni-base superalloys. In addition, the fracture mode changed from inter-granular to trans-granular. However, addition of B might result in the formation of B-carbides, effectively reducing the amount of available carbon for formation of strengthening precipitates. Therefore, it is crucial to study the influence of B addition on TaC precipitates. The findings are discussed in chapter 6.

2.1.4 Topologically close packed σ-phase

An addition of Cr to the alloy Co-17Re promotes the formation of the topologically closed packed (TCP) σ phase in Co-Re alloys [32]. The Cr-Re-rich (Cr_2Re_3) σ phase has a very high strength, but it is rather brittle as well. Therefore, it is generally undesirable in high temperature [33, 34]. On the other hand, Cr is essential for oxidation resistance in Co-Re alloys. Generally, the σ phase is stable to very high temperatures $> 1773\,\mathrm{K}$ (Fig. 2.1.1) in the Co-Re matrix. Several strategies were therefore adapted to refine the σ phase through heat treatment. Adding Ni to the alloy, stabilizes a mixed fcc + hcp Co-matrix, which results in a finely dispersed σ phase ($100 - 200\,\mathrm{nm}$) [19]. Although the σ phase is likely still brittle in these alloys, it is nearly defect free and therefore crack initiation is hindered. Alloys with addition of 23 at.% Cr still showed good RT ductility of $\varepsilon > 3\%$ [19].

Additionally, the instability of $Cr_{23}C_6$ carbides at temperatures $> 1273\,\mathrm{K}$ in Co-Re alloys results in a freed Cr reservoir from the carbide dissolution. Subsequently, Cr can combine with Re in the matrix and stabilize the brittle σ phase [26]. Therefore, the consequences of Cr addition and carbide formation is a crucial mechanism that is discussed in chapter 6.

2.2 Strengthening mechanisms in Co-Re alloys

Several strengthening mechanisms for Co-Re alloys have been found [15, 29, 35, 36]:

Solid-solution hardening	by large Re atoms
Precipitation hardening	Carbide precipitates ($M_{23}C_6$ and TaC MC type)
Second phase (composite) hardening	σ phase (Cr-Re rich close packed phase)
Grain boundary strengthening	by boron addition

The addition of Re results not only in an increase of melting temperature, but also provides solid-solution strengthening due to the large atomic size of Re. The local non-uniformities in the lattice create local stress fields, which makes plastic deformations more difficult. Co and Re crystallize in the hcp structure with lattice constants $a = 2.761$ Å, $c = 4.456$ Å for Re and $a = 2.5071$ Å, $c = 4.0695$ Å for Co. Thus, the Hume-Rothery rules predict the miscibility of Re and Co [37] (lattice constants differ by $\Delta d/d \approx 0.09 < 0.15$, Re has lower valency than Co and both metals have a similar electronegativity), which is also confirmed by experimental evidence [31].

Furthermore, hardening by carbide precipitates and second phase particles is applied. TaC precipitates and a procedure for refining the σ phase from Cr_2Re_3 can be effectively utilized in Co-Re alloys without loss of ductility. In this thesis, the focus is on the strengthening mechanism by nano scaled TaC precipitates (10-100 nm).

The strength of a precipitation hardened alloy, in its simplest form, is a function of precipitate size and volume fraction. If a dislocation migrates through the matrix and encounters a precipitate, it can either cut through the precipitate or bow around it [38]. The process of a dislocation bowing around a precipitate is schematically depicted in Fig. 2.2.1. The precipitate stability, when impeded by a dislocation, increases with its size. Hence, it is easier for a dislocation to cut through smaller precipitates than through larger ones. This relationship is given by

$$\Delta\tau = \frac{\pi r \Gamma}{b l_p} \quad , \tag{2.1}$$

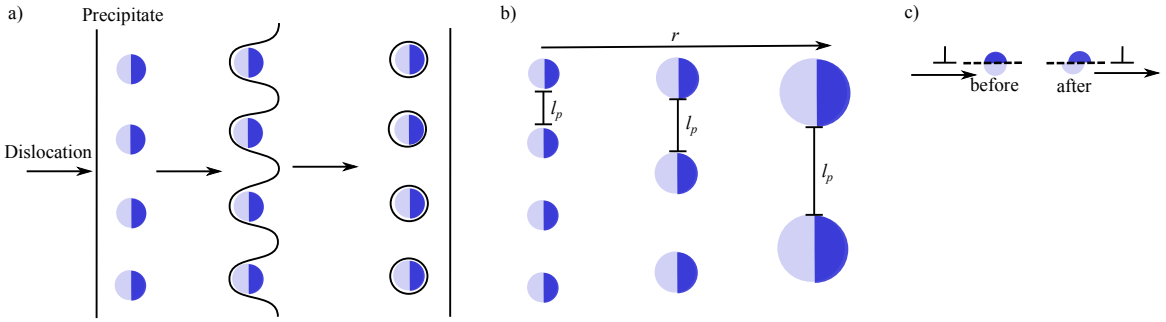

FIGURE 2.2.1: (a) Dislocation moving through the matrix. Energy is stored at precipitates due to Orowan bowing. (b) The precipitate distance l_p is a function of the precipitate radius r at constant precipitate volume fractions. (c) Small precipitates are easily cut by the dislocation.

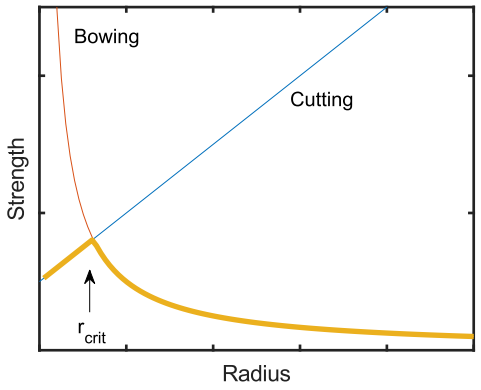

FIGURE 2.2.2: Schematic drawing of the strengthening effect of precipitates and optimal radius r_{crit} as a function of precipitate size at constant volume fraction. Since the dislocation chooses the path of minimal energy, the observed mechanism is a function of the precipitate radius r. Small precipitates are easily cut, for large radii, the precipitate distance increases.

with the material strength increase $\Delta\tau$, precipitate radius r, the matrix-precipitate surface energy Γ, the magnitude of the burgers vector b and the spacing between two pinning precipitates l_p.

The second contribution to the strengthening mechanism is the material strength against dislocation bowing or Orowan strengthening. The governing equation

$$\Delta\tau = \frac{Gb}{l_p - 2r} \quad , \tag{2.2}$$

with the shear modulus G. It shows that it gets exceedingly more difficult for a dislocation to bow around a precipitate for smaller r. Fig. 2.2.2 shows schematically the strength of a precipitation hardened material as a function of particle radius due to both described effects. Detailed discussions about the exact influence of r and l_p on $\Delta\tau$ can be found in [1, 39].

Although Co-Re alloys have a higher density in comparison to conventional Ni-base superalloys, their specific strength (strength/density) is comparable (table 2.2.1).

TABLE 2.2.1: Strength of a Co-Re alloy, compared with the commercially used SX Ni-base superalloy CMSX-4 at RT. The ultimate tensile strength (UTS) is the maximum stress that the material can withstand before breaking. The specific strength is the UTS normalized by the material's density. The rupture strain is the material's strain when breaking. Adapted from [40].

Alloy	Density (ρ) [g/cm^3]	UTS (σ) [MPa]	Specific strength [σ/ρ]	Rupture strain (ϵ) [%]
Co-17Re-23Cr + 500 ppm B	11.5	1276	110.9	20.3
CMSX-4	8.7	894	102.7	22

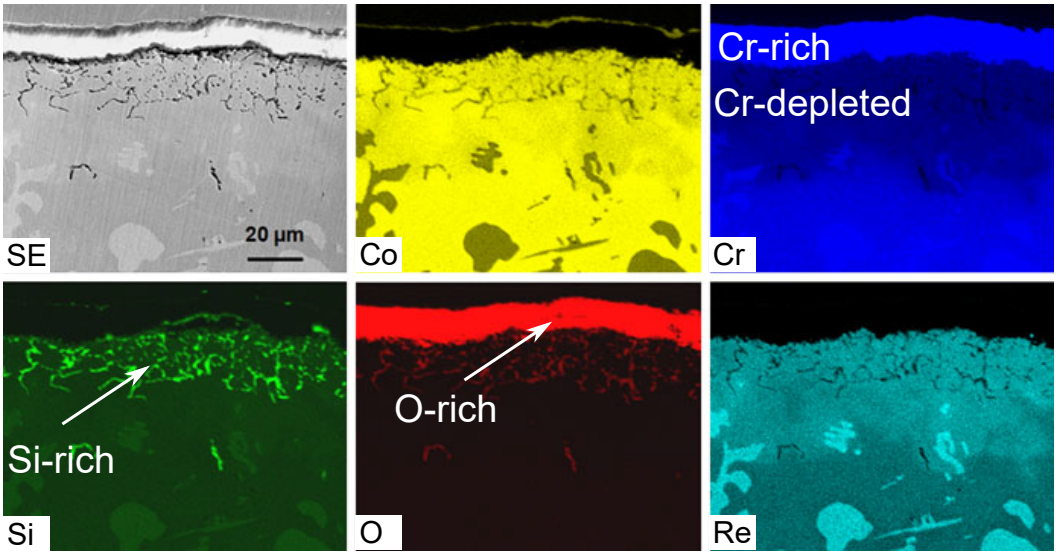

FIGURE 2.3.1: The secondary electron and element distribution maps of cross-section of Co-17Re-25Cr-2Si alloy after exposure in air at 1373 K for 72 h. A thick compact Cr_2O_3 layer has formed near the surface of the alloy, followed by a $\sim$ 50 µm Cr depletion zone. The very thin Co enriched layer on the alloy surface was identified as oxides of type CoO and $CoCr_2O_4$. Below these three oxide layers, a SiO_2 network-like structure has formed. Adapted from [41].

2.3 Oxidation resistance

The high application temperatures of Co-Re alloys impose severe demands on the material's oxidation behavior. In conventional Fe, Ni and Co alloys, addition of Cr promotes the formation of a protective oxide layer on the surface. The oxidation mechanisms are well understood in binary Co-Cr alloys [42–44]. A slow growing Cr_2O_3-scale forms on the surface which reduces the evaporation rate of matrix elements by oxidation. A similar positive effect was observed in Co-Re alloys with 25 at.% of Cr and 2 at.% of Si [45–47]. Cr does not significantly affect the Co melting temperature [48] (and is in fact advantageous for the alloy since it stabilizes the ϵ-Co phase [19]). Fig. 2.3.1 shows the formation of a protective, quasi-continuous Cr layer after exposure to air at 1373 K.

In addition, a very thin layer containing CoO and $CoCr_2O_4$ forms on the alloy surface. Below these outer oxidation layers, internal SiO_2 precipitates form in the matrix with a network-like structure. These act as a partial barrier to the metal outward diffusion.

Fig. 2.3.2 shows the mass change due to oxidation in a Co-17Re-30Cr-2Si alloy in comparison to the conventional Co-base HT reference alloy X-40. As a result of the addition of Cr and Si, the oxidation behavior of the Co-Re alloy can match up to the reference alloy.

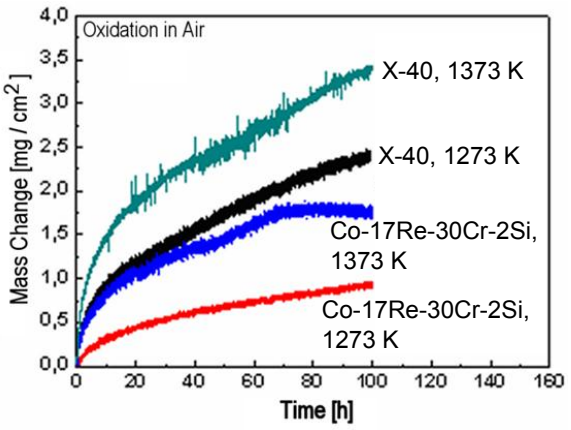

Figure 2.3.2: Oxidation behavior of Co-17Re-30Cr-2Si alloy at 1273 K compared to Co-base reference alloy X40. The mass-change as a result of oxidation is lower for the Co-Re reference alloy with Cr and Si additives. Adapted from [47, 49].

Chapter 3

Theory of Neutron Scattering and Precipitation Kinetics

3.1 Neutron scattering

In the following, a basic overview about the theory of neutron scattering is presented. It follows the textbooks [50–52]. *Fermi's golden rule* describes the transition probability of an initial eigenstate λ with energy E, spin σ and impulse k to a final eigenstate λ' with energy E', spin σ' and impulse k' of a neutron with mass m_n by adding a pertubative potential $\hat{U}$

$$\frac{\mathrm{d}^2\sigma}{\mathrm{d}\Omega d\omega} = \frac{m_n}{2\pi\hbar^2}\frac{k'}{k}\sum_{\lambda',\sigma'}\sum_{\lambda,\sigma} p_\lambda p_\sigma |\langle \vec{k}', \vec{\sigma}', \lambda', |\hat{U}|, \vec{k}, \vec{\sigma}, \lambda\rangle|^2 \times \delta(\hbar\omega + E_\lambda - E_{\lambda'}), \tag{3.1}$$

where the sum over the probabilities of all states

$$\sum_\lambda p_\lambda = \sum_\sigma p_\sigma = 1 \tag{3.2}$$

The δ function ensures conversion of energy of the process. If cold neutrons are used in small-angle scattering and diffraction, the statistical energy transfer $\hbar\omega$ is often very small, since the neutron energy is too low to change the energy of most nuclear processes. In this case $E_\lambda \approx E'_\lambda$, $k \approx k'$ and the δ-distribution in eq. (3.1) is essentially 1. The scattering process is considered elastic. Throughout this thesis, only nuclear scattering is considered, i.e. the spin states $\vec{\sigma}$ and $\vec{\sigma}'$ are neglected. Then, the scattering potential can be well approximated with the Fermi pseudopotential

$$\hat{U}(r) = \frac{2\pi\hbar^2}{m_n}\sum_j b_j \delta(\vec{R} - \hat{\mathbf{R}}_\mathbf{j}), \tag{3.3}$$

which assumes that the scattering centers (e.g. the atom nuclei) are much smaller than the neutron wavelength.

In the following considerations, the *kinematical* treatment of scattering theory is applied. It neglects multiple scattering effects and the solutions in the form of Bloch functions from the dynamical scattering theory. That is, it is assumed that the interaction of a neutron with a scatterer at position $\vec{R}_j$ does not depend on or interfer with the other scattering processes in the sample. For polycrystalline systems with high crystal statistics, this approximation is usually valid in neutron scattering, even if the density of scatterers is high. The locally

scattered intensities simply add over the illuminated volume V to the global *single differential cross-section*. The lengthy mathematical treatment of formula eq. (3.1) with the potential (3.3) can be found in the literature [51, 52]. The final cross section for neutron scattering is given by the formula

$$\frac{\mathrm{d}^2\sigma}{\mathrm{d}\Omega\,\mathrm{d}\omega} = \frac{k'}{k}\frac{1}{2\pi\hbar}\sum_{j,j'} b_j b_{j'} \int_{-\infty}^{\infty} \langle e^{-i\vec{Q}\cdot\hat{R}_{j'}(0)} e^{i\vec{Q}\cdot\hat{R}_j(t)}\rangle e^{-i\omega t}\mathrm{d}t \quad , \tag{3.4}$$

with the atomic scattering length b_j of atom j and the positions of atoms in the sample given by Heisenberg operators $\hat{R}_j(t)$. The matrix elements of eq. (3.4) describe the correlation of atom j and j' in space and time.

In the case of elastic scattering, i.e. no energy transfer between atom and neutron, the time dependence of eq. (3.4) is integrated. Then, the *elastic scattering cross section* reads

$$\frac{\mathrm{d}\sigma}{\mathrm{d}\Omega} = \int_{-\infty}^{\infty}\left(\frac{\mathrm{d}^2\sigma}{\mathrm{d}\Omega d\omega}\right)\mathrm{d}(\hbar\omega) = \sum_{j,j'} b_j b_{j'} \langle e^{-i\vec{Q}\cdot\hat{R}_{j'}} e^{i\vec{Q}\cdot\hat{R}_j}\rangle \quad . \tag{3.5}$$

This formalism can be further split into two contributions, depending on the coherent scattering from inter-atomic correlations $\left(\frac{\mathrm{d}\sigma}{\mathrm{d}\Omega}\right)_{\mathrm{coh}}$ and incoherent scattering from atomic self-correlations $\left(\frac{\mathrm{d}\sigma}{\mathrm{d}\Omega}\right)_{\mathrm{i}}$ of the N atoms in the sample. The sum over the scattering lengths b_j and $b_{j'}$ is averaged over the whole sample volume, assuming that there is no correlation between the scattering lengths. For the coherent and incoherent matrix elements this yields

$$\begin{aligned} \langle b_j b_{j'}\rangle &= \langle b_j\rangle\langle b_{j'}\rangle = \langle b\rangle^2 \quad \text{for } j \neq j' \\ \langle b_j b_{j'}\rangle &= \langle b_j^2\rangle = \langle b^2\rangle \quad \text{for } j = j' \quad . \end{aligned} \tag{3.6}$$

Further, the operator formalism is dropped for the following considerations, since the aim is to study the positions $\vec{R}_j$ of scattering sites with a (nearly) fixed position in space (the time dependence of $\vec{R}_j(t)$ is further discussed in section 3.1.1.2). Therewith, eq. (3.5) can be split into the coherent and incoherent scattering cross sections

$$\left(\frac{\mathrm{d}\sigma}{\mathrm{d}\Omega}\right)_{\mathrm{c}} = \langle b\rangle^2 \sum_{j,j'} \exp(-i\vec{Q}\cdot(\vec{R}_{j'} - \vec{R}_j)) \quad , \tag{3.7}$$

$$\left(\frac{\mathrm{d}\sigma}{\mathrm{d}\Omega}\right)_{\mathrm{i}} = (\langle b^2\rangle - \langle b\rangle^2) \sum_{j=j'} \exp(-i\vec{Q}\cdot(\vec{R}_{j'} - \vec{R}_j)) = N(\langle b^2\rangle - \langle b\rangle^2) \quad . \tag{3.8}$$

The coherent scattering cross section yields the information about spatial arrangement of the scattering structures. The incoherent scattering cross section only contains self-correlations of the scatterers and is therefore isotropic for neutron scattering on the Fermi pseudopotential eq. (3.3). It yields a constant background.

3.1.1 Neutron diffraction

ND is the application of elastic neutron scattering on atomic nuclei and/or their magnetic moments. A typical setting of the method is depicted in Fig. 3.1.1.

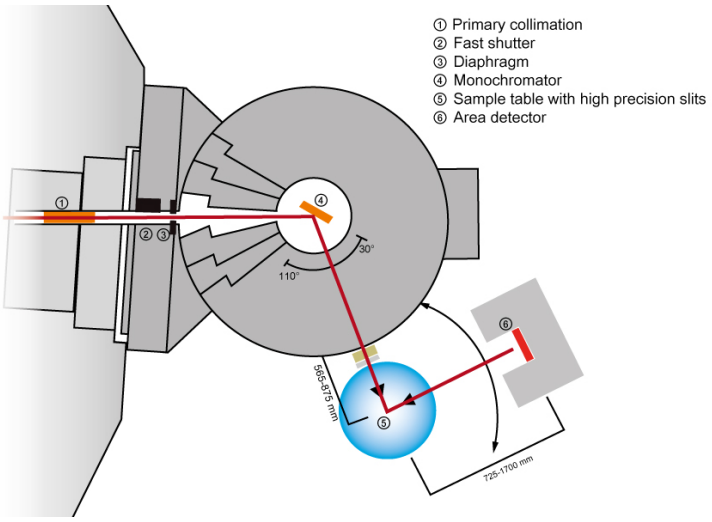

FIGURE 3.1.1: Stress-Spec instrument at MLZ. A single wavelength from the white neutron beam from the source is selected in the monochromator. Then, the monochromatized beam is directed on the sample. A movable detector system scans the angle dependent scattering from the sample. Adapted from [53].

3.1.1.1 Laue condition

The Laue equation yields the condition for diffraction on a crystal. The crystal consists of a Bravais lattice that is defined by the set of vectors $\vec{R} = \vec{l_j} + \vec{d_\alpha}$. The vectors $\vec{l_j}$ point on equal unit cells, that consist of atoms at the relative positions $\vec{d_\alpha}$. Introducing this in eq. (3.7) yields

$$\left(\frac{\mathrm{d}\sigma}{\mathrm{d}\Omega}\right)_\mathrm{c} = \sum_{j,j'} e^{-i\vec{Q}\cdot(\vec{l_j}-\vec{l_{j'}})} \sum_{\alpha,\alpha'} b_\alpha b_{\alpha'} e^{-i\vec{Q}\cdot(\vec{d_\alpha}-\vec{d_{\alpha'}})} \quad . \tag{3.9}$$

For the second sum in eq. (3.9), define $\vec{d} = \vec{d_\alpha} - \vec{d_{\alpha'}}$. Due to the symmetry of the unit cell, the sum can be simplified according to

$$\sum_{\alpha,\alpha'} b_\alpha b_{\alpha'} e^{-i\vec{Q}\cdot(\vec{d_\alpha}-\vec{d_{\alpha'}})} = \left| \sum_{\vec{d}} b_{\vec{d}} e^{-i\vec{Q}\cdot\vec{d}} \right|^2 \quad . \tag{3.10}$$

The first sum in eq. (3.9) can be reduced when using the theorem of lattice sums for a unit cell with volume v_0 [51]

$$\sum_{\vec{l}} e^{-i\vec{Q}\cdot l} = \frac{(2\pi)^3}{v_0} \sum_{\vec{\tau}} \delta(\vec{Q} - \vec{\tau}) \quad . \tag{3.11}$$

This yields for the coherent scattering cross section from N_0 unit cells

$$\left(\frac{\mathrm{d}\sigma}{\mathrm{d}\Omega}\right)_\mathrm{c} = N_0 \frac{(2\pi)^3}{v_0} \left| \sum_{\vec{d}} b_{\vec{d}} e^{-i\vec{Q}\cdot\vec{d}} \right|^2 \sum_{\vec{\tau}} \delta(\vec{Q} - \vec{\tau}) = N_0 \frac{(2\pi)^3}{v_0} \sum_{\vec{\tau}} |S_{\vec{\tau}}|^2 \delta(\vec{Q} - \vec{\tau}) \quad , \tag{3.12}$$

where the structure factor

$$S_{\vec{\tau}} = \sum_{\vec{d}} b_{\vec{d}} e^{-i\vec{Q}\cdot\vec{d}} \tag{3.13}$$

was introduced. The second step in eq. (3.12) can be performed, since the δ function assures that a scattering event only occurs if the Laue condition $\vec{Q} = \vec{\tau}$ is fulfilled, i.e. when the scattering vector is equal to a vector of the reciprocal lattice. Therefore, the scattered intensity depends on the structure factor $S_{\vec{\tau}}$.

3.1.1.2 Debye-Waller factor

When performing in-situ neutron diffraction (ND) experiments at high temperatures, it is crucial to consider the thermal excitement of the scattering atoms [54, 55]. The atoms can oscillate more than 10% of the lattice constant of the crystal [55]. Due to the oscillations of the lattice there is always a fraction of inelastically scattered neutrons, changing the modulus of outgoing wave vector k'. For ND, this yields a correction factor for the scattered intensity depending on the mean displacement of the atoms $u(t)$ and the modulus of the reciprocal lattice vector $\vec{G} = h\vec{a} + k\vec{b} + l\vec{c}$ of the peak

$$I = I_0 \exp\left(\frac{1}{3} G^2 \langle u^2(t)\rangle_t\right) \quad , \tag{3.14}$$

Assuming that the atoms scatter harmonically, their mean energy in 3 dimensions is temperature dependent and given by $3/2 k_B T$ (equipartition theorem). Therefore, their potential energy is given by

$$\langle U_t\rangle = \frac{1}{2} k \langle u^2(t)\rangle_t = \frac{1}{2} M\omega^2 \langle u^2(t)\rangle_t = \frac{3}{2} k_B T \quad , \tag{3.15}$$

with the stiffness constant k, atomic mass M and an oscillation frequency $\omega = \sqrt{k/M}$. With eq. (3.14), this yields

$$I_{hkl} = I_0 \exp\left(\frac{-k_B T}{M\omega^2} G^2\right) \quad , \tag{3.16}$$

for the reciprocal lattice indices (h, k, l) and $G = h\vec{a} + k\vec{b} + l\vec{c}$. Therefore, the scattering intensity of a diffraction peak decreases for larger (h, k, l) but its width remains constant. The inelastically scattered neutrons cause a diffusive background in the diffraction pattern that increases with T.

It is common to call the exponent of eq. (3.16) $2W(\vec{Q})$. Considering this so-called Debye-Waller factor, the elastic, coherent scattering reads

$$\left(\frac{\mathrm{d}\sigma}{\mathrm{d}\Omega}\right) = N_0 \frac{(2\pi)^3}{v_0} e^{-2W(\vec{Q})} \sum_{\vec{\tau}} |S_{\vec{\tau}}|^2 \delta(\vec{Q} - \vec{\tau}) \quad . \tag{3.17}$$

3.1.2 Small-Angle Neutron Scattering

In the following, the principles of a SANS experiment and of interpreting the results are presented.

3.1.2.1 A Small-Angle Neutron Scattering Experiment

In a classical SANS experiment, a beam of parallel neutrons is directed on a sample (Fig. 3.1.2a) to study scattering under low angles. The incoming neutrons have a specific wave vector $\vec{k}$ with wavelength $\lambda = 2\pi/k$. Behind the sample, there is a detector system, that is able to measure changes of the parameter $\vec{k} \rightarrow \vec{k}'$. The sample-detector-distance

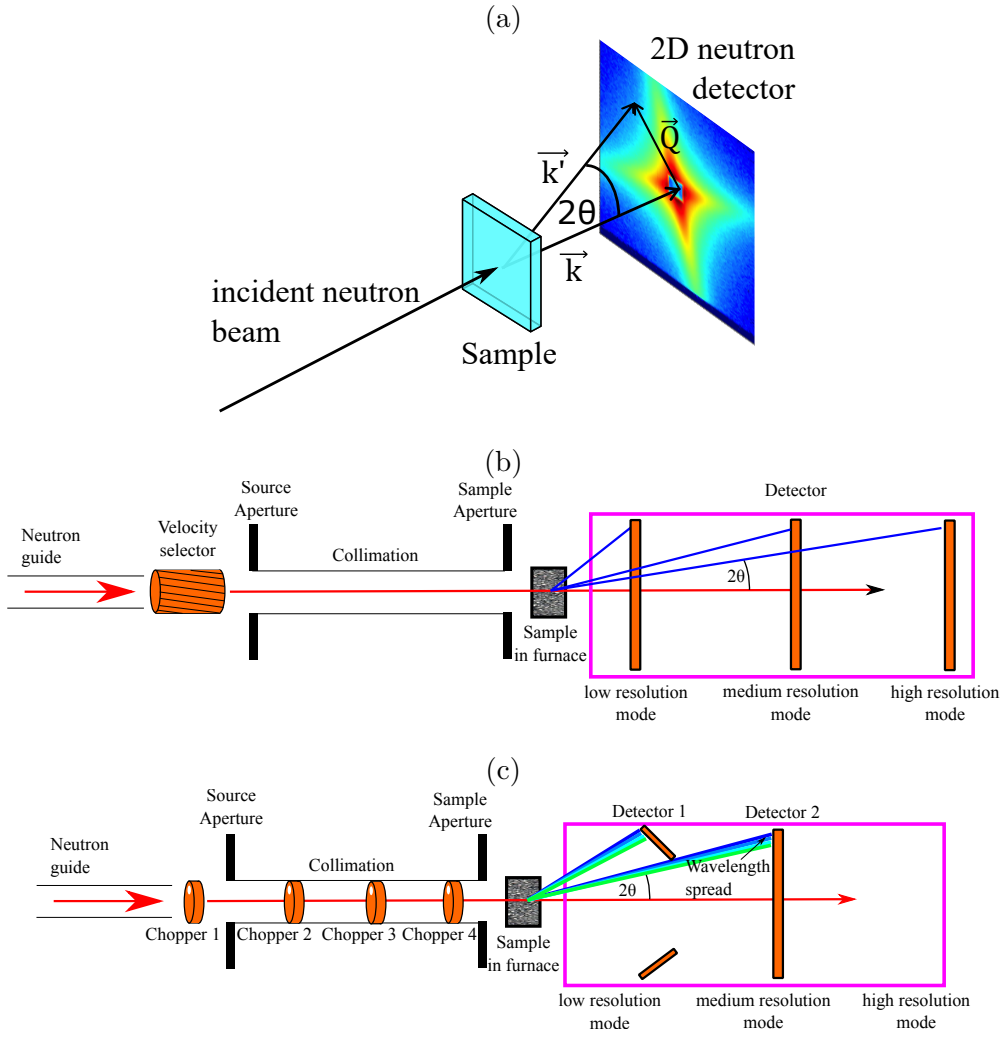

FIGURE 3.1.2: (a) basic principle of small-angle scattering; the sample is probed in transmission mode and the scattering under small angles is recorded. (b) A classical SANS setup, using a velocity selector to produce a monochromatic neutron beam, two apertures for collimation of the beam and several detector distances to maximize the measured Q-space. (c) TOF-SANS setup using a white, pulsed beam and a large detector area to maximize the recorded Q-space.

d_0, the neutron wavelength spread $\Delta\lambda/\lambda$ and a collimation system of length *col* define the resolution of the experiment.

In a classical SANS experiment a monochromatic neutron beam is created by a velocity selector. In order to cover a large Q-range, the collimation length and sample to detector distance are then varied several times while measuring the same sample at constant outer parameters (such as temperature or magnetic field) (Fig. 3.1.2b). The instruments use a $2D$ position sensitive detector. Since one measures scattering at small angles, i.e. for small $\vec{Q}$-vectors, the small-angle approximation $\vec{Q} \perp k$ usually applies.

Alternatively, an experiment can be performed in time of flight SANS (TOF-SANS) mode with a pulsed neutron beam. Instead of a constant monochromatic neutron beam, this method uses a chopper system and a pulsed white neutron beam. Due to the chopper system, the time resolved detector system can separate the different neutron wavelengths, which allows the measurement of a broader Q-range at one geometry (Fig. 3.1.2c).

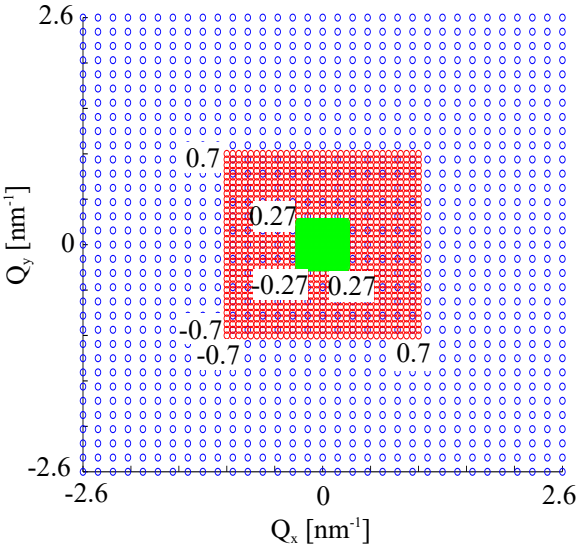

FIGURE 3.1.3: Solid angle projection of the varying Q-ranges from three measurements with different detector distances as seen from the sample. For increasing detector distance, the solid angle element size from the reciprocal space, decreases, but it is higher resolved. As an example, the distances $d_0 = 2, 8, 20\,\mathrm{m}$ are colored in blue, red and green.

The SANS setup gives rise to several smearing effects in both, real space and momentum space. Since the detector has a limited resolution, the geometry of the experiment has to be adjusted to the size of the structure under observation. The varying Q-range is depicted in Fig. 3.1.3. The resolution effects are discussed in detail in appendix A.

3.1.2.2 Scattering length and the SANS form factor

The fact that the scattering structures are of a much larger order than atomic nuclei (which act as the elastic scattering centers for neutrons) makes it possible to use an approximation of continuity for the elastic differential scattering cross-section eq. (3.17). Therefore, a transition from the discrete values of the scattering length b of individual atoms to a *scattering length density* $\rho(\vec{x}) := \langle b_i \rangle$ is done, i.e. ρ is the mean of scattering lengths b_i of i different atoms within an individual phase. Then the differential scattering cross section of a sample with volume V reads

$$I(\vec{Q}) \propto \left(\frac{d\sigma}{d\Omega}\right)_{\mathrm{c}} (\vec{Q}) = \left| \int_V \rho(x) e^{-i\vec{Q}\cdot\vec{x}} dx \right|^2 = |\mathcal{F}(\rho(\vec{Q}))|^2 \quad . \tag{3.18}$$

Therefore, the scattering from a SANS experiment is essentially the squared Fourier transform of the scattering length density function. Since ρ is usually a sufficiently smooth function (e.g. $\rho \in L_0^2(\mathbb{R}^3)$), convergence of this integral is generally given.

The task is to refine ρ from the measured intensity I. It is the defining factor for scattering of the sample and makes it possible to determine the kind and structure of particles.

If a sample with only local fluctuations of $\rho(x)$ from the main structure is investigated, the scattering length density reads

$$\rho(\vec{x}) = \langle \rho \rangle + \delta\rho(\vec{x}) \tag{3.19}$$

with the spatial average $\langle\rho\rangle$ of $\rho(\vec{x})$ in V and the fluctuation function $\delta\rho(\vec{x})$. The Fourier transform of the constant $\langle\rho\rangle$ in the integral of (3.18) is zero if $\vec{Q} \neq 0$ and hence

$$\left(\frac{d\sigma}{d\Omega}\right)_{\mathrm{c}}(\vec{Q}) = \left|\int_V \delta\rho(x) e^{-i\vec{Q}\cdot\vec{x}} dx\right|^2 . \tag{3.20}$$

In the simplest case, the system consists only of two phases, a matrix V_{m} and a set of mesoscopic scatterers V_{scat}

$$\rho(\vec{x}) = \begin{cases} \delta\rho, \vec{x} & \in V_{scat}, \\ \langle\rho\rangle, \vec{r} & \in V_m. \end{cases} \tag{3.21}$$

The integral (3.20) gives the same result, if eq. (3.21) is replaced by

$$\rho(\vec{x}) = \begin{cases} \Delta\rho = \delta\rho - \langle\rho\rangle, \vec{x} & \in V_{scat}, \\ 0, r & \in V_m. \end{cases} \tag{3.22}$$

The value $\Delta\rho$ is denoted as the *scattering contrast*. If the particles are *homogeneous*, that is $\Delta\rho = const.$, the scattering only depends on the value $\Delta\rho$ and the geometry of the particle

$$\left(\frac{d\sigma}{d\Omega}\right)_{\mathrm{c}}(\vec{Q}) = \Delta\rho^2 \left|\int_{V_{\mathrm{scat}}} e^{-i\vec{Q}\cdot\vec{x}} dx\right|^2 = \Delta\rho^2 F^2(\vec{Q}) \quad . \tag{3.23}$$

$F(\vec{Q})$ is the *form factor* of the scattering particle. Important form factors for the evaluation of precipitates are the *spherical, cylindrical* and *ellipsoidal* form factor. Explicit formulas are given in appendix B.1.

Remark 3.1 (i) The definition of the sets V_{m} and V_{scat} is arbitrary, due to Babinet's principle. In eq. (3.23), the same result is obtained for $\vec{Q} \neq 0$ if the two sets are interchanged (Fig. 3.1.4). However in material science, it is appropriate to define the material's matrix as V_{m} and scattering inhomogenieties as V_{scat}.

(ii) The SANS signal eq. (3.18) is smeared by the instrument resolution function K, which depends on the chosen geometry of the experiment. The SANS resolution functions are discussed in further detail in appendix A in section A.4.

(iii) The constant of proportionality in eq. (3.18) connects the recorded scattering pattern with the absolute values of the scattering phases. It can be calculated in order to determine the volume fractions of scatterers in the sample. Its calculation is discussed in the appendix A in section A.3.

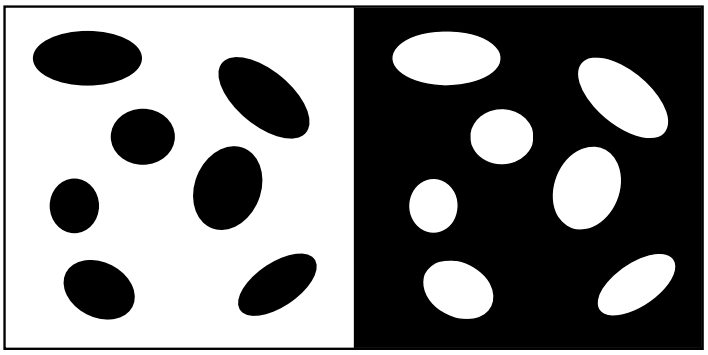

FIGURE 3.1.4: Particles in a sample. The white matrix V_m as background (left) and as particles (right). Both result in the same scattering image

3.1.2.3 Structure factor

If the set of scattering particles V_{scat} consists of N identical particles V^j_{scat} that are translated to the positions r_i in space, eq. (3.20) further simplifies to

$$\begin{aligned}\left(\frac{d\sigma}{d\Omega}\right)_{\text{c}}(\vec{Q}) &= \left|\int_{V_{\text{scat}}} \rho(x) e^{-i\vec{Q}\cdot\vec{x}} \mathrm{d}\vec{x}\right|^2 = \left|\sum_{j=1}^{N} \int_{V^j_{\text{scat}}} \rho(x) e^{-i\vec{Q}\cdot(\vec{r}_j+\vec{x})} \mathrm{d}\vec{x}\right|^2 \\ &= \left\{\sum_{j=1}^{N} e^{-i\vec{Q}\cdot\vec{r}_j} \int_{V^j_{\text{scat}}} \rho(x') e^{-i\vec{Q}\cdot\vec{x}'} \mathrm{d}\vec{x}'\right\} \left\{\sum_{k=1}^{N} e^{i\vec{Q}\cdot\vec{r}_k} \int_{V^k_{\text{scat}}} \rho(\vec{x}) e^{i\vec{Q}\cdot\vec{x}} \mathrm{d}\vec{x}\right\} \\ &= \frac{1}{N} \sum_{j=1}^{N} \sum_{k=1}^{N} e^{-i\vec{Q}\cdot(\vec{r}_j-\vec{r}_k)} N \int\limits_{V^j_{\text{scat}}} \rho(v) e^{-i\vec{Q}\cdot\vec{x}'} \mathrm{d}\vec{x}' \int\limits_{V^k_{\text{scat}}} \rho(u) e^{i\vec{Q}\cdot\vec{x}} \mathrm{d}\vec{x} \\ &= \frac{1}{N} \sum_{j=1}^{N} \sum_{k=1}^{N} e^{-i\vec{Q}\cdot(\vec{r}_j-\vec{r}_k)} N F_j(\vec{Q}) \overline{F_k(\vec{Q})} \quad .\end{aligned} \tag{3.24}$$

The exponential term arises from the spatial arrangement of the scattering particles and produces interference effects and is called the *structure factor* S. Throughout this thesis the monodisperse approximation is applied, i.e. it is assumed that the sum decomposes to

$$\left(\frac{d\sigma}{d\Omega}\right)_{\text{c}}(\vec{Q}) = S(\vec{Q})\, F^2(\vec{Q}) \quad , \tag{3.25}$$

i.e. the structure factor is simply multiplied with the scattering signal of the form factor convoluted with its size distribution. This simple model was chosen since the structure factor is usually weak in the case of Co-Re alloys with TaC volume fractions around 1vol.%. Therefore, the effect of the structure factor is very weak and hardly visible in the SANS data. For higher volume fractions, the local monodisperse approximation [56] or the decoupling approach [57] are usually the methods of choice for SANS. The former assumes that the size distribution is a global effect over the sample and locally the scatteres are of the same size. The latter is the opposite approach and assumes small polydispersities that are completely independent from the scatterer.

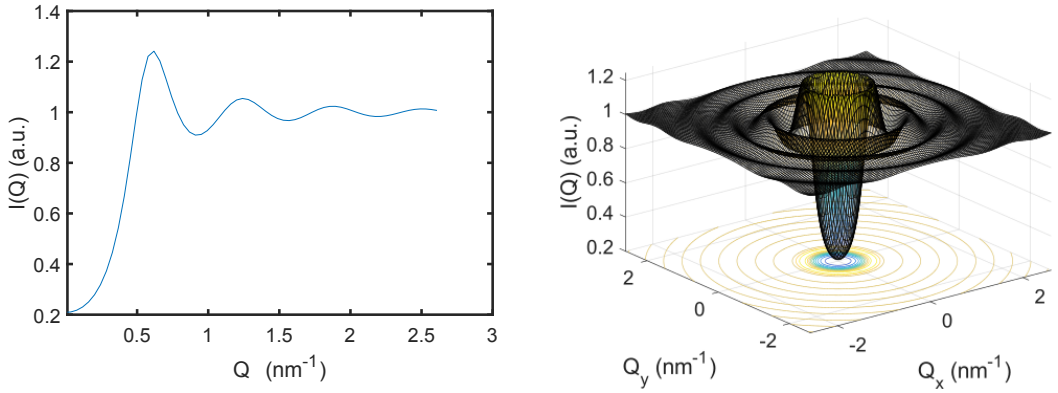

FIGURE 3.1.5: Structure factor from Percus and Yevick in a 1D azimuthal averaged and a 2D representation.

The structure factor S can be solved analytically under the assumption that a scattering particle is surrounded by a potential of the form

$$U(r) = \begin{cases} \infty & 0 < r < \sigma \quad , \\ 0 & r > \sigma \quad . \end{cases} \tag{3.26}$$

The result is the famous analytical formula from Percus and Yevick [58], depicted in Fig. 3.1.5.

3.1.2.4 Size Distributions

If a parameter of the form factor is distributed $F(\vec{Q}) = F(\vec{Q}, x)$, e.g. if the particles do not have an unimodal morphology, the signal from the different particles has to be added. This can be taken into account by a summation over all scattering signals

$$\left(\frac{d\sigma}{d\Omega}\right)_{\mathrm{c}}(\vec{Q}) = \sum_i \int_0^\infty N(x) F^2(\vec{Q}, x)\ \mathrm{d}x \quad . \tag{3.27}$$

Since the number of particles is usually very large, the sum can be replaced with an integral and the variation of the parameter is subjected to a distribution density

$$\left(\frac{d\sigma}{d\Omega}\right)_{\mathrm{c}}(\vec{Q}) = \int_0^\infty N(x) F^2(\vec{Q}, x)\ \mathrm{d}x \tag{3.28}$$

or in the case of the monodisperse approximation of a structure factor in eq. (3.25)

$$\left(\frac{d\sigma}{d\Omega}\right)_{\mathrm{c}}(\vec{Q}) = \left(\int_0^\infty N(x) F^2(\vec{Q}, x)\ \mathrm{d}x\right) S(\vec{Q}) \quad . \tag{3.29}$$

Common choices for the distribution are the Gaussian normal distribution $\mathcal{N}(x, p)$ or logarithmic normal distribution $\mathcal{N}(\log(x), p)$ with distribution parameters p. The logarithmic describes a parameter space x, where $\log(x)$ has a normal distribution, which is often the case due to thermodynamics [59].

3.1.2.5 Autocorrelation

The spatial autocorrelation function of the scattering length density ρ is defined by

$$\gamma(\vec{x}) = \frac{1}{V}\rho\hat{*}\rho(\vec{x}) = \frac{1}{V}\int_{\mathbb{R}^n} \rho(\vec{x}+\vec{\tau})\rho(\vec{\tau})\ d\vec{\tau} \quad , \tag{3.30}$$

for the sample volume V. The Wiener-Khinchin theorem [60] states that the SAS signal $I(\vec{Q})$ is the Fourier transform of the autocorrelation γ (see eq. (3.18))

$$\mathcal{F}(V\gamma) = |\mathcal{F}(\rho)|^2 \quad . \tag{3.31}$$

3.1.2.6 Azimuthally averaged data

For an isotropic particle (such as a single sphere), the SAS intensity eq. (3.23) only depends on the modulus of the scattering vector $Q = |\vec{Q}|$. Therefore, the azimuthally averaged scattering intensity contains all information about the scatterer and is calculated from the $2D$ SAS pattern. The azimuthally averaged scattering intensity is given by

$$\left(\frac{\mathrm{d}\Sigma}{\mathrm{d}\Omega}\right)(Q) = \frac{1}{2\pi}\int_0^{2\pi}\left(\frac{\mathrm{d}\sigma}{\mathrm{d}\Omega}\right)(Q\sin\varphi, Q\cos\varphi)\ \mathrm{d}\varphi \quad . \tag{3.32}$$

The azimuthally averaged coherent and incoherent scattering cross sections are defined equally.

3.1.2.7 Integral Parameters

An appropriate modeling is quite complex for complicated samples. Some parameters can be directly attained from the azimuthally averaged coherent scattering cross section in reciprocal space $\left(\frac{\mathrm{d}\Sigma}{\mathrm{d}\Omega}\right)_\mathrm{c}$, without or with very little knowledge about the sample structure. Fig. 3.1.6 shows a simulation of the $1D$ SANS signal from spherical particles (eq. (B.1)), with a Gaussian size distribution with a mean radius $R = 40$ nm and standard deviation $\sigma = 0.16$. In the following, the most important integral parameters are discussed on this example.

Scattering Invariant Since the scattering signal is the Fourier transform of the autocorrelation function eq. (3.31), one gets

$$V\gamma(r) = \frac{1}{2\pi^2}\int_0^\infty \mathrm{d}QQ^2\left(\frac{\mathrm{d}\Sigma}{\mathrm{d}\Omega}\right)_\mathrm{c}(Q)\frac{\sin Qr}{Qr} \quad , \tag{3.33}$$

where the the azimuthal kernel of the Fourier transform $Q^2\sin(Qr)/Qr$ was used. The function $Q \mapsto Q^2\left(\mathrm{d}\Sigma/\mathrm{d}\Omega\right)_\mathrm{c}(Q)$ is plotted in Fig. 3.1.6c. For a volume fraction w_p of scatterers in a dilute two-phase system, the eqs. (3.30) and (3.33) yield at $r = 0$

$$V\gamma(0) = \int_{\mathbb{R}^n}\rho(\vec{\tau})\rho(\vec{\tau})\ d\vec{\tau} = V\bar{\eta^2} = \frac{1}{2\pi^2}\int_0^\infty \mathrm{d}QQ^2\left(\frac{\mathrm{d}\Sigma}{\mathrm{d}\Omega}\right)_\mathrm{c}(Q) \quad , \tag{3.34}$$

with the average quadratic deviation of the scattering length density $\bar{\eta^2} = \eta_1^2 w_p + \eta_2^2(1-w_p)$ defined by the scattering length differences η_1, η_2 of the two phases from their mean scattering

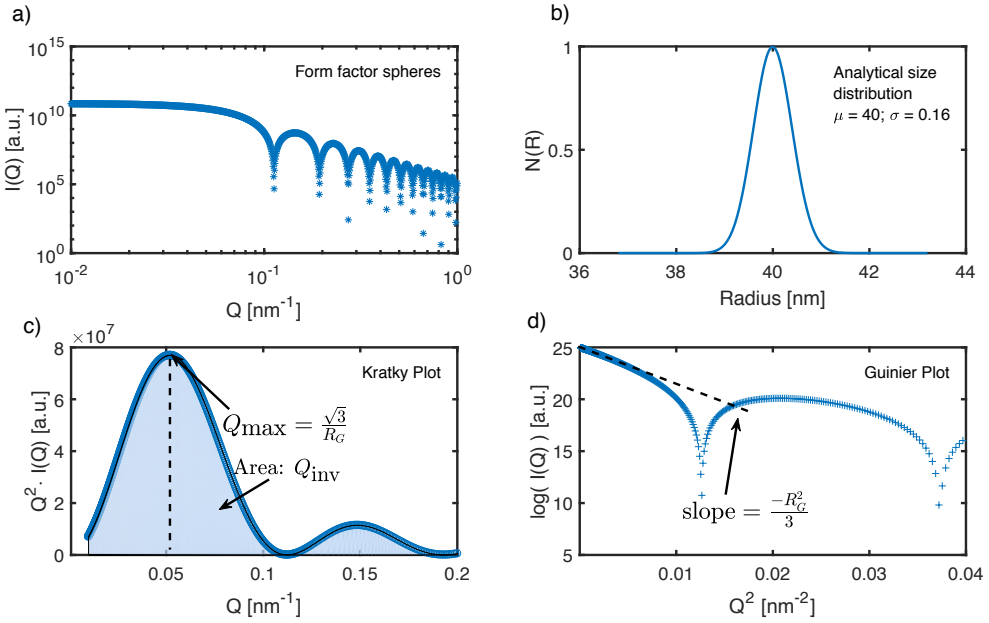

FIGURE 3.1.6: (a) Simulated SANS pattern Q vs $I(Q) = (\mathrm{d}\Sigma/\mathrm{d}\Omega)(Q)$ from (b) Gaussian distributed spherical particles. (c) Kratky plot $Q \to Q^2 \times (\mathrm{d}\Sigma/\mathrm{d}\Omega)_{\mathrm{c}}(Q)$ for determination of scattering invariant Q_{inv} and radius of gyration R_G and (d) Guinier plot $Q^2 \to \log((\mathrm{d}\Sigma/\mathrm{d}\Omega)_{\mathrm{c}}(Q))$ for determination of R_G. For the present example, (c) yields $R_G\sqrt{3}/Q_{\text{max}} = 34.6\,\text{nm}$, and (d) $R_G = \sqrt{-3m} = 31.1\,\text{nm}$, where m is the slope determined by a linear regression fit to the curve. Therefore, the methods yield comparable values to the true mean size of 40 nm.

length density $\bar{\rho} = (\bar{\rho} - \eta_1)w_p + (\bar{\rho} + \eta_2)(1 - w_p)$. Therefore, the scattering contrast is given by $\Delta\rho = \eta_1 + \eta_2$. Rearranging the terms yields [61]

$$\bar{\eta}^2 = \Delta\rho^2 w_p(1 - w_p) \quad . \tag{3.35}$$

This motivates the definition of the scattering invariant

$$Q_{\text{inv}} = \int \mathrm{d}Q\, Q^2 \left(\frac{\mathrm{d}\Sigma}{\mathrm{d}\Omega}\right)_{\mathrm{c}}(Q) = 2\pi^2 V \Delta\rho^2 w_p(1 - w_p) \quad . \tag{3.36}$$

which is independent of the shape of the scattering structure [61]. Q_{inv} is directly related to the volume fraction of scattering particles, without further knowledge of the particle's morphology or a model. For $w_p \approx 1\%$ $1 - w_p \approx 1$ and the scattering invariant is directly proportional to the volume fraction w_p. The integral of the curve depicted in Fig. 3.1.6c is therefore the *scattering volume*, i.e. the volume of the scattering particles.

Radius of Gyration The Guinier law describes the scattering behavior in the limit $Q \to 0$. For isotropic scattering (e.g. randomly distributed particles with maximum size of D), the *radius of gyration* is defined using the autocorrelation function eq. (3.30) [62, 63]

$$R_G^2 = \frac{1}{2}\frac{\int_{V_{\text{part}}} r^2\gamma(r)dr}{\int_{V_{\text{part}}} \gamma(r)dr}. \tag{3.37}$$

The radius of gyration R_G can be interpreted as the root mean square of the distances between scattering particles from their center of gravity and can be considered an intuitive measure of the spatial extension of a particle. The Guinier law for spheres states for $QR_G \ll 1$

$$\left(\frac{\mathrm{d}\Sigma}{\mathrm{d}\Omega}\right)_{\mathrm{c}}(Q) = e^{-(QR_G)^2/3}. \tag{3.38}$$

Therefore, the law gives a statement for the size of the scattering objects. Fig. 3.1.6d shows the scattering signal of spherical particles in the Guinier representation $Q^2 \mapsto \log((\mathrm{d}\Sigma/\mathrm{d}\Omega)_{\mathrm{c}}(Q))$. Considering eq. (3.38) the slope of this function for $Q \to 0$ can be used to extract the radius of gyration.

Porod scattering Scattering from large scale structures with sharp face boundaries and random spatial orientation is well known to follow the Porod scattering law [62]. The law gives a result for the scattering behavior in the limit $Q \to \infty$

$$Q^4 \left(\frac{\mathrm{d}\Sigma}{\mathrm{d}\Omega}\right)_{\mathrm{c}}(Q) \xrightarrow{Q\to\infty} 2\pi\Delta\rho^2 S = \text{const.} \tag{3.39}$$

S is the total area size of all surfaces from large scale scattering structures in the sample.

If the large scale structures are anisotropic and have a spatial orientation relationship, Porod scattering can also be anisotropic. A generalization of Porod scattering for this case is discussed in appendix B, section B.2.

Incoherent scattering The elastic scattering signal of a sample consists of the coherent and incoherent scattering contribution (eq. (3.7)). In order to evaluate the above described integral parameters, it is therefore necessary to correct for the incoherent scattering $(\mathrm{d}\Sigma/\mathrm{d}\Omega)_{\mathrm{i}}$. This can be accomplished by measuring the SANS signal up to large Q-values (e.g. $Q > 3\,\mathrm{nm}^{-3}$), where the signal is usually purely incoherent if the scattering particles are not extremely small (e.g. $R < 2\pi/3\,\mathrm{nm} = 2.1\,\mathrm{nm}$). Once the incoherent scattering signal from a samples with fixed composition is known, it can be used for any follow up measurements, since the incoherent signal only depends on the nominal composition.

3.1.2.8 Krakty, Guinier and Porod surfaces

The Kratky function $Q \mapsto Q^2 \times (\mathrm{d}\Sigma/\mathrm{d}\Omega)_{\mathrm{c}}(Q)$ is used to define the Kratky surface

$$K(Q,x) = Q^2 \times \left(\frac{\mathrm{d}\Sigma}{\mathrm{d}\Omega}\right)_{\mathrm{c}}(Q,x) \quad . \tag{3.40}$$

$x = x(t)$ is an outer parameter that can vary over time t (e.g. the temperature T). Since the integral below the function $K(Q,x_0)$ for a fixed parameter x_0 yields the volume fraction of scattering phase (cf.eq. (3.36)), the Kratky surface reflects the evolution of scattering phase with the parameter x.

Similarly, the Guinier function $Q^2 \mapsto \log((\mathrm{d}\Sigma/\mathrm{d}\Omega)_{\mathrm{c}}(Q))$ defines the Guinier surface

$$\begin{aligned} G(Q',x) &= \log\left(\left(\frac{\mathrm{d}\Sigma}{\mathrm{d}\Omega}\right)_{\mathrm{c}}(\sqrt{Q'},x)\right) \quad , \\ Q' &= Q^2 \quad . \end{aligned} \tag{3.41}$$

The partial derivative $\partial G/\partial Q'$ of the Guinier surface yields the evolution of radius of gyration of the scattering phase with the parameter x.

The Porod function $Q \mapsto A + B \cdot Q^4$ defines the Porod surface

$$P(Q, x) = A(x) + B(x) \cdot Q^4 \quad . \tag{3.42}$$

The Porod surface represents the background scattering from incoherent scattering $A = (\mathrm{d}\Sigma/\mathrm{d}\Omega)_\mathrm{i}$, which might change with the outer parameter (e.g. with temperature) and the total amount of scattering from large scale structures $B(x)$.

In a real experiment, the scattering intensity $(\mathrm{d}\Sigma/\mathrm{d}\Omega)_\mathrm{c}(Q, x)$ is often recorded while x is varied from x_0 to x_1

$$\left(\frac{\mathrm{d}\Sigma}{\mathrm{d}\Omega}\right)_\mathrm{c}(Q, x) = \int_{x_0}^{x_1} \left(\frac{\mathrm{d}\Sigma}{\mathrm{d}\Omega}\right)_\mathrm{c}(Q, x')\mathrm{d}x' \quad . \tag{3.43}$$

Although the SANS signal from each measurement might be noisy when performing only short exposure times, the course of this integral function is well defined and can be evaluated statistically for Kratky, Guinier or Porod surface. This yields the scattering volume from the Kratky surface and the mean particle radius from the Guinier surface from an in-situ scattering experiment.

3.1.2.9 Multiple Scattering

For elastic scattering, all atoms are nearly scattering in phase near $Q = 0$. Due to the intense signal, there is a higher probability for neutrons to scatter multiply. As a consequence, the scattering can depend on the sample thickness. For that reason, the measured samples within this work were confined to a thickness of ~ 1 mm. This leads to a significant neutron absorption from Re in the neutron experiments, especially for very small Q at $\lambda = 1.2\,\mathrm{nm}$ wavelength. However, multiple scattering from the non-dense system of fine TaC was negligible in their Q-range, which is mainly covered by neutrons with $\lambda = 0.6$ nm in the respective SANS experiments.

3.2 Kinetics of precipitates in alloys

Precipitation of a second phase of precipitates β in an supersaturated alloy matrix α_su is a transformation of the form

$$\alpha_\mathrm{su} \rightarrow \alpha + \beta \quad . \tag{3.44}$$

Usually, they are first-order phase transitions, since entropy (derivative of the Gibbs energy with respect to the temperature) and volume (derivative of the Gibbs energy with respect to the pressure) are discontinuous. Precipitation reactions in alloys are often induced by diffusion processes along concentration gradients in the supersaturated matrix α_su during changes of the temperature. The second phase β precipitates in order to achieve thermodynamic equilibrium of the matrix phase α. Thermodynamic equilibrium is reached in the global minimum of the free Gibbs energy G. Three major processes are involved in this process, namely nucleation, growth and coarsening. The two former processes are driven by the change of Gibbs free energy of the transformation. When the volume fraction of the

precipitating phase reaches equilibrium with the matrix phase at an actual holding temperature, they are already completed. In contrast, the coarsening of particles is driven by the reduction of surface energy in the system and may theoretically continue until one single particle is left over. However, it is crucial that the coarsening rate is very low and the particle size remains small for a long lapse of time to assure an effective strengthening of the alloy. The classical Kampmann-Wagner numerical (KWN) models are readily used to model precipitation kinetics of solute-rich particles from a supersaturated phase [64–66], while the Lifshitz-Slyozov-Wagner theories describe the precipitate coarsening [67–69].

The precipitation kinetics were measured by in-situ SANS during isochronal (during temperature changes with a constant rate) and isothermal (at constant temperature) aging of the Co-Re alloys. In the following, the theory for an adapted KWN multi-class model for kinetics during isochronal cooling (i.e. with constant cooling rate) is discussed.

3.2.1 Classic nucleation theory

Nucleation is an energy-driven process in classic theory that yields an expression for the formation rate of stable second-phase nuclei within a supersaturated primary parent phase [23, 70–75]. If the nucleation is spontaneous within fluids or perfect solid solutions, the process is homogeneous. The driving force for nucleation is the reduction in chemical Gibbs energy. Nucleation is prompted by a release of energy that is provided by a transformation of the crystal structure or a change of the temperature dependent chemical equilibrium. Due to the nucleation of a new phase, the overall Gibbs energy between particle and the parent phase is changed according to:

$$\Delta G = \Delta G_S + \Delta G_V + \Delta G_{EL} = 4\pi r^2 \Gamma + \frac{4}{3}\pi r^3 (\Delta g_v + \Delta g_{el}) \tag{3.45}$$

where ΔG_V is the Gibbs energy change of the transformation, ΔG_{EL} the elastic strain energy induced by the lattice misfit between coherent second-phase particle and parent phase, ΔG_S the interface energy between the matrix and the precipitate and Γ is the interfacial tension between the developing surface and solution. Δg_v, Δg_{el} and Δg_s denote the respective values per unit volume. The transformation has to overcome a nucleation barrier and the rate of nucleation depends on the amount of energy fluctuations in the solute. These fluctuations can be described by the Arrhenius reaction velocity equation [76]

$$\dot{N}(T(t)) = N_0 \exp(-\Delta G / k_B T), \tag{3.46}$$

with the Boltzmann constant k_B and a material depending coefficient N_0. Since the thermodynamic potential G is minimized in chemical equilibrium, a phase transformation occurs if $\Delta G < 0$. In the case of incoherent nucleation the elastic strain field is much less disturbed and therefore $\Delta g_{el} \approx 0$.

According to the classical Kampmann-Wagner approach [77], the constant in eq. (3.46) is given by

$$N_0 = \omega Z \beta^* \quad , \tag{3.47}$$

with a material specific characteristic frequency factor ω and the Zeldovich factor [66]

$$Z = \left(\frac{\Delta G}{3\pi k_B T n^{*2}} \right)^{1/2} \quad , \tag{3.48}$$

where n^* is the number of atoms within a particle of critical size. The non-equilibrium factor Z takes into account that thermal excitation can destabilize a formed nucleus. β^* is the atomic attachment rate and takes into account the jump frequency for atomic transport D_N

$$\beta^* = 4\pi r^{*2} \cdot \frac{C_\alpha}{a_\alpha^2} \cdot \frac{D_N}{a_\alpha^2} \quad . \tag{3.49}$$

In addition, it is experimentally observed that the nucleation is not starting instantaneously, but after a certain time lag τ that is required to establish a steady-state size distribution of solute clusters

$$\exp\left(-\frac{\tau}{t}\right) \quad , \tag{3.50}$$

where [78]

$$\tau = \frac{6 k_B T n^{*2}}{\beta^* \Delta G^*} \quad . \tag{3.51}$$

The values Γ and ΔG_V in eq. (3.45) are of opposite sign. Therefore, the Gibbs energy of formation ΔG has a maximum for a critical radius r^* according to

$$\frac{\mathrm{d}\Delta G^*}{\mathrm{d}r}\Big|_{r=r^*} = 0, \tag{3.52}$$

which yields

$$r^* = \frac{-2\Gamma}{\Delta g_v + \Delta g_{el}} \quad . \tag{3.53}$$

$\Delta g_v + \Delta g_{el} < 0$ is a precondition for nucleation. Particles with $r < r^*$ will tend to shrink, while particles with $r > r^*$ grow (Fig. 3.2.1). In order to reach the critical size, the process requires a critical amount of free energy

$$\Delta G^* = \frac{4\pi\Gamma r^{*2}}{3} = \frac{16\pi\Gamma^3}{3(\Delta g_v + \Delta g_{el})^2} \quad . \tag{3.54}$$

At this point, there is no full thermodynamic assessment available for the Co-Re system. Therefore, the maximum chemical driving force method is used to evaluate the $\Delta g_v = \Delta g_v(C_\alpha)$ by the tangent construction of the two phases matrix and precipitate [64, 79]. This yields

$$-\Delta g_v = \frac{RT}{v_\beta} \left(C_\beta \log\left(\frac{C_\alpha}{C_{\alpha,\mathrm{eq}}}\right) + (1 - C_\beta) \log\left(\frac{1 - C_\alpha}{1 - C_{\alpha,\mathrm{eq}}}\right) \right) \quad . \tag{3.55}$$

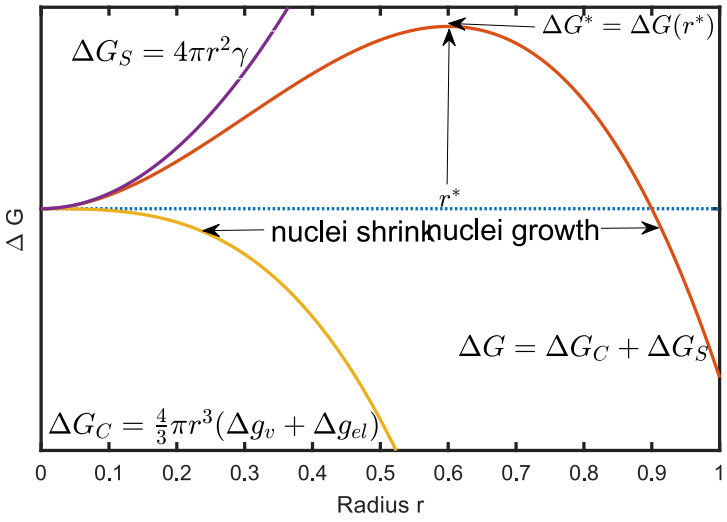

FIGURE 3.2.1: Scheme of the Gibbs free energy of nucleation. Particles of a size below of the critical size r^* tend to shrink, while larger particles grow.

Combining the eqs. (3.48), (3.49), (3.50), (3.51) yields the temperature and time depended nucleation rate

$$\dot{N}(T(t)) = \frac{2(C_\alpha)^2 v_\beta}{a_\alpha^4}\left(\frac{\Gamma}{k_B T}\right)^{1/2} D_{0,N}\exp\left(-\frac{Q_N}{RT}\right) \times \exp\left(-\frac{16\pi}{3}\frac{\Gamma^3}{(\Delta g_v + \Delta g_{el})^2 k_B T}\right) \times \exp\left(-\frac{8a_\beta^4}{v_\beta^2 C_\alpha D_N}\frac{\Gamma k_B T}{(\Delta g_v + \Delta g_{el})^2}\frac{1}{t}\right) \quad . \tag{3.56}$$

For non-isothermal processes, i.e. if the temperature T is not constant, the chain rule is applied

$$\frac{\mathrm{d}}{\mathrm{d}T}N(T(t)) = \dot{N}(T(t))\frac{\mathrm{d}t}{\mathrm{d}T} \quad . \tag{3.57}$$

This formula is utilized for the cooling experiments where the nucleation rate is utilized for changing temperature.

Remark 3.2 For simplification of the problem, the nucleation was considered to be homogeneous, i.e. to be spontaneous. This is rarely the case in real alloys, since there often exist impurities such as defects or grain boundaries (gb), acting as nucleation sites. In this case, the nucleation is heterogeneous and the activation energy for nucleation might be considerably lowered. The results have to be treated within this limitation.

3.2.2 Growth

After the nucleation of N particles with size $r > r^*$, it is energetically favorable to reduce the total surface area A. Therefore, there is a driving force for particle growth of particles with larger volume V – where V/A is larger – at the cost of smaller particles – where V/A is smaller. For the non-isothermal state, a rate equation for particle growth depends on the diffusion D of the solute β in the matrix α. The temperature dependence of the concentration

of the solute in the matrix C_α can be given for $3D$ growth according to [80]

$$\frac{\partial C_\alpha(r,T)}{\partial T} = \frac{\partial C_\alpha(r,T)}{\partial t}\frac{\partial t}{\partial T} = \phi^{-1} D(T)\nabla^2 C_\alpha(r,T) + \frac{2D(T)}{r}\nabla C_\alpha(r,T) \quad . \tag{3.58}$$

The concentration C_α changes depending on temperature T and distance from a transformed particle r. There is no analytical solution to this partial differential equation [81]. To solve eq. (3.58), a linear solute concentration profile is assumed around each nucleated particle throughout this thesis. In this case, a rate equation for diffusion controlled growth is given by [66, 82]

$$\frac{\mathrm{d}r}{\mathrm{d}t} = \frac{C_\alpha - C_{\alpha,\mathrm{int}}}{v_\alpha/v_\beta C_{\beta,\mathrm{int}} - C_{\alpha,\mathrm{int}}}\frac{D_G(T)}{r} \quad . \tag{3.59}$$

v_α and v_β are the molar volumes of matrix and precipitate, $C_{\alpha,\mathrm{int}}$ is the solute concentration at the particle interface and precipitate and D_G is the diffusion coefficient. The concentration at particle surface is given by the particle radius r and the Gibbs-Thomson equation [83]

$$C_{\alpha,\mathrm{int}}(r,T) = C_\alpha(r\to\infty)\exp\left(\frac{2\Gamma v}{RT\ r}\right) \quad . \tag{3.60}$$

During isochronal cooling with a constant cooling rate $\phi = \mathrm{d}T/\mathrm{d}t$, the temperature dependence of the growth rate is given by

$$\frac{\mathrm{d}r}{\mathrm{d}T} = \frac{\mathrm{d}r}{\mathrm{d}t}\frac{\mathrm{d}t}{\mathrm{d}T} = \frac{1}{\phi}\frac{C_\alpha - C_{\alpha,\mathrm{int}}(r,T)}{v_\alpha/v_\beta C_\beta - C_{\alpha,\mathrm{int}}(r,T)}\frac{D_G(T)}{r} \quad . \tag{3.61}$$

Therefore, for non-isothermal precipitation, the rate depends on the diffusion at a given temperature and the diffusion gradient between the concentration in the matrix C_α and at the precipitate/matrix interface $C_{\alpha,\mathrm{int}}$. These values change constantly during isochronal cooling, since an increased volume fraction of precipitates lowers the solute concentration C_α and $C_{\alpha,\mathrm{int}}(r,T)$ depends on the particle size r and the changing temperature T. As a consequence of the Gibbs-Thomson effect, the state of equilibrium between matrix and precipitate phase can strongly deviate from the state of equilibrium for small particle sizes, i.e. for a large ratio of interface area to particle volume.

In this thesis, the equilibrium solute concentration $C_\alpha(T)$ will be experimentally determined by in-situ ND and phase analysis of the recorded patterns at varying temperatures (cf. section 5.2).

3.2.3 Lifshitz-Slyozov-Wagner Theory of particle coarsening

There are two mechanisms that result in a particle coarsening. The general theoretical approach of Zener's theory describes particle coarsening by long-range diffusion due to a solute concentration gradient in the matrix [82, 84], while Ostwald ripening theory explains coarsening due to the decrease of total surface energy of the system [67, 68]. The basic equation is the Gibbs-Thomson equation (3.60) for the surface concentration of a solute in equilibrium. The theory from Lifshitz-Slyozov-Wagner (LSW) for *diffusion-limited coarsening* growth is based on the following three fundamental equations [85].

$$\frac{\mathrm{d}r}{\mathrm{d}t} = \frac{2\Gamma D C_{\alpha,\mathrm{eq}}}{{C_\beta}^2 RT}\frac{1}{r}\left(\frac{1}{r^*} - \frac{1}{r}\right) \quad , \tag{3.62}$$

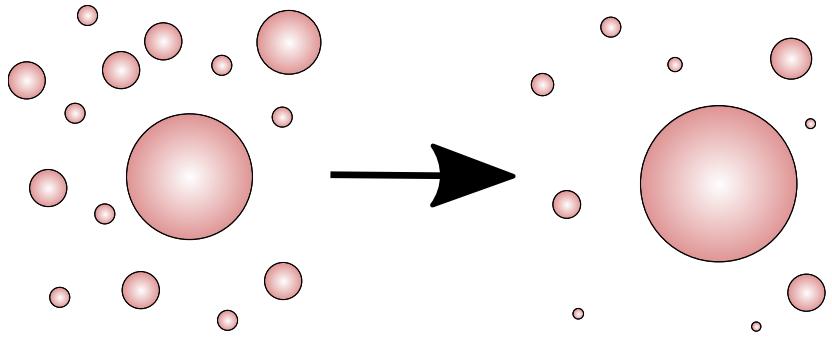

FIGURE 3.2.2: Ostwald ripening: Larger particles grow at the expense of smaller ones. The driving force for coarsening can be the diffusion concentration gradient or the decrease in total surface free energy.

$$\frac{\partial f}{\partial t} + \frac{\partial (N\dot{r})}{\partial r} = 0 \quad , \tag{3.63}$$

$$\frac{C_0 - C_{\alpha,\mathrm{eq}}}{C_{\alpha,\mathrm{eq}}} = \frac{C_\alpha - C_{\alpha,\mathrm{eq}}}{C_{\alpha,\mathrm{eq}}} + \frac{C_\beta}{C_{\alpha,\mathrm{eq}}} \frac{4\pi}{3} \int_0^\infty r^3 N(r,t) \mathrm{d}r \quad . \tag{3.64}$$

Equation (3.62) is a differential equation that describes diffusion-limited growth of a particle with radius r with consisting of a solute with effective diffusion coefficient D. The growth rate depends on the volume concentration of the segregating component in the newly evolving phase C_β. Equation (3.63) is the continuity equation for a size distribution $N(r,t)$ and equation (3.64) an implication from the conservation of matter with C_0 the initial concentration of the segregating component and C_α the concentration in the matrix at sufficient distance from a particle. This set of equations leads to

$$\langle r(t) \rangle^3 - \langle r_0 \rangle^3 = \frac{8\Gamma v_\beta^2 D C_{\alpha,\mathrm{eq}}}{9 C_\beta^2 RT} t = Kt \quad . \tag{3.65}$$

K is the rate constant of coarsening.

In the case that *reaction-limited* growth is the dominant factor, one replaces eq. (3.62) with

$$\frac{\mathrm{d}r}{\mathrm{d}t} = \frac{2\Gamma C_{\alpha,\mathrm{eq}}}{{C_\beta}^2 R} \frac{1}{l_0} \left(\frac{1}{r^*} - \frac{1}{r} \right) \quad , \tag{3.66}$$

were l_0 is a length of molecular dimensions. In this case, the result for particle growth is

$$\langle r(t) \rangle^2 - \langle r_0 \rangle^2 = \frac{K}{l_0} t \quad . \tag{3.67}$$

3.2.4 Modified LSW theory

The standard LSW theory usually predicts size distributions that cannot be experimentally confirmed [69]. This is caused by the fact that the theory is only valid in limit $w \to 0$ and therefore predicts too narrow distributions. There exist various corrections to take larger w and the change of volume fraction over time into account, most prominently the Modified LSW (MLSW) theory [86]. It is equivalent to LSW theory in the limit $w \to 0$, but incorporates that the diffusion gradients between particle and matrix are altered if other

particles are close (i.e. at higher volume fractions). The theory yields the rate constant

$$K(w) = \frac{6\Gamma D\ C_{\alpha,\mathrm{eq}} v_\beta^2 \rho_m^3}{v\ C_\beta^2 RT} \quad , \tag{3.68}$$

with the gas constant R, a theoretical maximum particle size ρ_m depending on w, $v = \frac{3\rho_m^2}{1+2\beta\rho_m-\beta}, \beta = \frac{6w^{1/3}}{e^{3w}\Gamma(w)}, \rho_m = ((\beta^2+\beta+1)^{1/2} - (1-\beta))/\beta$, and the volume fraction of precipitates w. Since particle volume fractions are available from the SANS measurements, the MLSW theory was applied for the fits.

Chapter 4

Experimental Methods

In this chapter, the experimental methods used for investigating *Co-Re* alloys are presented. In particular, the focus is on neutron scattering techniques such as ND and SANS which are powerful methods to investigate phase transformations and kinetics of precipitation in bulk samples *in-situ* at HT. These experiments were supplemented with laboratory X-ray diffraction (XRD) and complementary techniques: scanning electron microscopy (SEM), energy-dispersive X-ray spectroscopy (EDX) and electron backscatter diffraction (EBSD). In addition, *in-situ* synchrotron experiments under load and SAXS experiments with very high cooling rates were performed in order to study the creep behavior and first nucleation of precipitates.

4.1 Casting of the alloy

The alloys investigated in this study were produced by vacuum induction melting from high purity elementary metals and graphite powder ($> 99.8\%$ purity). The bath was superheated to 1900 K under argon atmosphere (175 mbar), when Co melted and dissolved Re, Ta and C into the liquid in short time. The alloys were cast into solid Cu mold to obtain 1.2 kg cast blocks and subsequently subjected to a standard three step homogenizing heat treatment (denoted ST: 1623 K/5 h + 1673 K/5 h + 1723 K/5 h and cooled in 5 bar Argon gas to RT). The alloy bars were cut after heat treatments into flat $12 \times 12 \times 1\,\mathrm{mm}^3$ pieces for in-situ SANS, the XRD and microscopy measurements (Fig. 4.1.1a), or machined to 6 mm diameter and 15 mm long cylindrical pieces for ND (Fig. 4.1.1b), respectively.

Additionally, several ex-situ aging treatments were performed for studying the precipitation and long-term behavior of TaC at HT. They are separately described and discussed in the text.

4.2 Sample environment

4.2.1 Furnaces

An ILL type vacuum furnace was used for the *in-situ* SANS and ND experiments. At HZB, ILL and PSI, the same type of furnace, manufactured by ILL was used (ILL furnace code 04TL20AN50). The furnace reaches a vacuum of 1×10^{-6}mbar and temperatures up to 1870 K − 2070 K, depending on quality of the shielding and in-house modifications. At MLZ

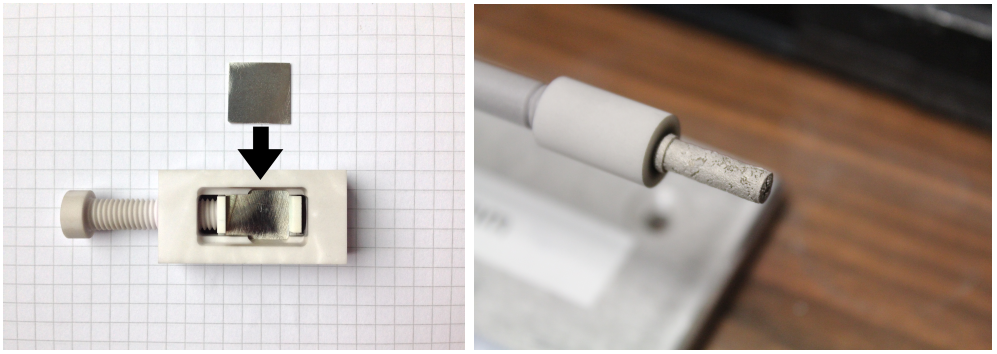

Figure 4.1.1: (left) Flat sample and a specially designed SANS sample holder made of Al_2O_3. (right) Cylindrical sample connected to a specially designed ND sample holder with a core thread made of Al_2O_3.

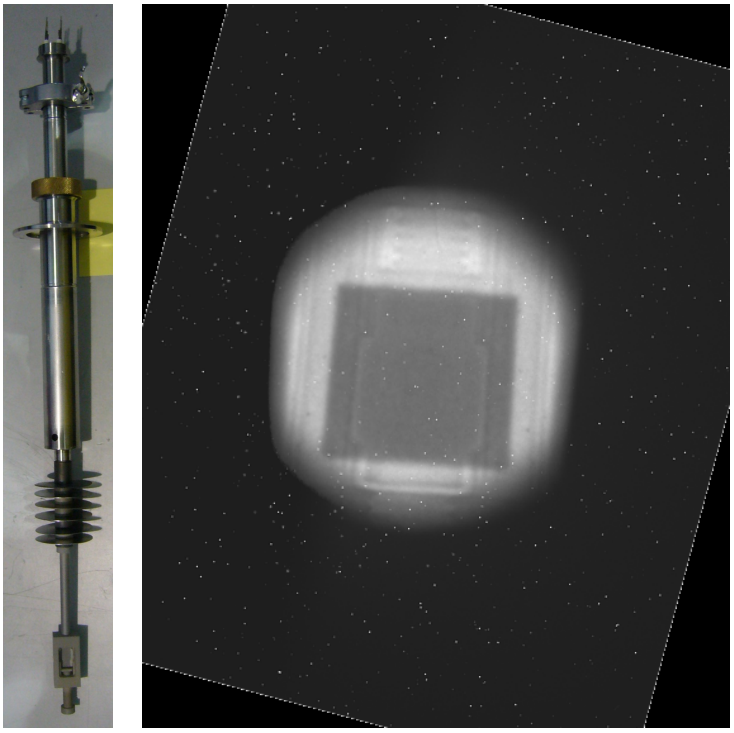

Figure 4.2.1: (left) The sample stick with attached sample holder and sample on the bottom; (right) Image of the sample in furnace with the neutron camera. The dark square is caused from the neutron absorption of the sample. A slight shadow from the highly transmitting Al_2O_3 sample holder with screw thread is visible.

a similar furnace (in-house production) is available. It reaches a vacuum of 10^{-7}mbar and temperatures of 1870 K and was used for the respective experiments there.

A special Al_2O_3 sample holder was manufactured to install the samples in the furnace (Fig. 4.2.1a). The sample position in the neutron beam was adjusted using a neutron camera *Neutronoptics slim* 100 × 50. A recorded neutron radiography image of the sample within the furnace is shown in Fig. 4.2.1b, taken during the sample adjustment.

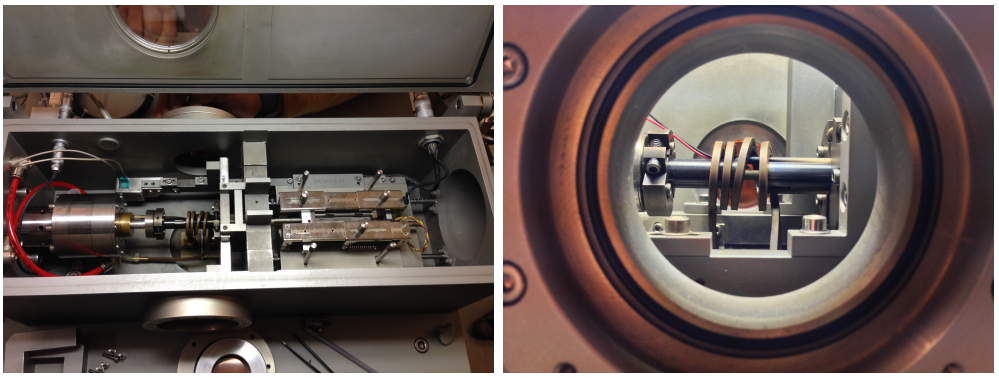

Figure 4.2.2: The DESY Dilatometer with deformation unit and induction coil for heating. (left) top view, (right) side view through the synchrotron beam window. The deformation unit and induction coil for heating can be seen.

4.2.2 Dilatometer

A DIL 805A/D (Bähr-Thermoanalyse GmbH, by now TA instruments) Dilatometer was used for the Synchrotron SAXS measurements at the HEMS beamline at Petra III at DESY [87]. The samples are heated with an induction coil with a rate up to $4000\,\mathrm{K\,s^{-1}}$. Quenching cooling rates of $\sim 2500\,\mathrm{K\,s^{-1}}$ are possible with hollow samples by blowing with gas. In addition, the dilatometer is equipped with a deformation unit. The experiments were performed in Argon atmosphere. Fig. 4.2.2 shows a top and side view of the dilatometer.

4.3 Small-Angle Scattering

Two types of measurements were combined in the *in-situ* experiments:
(a) Long time annealing measurements of the complete available Q-range from the different instruments. The temperature was held constant for up to 15 h in order to study the evolution of precipitates. (b) During temperature ramps, series of quick $10\,\mathrm{s} - 30\,\mathrm{s}$ (depending on the neutron flux) measurements were performed. Although the statistics is very limited for such short measurements, several tools were developed to determine the time of first precipitation or dissolution of TaC precipitates. The data evaluation and instrument calibration is described in detail in the appendix A.

This work is based on experiments at the SANS instruments SANS-1@MLZ, D33@ILL, V4@HZB and SANS-I@PSI. In the following, these SANS instruments are introduced.

4.3.1 SANS-1 at Heinz Maier-Leibnitz Zentrum

The instrument SANS-1 at the Heinz Maier-Leibnitz Zentrum (MLZ) [88, 89] was extensively used for the investigation of Co-Re alloys. The instrument is fed by the cold neutron source of FRM II with an S-shaped neutron guide system. An important feature is the large accessible Q-range, facilitated by a detector that can be moved sideways and additionally rotated. The beam can be collimated up to 23 m and sample to detector distances (SDD) of up to $d_0 = 20\,\mathrm{m}$ are possible. A monochromatic neutron beam with $\Delta\lambda/\lambda = 10\%$ was used for the experiments. The instrument was set up in the three geometries (1) $\lambda = 0.6\,\mathrm{nm}$, collimation 6 m, $d_0 = 2\,\mathrm{m}$, (2) $\lambda = 0.6\,\mathrm{nm}$, collimation 8 m, $d_0 = 8\,\mathrm{m}$ and (3) $\lambda = 1.2\,\mathrm{nm}$, collimation 20 m and $d_0 = 20\,\mathrm{m}$. With these settings a Q-range of $0.01\,\mathrm{nm^{-1}}$ to $3.1\,\mathrm{nm^{-1}}$ was

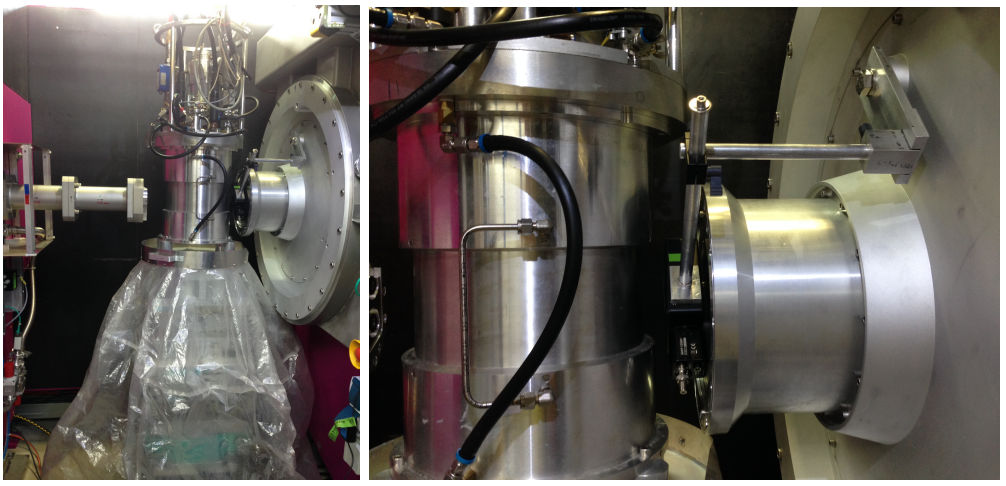

FIGURE 4.3.1: Sample position at SANS-1 instrument at MLZ. The beam is directed on the Al high vacuum furnace (from left to right). Afterwards, the scattering is monitored on the ^{3}He detector system in a vacuum chamber.

covered and excellent statistics of the nuclear scattering from Co-Re alloys could be achieved in a 60 min measurement. During temperature ramps, images with an exposure time of 10 s were recorded on the fixed medium Q-resolution range 0.067 nm^{-1} to 0.916 nm^{-1}.

4.3.2 V4 at Helmholtz Zentrum Berlin

The instrument V4 at the Helmholtz Zentrum Berlin [90] was set up in the three geometries $\lambda = 0.6$ nm, a collimation of $6, 8, 18$ m and SDD of $d_0 = 2, 8, 16.8$ m. With these settings a Q-range of 0.02 nm^{-1} to 1.7 nm^{-1} was covered. The measurement of the whole Q-range took 150 min in order to get reasonable statistics. During temperature ramps, images with an exposure time of 30 s were recorded on the fixed medium Q-resolution range 0.08 nm^{-1} to 0.70 nm^{-1}. A monochromatic neutron beam with $\Delta\lambda/\lambda = 10\%$ was used for the experiments.

4.3.3 SANS-I at Paul Scherrer Institute

The instrument SANS-I at the Paul Scherrer Institute [91] was set up in the three geometries $\lambda = 0.6$ nm, a collimation of $6, 8, 18$ m and SDD of $d_0 = 2, 8, 20$ m. With these settings a Q-range of 0.02 to 2.9 nm^{-1} was covered. The measurement of the whole Q-range took 60 min. During temperature ramps, images with an exposure time of 30 s were recorded on the fixed medium Q-resolution range -0.07 nm^{-1} to -0.75 nm^{-1}. A monochromatic neutron beam with $\Delta\lambda/\lambda = 10\%$ was used for the experiments.

4.3.4 D33 at Institut Laue-Langevin

The instrument D33 at Institut Laue-Langevin [92] has the possibility to be operated in TOF mode. In order to get a high time resolution on an enhanced dynamical Q-range, this mode is advantageous, since the detector can be left on a fixed SDD for *in-situ* experiments. For this purpose, the neutrons are passing a chopper system, yielding a pulsed beam of cold neutrons. A wavelength band of approximately 0.3 nm to 1.5 nm from the cold neutron source gave reasonable flux and transmission for the Co-Re alloys. A SDD of $d_0 = 7.8$ m yielded a Q-range of 0.032 nm^{-1} to 3.140 nm^{-1}, which was measured with good statistics within 5 min.

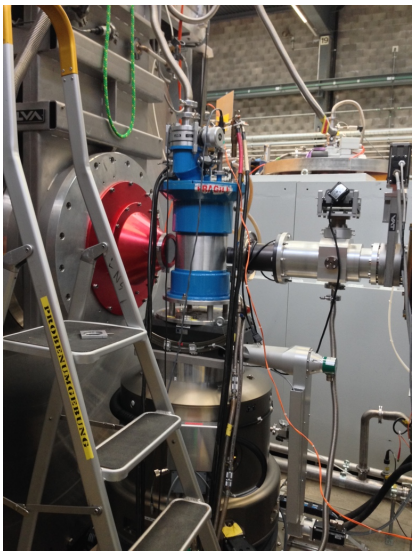

Figure 4.3.2: Sample position at SANS-I instrument at PSI. The beam is directed on the Al high vacuum furnace (from right to left).

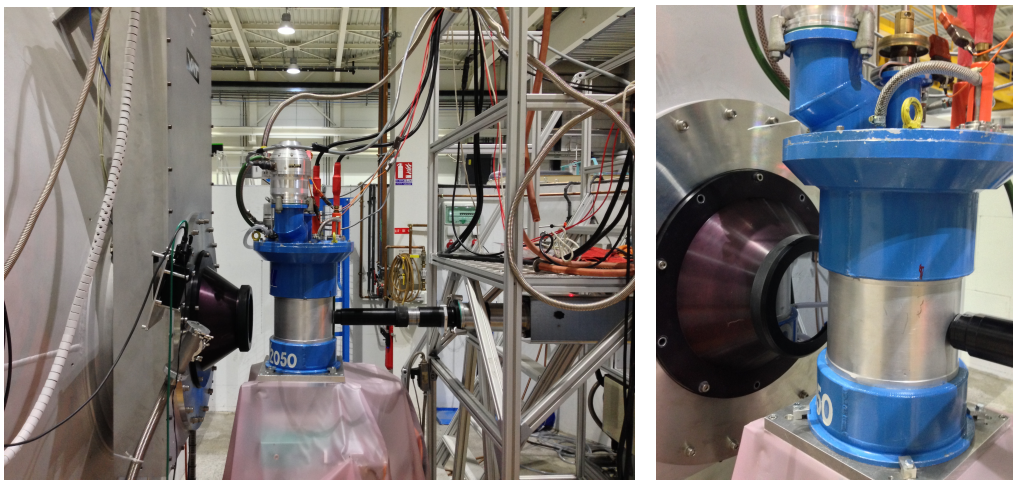

Figure 4.3.3: Sample position at D33 instrument at ILL.

However, the Q-resolved SANS patterns could already be evaluated for their trend with an exposure time of 15 s.

4.3.5 HEMS at Petra III, DESY - SAX

Experiments with synchrotron radiation were conducted at the High Energy Material Science Beamline (HEMS) at Petra III at DESY [87]. A radiation energy of $30-200\,\mathrm{keV}$ is accessible, for the present experiment a wavelength of $\lambda = 0.015\,75\,\mathrm{nm}$ was used. A Perkin Elmer XRD1621 image detector with a spatial pixel size of $200 \times 200\,\mu\mathrm{m}^2$ and theoretical time resolution of $100\,\mu\mathrm{s}$ was used to record the images. In the case of small-angle scattering, this means that only a limited Q-range is accessible, because the scattering angles are much smaller. An SDD of $d_0 = 10.8\,\mathrm{m}$, yielded a Q-range of $0.075\,\mathrm{nm}^{-1}$ to $2.0\,\mathrm{nm}^{-1}$.

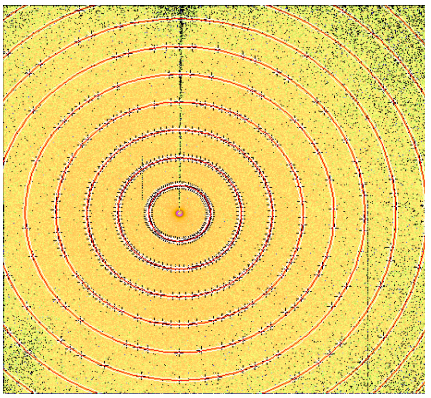

Figure 4.3.4: Measurement and fit of AgBE standard, used to calibrate the instrument in SAXS mode.

The exact instrument parameters were fitted with a silver behenate (AgBE) standard (Fig. 4.3.4). One image could be recorded every 10 s with an exposure time of 5 s.

4.3.6 Data evaluation

The SAS data reduction was performed with the software BerSANS [93]. The fits of the data were performed with the software packages SASFit [61], SASView [94] and a program developed within the frame of this thesis. Several tools for calibration of the SANS-1 instrument (cf. appendix A) and evaluation of SAS data (cf. appendix B) are implemented. The data from HEMS were treated with the software package Fit2D [95] and evaluated with the developed program. The software is written with the commercial software package MATLAB 9.1 (The MathWorks Inc., Natick, MA, 2016).

4.4 Diffraction

ND measurements were performed for phase analysis *in-situ* at HT. The ND measurements were done in Debye-Scherrer geometry, which probes a large sample volume. The cylindrical Co-Re samples were installed in the HT vacuum furnace. In the following the different instruments are briefly described.

4.4.1 Stress-Spec at Heinz Maier-Leibnitz Zentrum

The high flux instrument Stress-Spec at MLZ [96] is equipped with a two-dimensional position-sensitive detector and the measurement was performed with a neutron wavelength $\lambda = 0.1636(2)\,\mathrm{nm}$. The covered angular range for one fixed position of the detector is $\pm 7°$. The diffractograms were collected during $10min$ holding for a given detector position. The detector was moved to several positions to cover the angular range of 2θ between 42.5° and 114.5°.

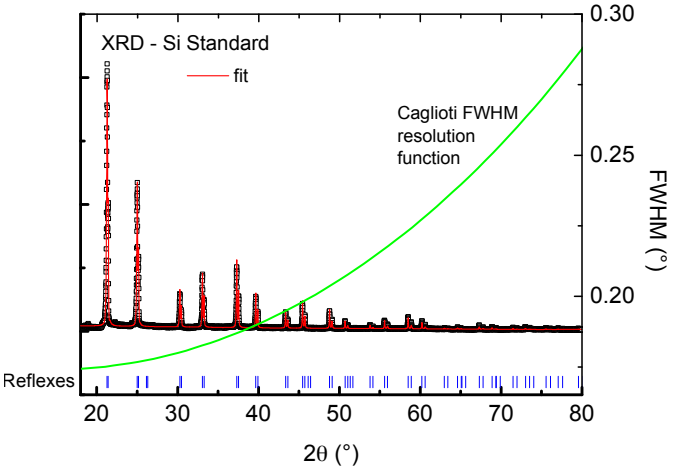

FIGURE 4.4.1: Diffractogram of a Si standard (NIST 604d), showing the resolution of the laboratory diffractometer. In addition, the instrumental FWHM is plotted as a function of 2θ.

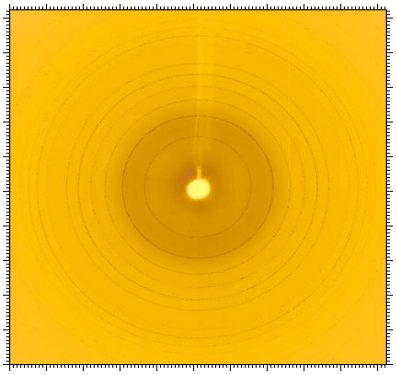

FIGURE 4.4.2: NIST LaB_6 standard measurement used to calibrate the instrument in WAXS mode.

4.4.2 SPODI at Heinz Maier-Leibnitz Zentrum

The high resolution instrument SPODI at MLZ [97] is equipped with 80 position sensitive detector tubes. An angular range of 2θ up to 160° was covered for these measurements with $\lambda = 0.1548(2)$ nm. The performed experiments in the context of this study were done *ex-situ*. The cylindrical Co-Re samples were mounted in a vanadium sample holder and measured for 4 h.

4.4.3 Laboratory X-ray diffractometer at Heinz Maier-Leibnitz Zentrum

A laboratory X-Ray diffractometer PANalytical Empyrean high-resolution powder diffractometer was used to perform complementary measurements on all samples before and after in-situ neutron experiments. The measurements were performed with a Mo-Kα radiation source (mean wavelength $\lambda_{Mo} = 0.071\,07$ nm, energy 17.4 keV), which has a penetration depth of approximately 1 µm in the Co-Re alloys. The instrument is equipped with a 1D linear real time multistrip X'Celerator detector with an efficiency of 30% for Mo $K\alpha_1$ radiation and a pixel resolution of 0.002° in 2θ. A sample spinner with 0.25 rpm was applied to improve the crystallite statistics over the whole surface of the sample. The measurements were performed in Bragg-Brentano reflection geometry with a beam slit of 10 mm, an incoming beam divergence slit of 1/4°. The axial divergence was reduced by inserting soller collimators with an opening of 0.04 rad at the incident and reflected beam path. An angular range from 10° to 80° was covered, in a total measurement time of 6 h.

The diffractometer was calibrated with a Si standard (NIST 604d). Fig. 4.4.1 shows the diffractogram of the Si standard. The resolution width for the PANalytical diffractometer with the chosen resolution settings is also shown in the graph. It was determined by the *Thompson-Cox-Hastings pseudo-Voigt* convoluted with the axial divergence asymmetry function throughout this thesis [98].

4.4.4 HEMS at Petra III, DESY - WAXS

The HEMS beamline was used in WAXS mode for in-situ XRD during a creep experiment with a dilatometer [87]. The fine X-Ray beam from the synchrotron source has a very low divergence and in combination with the flat panel detector with 2048×2048 pixel resolution, extremely sharp Bragg reflections are achieved. A Perkin Elmer XRD1621 image detector with a spatial pixel size of $200 \times 200\,\mu m^2$ and theoretical time resolution of 100 µs was used to record the images. The detector was positioned such that the incoming neutron beam hit it in the center, allowing to record complete Debye-Scherrer rings. The exact position of the detector was refined with a NIST LaB_6 standard (Fig. 4.4.2). The sample to detector distance was 1930 mm, with a synchrotron wavelength of $\lambda = 0.0122\,nm$, covering Q-vectors up to $73\,nm^{-1}$. Due to the heavy transition metal Re, the absorption was rather high. Therefore, the beam had to be positioned close to the edge of the sample in order to get a reasonable signal. With these settings, one image could be recorded every 10 s.

4.4.5 Data evaluation

The Co-Re alloys were modeled with their three phases, namely ϵ-Co (hcp, spacegroup $P\,63/m\,m\,c$), γ-Co (fcc, spacegroup $F\,m\,\bar{3}\,m$) and TaC phase (rock salt structure, spacegroup $F\,m\,\bar{3}\,m$). With this modeling, all observed peaks could be fitted, only the ND measurements sometimes showed weak (non overlapping) peaks from the sample holder.

The data evaluation of ND and XRD data was performed with the Rietveld method [99] using the FullProf package [100]. In addition, the $2D$ patterns from synchrotron were treated with the software package Fit2D [95]. In order to evalute coherence relationships of precipitate and matrix a software package was written in Matlab. In addition, the Vesta software [101] was used for visualization.

The Panalytical Highscore Plus software [102] was used for the Rietveld refinement of the laboratory XRD data.

In order to determine coherence relationships of precipitate and matrix, a Matlab program was developed. The program can create 3D crystal structures from the most common space groups and determine and visualize the crystal directions or lattice planes with the smallest misfits.

4.5 Microscopy

The presented micrographs within this thesis were provided by the Technical University Braunschweig, Institut für Werkstoffkunde [49].

Before and after all the in-situ experiments, the Co-Re samples were investigated by scanning electron microscopy. The instrument is manufactured by the company FEI (Helios Nanolab 650i). The microscope has a dual beam (electron and ion) mode and was used for SEM, EDX and EBSD.

4.5.1 Scanning Electron Microscopy

The microscope is equipped with different imaging modes for Scanning Electron Microscopy (SEM), which include beam deceleration (BD) mode and annular-segmented central backscatter detector (CBS). This allows distinguishing different phases and crystal orientations in the

Co-matrix according to the composition (by atomic number Z contrast and channeling contrast, respectively) [46, 103].

4.5.2 Energy-dispersive X-ray spectroscopy and electron backscatter diffraction

Energy-Dispersive X-Ray Spectroscopy (EDX) was used to perform elemental mapping on the sample surface in order to record elemental partitioning of the Co matrix and to identify Ta and C.

EBSD measurements were performed using the TEAM software platform from EDAX. The samples were carefully ground and polished to minimize surface strain in order to obtain quality Kikuchi patterns from the backscattered electrons. The different phases were identified by pattern matching, using the lattice parameters of the ϵ- and γ-Co and TaC phase that were obtained from neutron diffraction.

The TEAM software platform from EDAX was used for the evaluation of the data.

Chapter 5

TaC Precipitates in Co-Re-Ta-C Alloys

The results presented in the paragraph are published in [10, 20]. In the following, an overview of these results is presented.

As a result of the standard homogenization heat treatment (denoted *ST*, cf. section 4.1), the mono-carbide phase of Ta forms finely distributed precipitates in the Co-Re matrix (cf. 2.1.2). The TaC phase is required as one main strengthening phase of the Co-Re matrix by impeding the movement of dislocations. It is well known that binary TaC is a strongly non-stoichiometric interstitial compound, which is stable over a wide range of C/Ta ratios [28] (Fig. 2.1.4). However, the stability of the phase in the Co-Re alloy system was not investigated yet and the stability and morphology of TaC precipitates as function of carbon content in the alloy is of key interest. In order to study the TaC precipitates, Co-Re-Ta-C alloys containing different amounts of C were chosen such that the y =C/Ta cover the entire stoichiometric range of the TaC-phase in the binary phase diagram, e.g. $y = 0.5, 0.7, 0.9, 1.0$ (see table 5.0.1). The alloys with $y = 0.5, 0.7$ are denoted as low C content alloys TaC05, TaC07 and $y = 0.9, 1.0$ are denoted as high C content alloys TaC09, TaC10. The alloys were deliberately kept free of additional elements like Cr and B to prevent the formation of other phases (e.g. $Cr_{23}C_6$ carbides, borides or σ phase).

An important factor for the stability of TaC precipitates is the Co-Re phase transformation $\epsilon \leftrightarrow \gamma$. This transformation was studied in detail with in-situ neutron and XRD. The present phases after the homogenization treatment *ST* condition are shown in the diffractogram Fig. 5.0.1 (measured by ND). Peaks from both, ϵ and γ-Co phase are revealed and the results from Rietveld refinement are presented in table 5.0.2. The Co matrix consists of a mixture of ϵ- and γ-Co phase, each with 45-55 % volume fraction. Apparently, the HT γ-Co phase is metastably retained at RT during the cooling after the ST homogenization heat treatment. In the following, this metastable phase is denoted γ_m-Co phase. The TaC phase

Alloy	type	Co	Re	Ta	C	y =C/Ta
TaC05	low C content	81.20	17	1.2	0.6	0.5
TaC07		80.96	17	1.2	0.84	0.7
TaC09	high C content	80.72	17	1.2	1.08	0.9
TaC10		80.60	17	1.2	1.2	1.0

Table 5.0.1: Composition of alloys with varying C/Ta ratio in at.%.

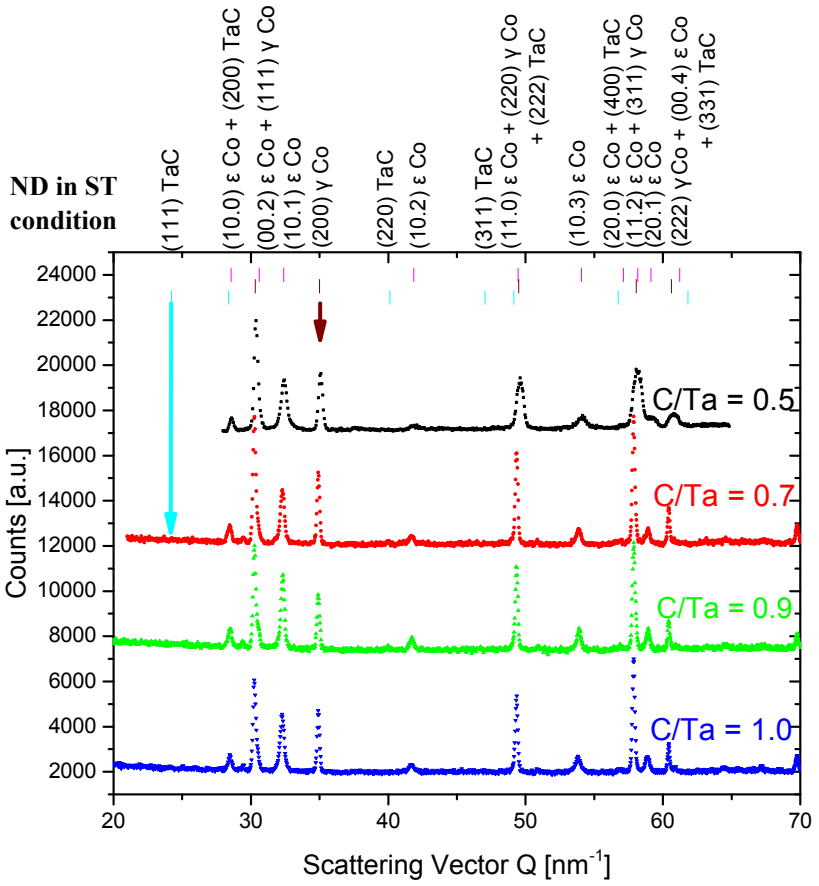

FIGURE 5.0.1: Phases in Co-Re-Ta-C alloys in ST condition. ϵ-Co and γ-Co phase are observed. The isolated peaks from TaC phase are not visible in ST condition. The TaC05 samples was measured at Stress-Spec, while TaC07-10 were measured at SPODI. Adapted from [10].

ST condition	ϵ-matrix a [nm]	ϵ-matrix c [nm]	γ-matrix a [nm]	TaC a [nm]	ϵ-matrix vol.%	γ-matrix vol.%	TaC vol.%	C/Ta calculated
TaC05	2.543	4.119	3.591	4.442	46.2	53.6	0.2	0.91
TaC07	2.552	4.122	3.604	4.449	42.7	56.9	0.4	0.96
TaC09	2.552	4.123	3.604	4.450	52.5	46.7	0.8	0.96
TaC10	2.553	4.121	3.604	4.444	50.9	48.4	0.7	0.93

TABLE 5.0.2: Results from Rietveld fits of ND data from alloys with varying C/Ta ratio in ST condition.

was taken into account in the fits, but the isolated TaC peaks are too weak to be observed in the alloys in ST condition. However, the presence of the Co-Re matrix phases and the TaC precipitates could be confirmed by SEM and EDX. In-situ SANS enabled the investigation of TaC precipitates at HT.

5.0.1 Stoichiometry of TaC_y phase

Gusev et al. [104] showed that the TaC lattice constant is strongly depending on the exact composition of TaC_x. Therefore, the TaC composition can be approximated from the measured value of its lattice constant [19]. He derived the linear dependence shown in Fig. 5.0.2. The C/Ta ratio and calculated stoichiometry within the TaC phase is included in table 5.0.2.

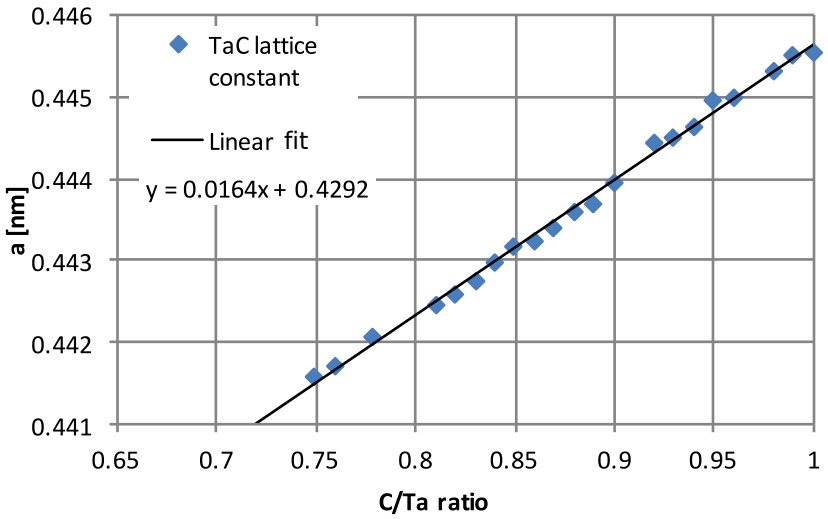

FIGURE 5.0.2: TaC lattice constant as a function of atomic ratio C/Ta. After [104].

5.1 Microscopy

The existing phases in Co-Re-Ta-C alloys were investigated by SEM. Selected micrographs from the different alloys with $y = 0.5-1.0$ before and after the respective heat treatments are presented in the following. The type and composition of the different phases was investigated with EDX and EBSD.

5.1.1 Condition after standard heat treatment

Fig. 5.1.1 shows the general features of the microstructure in low magnification after the standard heat treatment (ST). The microstructure is similar in the four investigated Co-Re-Ta-C alloys with $y = 0.5 - 1.0$. A lath-type structure of the Co matrix can be seen as well as the presence of large facetted and blocky TaC precipitates and pores. A BSE image of the as polished sample of the TaC alloy is shown in Fig. 5.1.1a. The lath structure of the Co-Re matrix is more prominent in the sample after etching, as seen in SE image in Fig. 5.1.1b. Due to the different hardness of the different phases, the etching produces a topographic effect. The laths appear as a result of the martensitic phase transformation $\gamma \rightarrow \epsilon$ during cooling after the ST homogenization treatment and are oriented along crystallographic directions .

The fine TaC precipitates are observed in Fig. 5.1.2. A dispersion of fine globular TaC precipitates in the size range of $\sim$ 30 nm, homogeneously distributed within the laths, is imaged with the BD mode at high magnification. A second TaC population of globular TaC with larger size in the order of $\sim$ 100 nm is observed in the matrix laths.

Further, a second contribution of elongated TaC precipitates is observed within some of the laths (Fig. 5.1.3). Their presence is independent of the applied heat treatment and alloy composition. These TaC particles grow along specific crystallographic directions within the laths.

5.1.2 Influence of aging treatments

Irrespective of the C/Ta ratio, the lath type microstructure, fine and facetted TaC are still found after aging of the alloy at the HT 1173 K, 1373 K and 1473 K. Four micrographs,

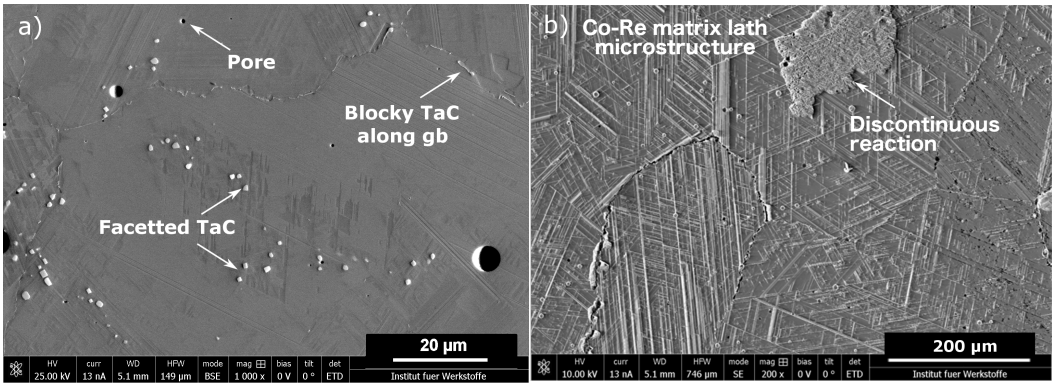

Figure 5.1.1: Low magnification image of a TaC10 sample. (a) Image from unetched sample. Large pores, facetted TaC and blocky TaC along grain boundaries are observed; (b) etched sample shows the lath structure of the Co-Re matrix. An area showing a discontinuous reaction front is marked. These areas are scarcely found in the matrix and represent abrupt changes in orientation and composition in the matrix phases. The images are taken from high C content alloy. Adapted from [10].

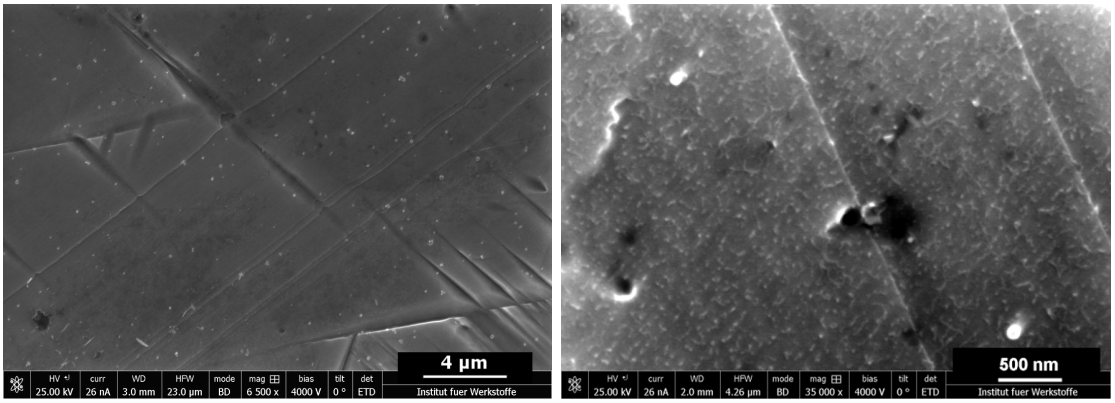

Figure 5.1.2: Different morphologies of nano-sized TaC precipitates. (left) Larger globular TaC precipitates $\sim 200\,\mathrm{nm}$ can be seen in the Co-Re laths (TaC05 alloy). (right) Fine TaC precipitates with a size of $\sim 30\,\mathrm{nm}$ are observed in high magnification (TaC10 alloy). These findings are representative for alloys TaC05-10.

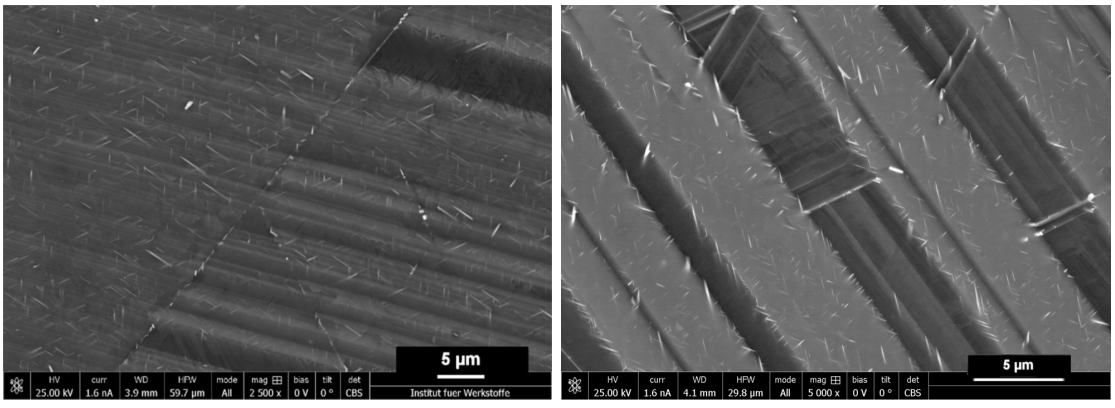

Figure 5.1.3: Oriented nano scaled TaC precipitates suggest a coherence relationship of precipitate to matrix and $2D$ growth of some TaC particles. It can be seen that most TaC precipitates orient along a threefold symmetry to the Co-Re matrix. (left) TaC10 alloy, (right) TaC09 alloy. These findings are representative for alloys TaC05-10. Adapted from [10].

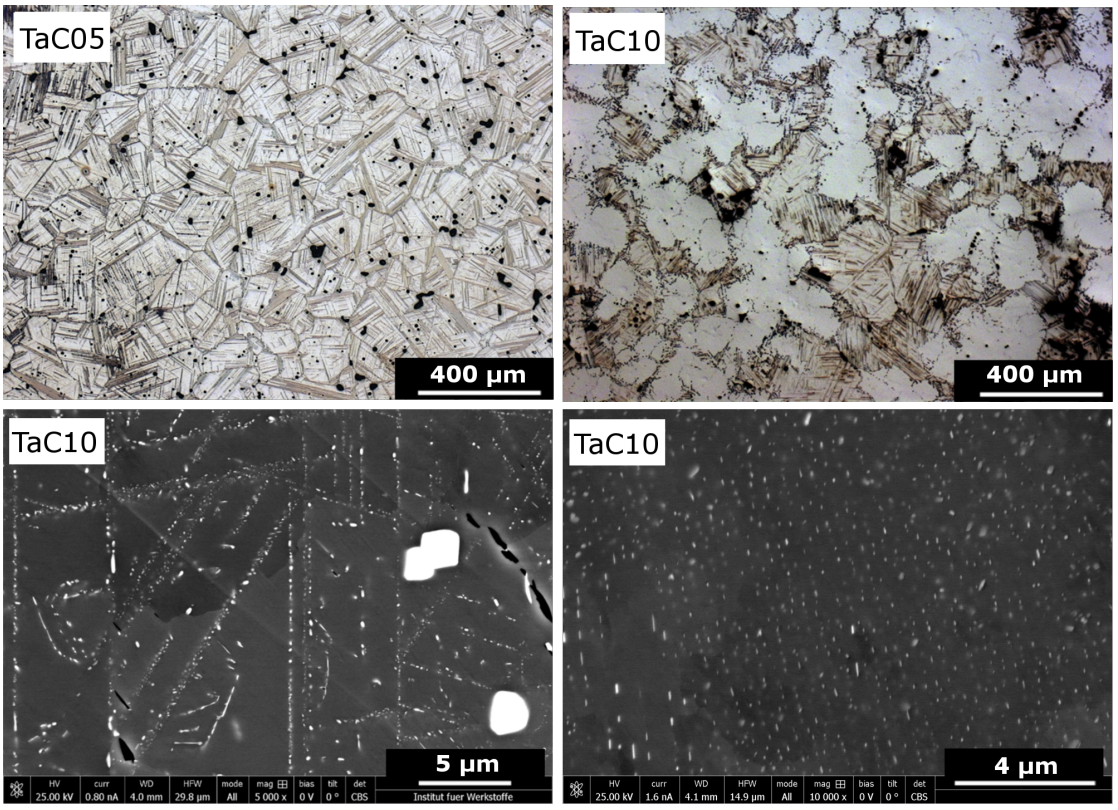

Figure 5.1.4: (top) Low and high C alloy after aging. The matrix shows partly transformed regions and the lath structure is more prominent in the low C alloy. The high C alloy shows completely untransformed areas. The high magnification images show that a higher volume fraction of fine globular TaC particles has precipitated along lath boundaries and within the laths (5.1.4c). The larger regions of untransformed ϵ-Co contain a dispersion of fine globular TaC precipitates (Fig. 5.1.4d). These fine TaC precipitates have coarsened due to the heat treatments and are in the size range of $\sim 100\,\text{nm}$. (bottom) Nano scaled TaC precipitates after aging. Adapted from [10].

taken from alloys aged for $15h$ at 1173 K are presented in Fig. 5.1.4 to show the influence of the heat treatments on Co-Re matrix and TaC precipitates. Fig. 5.1.4a and b present low magnification images of a low and a high C content alloy (TaC05 and TaC10). The lath structure of the matrix with partly transformed microstructure is much more prominent in the low C alloy. The high C content alloy shows larger completely untransformed areas. The high magnification images show that a higher volume fraction of fine globular TaC particles has precipitated along lath boundaries and within the laths (5.1.4c). The larger regions of untransformed ϵ-Co contain a dispersion of fine globular TaC precipitates (Fig. 5.1.4d). These fine TaC precipitates have coarsened due to the heat treatment and are in the size range of $\sim 100\,\text{nm}$.

5.1.3 Energy-dispersive X-ray spectroscopy and electron backscatter diffraction

The transformed areas, visible in Fig. 5.1.4 were investigated by EDX and EBSD to identify the type and state of the Co-matrix phases. Fig. 5.1.5 (top) shows a typical EDX mapping of the lath structure in an TaC05 alloy after a 15 h heat treatment at 1373 K. The ϵ-Co phase enriches in Re, while the γ-Co phase is depleted due to diffusion during holding at

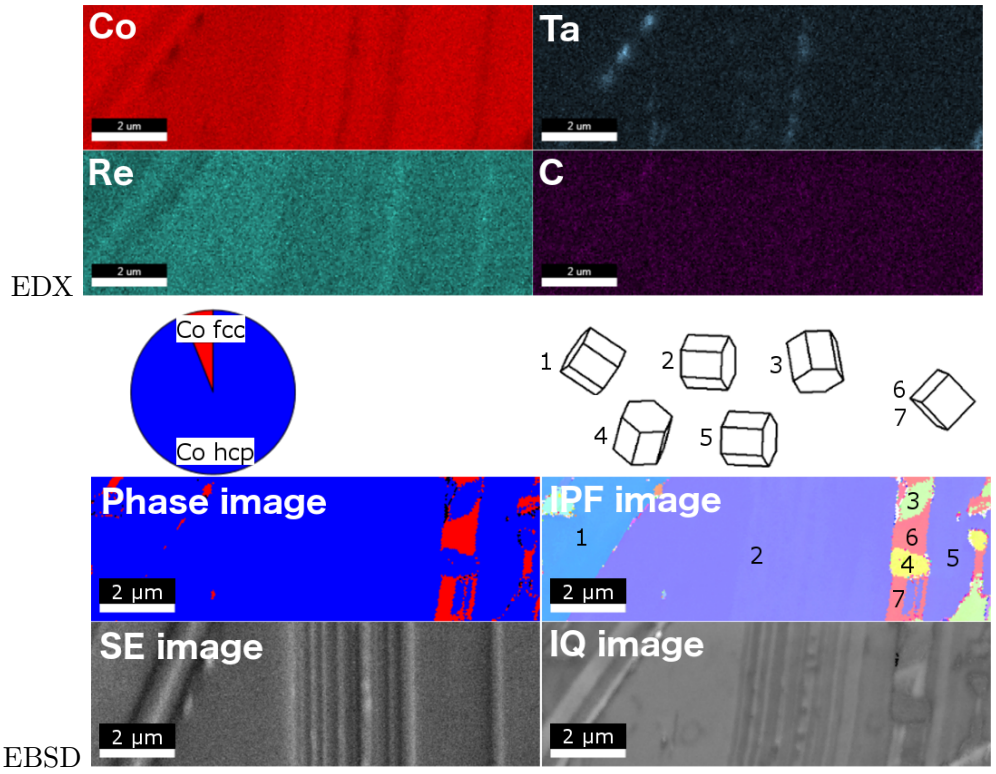

Figure 5.1.5: Typical EDX and EBSD maps of TaC05 alloy in after 15 h heat treatment at 1373 K. (top) The Co-Re matrix laths with two different elemental distributions can be seen in the EDX maps, namely a Re-rich ϵ-Co phase and Co-rich γ-Co phase. (bottom) Results from EBSD with IPF, SE, phase and IQ image. Most of the matrix is present in form of ϵ-Co phase, that has partly grown into the γ-Co grains during cooling from 1373 K. Adapted from [10].

HT [20, 105]. The element distribution is the one from HT, because no diffusion is expected during the fast cooling to RT. A partitioning of Co and Re in the different laths can be seen. The brighter color in the elemental maps show an enrichment of the element. The Fig. reveals that the laths were partly ϵ- and partly γ-Co phase at HT. In addition, TaC precipitates along lath boundaries can be identified.

In order to investigate the state of the matrix phase after cooling, EBSD was applied. The technique records the *Kikuchi*-patterns from electron backscattering and calculates an inverse pole figure (IPF) and image phase map. The results are shown in Fig. 5.1.5 (bottom) together with the secondary electron (SE) image and image quality (IQ) map of the mapped area. There is a small orientation mismatch between the SE image and the others due to the applied tilt correction of the software. After cooling from HT, the Co-Re matrix consists mostly of the low temperature ϵ-Co phase that has partly grown into the γ-Co laths during cooling from HT. The matrix transformation on cooling is a diffusionless, martensitic mechanism. Hence, the distribution of phases does not match the lath morphology represented by the SE and IQ image and the EDX elemental maps. Due to the retained partitioning of Co and Re, the matrix regions have different hardness and are therefore polished to a different extent. Re rich regions are generally harder, leading to a topographical surface that visualizes the lath structure from HT. The different crystallographic orientations of ϵ-Co and γ-Co laths in the Co-Re matrix are revealed in the IPF map.

Element	Composition [at.%] Co	Re	Ta	C	Density g cm^{-3}	Molar volume m^3 mol^{-1}	Scattering-length density cm
ϵ-Co	62.41	17.82	0.97	18.80**	12.69	6.96	3.47
γ-Co	75.62	11.68	0.22	12.48**	10.86	7.02	2.91
TaC	33.7	7.5	17.1	41.8**	16.67	6.65	7.89
TaC*	-	-	58.5	41.5	16.67	6.65	6.16

TABLE 5.1.1: Composition in TaC05 alloy from EDX mapping of the matrix and TaC. (*) TaC composition is taken from lattice constant measurement in [19, 104]. (**) C was not considered for SLD calculation due to high error from EDX measurements.

The composition results from EDX were used to calculate the scattering length density (SLD) of the different phases, which is essential for the determination of volume fractions in SANS. The compositions of the ϵ-Co matrix and the γ-Co matrix are presented in table 5.1.1. Recent atom probe measurements revealed that EDX values are reliable for the matrix composition ($\sim$ 5% relative error) [27]. The composition estimates for the TaC phase are included as well, but the light element C generally shows a large error. Further, the TaC precipitates are present in form of nano scaled precipitates in the present alloys, which makes the determination of their composition impossible by EDX due to the limited spatial resolution of the technique. Consequently, the TaC composition was approximated indirectly from the measured value of its lattice constant as described in section 5.0.1. The determined composition was used for the SLD calculation. It has to be noted that the exact SLD (and therefore the evaluated volume fraction from SANS) for TaC does not strongly depend on stoichiometric ratio of Ta and C, since the scattering length of both elements is very close to each other [106]. The estimation of volume fraction of the fine TaC from the SANS measurement should therefore be considered with these limitations.

Using the SLD values from table 5.1.1, a squared scattering contrast of 7.21×10^{20}cm^4 for TaC in the ϵ-Co matrix and 1.05×10^{21}cm^4 in the γ-Co matrix was calculated. At temperatures 1173 K - 1473 K, the matrix is mainly in ϵ-Co phase as will be shown in section 5.2, therefore the SLD from that phase was taken. At low temperatures, the SLD was approximated by considering the Co-matrix to be a mixture of ϵ- and γ-Co phase and the SLD was chosen according to their proportion.

5.2 Diffraction

The Co-Re matrix phase transformations and TaC phase were monitored in-situ at HT by ND. For the experiments, a low C content sample TaC05 and a high C content TaC09 were prepared by the standard homogenization treatment ST. The temperature history during the in-situ experiment is depicted in Fig. 5.2.1. Fig. 5.2.2 shows the evolution of the diffraction patterns during heating to 1773 K and subsequent cooling to RT as contour plots in a TaC05 and TaC09 alloy. The transformation of the Co-Re matrix phase $\gamma \leftrightarrow \epsilon$ is observed. Fig. 5.2.3 shows the intensities of the matrix peaks hcp (101) from ϵ-Co phase, fcc (200) from γ_m-Co phase and the isolated TaC peak (220) of a low C alloy on the left and a high C alloy on the right. The kinetics of the matrix phase transformation is very slow at first and the phase fractions remain mostly unchanged during heating from RT to 1173 K. Just when reaching 1173 K, there is enough thermal activation in the matrix to start the transformation of the metastable γ_m-Co phase to thermodynamically stable ϵ-Co phase. This transformation

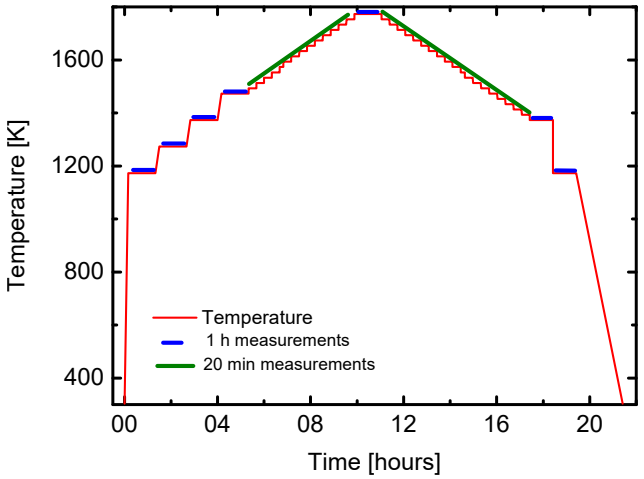

Figure 5.2.1: Temperature vs. Time history of in-situ ND measurements up to 1773 K. The temperature was initially increased to 900 K and diffractograms were recorded during step-wise increase of the temperature up to 1770 K. At several temperature steps, full diffractograms were recorded, while at others, only short measurements of the main peaks were measured.

is nearly complete on holding for 2 h at 1173 K in high C content alloy, while a significant amount of γ-Co phase remains in low C content alloys. Hence, the Co-Re alloys have different equilibrium γ- and ϵ-Co phase contents at temperatures $1173 - 1473$ K in low and high C content alloys. Only upon heating to $1600 - 1650$ K, the Co-matrix transforms fully to the HT γ-Co phase for the investigated C/Ta ratios.

The overall TaC phase fraction shows a correlation with the matrix phase as the volume fraction increases, during the transformation $\gamma_m \rightarrow \epsilon$ upon heating. This can be attributed to a lower solubility of the elements Ta and C in the ϵ-Co phase, which results in precipitation of the TaC phase. When the matrix starts transforming to HT phase $\epsilon \rightarrow \gamma$, the TaC content is at its maximum. However, the TaC phase starts to decrease during the transformation with an offset of $\sim$ 100 K. Moreover, the TaC phase lattice constant exhibits a small jump during the phase transformations.

The temperatures 1173 K, 1373 K and 1473 K are particularly interesting because they approximately represent the starting temperature of the transformation $\gamma_m \rightarrow \epsilon$ phase, the temperature of maximum ϵ-Co content and the starting temperature of the transformation $\epsilon \rightarrow \gamma$ (Fig. 5.2.3). For that reason, these temperatures were selected for aging treatments of the alloy and subsequent determination of the phase fractions by XRD. The treatments were performed during in-situ SANS measurement (cf. section 5.3). The XRD patterns are presented in Fig. 5.2.4 and results from Rietveld refinement in table 5.2.1. After the long hold at HT during the in-situ SANS experiments and subsequent slow cooling to RT, the samples contain mostly ϵ-Co phase in the matrix. The γ-Co content has reduced ($1 - 12$ % volume fraction), while the TaC content has considerably increased (2-4 % volume fraction). However, the low C alloys, especially TaC05 alloy shows a higher amount of γ-Co phase at RT. Since the Co-Re matrix is in a mixed γ/ϵ state during the three selected temperature treatments, these results mainly represent the HT state, only some additional transformation from HT phase to RT phase $\gamma \rightarrow \epsilon$ is expected.

The ND and XRD results are in good agreement. Low C content alloys show a higher amount of γ-Co phase at HT between 1173 K and 1473 K. In addition, a higher amount of

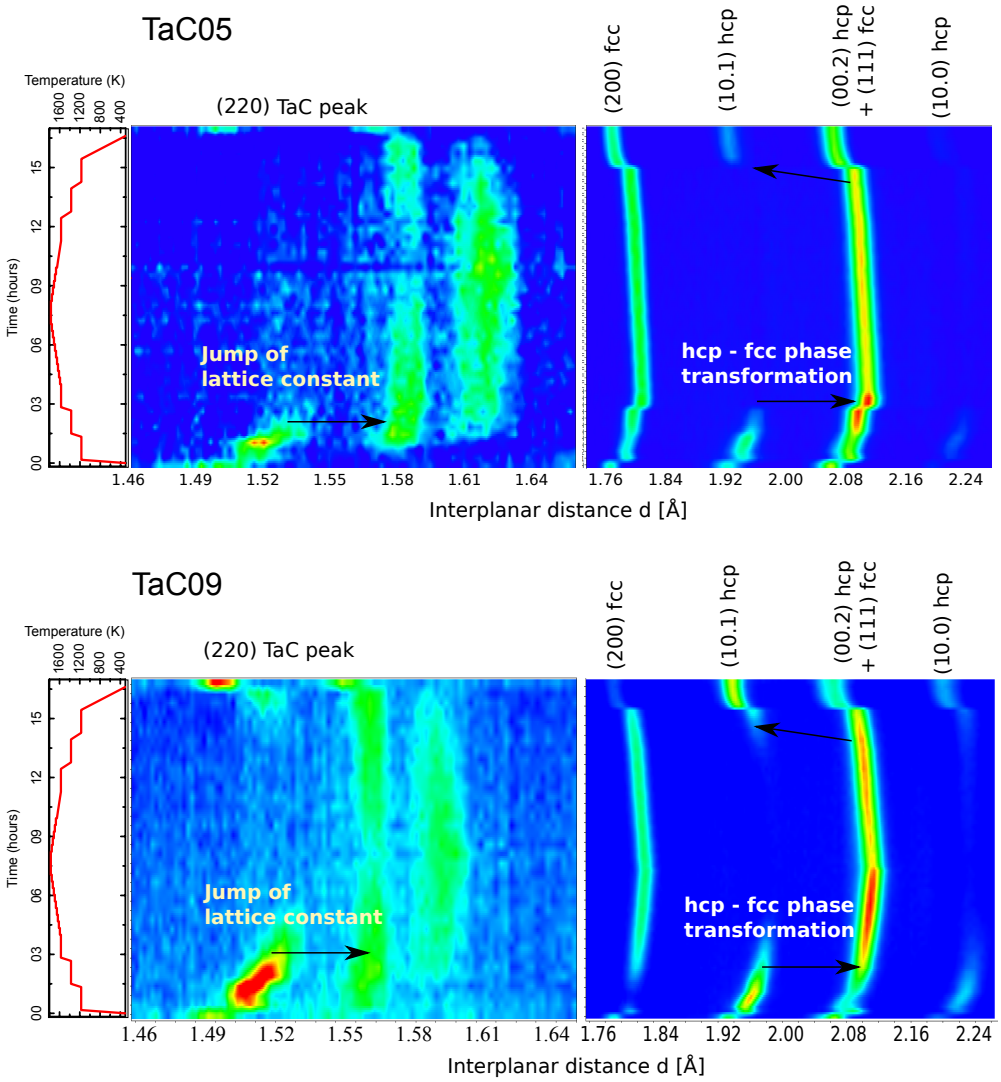

FIGURE 5.2.2: Contour plots of phase evaluation during heating and cooling of low (TaC05) and high C content (TaC09) alloys.

metastable γ_m phase is present at RT. Since the Ta content is constant in the four alloys, the different level of Ta and C supersaturation is likely the reason for the different equilibrium mixing ratios of γ- and ϵ-Co phase at HT in low and high C content alloys. Both elements are known to be strong fcc stabilizers (Fig. 5.2.5). The effect is strong on the Co-Re matrix, although only small amounts of C are present in the alloys.

The TaC lattice spacing a_{TaC} is generally increased after the heat treatments and larger for higher aging temperatures. It is known that a_{TaC} depends on the exact phase stoichiometry and higher values mean a larger content of interstitial C within the phase [104]. Therefore, the aging enriches the TaC phase with C.

5.3 In-situ small-angle neutron scattering aging experiments

To assess the morphology and volume fractions of fine TaC precipitates, in-situ SANS measurements were performed at 1173 K, 1373 K, 1473 K and 1573 K (Fig. 5.3.1). ND confirms the presence of TaC phase at these four temperatures (cf. section 5.2). SANS is performed on

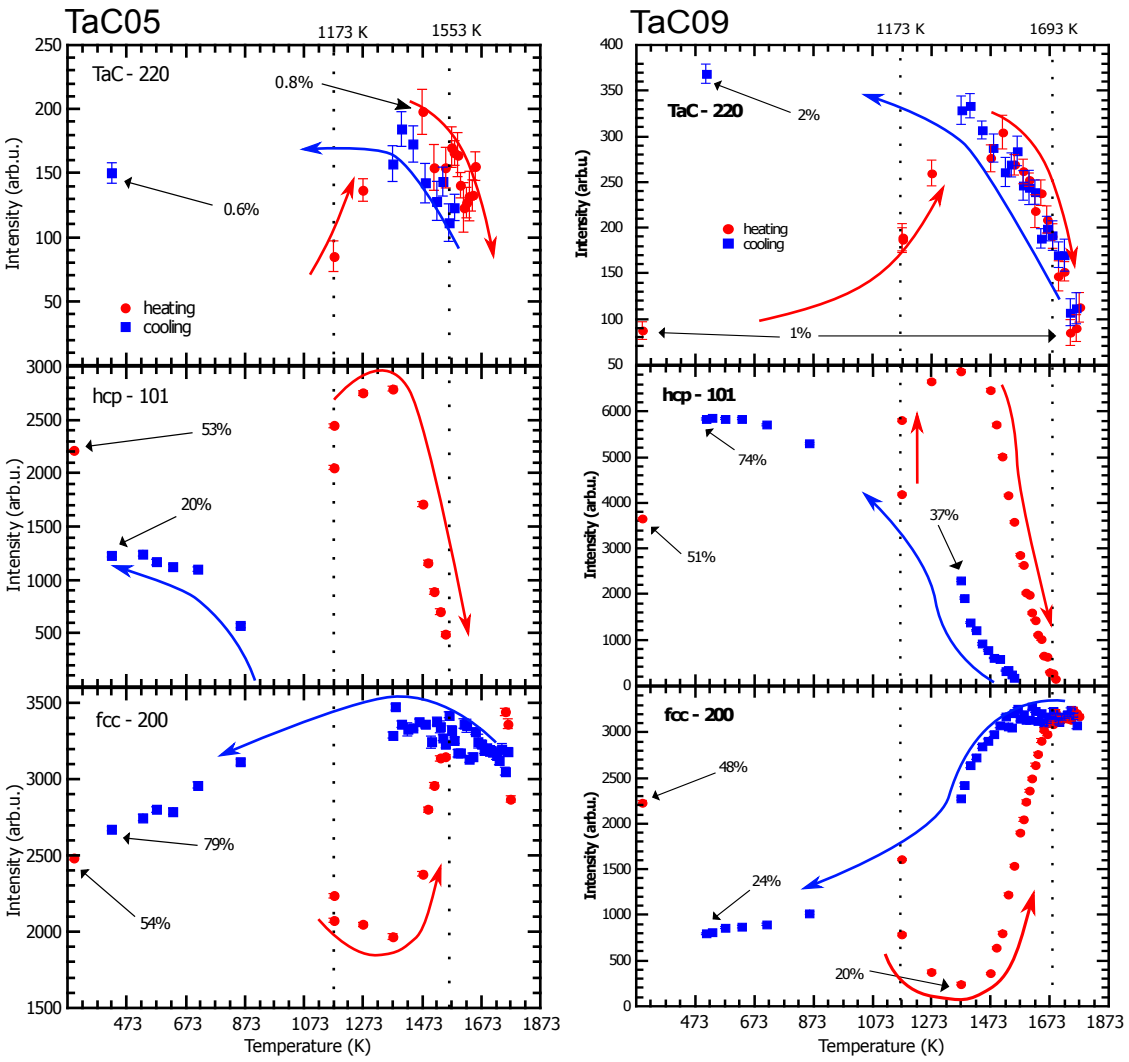

FIGURE 5.2.3: Peak intensity evolution during heat treatment to 1773 K, measured by neutron diffraction. The corresponding fitted volume fractions are marked in the plots.

Alloy	ϵ-matrix a [Å]	ϵ-matrix c [Å]	γ-matrix a [Å]	TaC a [Å]	ϵ-matrix vol.%	γ-matrix vol.%	TaC vol.%	C/Ta calculated
1173 K								
TaC05	2.552	4.122	3.604	4.449	86.84	12.16	0.4	0.94
TaC07	2.558	4.123	3.606	4.451	95.0	2.8	2.2	0.97
TaC09	2.554	4.136	3.602	4.451	96.2	1.0	2.0	0.99
TaC10	2.569	4.124	3.599	4.459	95.1	1.0	2.3	1.02
1373 K								
TaC05	2.552	4.123	3.604	4.450	92.4	6.5	0.8	0.96
TaC07	2.557	4.122	3.606	4.454	95.1	2.9	2.8	0.97
TaC09	2.560	4.119	3.599	4.455	95.7	1.9	2.4	0.99
TaC10	2.568	4.131	3.597	4.459	93.7	2.8	2.7	0.99
1473 K								
TaC05	2.553	4.121	3.604	4.444	93.6	4.7	0.7	0.96
TaC07	2.557	4.123	3.601	4.454	95.8	1.9	3.9	1.02
TaC09	2.561	4.128	3.594	4.453	95.4	1.9	3.5	1.02
TaC10	2.574	4.119	3.593	4.469	94.6	1.9	3.5	1.08

TABLE 5.2.1: Lattice parameters of different phases in the Co-Re alloys at RT obtained from XRD (ST + in-situ 15 h at 1173 K, 1373 K and 6 h at 1473 K, respectively). There is very little remnant γ-Co phase after HT in the samples. Lattice constants and volume fraction of TaC are slightly larger after heat treatment. All lattice constants are given with an accuracy of at least $\pm$ 0.001 nm and TaC vol.fr with $\pm$0.5%.

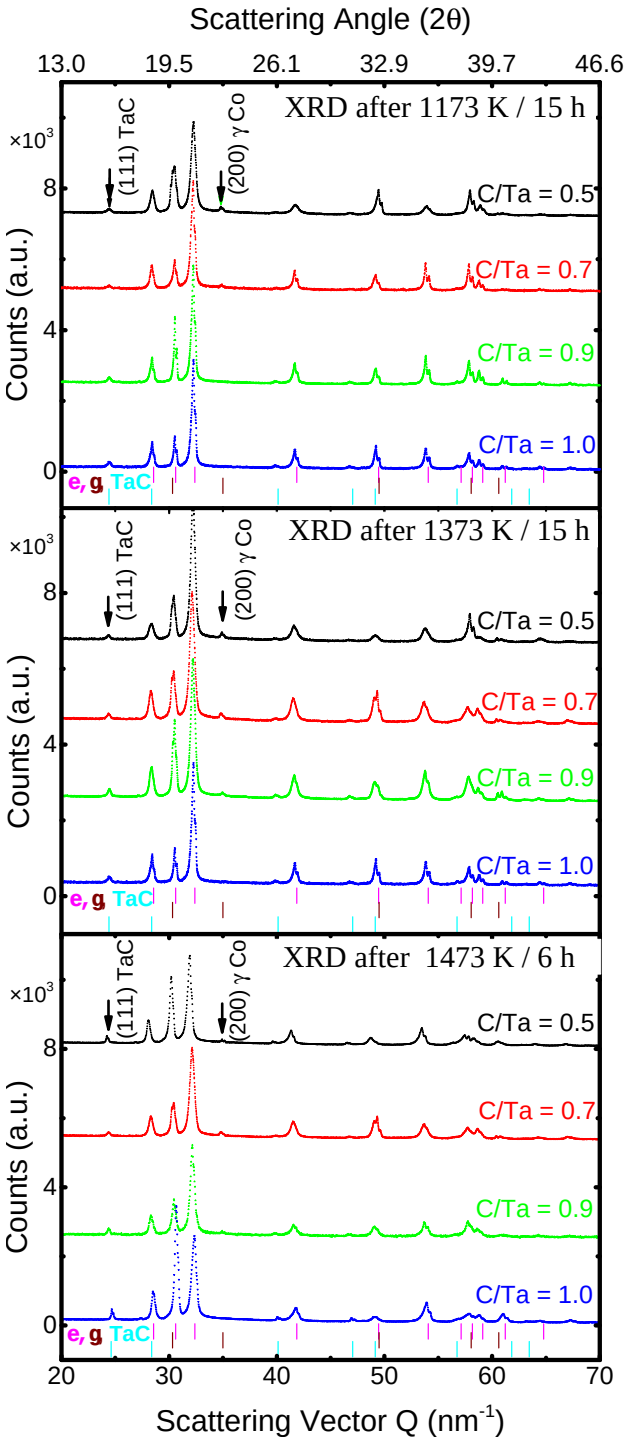

Figure 5.2.4: XRD from aged Co-Re-Ta-C samples after heat treatments at 1173 K, 1373 K and 1473 K. All alloys show remnant γ-Co phase and TaC-phase. Adapted from [10].

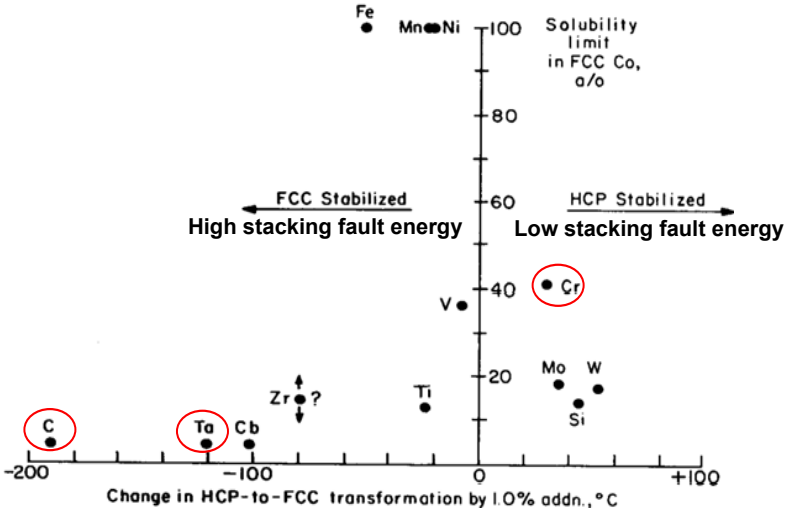

FIGURE 5.2.5: Stabilizing properties of elemental additions in cobalt. C and Ta stabilize fcc γ-Co phase, while Cr stabilizes hcp ϵ-Co phase. The fcc γ-Co phase has a generally higher stacking fault energy than the hcp ϵ-Co phase. Adapted from [107].

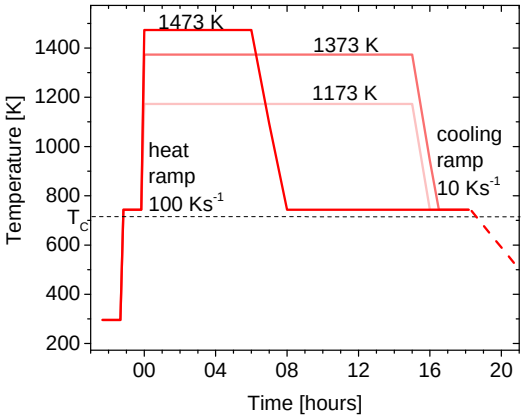

FIGURE 5.3.1: (left) The in-situ heat treatments on the Co-Re samples at 1173 K, 1373 K and 1473 K. At HT, the available SANS Q-range was scanned in 1 h intervals.

the sample bulk and the following results represent average values over a cylindrical sample volume of $5^2 \times \pi \times 1\,\mathrm{mm}^3$. It has to be mentioned, that there exist inhomogeneous areas in the alloy (cf. section 5.1), which can show different results locally.

The Co-Re-Ta-C alloys are ferromagnetic at 300 K and have a Curie temperature of $T_C \approx 700\,\mathrm{K}$. Hence, the SANS signal from TaC precipitates is overlapped by magnetic scattering from domain walls (Fig. 5.3.2 left). For that reason, the samples were measured before and after the in-situ cycles at 723 K, which is above the Curie Temperature T_C of Co-Re alloys. These measurements are considered RT measurements, since the existing phases are practically unchanged below 1100 K (cf. section 5.2.3). While heating the sample to HT, the total intensity after small-angle scattering was monitored by a series of quick measurements. The scattering intensity nicely shows the disappearance of magnetic domains and e.g. can be used as a tool to determine T_C (Fig. 5.3.2 left inset).

Fig. 5.3.3 presents the $2D$ scattering pattern of TaC07 alloy at RT, at 723 K and after 1 h at 1173 K. The image taken at RT is superimposed by the strong magnetic signal. At 723 K, the SANS measurements reveal that the nuclear scattering from the polycrystalline Co-Re

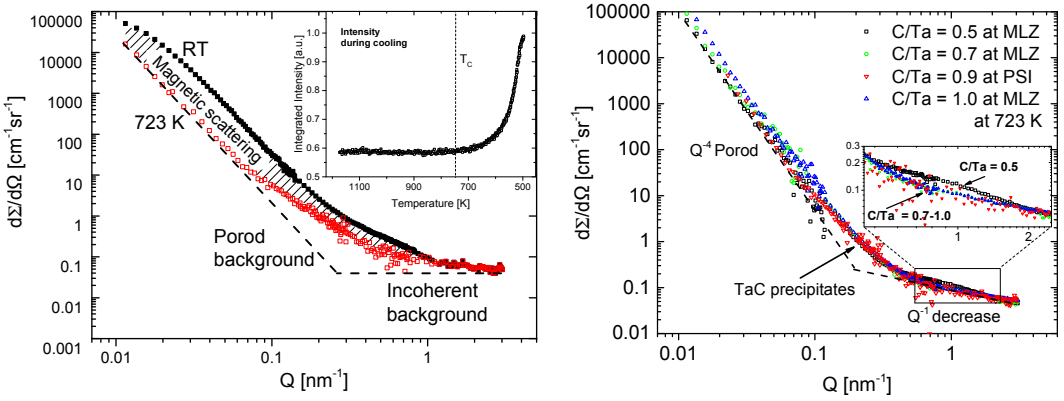

FIGURE 5.3.2: (left) The SANS signal from nuclear Co-Re-Ta-C alloys is overlapped by magnetic scattering from domain walls of the ferromagnetic alloy. The magnetic scattering was observed by SANS during cooling and yields a Curie temperature $T_C \approx 700\,\mathrm{K}$ (left inset). (right) Scattering in ST condition from alloys TaC05-10, taken above T_C. There is a Q^{-1} decrease of the scattering intensity towards large Q, suggesting elongated, very fine scattering structures. For $Q \to 0$, the scattering intensity is different for the four alloys, due to different amount of scattering from large scale structures in the alloy matrix. Adapted from [10].

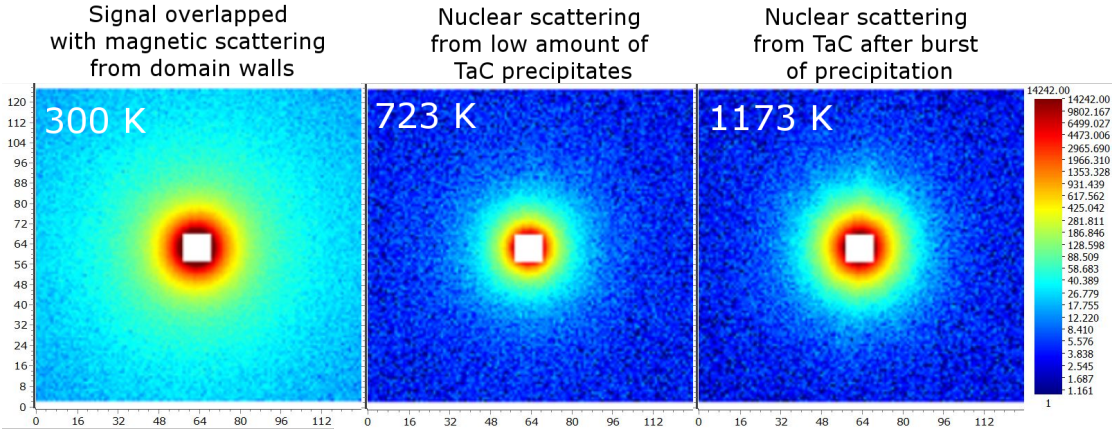

FIGURE 5.3.3: Comparison of the signals from SANS at RT (left), $723\,\mathrm{K} > T_C$ of the Co-Re alloy (middle) and at 1173 K after the burst of TaC precipiates (right).

alloys is isotropic (i.e. no azimuthal dependence of the signal exists on the $2D$ detector). Even though the TaC precipitates are not always perfectly spherical as visible in SEM images (Fig. 5.1.3), their random orientation distribution in different grains over the whole sample volume results in an isotropic scattering pattern. After reaching HT, the scattering strongly increases, due to an additional precipitation of TaC particles.

The data were calibrated by a H_2O standard to absolute intensity and azimuthally averaged (cf. appendix A). The 1D azimuthally averaged SANS patterns of the four samples (in ST condition) are shown in Fig. 5.3.2 (right). The coherent SANS peaks originate from the fine TaC precipitates, as diffraction and microscopy identified the TaC phase in form of precipitates as the only phase in the measured SANS Q-range (cf. sections 5.2, 5.1). In the limit of large Q-values the coherent scattering is superimposed by the incoherent scattering from Co, Re, Ta and C atoms. Additionally, large-scale interfaces from the Co lath and defect boundaries in the matrix (e.g. stacking faults and possibly micro twins

$> 300\,\text{nm}$) produce a Porod background $I(Q) \propto Q^{-4}$. Notably, the Porod background is different for the four samples, as can be seen in the limit of small Q. In ST condition, all samples show weak scattering from the TaC precipitates in the range $0.07 - 0.6\,\text{nm}^{-1}$ and their volume fraction changes only slightly with C/Ta ratio y from 0.10 vol.% for TaC05 to 0.15 vol.% for TaC09 alloy. Additionally, the Porod background does not level out in a constant incoherent background for large Q-values in the resolution range $0.3 - 3\,\text{nm}^{-1}$, but rather decreases with a slope (Fig. 5.3.2 right inset). This suggests the presence of very fine elongated inhomogeneities in the matrix [108]. A fit with the form factor of a flat Porod cylinder yields a length of $2 \pm 1\,\text{nm}$ and radius of $3.5 \pm 1\,\text{nm}$ for all alloys. The contribution is nearly the same for the three alloys TaC07-10, but stronger for the TaC05 sample. These inhomogeneities are too small to be detected by SEM, but since ND does not show additional phases, they are assigned to the TaC phase. This yields an additional volume fraction of 0.2 vol.% for TaC07-10 samples and 0.3 vol.% for TaC05 sample of TaC precipitates at RT.

5.3.1 In-situ experiments at high temperature

Fig. 5.3.4 shows the detailed evolution of scattering from TaC precipitates in the TaC09 alloy during in-situ HT experiments at (left) 1173 K and (right) 1373 K. The resulting precipitate size distribution is shown in the Fig. inset on top right. The general behavior is representative for all alloy compositions, only the exact size and volume fraction values vary. After reaching HT, there is a strong increase of the scattering signal, caused by TaC precipitation. The kinetics of precipitation is very fast and is much quicker than the time that was needed by the movements of instrument components in order to change the Q-range. This is seen at 1173 K as a discontinuous SANS curve marked by an arrow in Fig. 5.3.4a in which the movement took about 10 min. At 1373 K, the precipitation kinetics is even faster and the discontinuous SANS curve is not observed, since there is already a significant amount of TaC precipitation during heating. In addition, it is seen that the Q^{-1} scattering slope in the large Q-range completely vanishes on reaching 1173 K, indicating dissolution or morphology change of the very fine needle-like particles. Therefore, this contribution was not taken into account in the depicted size distributions.

The details of the fine TaC precipitate evolution in all samples at HT are shown in 5.3.5 (modeled with a spherical form factor). After holding for at most 4 h at HT, the volume fraction of fine TaC precipitates no longer changes, but they coarsen during the subsequent holding at HT. The kinetics is already slow at the end of the 15 h in-situ cycle at 1173 K and 1373 K and after 6 h at 1473 K, respectively. However, the C/Ta ratio y significantly influences the precipitated volume fraction and the speed of coarsening. A higher y results in a higher volume fraction at all measured HT (Fig. 5.3.5a, b, c). Also, the coarsening rate is quicker for higher y at 1173 K and 1373 K, only at 1473 K no such systematic could be observed (Fig. 5.3.5d, e, f). In the end of the in-situ heat cycles 1173 K/15 h, 1373 K/15 h and 1473 K/6 h, maximum precipitate sizes of 47 nm, 92 nm and 90 nm, respectively, were reached. The corresponding maximum measured volume fractions were 1.27 vol.%, 1.24vol.% and 1.15 vol.%. In addition, the respective samples were ex-situ heat treated at 1173 K/15 h and 1373 K/15 h. The SANS measurements show that sizes and volume fraction remain nearly constant afterwards.

From the determined volume fraction and size distribution, the inter-particle distance of TaC precipitates was calculated according to eq. (B.17). Their evolution at the respective HT

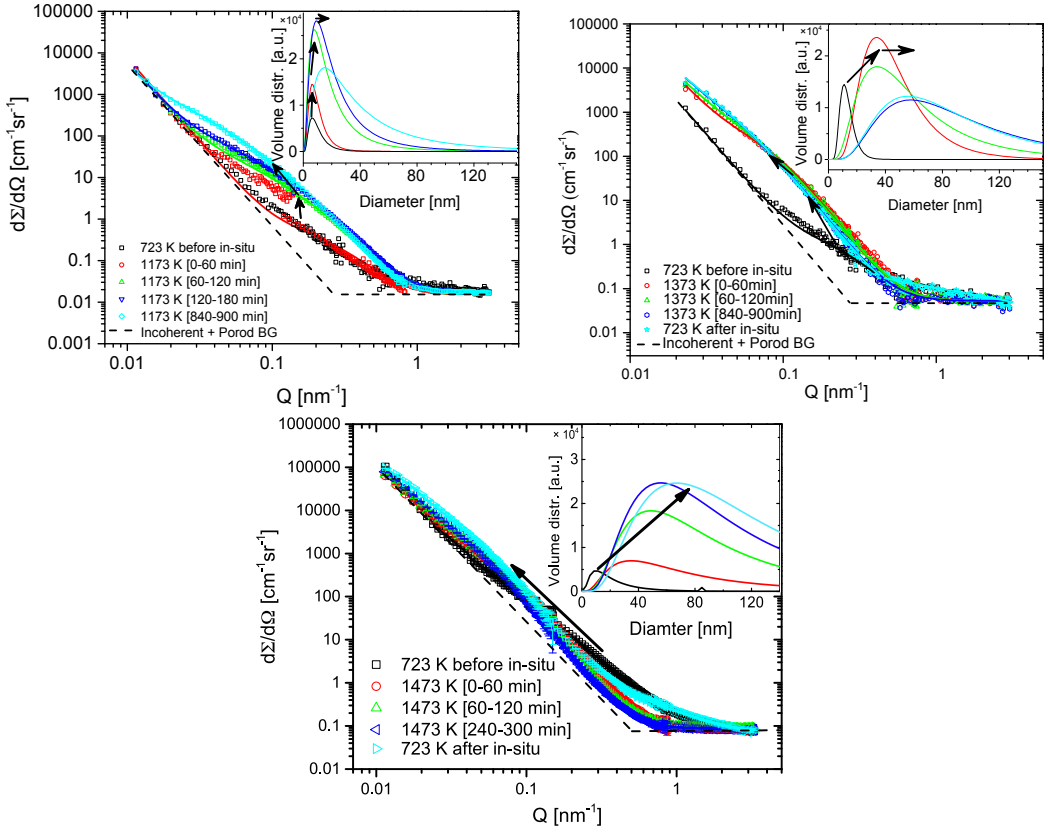

Figure 5.3.4: Evolution of the SANS signal from TaC precipitates at 1173 K (left), 1373 K (middle) and 1473 K (right). The insets depict the fitted log-normal particle size distributions, fitted with a spherical form factor. Adapted from [10].

is shown in Fig. 5.3.5g, h, i. The values are large in ST condition ($l_m = 2200-2400$ nm) due to the low volume fraction. During the HT cycles, the behavior is considerably changed for the different temperatures. The distance strongly decreases directly after reaching 1173 K. After $3h$ at HT, the values remain rather constant and approach $l_m \approx 500$ nm in $y = 0.7-1.0$ alloy and $l_m \approx 700$ nm in TaC05. The longer term trend from the ex-situ samples shows that size and volume fraction values are almost constant and inter-particle distance values converge to $l_m \approx 600$ nm for all four y ratios. At 1373 K, the inter-particle distance is considerably larger because of the larger particle sizes and broader size distributions of precipitates and shows a clear dependence on the C/Ta ratio y. Values of $l_m = 1500\,\text{nm}, 200\,\text{nm}, 2500\,\text{nm}$ are reached for alloys TaC09,07,05, respectively. At 1473 K, the inter-particle distance is still increasing after 6 h, but there is a clear distinction for high and low C content alloys. Already after 2 h at HT the distance differs and increase with ~ 2 times higher slope for low C content alloys. After 6 h at HT low C content alloys reach an inter-particle distance of $l_m \approx 4400$ nm and high C content alloys $l_m \approx 1800$ nm.

During cooling from 1373 K (Fig. 5.3.4 middle) to RT, there are almost no changes in the smaller Q-range of the SANS signal. This suggests that the TaC precipitate morphology remains unchanged during the slow cooling in the furnace with a ramp $10\,\text{K}\,\text{min}^{-1}$. However, the scattering contribution reappears with only slightly changed shape, suggesting a second precipitation of very fine elongated TaC in the Co-matrix during cooling. This behavior was observed in all samples after cooling from any HT to RT.

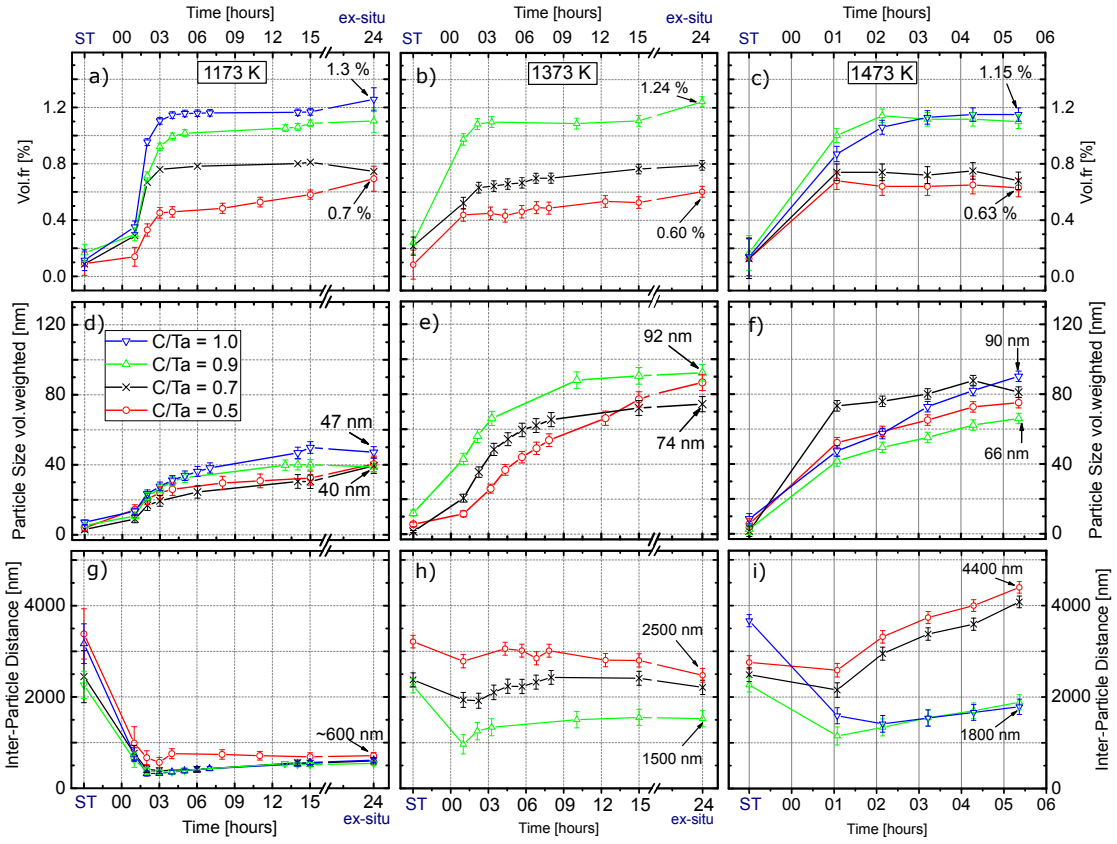

FIGURE 5.3.5: Evolution of volume fraction, particle size and inter-particle distance of alloys TaC05-10 at the temperatures 1173 K, 1373 K and 1473 K. Adapted from [10].

5.3.2 Dissolution of TaC precipitates at 1573 K

The dissolution of fine TaC precipitates at 1573 K was qualitatively monitored by in-situ SANS. One low C alloy (TaC05) and one high C alloy (TaC09) were kept at the temperature while monitoring the scattering from TaC precipitates. The result is shown in Fig. 5.3.6. Already within the first 2 h at the temperature, the scattering has considerably reduced in both alloys. After 4 h the scattering comes to a minimum and all fine precipitates have dissolved or have grown out of the SANS resolution range. From the in-situ ND (cf. 5.2) it is known that there is still TaC phase in the alloy, but the total amount has decreased. In addition, the matrix is mostly present in the form of γ-Co phase.

On the one hand, the fine TaC strongly precipitates during the transformation $\gamma_m \rightarrow \epsilon$, while on the other hand they quickly dissolve during the transformation $\epsilon \rightarrow \gamma$. Therefore, it can be concluded that the TaC phase in form of fine precipitates is only stable in the $\epsilon - Co$ phase at HT.

5.4 Discussion

5.4.1 Effect of $\gamma \leftrightarrow \epsilon$ matrix transformation on fine TaC precipitates

It is well known that the γ-Co phase (fcc) is often metastably retained at RT in pure Co [25]. The present ND measurements show a similar behavior for Co-Re alloys in ST condition, where 45-55 vol.% of γ_m-Co phase is retained (depending on y, table 5.0.2). Notably, the

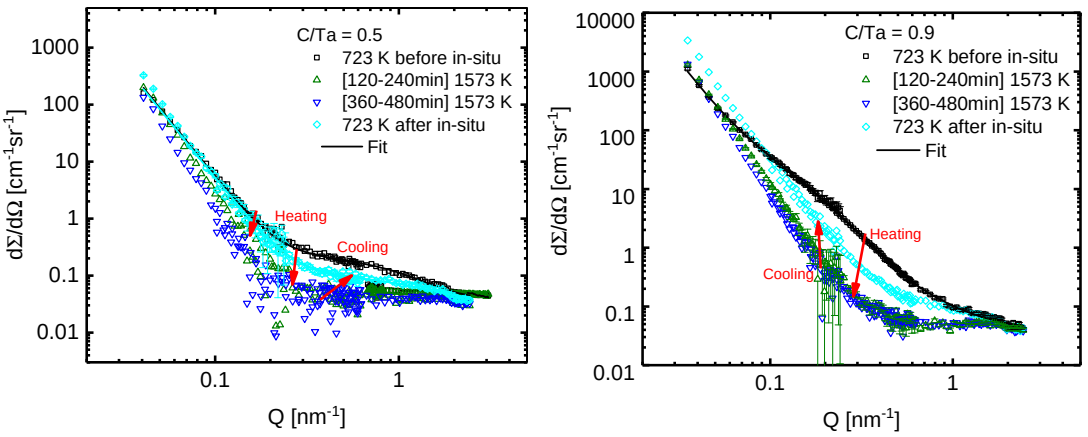

FIGURE 5.3.6: At 1573 K, the nano scaled TaC precipitates dissolve or grow out of SANS resolution range. Only a Porod-type Q^{-4} background remains, after 3 h. (left) TaC05, (right) TaC09 alloy.

variation is not linear with y, but in low C alloys, there is generally a higher amount of metastable γ_m-Co phase than in high C alloys.

The in-situ ND measurements show that the kinetics of matrix phase transformation is slow during heating below 1173 K and the γ_m/ϵ-Co phase fraction remains mostly unchanged during heating from RT to 1173 K (Figs. 5.2.2, 5.2.3). The required thermal activation energy for the transformation of the metastable γ_m-Co phase to thermodynamically stable ϵ-Co phase is reached just when reaching 1173 K. This transformation is nearly complete on holding for 2 h at 1173 K in high C content alloy TaC09, while a significant amount of γ-Co phase remains in low C content alloy TaC05. It follows that the equilibrium γ- and ϵ-Co phase content at temperatures $1173 - 1473$ K varies for Co-Re alloys with different y. The Co-matrix transforms fully to the HT γ-Co phase upon heating to $1600 - 1650$ K for TaC05-10.

The precipitation of fine TaC particles < 100 nm coincides with the transformation of the matrix from γ_m to ϵ-Co phase (Fig. 5.3.5). The SANS signal is scattering from the fine TaC carbides as the in-situ ND experiments do not show any additional phases (Fig. 5.2.2). The strong burst of TaC precipitation, observed by the in-situ SANS experiment (Fig. 5.3.4) at 1173 K, occurs during the transformation of metastable γ_m-Co phase to stable ϵ-Co phase. The strong nucleation of fine TaC precipitates may be attributed to an expected lower solubility of Ta and/or C in the ϵ-Co-Re matrix. SEM shows that a high amount of TaC particles precipitate in the lath and within the larger untransformed ϵ-Co regions (Fig. 5.1.4).

The nucleation of TaC precipitates is quicker for higher y, i.e. higher C content with constant Ta content (Fig. 5.3.5). The differing C supersaturation is likely the reason for the different nucleation rates in the first hour at HT. In addition, the vol.% of TaC precipitates is higher for higher y. Consequently, the ϵ-Co matrix in alloys with higher y value is more depleted of Ta at the end of the in-situ cycles. This results in the different equilibrium mixing ratios of γ- and ϵ-Co phase at HT in low and high C content alloys that were revealed by in-situ ND and XRD measurements taken after the in-situ SANS measurements (table 5.2.1): high C content alloys retain less γ-Co phase and have a higher TaC volume fraction than low C content alloys.

As a consequence, there is an indirect influence of TaC precipitation on the γ/ϵ equilibrium ratio at HT, since the amount of retained γ_m-Co matrix is lower for alloys with higher y value. Subsequently, the amount of dissolved Ta and C have a stabilizing effect on the γ-Co matrix in Co-Re alloys. Although only small amounts of Ta and C are present in the alloys ($0.6-1.2$at.%), the effect is strong on the matrix. This conclusion is supported by the ND results that showed that the rate and temperature of allotropic phase transformation is controlled by the C/Ta ratio (Fig. 5.2.3). A lower y value results in a less complete and slower transformation $\gamma \rightarrow \epsilon$-Co transformation at HT. Hence, the nature of Co-Re matrix phase is significantly influenced by TaC precipitation (and subsequent depletion of the elements from the matrix).

The present results strongly suggest Ta to be an fcc stabilizer of the γ-Co phase. There are contradicting phase diagrams on the stabilizing nature of Ta in the literature. Older phase diagrams indicate it to stabilize the ϵ-Co phase [109], while recent theoretically calculated binary Co-Ta phase diagrams support the present result of Ta to be a γ-Co phase stabilizer [110].

5.4.2 TaC precipitates at 1173 K, 1373 K and 1473 K

In initial ST condition, the mean TaC precipitate size is small (~ 10 nm) in all alloys with $y = 0.5-1.0$. Their volume fraction in the matrix, observed by SEM (Figs. 5.1.1, 5.1.2) and quantified by SANS (Fig. 5.3.5), is quite low ($< 0.3\%$). The diffraction experiments revealed weak peaks from the TaC phase as well (Figs. 5.0.1, 5.2.4).

During the in-situ heat treatment, the TaC volume fraction increases by a factor $\sim 5-10$ in the four alloys TaC05-10. As expected, the increase is larger for alloys with larger C/Ta ratio y, i.e. with higher C content. After holding for 4 hours at HT (1173 K, 1373 K, 1473 K) in the in-situ SANS experiments, the fine TaC precipitates reach a constant volume fraction in high C content alloys, and a nearly constant volume fraction in low C content alloys. A maximum volume fraction of ~ 1.3 % (Fig. 5.3.5) was observed at 1173 K. This value slightly lowers with higher temperature, explained by an increasing solubility of Ta and/or C in the Co-Re matrix. Assuming zero solubility of Ta and C in the matrix results in a maximum possible TaC volume fraction in the ϵ-Co phase of:

$$1.2\text{at.}\%(Ta) + 1.032\text{at.}\%(C) = 2.1\text{vol.}\%(\text{TaC}_{0.9}), \tag{5.1}$$

using the stoichiometry $\text{TaC}_{0.9}$ of precipitates and the molar volume of matrix $6.96 \times cm^3mol^{-1}$ and TaC $6.65 \times cm^3mol^{-1}$ determined from their measured lattice constant in the ND experiment (table 5.1.1). Since this number is larger than what is observed in the SANS experiments, not all of the available Ta and C precipitates as fine TaC phase (i.e. TaC detectable by SANS). The remaining Ta and C is partially dissolved in the matrix and partially present in the form of large TaC precipitates (facetted and blocky), which were observed by SEM (Fig. 5.1.1). In addition, these precipitates cause differing intensities of Porod background in SANS (Fig. 5.3.2). These large TaC particles are quite stable in the matrix at temperatures < 1500 K, as they can be seen before and after in-situ SANS experiment and the Porod background does not alter during the heating/cooling cycle.

The evolution of inter-particle distances l_p shows different features for the various aging temperatures. The SANS measurements reveal that the parameter is quite stable and similar

in the long-term trend at 1173 K and 1373 K (Fig. 5.3.5g,h). However, the low C content alloys show considerably larger l_p distance than high C content alloys at 1373 K. This trend is even more obvious at 1473 K heat treatment, where l_p increases by a factor of ~ 2 faster in low C content alloys than in high C content alloys. The main reason for the different l_p is the different precipitated TaC volume fraction. In addition, a higher temperature leads to much broader TaC precipitate size distributions (Figs. 5.3.4 insets), i.e. the logarithmic standard deviation σ increases. Consequently, l_p gets larger as well, although mean particle size and volume fraction are similar (see eqs. (B.12), (B.17)). Further, the high C content alloys retain less γ-Co phase at the end of the heat treatments (Fig. 5.2.4, table 5.2.1), which might result in a more homogeneously distributed precipitation and thus influences l_p.

Cooling of the samples from temperatures $\leq 1473K$ leaves the SANS signal of TaC precipitates essentially unchanged in the Q-range $0.03 - 0.3\,\mathrm{nm}^{-1}$ (Fig. 5.3.4). It can be concluded that the morphology of fine TaC remains unchanged during cooling. However, the Q-range $0.3 - 3\,\mathrm{nm}^{-1}$ is altered during cooling. This suggests a secondary precipitation of very fine particles, which could only be deduced from SANS, since their size ($< 10\,\mathrm{nm}$) is too small to be detected by the SEM. Since ND shows that the Co-Re matrix state is essentially stable in this temperature range (Fig. 5.2.3), it cannot affect the changed SANS signal. Therefore, the solubility of Ta and C further diminishes during cooling to RT and the secondary particles re-precipitate at lower temperatures than 1173 K during cooling. The higher amount of dissolved Ta in low C content alloys might explain the stronger secondary precipitation in these alloys (Fig. 5.3.2 right).

Notably, the discrepancy between the volume fraction measured by SANS and by XRD is up to 2.6 % (Fig. 5.3.5, table 5.2.1), which is, however, in the range of realistic error bounds of the latter method. This shows the necessity of the generally more accurate SANS measurement where the accuracy is limited mostly by the SLD calculation and less by the count statistics of the very small TaC diffraction peaks.

5.4.3 Coherence of TaC precipitates in Co-Re matrix

The lattice constants from ND were used for determining the TaC // Co-Re coherence relationship. The coherence of TaC precipitates is evident from the oriented, plate-like TaC precipitates observed by SEM (cf. Fig. 5.1.3). Several overlapping peak positions of TaC precipitates and ϵ-Co matrix can be seen in the ND pattern (cf. Fig. 5.0.1). The result shows a good matching of several interplanar distances in the two phases (i.e. ϵ-Co and TaC). It is likely that the fine TaC particles precipitate (semi-)coherently along these directions to reduce their interface energy.

A good match is found with a Matlab program, developed in the frame of this thesis (cf. section 4.4.5). The match is found according to the edge-to-edge matching model [111] with $a_{\mathrm{TaC}} = [100]_{\mathrm{TaC}} || a_\epsilon = [10\bar{1}0]_\epsilon$, $a_{\mathrm{TaC}} = [021] || a_\epsilon = [1\bar{2}1\bar{0}]_\epsilon$, together with a low d-value mismatch of the corresponding lattice planes $(012)_{\mathrm{TaC}}/(0001)_\epsilon$ (Fig. 5.4.2 left). The misfit of the matching directions is calculated according to $\delta = 2(a_1 - a_2)/(a_1 + a_2)$ (where a_1 and a_2 are the respective crystallographic lattice constants of the TaC and ϵ-phase). The calculation gives a maximum mismatch of $\delta < 0.21\%$ in $[100]_{\mathrm{TaC}} || [10\bar{1}0]_\epsilon$ and of $\delta < 2.73\%$ in $[021]_{\mathrm{TaC}} || [1\bar{2}1\bar{0}]_\epsilon$ (Fig. 5.4.2 right, table 5.4.1). A slight change of the misfit to smaller values is observed for the in-situ aging heat treatments related to the directions $a_{\mathrm{TaC}} = [100]_{\mathrm{TaC}} || a_\epsilon = [10\bar{1}0]_\epsilon$. This is most likely caused by an enrichment of Re in the ϵ-phase by

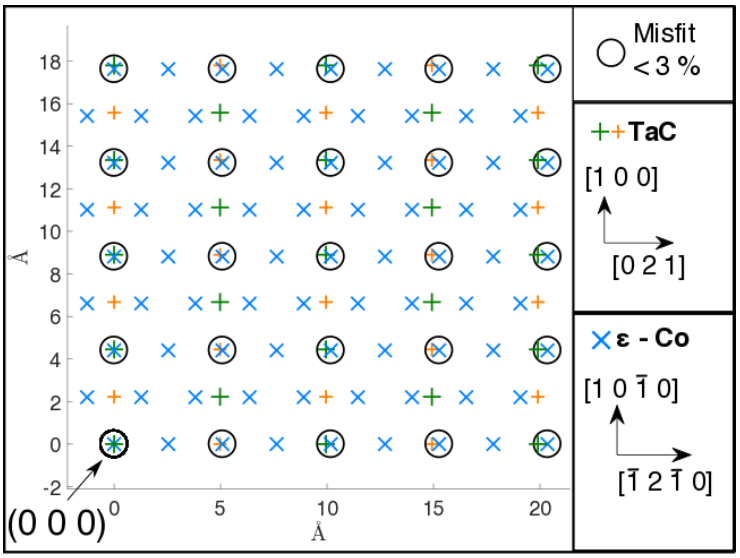

FIGURE 5.4.1: Representation of misfit from TaC09 sample as projection onto the matching planes $(01\bar{2})_{\mathrm{TaC}}/(0001)_{\epsilon}$ with real lattice constants in ST condition. The matching positions of TaC and matrix are marked by a circle. The matching is much better in $[100]_{\mathrm{TaC}}$ direction with a misfit $< 0.3\%$. Adapted from [10].

diffusion during the heat treatment, leading to an increase of lattice constant and decrease of the misfit in the directions $a_{\mathrm{TaC}} = [100]_{\mathrm{TaC}} || a_{\epsilon} = [10\bar{1}0]_{\epsilon}$. During ST treatment, the $\gamma \rightarrow \epsilon$ phase transformation occurs on cooling to RT, leaving not enough time for element partitioning of the phases by diffusion, as can be seen by the EBSD measurements (cf. section 5.1.3, Fig 5.1.5). Therefore, the ϵ- and γ-Co phase are not in chemical equilibrium in ST condition, explaining the larger misfit value. The directional misfits of matrix and precipitate are visualized in Fig. 5.4.1 for the TaC09 alloy.

	$\delta[100]_{TaC}$ $\|\|[10\bar{1}0]_\epsilon$ [%]	$\delta[021]_{TaC}$ $\|\|[\bar{1}2\bar{1}0]_\epsilon$ [%]	$\delta[02\bar{4}]_{TaC}$ $\|\|[0001]_\epsilon$ [%]
ST			
TaC05	0.21	-2.58	-0.89
TaC07	0.12	-2.67	-0.88
TaC09	0.13	-2.66	-0.86
TaC10	0.05	-2.73	-0.92
1173 K			
TaC05	0.16	-2.62	-0.93
TaC07	0.11	-2.67	-0.87
TaC09	0.15	-2.63	-0.88
TaC10	0.05	-2.73	-0.91
1373 K			
TaC05	0.17	-2.62	-0.89
TaC07	0.14	-2.65	-0.86
TaC09	0.12	-2.67	-0.85
TaC10	0.06	-2.72	-0.81
1473 K			
TaC05	0.12	-2.66	-0.96
TaC07	0.14	-2.65	-0.85
TaC09	0.10	-2.69	-0.86
TaC10	0.06	-2.73	-0.80

TABLE 5.4.1: The misfit δ of two in-plane directions of TaC precipitate and ϵ-Co phase and the corresponding d-value spacing.

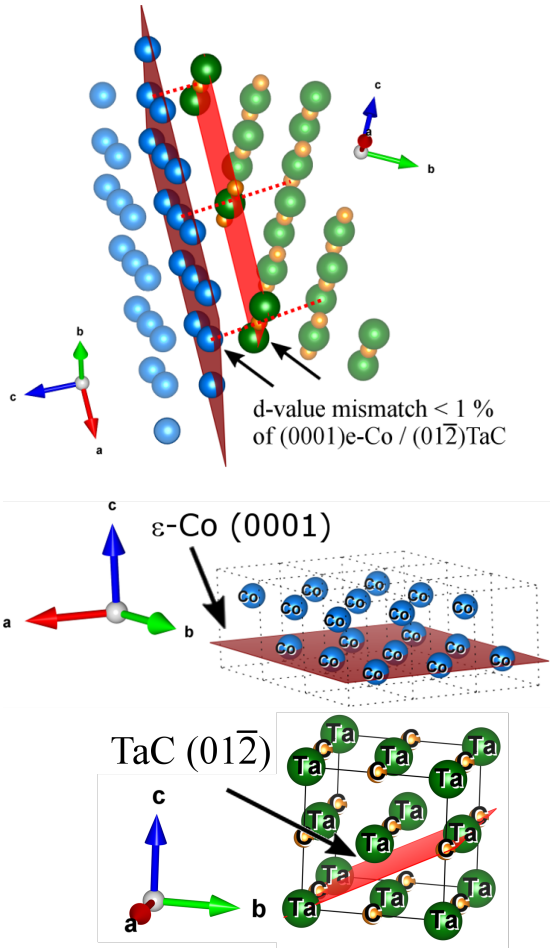

FIGURE 5.4.2: (top) ϵ-Co and TaC phase, matching planes are marked in red. (middle and bottom) Matching of ϵ-Co and TaC precipitates with planes $(01\bar{2})_{TaC}/(0001)_\epsilon$ and the matching directions $[100]_{TaC}||[10\bar{1}0]_\epsilon$ and $[021]_{TaC}||[\bar{1}2\bar{1}0]_\epsilon$; the matching atoms are marked with dotted lines. Adapted from [10].

Chapter 6

Boron and Chromium Addition

In this chapter, the effects of Cr and B to the Co-Re matrix are studied. Both elemental additions are required for the alloy's performance at HT. Cr promotes the formation of a protective Cr_2O_3 oxide layer in other conventional iron, nickel and cobalt base alloys. An improvement of the oxidation resistance in Co-Re alloys as a result of Cr addition was shown in [41, 45, 112].

Since the Co-Re alloys are a polycrystalline material, grain boundary embrittlement can result in a loss of the alloy's ductility. The addition of B largely improves the ductility in Co-17Re-23Cr alloys, because borides in low volume fraction prevent continuous carbide films at the matrix grains [30]. The positive effect of B on the grain boundary cohesion in Co-Re alloys was experimentally shown [29–31]. The fracture mode changes from intergranular to transgranular when adding 200 ppm B to the alloy. However, borides are difficult to detect by SEM since the volume fraction is very low and the exact mechanism for the improved ductility is still unknown. Secondary effects on the allotropic Co-Re matrix transformation or the formation of Cr-carbides and borides are investigated by means of scattering experiments and microscopy. These compounds can bind available C, which is subsequently lacking for TaC precipitate formation [26].

6.1 Cr addition in Co-Re alloys

In order to achieve a good oxidation resistance of the Co-Re matrix at high service temperatures, Cr is added to the matrix. Cr forms a dense Cr_2O_3 layer on the sample surface. However, other unwanted phases can form as a result of a higher Cr content. A previously investigated alloy with 23 at.% addition (Co-17Re-23Cr-1.2Ta-2.6C) was already studied in detail [9, 17] and showed the presence of Cr-carbides. These deplete the available C content for the formation of strengthening TaC precipitates from the matrix. Upon heating to temperatures near the envisaged application temperature of the Co-Re alloys ($> 1300\,\mathrm{K}$), these Cr-carbides showed a thermal instability and they started dissolving into the matrix. In addition, a brittle, Cr containing σ-phase (cf. section 2.1.4) formed in the matrix. This phase depletes the Co matrix from Re, which is disadvantageous for the HT stability.

For these reasons, both phases are unwanted in the alloy. In order to understand the dependence of these phases on Cr content, two additional samples with an addition of 5 and 15 at.% (cf. table 6.1.1) were investigated. The C and Ta content was chosen with the optimal determined ratio C/Ta$= y = 0.9$, described in chapter 5. In the following, the alloy

Alloy	type	Co	Re	Ta	C	Cr	SLD matrix [cm^{-2}]	SLD TaC [cm^{-2}]
5Cr	low Cr content	75.72	17	1.2	1.08	5	7.21×10^{10}	6.14×10^{10}
15Cr	high Cr content	65.72	17	1.2	1.08	15	7.65×10^{10}	6.14×10^{10}

Table 6.1.1: Composition of alloys with Cr addition in at.%. The scattering length density was calculated from the nominal composition of the matrix.

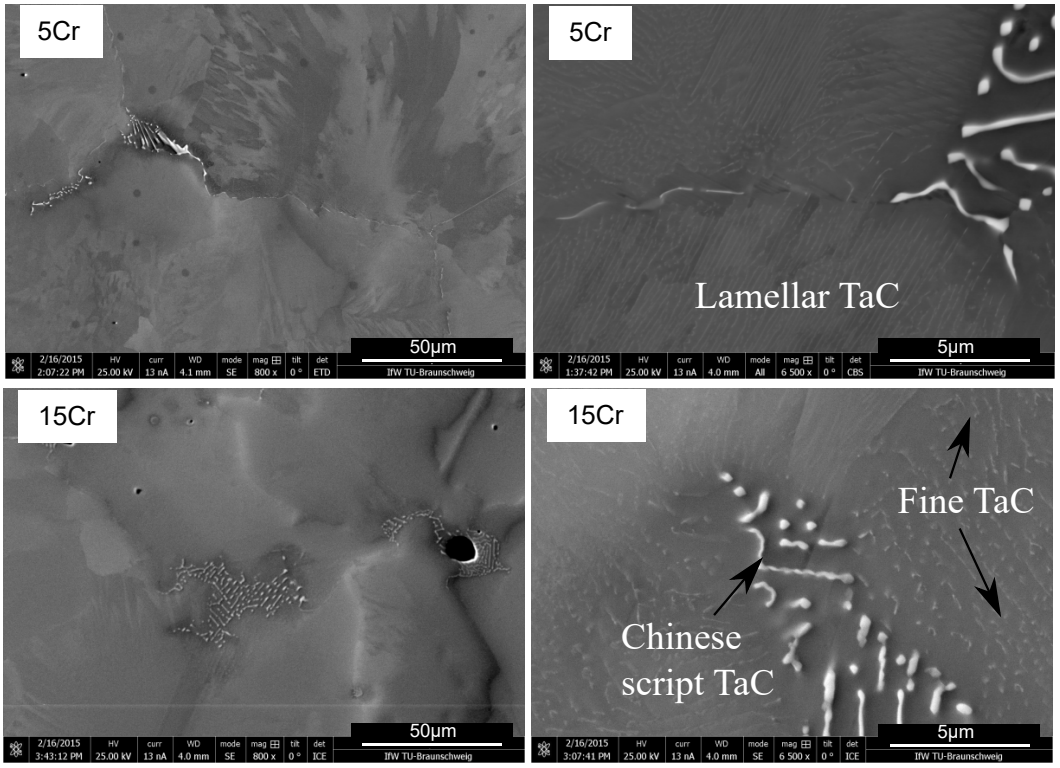

Figure 6.1.1: SEM images of Cr containing alloys in ST condition. 5Cr alloy (top) and 15Cr alloy (bottom) images are depicted. The matrix is single ϵ-Co phase. A low volume fraction of TaC precipitates with various morphologies is observed.

with 15 at.% Cr content is denoted high Cr alloy 15Cr, while the alloy containing 5 at.% Cr is denoted low Cr alloy 5Cr.

The following results are partly published in [113].

6.1.1 Microscopy

The SEM micrographs of low and high Cr alloy in ST condition are presented in Fig. 6.1.1. Fig. 6.1.1a and c are low magnification images, while b and d are higher magnification images. Clearly, the matrix is single phase, and shows no evidence of a twinned, lath-type structure, in contrast to the alloys without Cr (cf. chapter 5). In contrast to the alloys without Cr, there is no metastable γ_m phase at RT. At the same time, the TaC volume fraction is considerably higher in ST condition. However, the TaC morphologies are different. There is a population of lamellar and Chinese script type in addition to the fine TaC precipitates. The lamellar TaC are present in the Co-Re matrix while the Chinese Script have precipitated at the grain boundaries. The fact that the single ϵ-Co phase contains higher amounts of TaC was already observed in the alloy from Chapter 5, where the TaC nucleation and precipitation was very strong when the Co-Re matrix transformed to $\epsilon-$Co phase at $\sim$ 1173 K. The solubility of

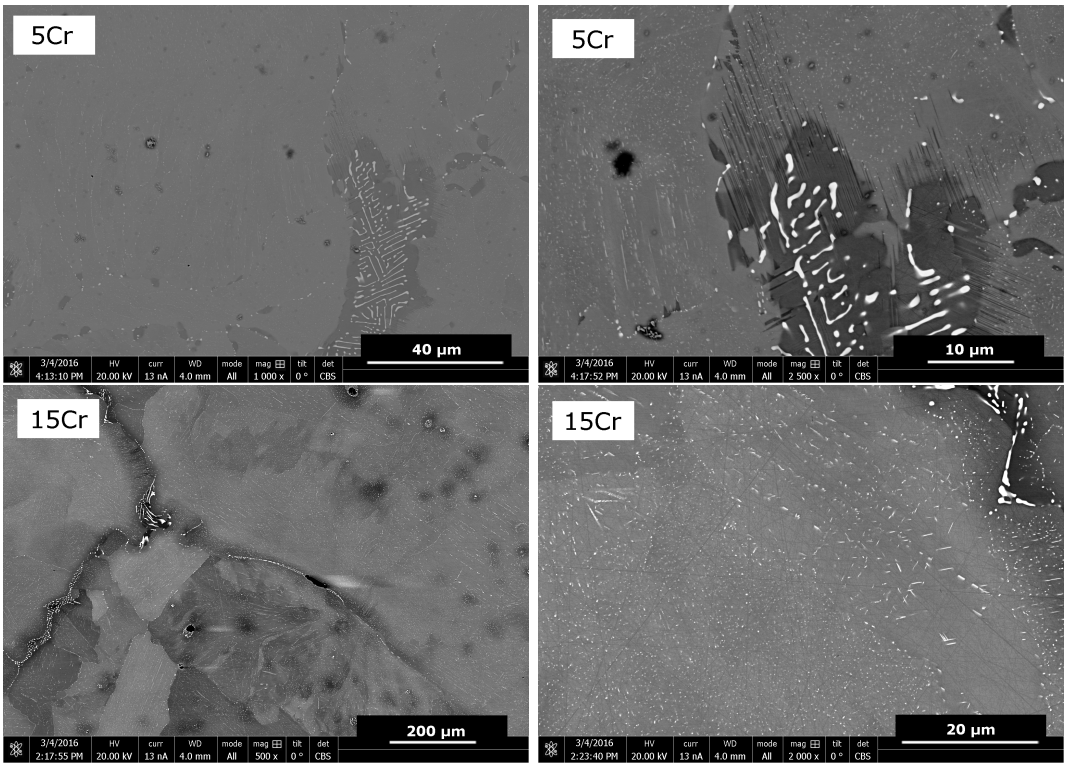

Figure 6.1.2: Representative micrographs after an 15 h aging heat treatment at 1473 K. The matrix is single ϵ-Co phase and TaC precipitates are present in form of nano scaled, globular, elongated and chinese script morphology.

C and Ta is apparently lower in $\epsilon-$Co phase. Neither of the alloys 5Cr and 15Cr show any evidence of Cr-carbides or σ-phase. The added Cr shows complete miscibility in the Co-Re matrix.

The microstructure after heat treatment 15 h at 1473 K is shown in Fig. 6.1.2. All general features are still present. The matrix is still single phase. The TaC phase is present in form of nano scaled precipitates and Chinese script morphology. It can be seen that the TaC precipitates have coarsened to larger size. A considerable fraction of the TaC precipitates has an elongated morphology that can have a length of $\sim 1\,\mu m$ and a thickness of $\sim 200\,nm$. The globular TaC precipitates have a size of $50 - 100\,nm$.

6.1.2 Energy-dispersive X-ray spectroscopy

Fig. 6.1.3 presents EDX results of a high Cr content alloy. The elemental distribution of matrix and precipitates was obtained. The results confirm the single phase nature of the matrix. The fine TaC precipitates are too small for the method, but the larger Chinese Script TaC could be identified. Other Cr containing phases, such as σ or Cr-carbide phase are not present in the alloy. Since the Cr containing alloys essentially consist of two phases ϵ-Co and TaC, the SLDs for SANS evaluation were calculated from the nominal composition (table 6.1.1).

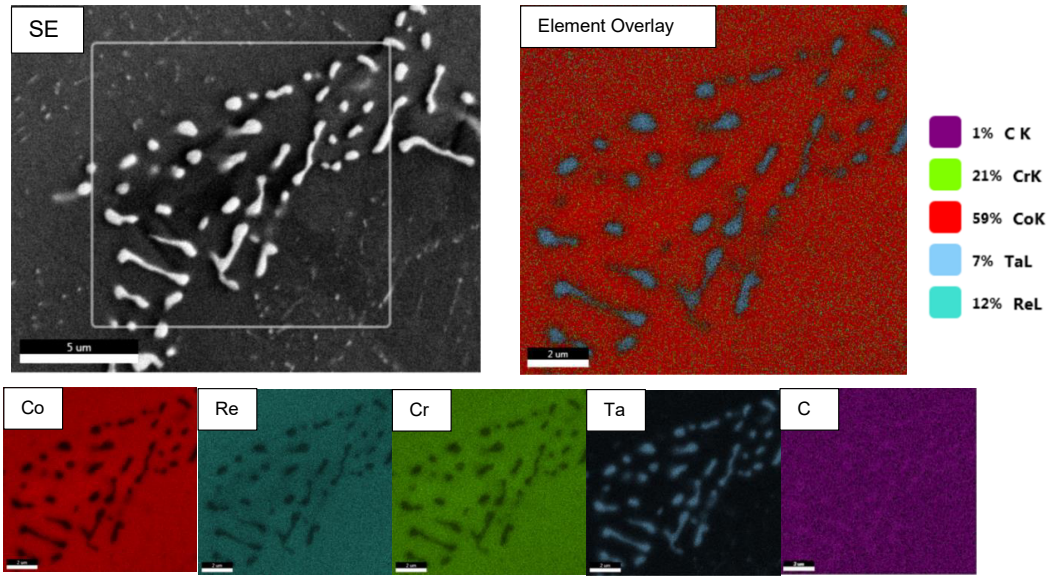

FIGURE 6.1.3: EDX results from high Cr content alloys. Brighter colors result from an enrichement of the element. The precipitates can therefore be identified as TaC and no Cr-carbides were detected in the alloy.

	ϵ-matrix		γ-matrix	TaC	ϵ-matrix	γ-matrix	TaC	C/Ta
ST condition	a [Å]	c [Å]	a [Å]	a [Å]	vol.%	vol.%	vol.%	calculated
5Cr	2.552(3)	4.121(7)	-	4.434(9)	98.7	-	1.3	0.87
15Cr	2.562(3)	4.135(8)	-	4.435(7)	98.3	-	1.7	0.91

TABLE 6.1.2: Results from Rietveld fits for ND data of Cr containing alloys.

6.1.3 Diffraction

The present phases in low and high Cr content alloys were determined using in-situ ND and XRD. Fig. 6.1.4 presents the ND diffractograms in ST condition. The result from Rietveld refinement are presented in table 6.1.2.

The results confirm that there is no $Cr_{23}C_6$ phase present in the alloy in contrast to the previous alloys. Either the Co-Re matrix can absorb up to 15 at.% of Cr or the high affinity of Ta for C suppresses the formation of Cr carbides in these alloys. However, secondary effects arise from Cr concerning the allotropic Co-Re matrix phase transformation.

The $\epsilon \rightarrow \gamma$ phase transformation of the Co-Re matrix was followed using in-situ ND with the same time/temperature history as non Cr containing alloys (cf. Fig. 5.2.1). Fig. 6.1.5 presents the evolution of matrix and TaC phases at HT as contour plots in both alloys. Evidently, the transformation temperature is shifted to higher temperatures when Cr is contained in the matrix. It is well known that Cr is an ϵ-Co stabilizer (cf. Fig. 5.2.5). In both alloys, the transformation $\epsilon \rightarrow \gamma$ starts at the temperature 1533 kelvin, which is 160 K higher than without Cr. When cooling from the HT phase to RT, the matrix transformation $\gamma \rightarrow \epsilon$ is complete, e.g. there is no retained metastable γ_m-Co phase at RT (in contrast to alloys without Cr, cf. section 5.2). The transformation is completed in the low Cr alloy at 1373 K and in the high Cr alloy at 1523 K. This again shows the ϵ stabilizing nature of Cr.

The TaC phase shows changes in the same temperature region. First, the TaC phase volume fraction increases slightly during heating. During the $\epsilon \rightarrow \gamma$ transformation of the matrix, the TaC phase also starts to diminish, but it is still present at the highest temperature

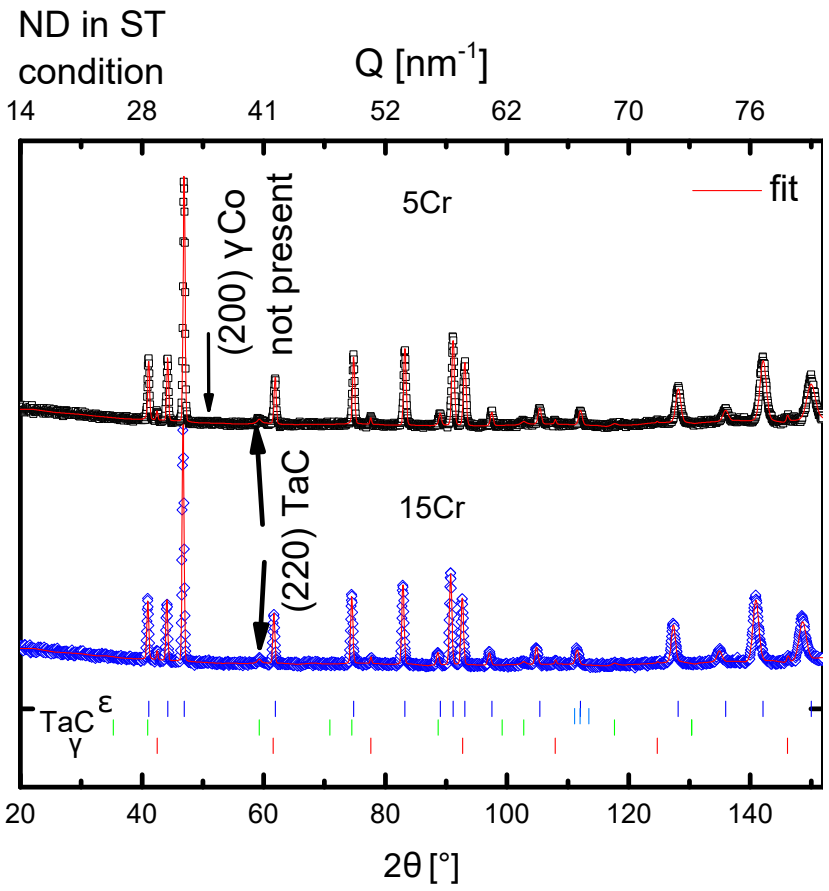

Figure 6.1.4: (top) 5Cr alloy (bottom) 15Cr alloy, taken from ND. Reflexes from ϵ-Co and TaC phase are observed, but the γ-Co phase is not present. Small peaks from the sample holder made of vanadium were considered in the fit.

of 1773 KK. During cooling and the transformation $\gamma \rightarrow \epsilon$, the TaC volume fraction is again increased and comes to a value of $\sim$ 2 vol.% at RT. However, the exact morphology of the precipitates is unknown and therefore studied with in-situ SANS (cf. section 6.1.4).

The phase content was quantified using Rietveld refinement during the in-situ measurement. The evolution of the phases is depicted in Fig. 6.1.6. During heating, the content of TaC slightly increases, showing that the matrix was oversaturated with C and/or Ta in ST condition. However, the amount of TaC precipitates is considerably higher in ST condition than in alloys without Cr (cf. section 5.2). The allotropic Co-Re matrix transformation $\epsilon \rightarrow \gamma$ upon heating starts at 1563 K in 5Cr alloy and at 1603 K in 15Cr alloy. The transformation is completed at $\sim$ 100 K higher temperature. In addition, the TaC content starts to drop at this exact temperature. During cooling, a hysteresis of the transformation is observed. The matrix transformation is completed at 1383 K in 5Cr alloy and at 1533 K in 15Cr alloy. In contrast to alloys without Cr, the transformation is complete and not sluggish and there is no remnant metastable γ_m-Co phase at RT. The transformation occurs at higher temperature and is faster for higher Cr content, emphasizing the fact that Cr is hcp stabilizer in Co-Re alloys. The TaC content increases during and after the matrix transformation, showing the lower solubility of TaC phase in ϵ-Co phase than in γ-Co phase.

In addition, the samples were aged for 15 h at the temperatures 1173 K, 1373 K and 1473 K in order to investigate the long term stability of phases (the experiments were performed

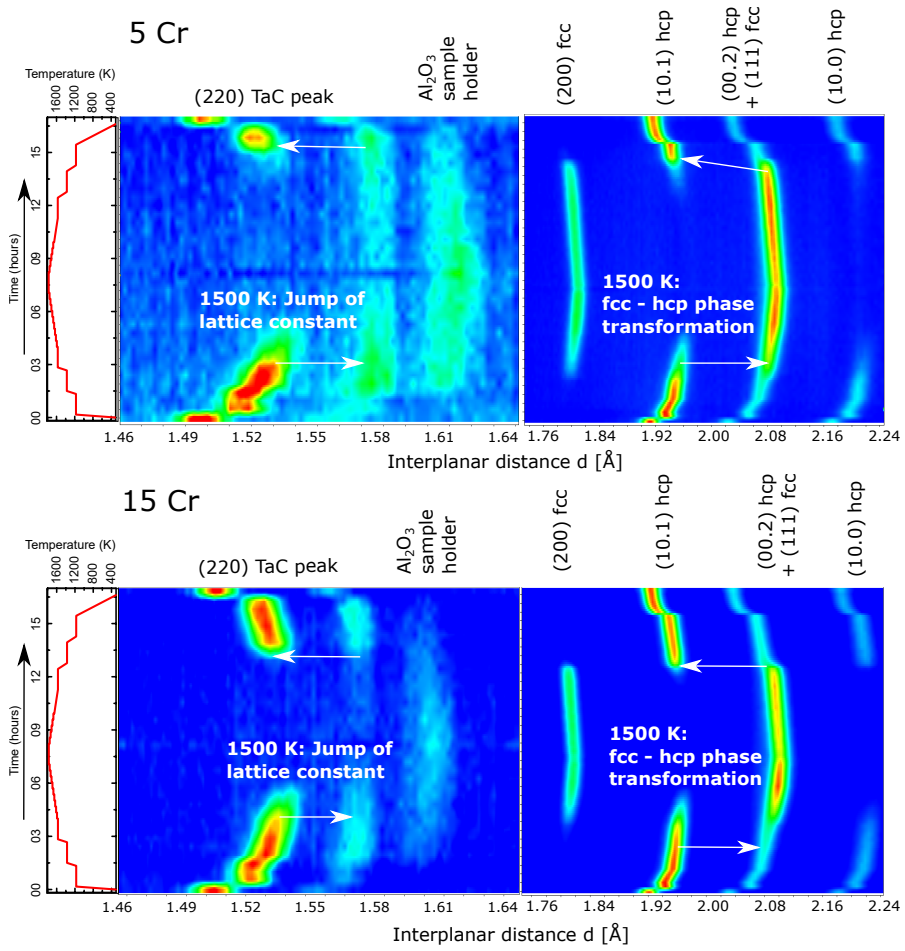

FIGURE 6.1.5: Contour plots of phase evaluation during heating in cooling of 5Cr and 15Cr alloys.

during in-situ SANS, cf. section 6.1.4). After the aging, the samples were measured by XRD. The diffraction patterns are shown in Fig. 6.1.7. The results from the Rietveld refinement are presented in table 6.1.3. The γ-Co phase is not present in any of the patterns. Therefore, even the low amount of 5at.% Cr addition is enough to completely stabilize the low temperature ϵ-Co phase at temperatures $< 1473\,\mathrm{K}$. The TaC stoichiometry, calculated from the lattice constants shows that the composition is close to the nominal content in the matrix $y = 0.9$. After the aging treatments, only a slight increase of the C/Ta ratio is observed according to the lattice constant.

The TaC precipitate coherence to the Co-Re matrix is shown in table 6.1.4. It can be seen that the coherence in $\delta[100]_{\mathrm{TaC}}||[10\bar{1}0]_{\epsilon}$-direction has slightly improved in comparison to alloys without Cr (cf section 5.4.3).

6.1.4 Small-angle neutron scattering

In order to study the stability of nano scaled TaC phase in Cr containing alloys, several aging treatments at temperatures $1173\,\mathrm{K}, 1373\,\mathrm{K}$ and $1473\,\mathrm{K}$ were performed (Fig. 5.3.1). The samples were measured by in-situ SANS during the heat treatments. A comparison of the scattering signal before and after the heat treatments at $1173\,\mathrm{K}$ and $1373\,\mathrm{K}$ is shown in Fig. 6.1.8. It can be seen that there is already a considerable scattering from TaC precipitates

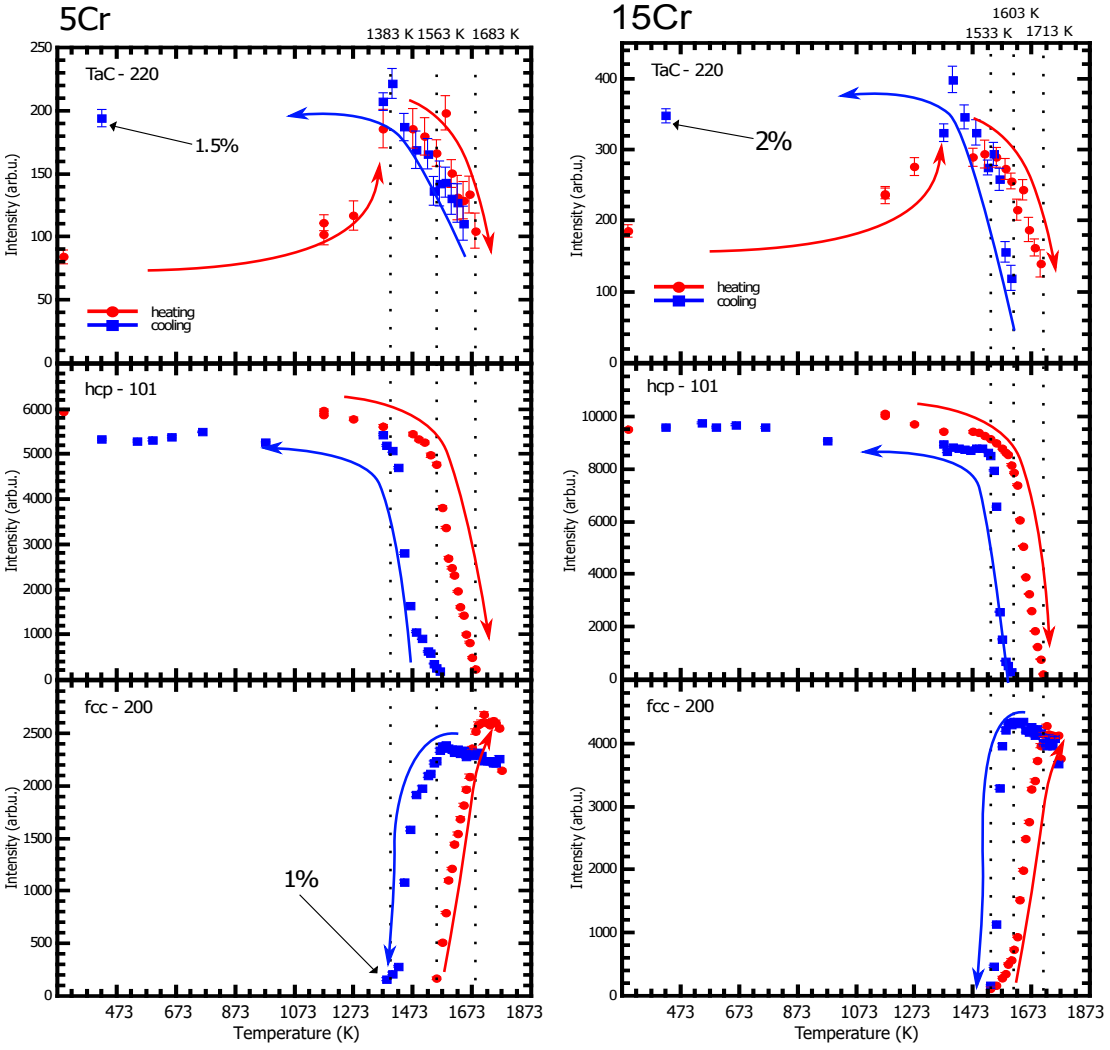

Figure 6.1.6: Evolution of peak intensity from the phases in Cr containing alloys.

Alloy	ϵ-matrix a [Å]	ϵ-matrix c [Å]	γ-matrix a [Å]	TaC a [Å]	ϵ-matrix vol.%	γ-matrix vol.%	TaC vol.%	C/Ta
ST +1173 K								
5Cr	2.554	4.118	-	4.441	97.9	-	2.1	0.91
15Cr	2.560	4.127	-	4.440	97.8	-	2.2	0.90
ST +1373 K								
5Cr	2.559	4.128	-	4.452	96.7	-	3.3	0.99
15Cr	2.568	4.135	-	4.449	98.2	-	1.8	0.95
ST +1473 K								
5Cr	2.571	4.136	-	4.450	99.0	-	1.0	0.96
15Cr	2.564	4.128	-	4.449	97.8	-	2.2	0.95

Table 6.1.3: Results from Rietveld fits for ND and XRD data of Cr containing alloys after the heat treatments.

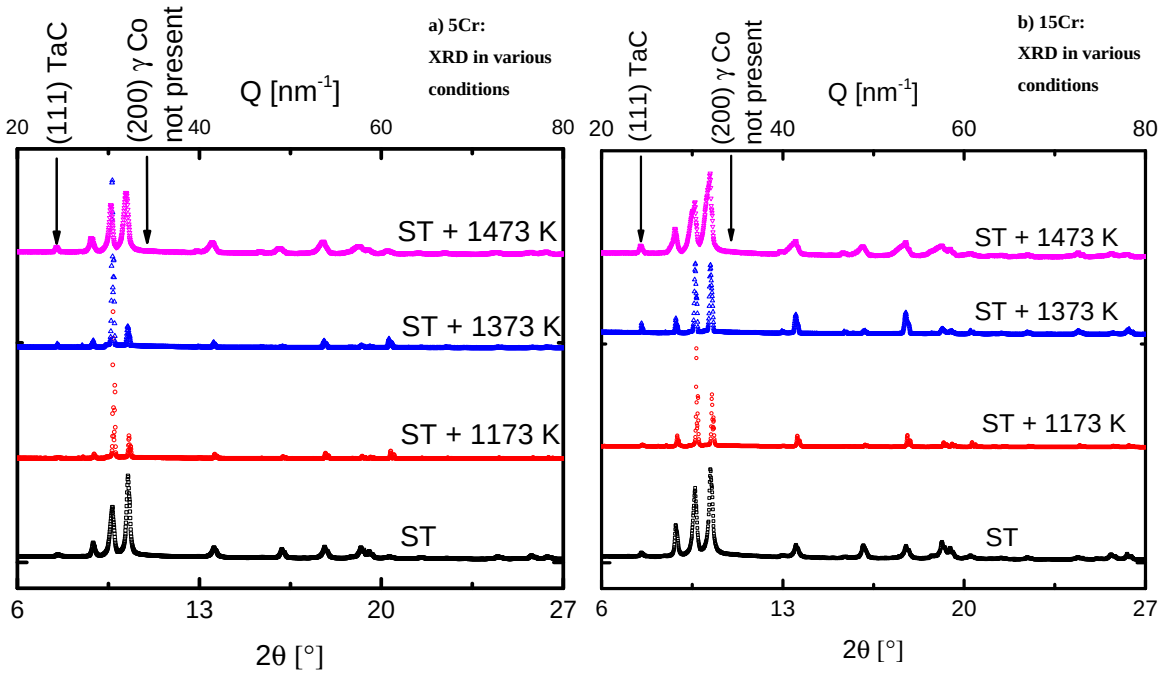

FIGURE 6.1.7: XRD patterns of (a) 5Cr alloy and (b) 15Cr alloy. The present phases in ST condition and after additional heat treatment at 1173 K, 1373 K and 1473 K are compared. γ-Co phase is suppressed in both alloys in all conditions. The peaks show a strong preferred orientation, due to the low grain statistics of XRD method.

Alloy	$\delta[100]_{TaC}\|\|[10\bar{1}0]_{\epsilon}$ [%]	$\delta[021]_{TaC}\|\|[\bar{1}2\bar{1}0]_{\epsilon}$ [%]	$\delta[02\bar{4}]_{TaC}\|\|[0001]_{\epsilon}$ [%]
ST			
5Cr	0.08	-2.71	-0.96
15Cr	-0.01	-2.80	-1.04
1173 K			
5Cr	0.10	-2.69	-0.90
15Cr	0.03	-2.75	-0.96
1373 K			
5Cr	0.13	-2.66	-0.88
15Cr	0.01	-2.78	-0.96
1473 K			
5Cr	-0.02	-2.80	-0.96
15Cr	0.05	-2.74	-0.92

TABLE 6.1.4: The misfit δ of two in-plane directions of TaC precipitate and ϵ-Co phase and the corresponding d-value spacing.

in ST condition. The signal is essentially unchanged after the treatment at 1173 K in both alloys. At 1373 K, the scattering signal has shifted towards smaller Q-values, i.e. larger particles due to coarsening. The coarsening rate is stronger for lower Cr content.

In addition, in the scattering curves show differences in the limit towards large Q-values. On the one hand, the different amount of Cr results in a different amount of incoherent scattering in 5Cr and 15Cr alloy. On the other hand, the scattering levels out nearly constant in the Q-range $1 - 3\,\mathrm{nm}^{-1}$ and is therefore almost completely incoherent. This is a different result than in non Cr containing alloys, where the presence of very fine, elongated particles produces a Q^{-1} decrease of scattering in this Q-range (cf. section 5.3).

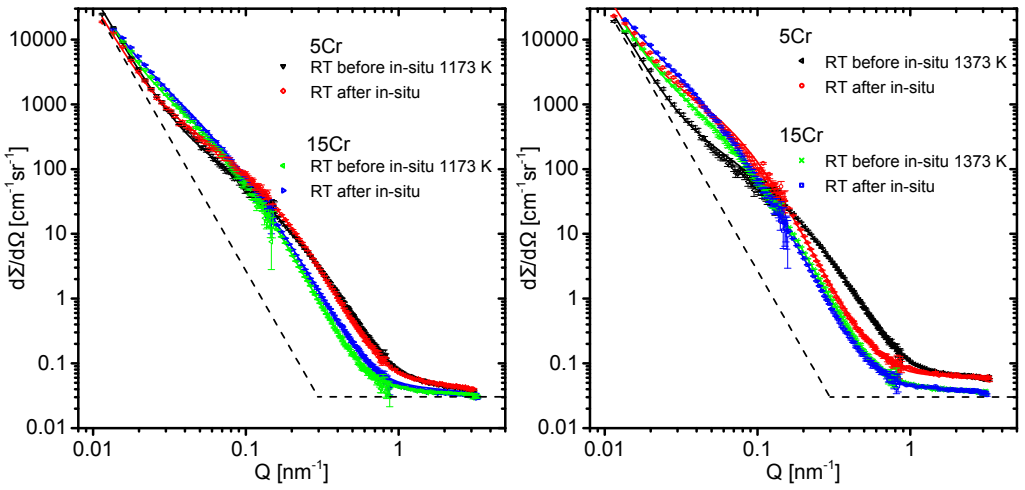

Figure 6.1.8: Addition of 5 and 15 at.% to the Co-Re system. During aging at 15 h at 1173 K, the SANS signal – and therefore the TaC precipitates – remain essentially unchanged. At 1373 K, the 5 at.% alloy shows some considerable coarsening, while the 15 at.% alloy is essentially unchanged.

Fig. 6.1.9(left) shows the evolution of nano scaled TaC phase at 1173 K. The scattering signal in both alloys is almost unchanged during heating, holding for 15 h and subsequent cooling to RT. The volume fraction in 5Cr alloy is constant during heating, holding at HT and cooling in both alloys. In the 15Cr alloy, however, the scattering signal slightly increases in intensity during the hold. New TaC precipitates continuously nucleate in this alloy during the heat treatment. in contrast to alloys without Cr, TaC precipitates are already present in considerable amount in ST condition in both alloy types.

Fig. 6.1.9(middle) shows the evolution at 1373 K. While the alloy containing 15 at.% Cr still shows very little changes, the alloy with the lower Cr content of 5 at.% shows some coarsening. However, the volume fractions are essentially constant in both alloys and do not change much in comparison to ST condition. Fig. 6.1.9(right) depicts the evolution at 1473 K. The coarsening kinetics are considerably accelerated. The scattering intensity is still essentially constant, showing that nano scaled TaC precipitates are present in the alloy matrix.

The corresponding particle size distributions of TaC precipitates were calculated and are presented in Fig. 6.1.10. During the 15 h in-situ experiment at 1173 K, the SANS signal remains essentially unchanged, e.g. the TaC precipitates are almost unaffected due to the heat treatment. The details of the evolution of TaC vol.%, size and the calculated inter-particle distance of TaC particles are presented in Fig. 6.1.11. All alloys show a small increase of TaC vol.% after reaching HT and then a minor increase throughout the aging. The TaC particles have a moderate coarsening rate at 1173 K and 1373 K and remain below 90 nm during the 15 h of aging. The particles are smaller in the low Cr alloy at 24 nm in ST condition and coarsen to a size of 32 nm, while high Cr alloy starts with a particle size of 58 nm that coarsens to 76 nm. At 1373 K, the particles coarsen only a little stronger. This behavior mirrors in the evolution of inter-particle distances with a very stable behavior at temperatures $\leq$ 1373 K, remaining $<$ 1200 nm. Only at 1473 K the rate considerably accelerates. The size distributions become considerably broader and maximum particle sizes

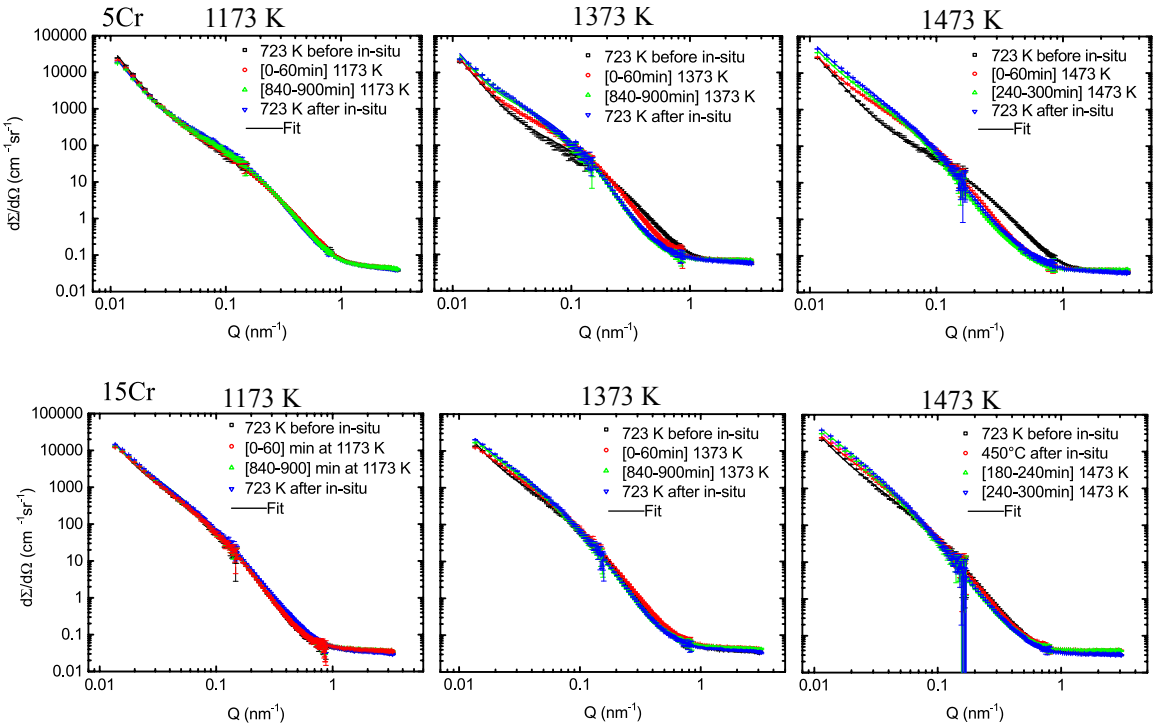

FIGURE 6.1.9: In-situ HT SANS curves of low Cr (top) and high Cr content alloys (bottom). The influence of heat treatment at 1173 K is small for both alloys. At 1373 K, TaC precipitates coarsen more in 5Cr alloy and are almost unchanged in 15Cr. At 1473 K, the coarsening is quicker. An almost unchanged fraction of TaC precipitates is presenet in both alloys at all temperatures. All measurements were performed at SANS-1, MLZ.

of 103 nm in 5Cr alloy and 186 nm in 15Cr alloy are reached. However, there is already a deceleration trend in the end of the 6 h heat treatment.

6.1.5 Discussion

The results for Cr containing alloys with C/Ta ratio $y = 0.9$ are considerably different, from the alloys without Cr TaC05-10 (Co-Re-Ta-C alloys). The matrix consists of single ϵ-Co phase in ST condition (Fig. 6.1.5) due to the addition of the strong hcp stabilizer Cr ($5 - 23$ at.%). The metastable γ_m-Co phase is completely suppressed during cooling to RT from the homogenizing heat treatment ST and the matrix does not have the lath type, heavily twinned microstructure. In addition, the onset temperature of $\gamma \rightarrow \epsilon$ transformation is higher. As a consequence, the transformation $\gamma \rightarrow \epsilon$ is far less sluggish and large single-phase ϵ-Co grains are formed.

Remarkably, the alloys show no evidence of σ phase or Cr-carbides by microscopy or diffraction experiments. Therefore, it can be concluded that Cr is completely miscible with a content ≤ 15 at.% in the Co-Re matrix. This is in contrast to a previously investigated alloy containing a higher amount of 23 at.% Cr, where the matrix seemed to be oversaturated and Cr-carbides precipitated. As a result, the Co-Re matrix lattice constants are slightly shifted, which also improves the TaC coherence in the direction $\delta[100]_{\mathrm{TaC}}||[10\bar{1}0]_{\epsilon}$ (table 6.1.4). This might be the reasons for the observed large amount of directional coarsened TaC precipitates after the heat treatments (Fig. 6.1.2).

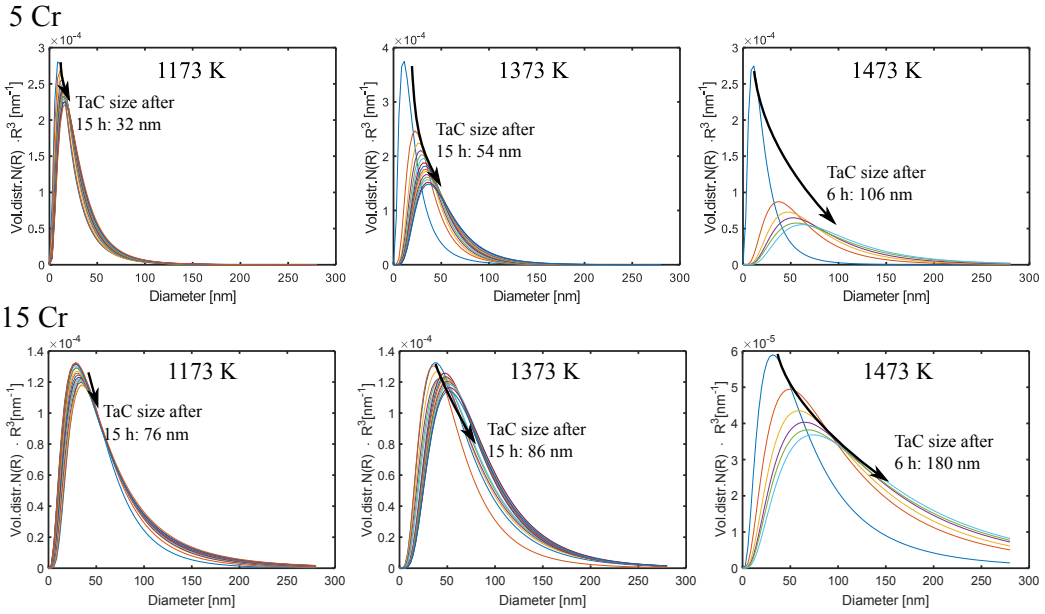

Figure 6.1.10: Evolution of the volume weighted TaC size distributions of 5Cr (top) and 15Cr alloys (bottom), at 1173 K, 1373 K and 1473 K calculated from in-situ SANS curves Fig. 6.1.9. The fits were performed with a log-normal particle size distributions, with a spherical form factor. Due to its assymetry, the mean particle size considerably varies from the peak position for the log-normal size distribution.

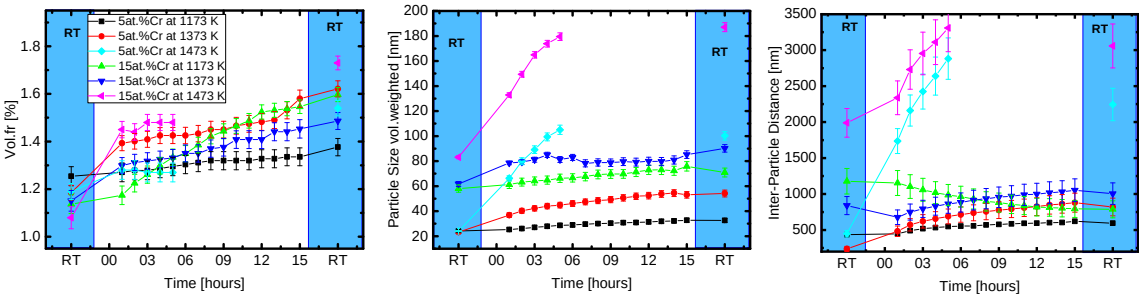

Figure 6.1.11: Evolution of volume fraction, particle size and the inter-particle distance during 15 h in-situ measurement at 1173 K and 1373 K in 5Cr and 15Cr alloys.

Although there were no other phases detected in Co-Re alloys with Cr addition (cf. section 6.1.3), the absence of γ-Co phase at RT has a considerable influence on TaC stability during the in-situ experiments. The TaC volume fraction in ST condition is already essentially in equilibrium, since there is nearly no additional precipitation during the aging treatments. The TaC precipitates in 15Cr alloy have a considerably larger size in ST condition than in 5Cr alloy and alloys without Cr (cf. section 5.3). This can be explained by the fact that a higher amount of Cr increases the temperature of the $\gamma \rightarrow \epsilon$ transformation during cooling from ST heat treatment. The TaC phase starts to precipitate during and after the transformation due to the lower solubility of Ta and C in ϵ-Co phase (cf. section 5.2). Hence, the particles have more time to nucleate in the completely transformed single ϵ-Co phase than in alloys without Cr that are showing a sluggish and incomplete $\gamma \rightarrow \epsilon$ transformation during cooling. After first nucleation and growth of the particles, they have more time for coarsening during cooling.

Alloy	type	Co	Re	Ta	C	B
01B	low B content	80.62	17	1.2	1.08	0.1
04B	high B content	80.32	17	1.2	1.08	0.4

Table 6.2.1: Composition of alloys with varying B content in at.%.

The increase of TaC volume fraction upon reaching HT in the in-situ SANS aging experiments, shows that the TaC content is not in complete equilibrium with the matrix in initial state ST. The ND results indicate that the solubility of TaC phase only decelerates with lower temperatures towards RT. As a result there is a slow precipitation of new, fine TaC precipitates during the holding. This effect is strongest in the 15Cr alloy at 1173 K, where it even results in a decrease of inter-particle distances during aging.

During cooling from any HT treatment, no changes in small-angle scattering are observed in any alloy. It is therefore concluded that the nano scaled microstructure is stable during cooling from 1473 K $\rightarrow$ RT

6.2 Boron addition

In this section, the influence of B on the other present phases – i.e. matrix and TaC precipitate phases – is investigated by means of ND and SANS. The alloy system Co-Re-Ta-C-B was investigated and the Ta and C content were fixed in order to study the influence of the B addition (table 6.2.1). It was found that the B content significantly lowers the temperature of the allotropic $\gamma \leftrightarrow \epsilon$-Co phase transformation and slightly lowers the volume fraction of TaC precipitates. Addition of 0.4 at.% B lowers the starting temperature of the allotropic $\epsilon \rightarrow \gamma$ Co-phase transformation to < 1473 K, which results in a considerable instability of TaC precipitates at these temperatures. The coarsening behavior of TaC precipitates at temperature up to 1373 K is not too much altered from alloys without B addition.

The following results are partly published in [114].

6.2.1 Diffraction

The evolution of phases in samples containing 0.1 at.% and 0.4 at.% of B, respectively, was measured using in-situ ND with the temperature history depicted in Fig. 5.2.1. Fig. 6.2.1 presents ND patterns of both alloys in ST condition, measured by ND and XRD. The corresponding results from Rietveld refinement are given in table 6.2.2. Both methods are unable to detect additional boride phases, either since they are not present or due to the detection limit of the methods. The results from Rietveld refinement show that the matrix consists of a mixture of γ/ϵ-Co, similar to alloys without B and without Cr. A weak reflection from TaC phase is visible with both neutron as well as X-ray radiation. XRD yields a fraction of 0.56 vol.% in low B alloy and 0.46% in high B content, while neutrons yield 0.72% in low B alloy and 0.36% in high B content alloy. Since the XRD only probes the sample surface (due to its limited penetration depth), the results from ND are generally more reliable for the bulk sample.

The alloys were subjected to an in-situ heat treatment with stepwise heating to 1773 K and subsequent cooling to RT (cf. Fig. 5.2.1). The evolution of γ, ϵ and TaC phase is depicted in Fig. 6.2.2. Similarly to alloys without B (cf. section 5.2), the metastable γ_m-Co

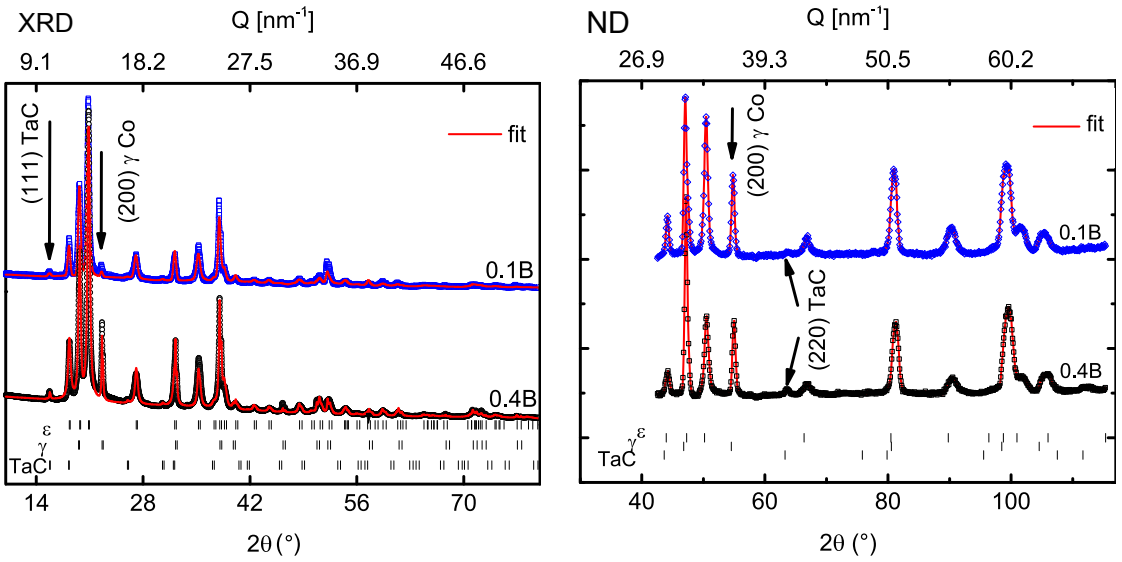

FIGURE 6.2.1: Comparison of XRD (left) and ND patterns (right, Stress-Spec) from B containing alloys. The matrix consists of a mixture of γ/ϵ-Co, similar to alloys without B. A reflection from TaC phase is visible. No additional reflexes from boride phases are observed.

ST condition	ϵ-matrix a [Å]	ϵ-matrix c [Å]	γ-matrix a [Å]	TaC a [Å]	ϵ-matrix vol.%	γ-matrix vol.%	TaC vol.%	C/Ta calculated
X-ray: 01B	2.560	4.121	3.607	4.444	86.24	13.2	0.56	0.93
04B	2.559	4.125	3.604	4.455	80.5	19.04	0.46	0.99
Neutrons: 01B	2.553	4.120	3.603	4.435	56.98	42.3	0.72	0.93
04B	2.549	4.113	3.595	4.452	35.9	63.74	0.36	0.99

TABLE 6.2.2: Results from Rietveld refinment from B containing alloys, measured by ND and XRD.

phase starts transforming to thermodynamic stable ϵ-Co phase at 1173 K. In addition, the TaC volume fraction increases, while the matrix is in ϵ-Co phase, in the temperature range of 1173 K−1473 K. However, the onset temperature for transforming to HT γ-Co phase is considerably reduced in comparison to alloys without B. The effect is stronger for the alloy with higher B content. The 01B alloy starts transforming at 1490 K, while the 04B alloy is already partly in γ-Co phase at 1473 K. This finding suggests that B is a strong fcc stabilizer in Co-Re. In addition, there is a secondary influence on the stability of fine TaC precipitates, which are unstable in the high temperature γ-Co phase. This is investigated in detail by in-situ SANS (cf. section 6.2.2).

The behavior of the Co-Re matrix upon further heating to the HT phase $\epsilon \rightarrow \gamma$ shows an unexpected behavior. The monitored (200) fcc γ-Co peak increases up to a temperature of 1673 K. When heating further, the fcc peak intensity – corrected for the Debye-Waller factor – strongly starts to decrease. The effect is stronger in 04B alloy. At the same time, the ϵ-Co phase hcp (101) peak starts to reappear in 04B alloy. The behavior of B containing Co-Re matrix transformation during heating from RT to 1770 K therefore follows the scheme

$$\gamma_m + \epsilon \rightarrow \epsilon \rightarrow \gamma \rightarrow \gamma + \epsilon \quad , \tag{6.1}$$

where γ_m denotes the metastable nature of the phase in initial condition. This behavior is very unusual and could not yet be explained thoroughly. Most likely, B containing alloys

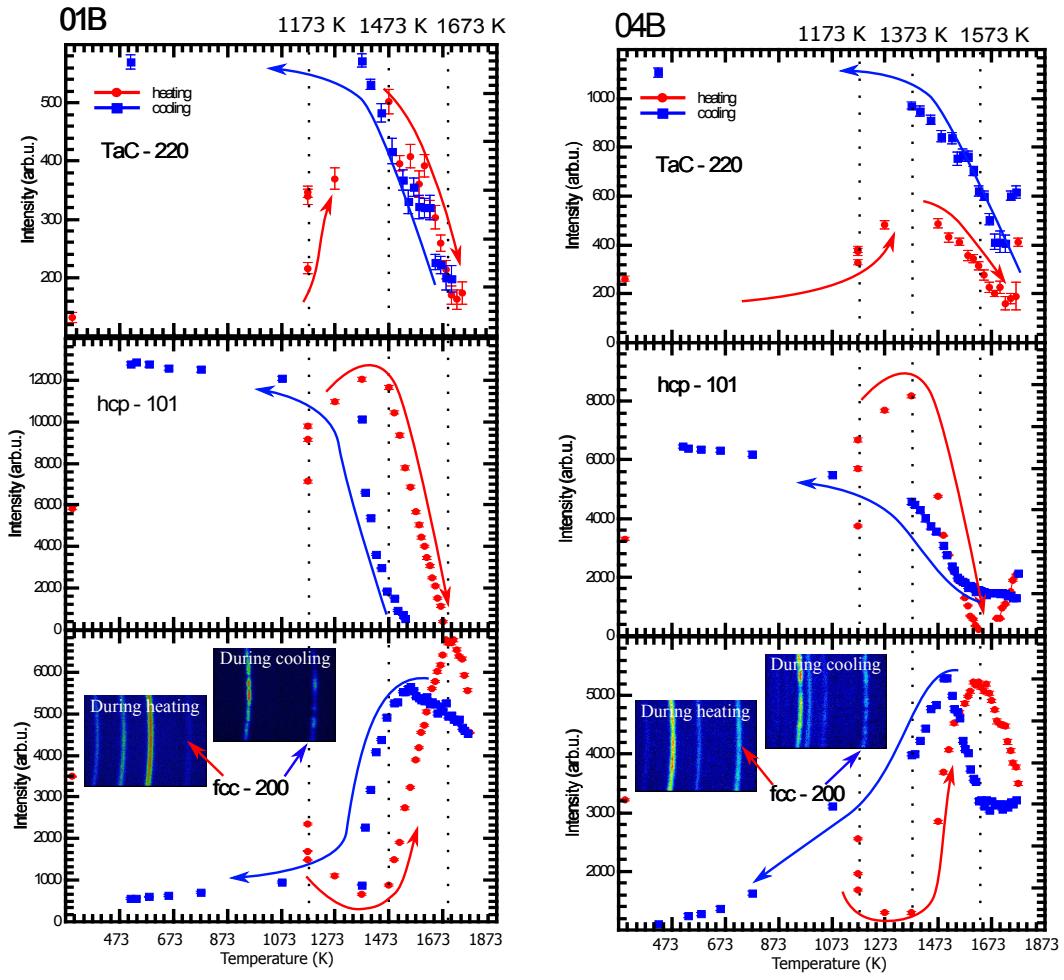

FIGURE 6.2.2: Evolution of peak intensity from the phases in B containing alloys.

exhibit Co evaporation at the sample surface at temperatures $> 1700\,\mathrm{K}$. As a result, surface near areas enrich in Re, which has a natural hcp (ϵ-Co) crystal structure and therefore, the matrix transforms back. This is supported by the fact that the lattice constants of the newly evolving ϵ-Co phase are shifted towards larger values, towards the values of pure Re. Notably, this behavior is only present in B containing alloys. Therefore, the dissolved B content seems to lower the strength of the metallic bonding in the matrix phase.

Further, the diffraction patterns from γ-Co phase become very spotty (Fig. 6.2.2 insets). This suggests a substantial grain growth and possibly recrystallization of the matrix. Therefore, the matrix grains acquire a strong preferred orientation, which had to be taken into account in the Rietveld refinement.

During cooling, both alloys retain metastable γ_m-Co phase at RT. The transformation $\epsilon \rightarrow \gamma$ is very sluggish and is active in the temperature interval starting at $\sim 1513\,\mathrm{K}$ down to $473\,\mathrm{K}$. The amount of retained $\gamma - Co$-phase is in a similar range as for alloys without Cr.

In addition, the samples were aged for 15 h at the temperatures 1173 K, 1373 K and 1473 K in order to investigate the long term stability of phases (the experiments were performed during in-situ SANS, cf. section 6.1.4). After the aging, the samples were measured by

Alloy	ϵ-matrix a [nm]	ϵ-matrix c [nm]	γ-matrix a [nm]	TaC a [nm]	ϵ-matrix vol.%	γ-matrix vol.%	TaC vol.%	C/Ta
ST +1173 K								
01B	2.55804	4.1220	3.6086	4.4562	93.6	3.0	3.5	1.00
04B	2.54825	4.1129	3.5602	4.4486	93.6	1.6	4.8	0.95
ST +1373 K								
01B	2.55779	4.1220	3.5732	4.4515	94.0	1.8	4.2	0.97
04B	2.55984	4.1254	3.5987	4.4667	96.1	1.4	2.5	1.07
ST +1473 K								
01B	2.5614	4.1259	3.5738	4.4587	97.5	0.7	1.8	1.01
04B	2.55802	4.1215	3.5940	4.4626	95.9	2.5	1.6	1.04

Table 6.2.3: Results from Rietveld fits for ND and XRD data after the heat treatments.

Alloy	$\delta[100]_{\mathrm{TaC}}\|\|[10\bar{1}0]_{\epsilon}$ [%]	$\delta[021]_{\mathrm{TaC}}\|\|[\bar{1}2\bar{1}0]_{\epsilon}$ [%]	$\delta[02\bar{4}]_{\mathrm{TaC}}\|\|[0001]_{\epsilon}$ [%]
ST			
0.1B	0.04	-2.75	-0.97
0.4B	0.21	-2.57	-0.81
ST + 1173 K			
0.1B	0.14	-2.64	-0.84
0.4B	0.20	-2.59	-0.83
ST + 1373 K			
0.1B	0.12	-2.67	-0.87
0.4B	0.18	-2.60	-0.80
ST + 1473 K			
0.1B	0.12	-2.66	-0.85
0.4B	0.18	-2.61	-0.80

Table 6.2.4: The misfit δ of two in-plane directions of TaC precipitate and ϵ-Co phase and the corresponding d-value spacing.

XRD. The results from a Rietveld refinement are shown in table 6.2.3. The metastable γ_m-Co phase is weakly present at RT after the heat treatments. This shows that the γ-Co phase does not completely dissolve during the aging heat treatments at temperatures $\leq 1473\,\mathrm{K}$.

The TaC stoichiometry, calculated from the lattice constants shows that the composition is close to the nominal content in the matrix $y = 0.9$ in ST condition. After the aging treatments, a slight increase of the C/Ta ratio is observed according to the lattice constant. This is most likely caused by an enrichment of C in the TaC phase during the heat treatment.

The misfit of TaC particles to Co-Re matrix was calculated according to the procedure described in section 5.4.3. The results are presented in table 6.2.4. The values are similar to alloys without B. The matching in $\delta[100]_{\mathrm{TaC}}||[10\bar{1}0]_{\epsilon}$ direction is $< 0.21\%$.

6.2.2 Small-angle neutron scattering

The evolution of TaC particles in alloys containing B was investigated using SANS. The in-situ measured scattering curves at 1173 K, 1373 K and 1473 K are presented in Fig. 6.2.3. It is directly visible that the amount of scattering from TaC strongly increases upon reaching HT (similar to alloys without B and different to alloys with Cr). In addition, a Q^{-1} decrease of scattering intensity at larger Q-values is observed, suggesting a second precipitation morphology with elongated shape. This indicates a second contribution of elongated

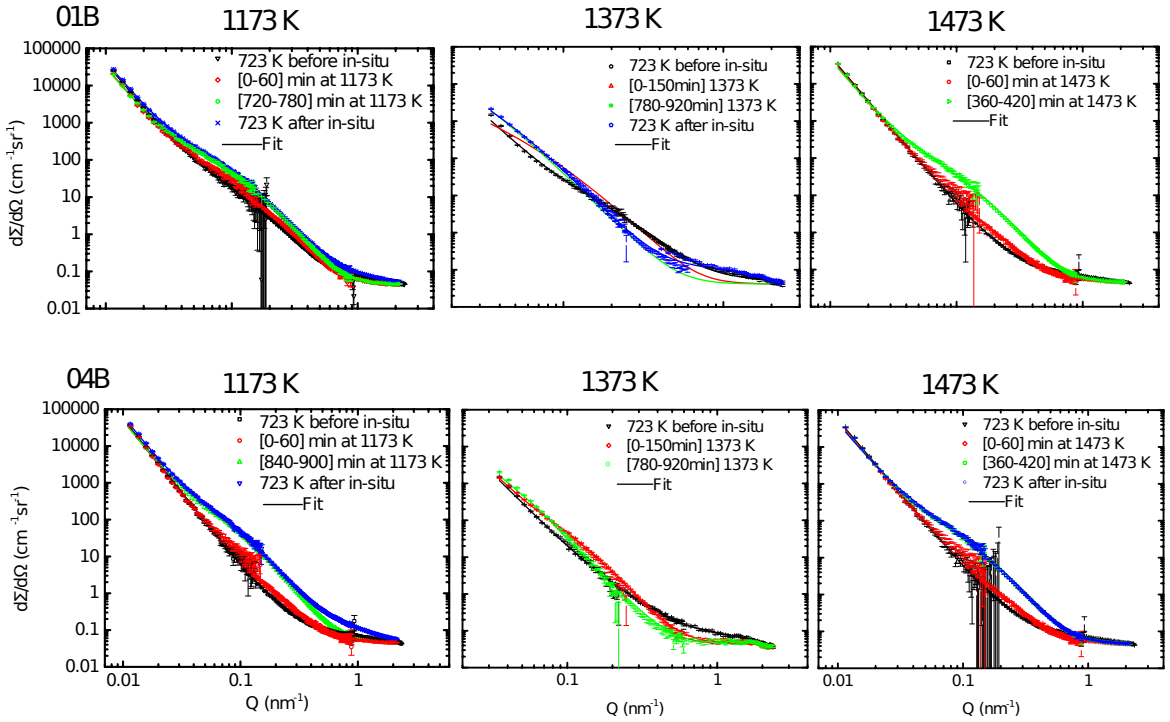

Figure 6.2.3: SANS curves, from scattering on nano scaled TaC precipitates. The curves show a similar behavior as samples without B addition. Measurements at 1173 K and 1473 K were performed at SANS-1, MLZ and measurement at 1373 K was performed at SANS-I, PSI.

TaC precipitates, similarly to alloys without B (cf. section 5.3). Generally, higher temperatures expectedly result in a stronger shift of scattering signal towards small Q-values, hence faster coarsening kinetics.

The particle size distributions of TaC precipitates during the in-situ experiments at HT were calculated and are presented in Fig. 6.2.4. The evolution of volume fraction, size and inter-particle distance values is quantified in Fig. 6.2.5. The overall behavior is very similar to samples without B. In ST condition, the high B alloys show a low amount of ~ 0.1 vol.% TaC, while low B alloys have an amount of 0.5 vol.% TaC. This discrepancy is most likely caused by the altered Co-Re phase transformation temperature. The high B alloys transform at lower temperatures and only partly $\gamma \rightarrow \epsilon$. Therefore, the precipitation starts at lower temperatures and there is less time for the precipitation. The precipitate sizes are in the range ~ 20 nm.

Right after reaching HT, there is a burst of TaC precipitation up to of ~ 1 vol.%. During holding the alloys at HT, the volume fraction is essentially stable. The equilibrium TaC content is similar in low and high B alloys at 1173 K and 1373 K. Only during holding at 1473 K the TaC content in high B alloy is reduced in comparison to low B alloy by a factor of 2. This is caused by the fact that the high B content influences the Co-Re matrix to partly transform to HT γ-Co phase at this temperature, as shown by in-situ ND (Fig. 6.2.2). The lower volume fraction of TaC precipitates is an additional indicator for the higher solubility of C and/or Ta in γ-Co phase. Most likely, the TaC precipitates dissolve into regions of the matrix that are transforming to γ-Co phase.

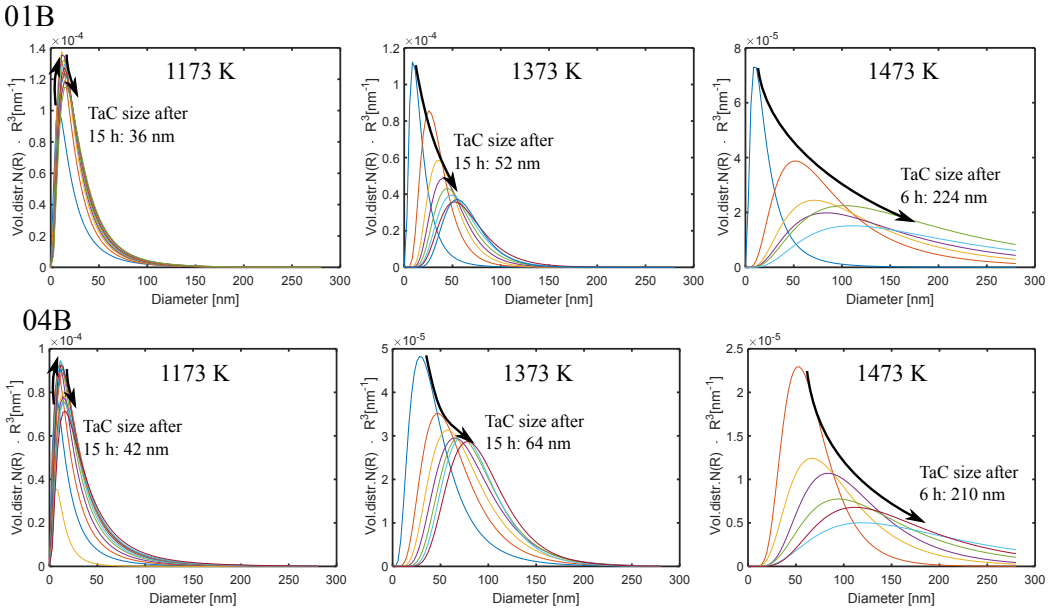

Figure 6.2.4: Evolution of the volume weighted TaC size distributions of low B (top) and high B content alloys (bottom). The fits were performed with a log-normal particle size distributions, with a spherical form factor. The coarsening rate is very low at 1173 K and expectedly increases for higher temperatures. Due to its assymetry, the mean particle size considerably varies from the peak position for the log-normal size distribution.

The TaC coarsening rate is rather moderate at temperatures up to 1373 K. During holding the alloys for 15h at 1173 K, the sizes coarsen from 20 nm up to to 44 nm and the rate is very low after 15 h at HT. The inter-particle distances of TaC precipitates are essentially constant since the size distributions are nearly unaltered. The burst of TaC volume fraction decreases the particle distance when reaching 1173 K, while at higher temperatures, the rapid coarsening in the beginning already increases the distances. At 1373 K, the distributions considerably broaden and the coarsening rate is faster. The TaC precipitates reach a size of 84 nm after holding the temperature for 15 h. This also causes the inter-particle distances to increase.

At 1473 K, the sizes of both alloys are still increasing in the end of the 6 h in-situ cycle and do not allow a conclusion if the precipitate size is stable in the nano scaled size range in B containing alloys. As a result of the large size increase, the inter-particle sizes reach sizes of about 10 000 nm and are therefore rather too large for an effective strengthening of the alloy.

Generally, the particle sizes are larger in 04B alloys than in 01B and alloys without B at HT (cf. section 5.4.2). This might be caused by a higher diffusivity in the matrix as a result of the B addition, enhancing the particle coarsening rate. There is no systematic change in the TaC phase lattice constant observable in comparison to alloys without B, which is an indication that the TaC phase itself is not changed by the B addition. Additionally, B addition results in a matrix transformation at lower temperatures and is already partly starting at 1473 K. Therefore, the nano scaled TaC precipitates might be unstable in size in the γ-Co phase.

During cooling to RT, the values remain nearly constant, only the 04B alloy that is cooled from 1473 K shows an increase in TaC volume fraction and subsequently a decrease of inter-particle distance. This is most likely a consequence of the partly transformed $\epsilon \rightarrow \gamma$ Co-Re

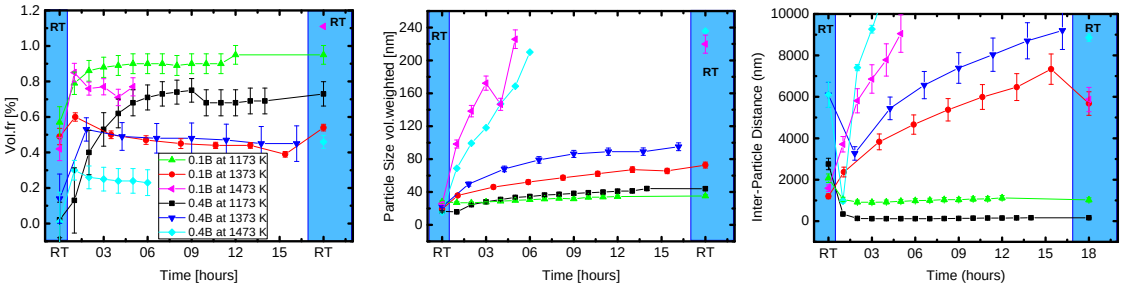

Figure 6.2.5: Evolution of volume fraction, particle size and the inter-particle distance during 15 h in-situ measurement at 1173 K, 1373 K and 1473 K.

matrix, during the aging treatment. During cooling, the ϵ-Co phase content increases, which allows a re-precipitation of nano scaled TaC phase.

Chapter 7

Kinetics of Nano Scaled TaC Precipitates

In the first part of this chapter, the coarsening kinetics in dependence of C, Cr and B content are studied in detail by means of in-situ SANS measurements at various HT. The kinetic mechanism of TaC precipitation is of great interest for the alloy development, since it allows the development of effective age hardening heat treatments. In the second part, the TaC dissolution and precipitation kinetics are studied in dependence of the temperature. Theoretical thermodynamic models are applied and fitted to the data (cf. section 3.2.3). These yield insight to the nucleation, growth and coarsening behavior of the Co-Re alloys. Activation energies for the respective mechanisms were extracted from the models. In order to improve effective precipitation hardening heat treatments, such a theoretical understanding is very important. Table 7.0.1 summarizes the compositions and designated sample names of Co-Re alloys for these studies.

7.1 Coarsening kinetics

In order to determine the coarsening of the nano scaled TaC precipitates at HT, the theory of Lifshitz, Slyozov and Wagner (LSW) (cf. section 3.2.3) was applied to the size distributions determined by in-situ SANS. Fig. 7.1.1 summarizes the alloys studied for the TaC coarsening kinetics and shows a scheme of the behavior of the TaC phase during the HT treatments. The samples were measured at the temperatures 1173 K, 1373 K and 1473 K. A fit to the mean particle sizes at the varying temperatures yields the activation energies for coarsening. The low and high carbon content alloys and the influence of Cr and B addition are compared. The required values for the solubility of the TaC phase in the Co-Re matrix in dependence of temperature were obtained by in-situ ND.

name	type	Co	Re	Cr	Ta	C	B
TaC05	low C content alloy	81.20	17	0	1.20	0.60	0
TaC09	high C content alloy	80.72	17	0	1.20	1.08	0
5Cr	low Cr content alloy	75.72	17	5	1.20	1.08	0
15Cr	high Cr content alloy	65.72	17	15	1.20	1.08	0
01B	low B content alloy	80.71	17	0	1.20	1.08	0.1
04B	high B content alloy	80.68	17	0	1.20	1.08	0.4

Table 7.0.1: Compositions of Co-Re samples for the investigation of TaC kinetics.

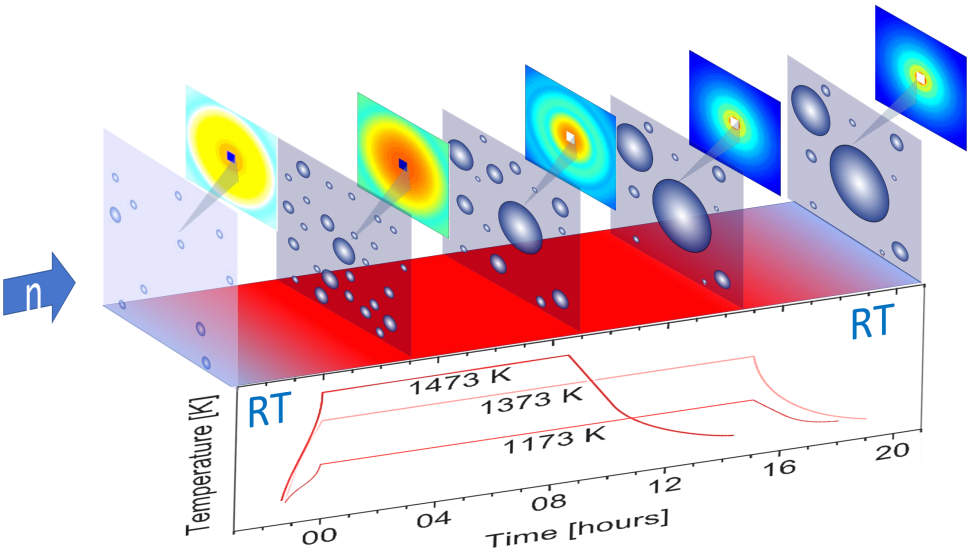

FIGURE 7.1.1: Scheme of the applied SANS experiments in order to determine the coarsening kinetics. The samples were heated to three different temperatures 1173 K, 1373 K and 1473 K and held constant for 6 h-15 h. The variation of the holding time was a result of the limited available neutron beam time. The particle coarsening is measured by in-situ SANS and a coarsening rate law is determined with the LSW theory.

7.1.1 Rate constants of diffusion and surface limited coarsening

There exist two extreme cases of coarsening, namely diffusion limited and surface limited. In the former, elemental diffusion effects are dominant, while in the latter surface reactions yield the driving force for particle coarsening (cf. section 3.2.3). Fig. 7.1.2 depicts the evolution of particle size in the representations $t \mapsto \langle R(t)\rangle^3$ and $t \mapsto \langle R(t)\rangle^2$ for the alloys TaC10 and TaC07. If the coarsening mechanism is diffusion ($\langle R(t)\rangle^3$) or surface reaction limited ($\langle R(t)\rangle^2$), respectively, the points should appear on a line in the respective plot. In this way, the plots are used to decide which mechanism is dominant for TaC particle coarsening in Co-Re alloys. A linear regression analysis yields the rate constants of coarsening K for diffusion or surface reaction limited growth kinetics, respectively.

The plots show that the diffusion limited model generally applies. The confidence bounds of the fit are smaller and the general linear behavior is better represented. Therefore, diffusion limited coarsening is considered to be the main driving mechanism of coarsening in the Co-Re alloys.

The rate constants of coarsening K for diffusion limited growth were evaluated at the three distinct temperatures 1173 K, 1373 K and 1473 K. The data was obtained from the in-situ SANS measurements, described in sections 5.3, 6.1.4 and 6.2.2. Fig. 7.1.3 shows the evolution of mean particle radii in the representation $T \to \langle R(T)\rangle^3$ for low and high C, B and Cr content alloys at the three temperatures. For the low and high C and B content alloys the relationship matches quite well. These alloys have a similar behavior of allotropic matrix transformation from metastable γ_m-Co to stable ϵ-Co at 1173 K (cf. section 6.2.1).

However, the Cr containing alloys show a different behavior. In the 5Cr alloy, the slope is not linear, but rather decelerates at 1373 K. Hence, the rate constant K lowers over time. This effect is well known if the volume fraction of coarsening particles is considerably larger than 0 which is described by the modified LSW theory (cf. section 3.2.4). The reason for

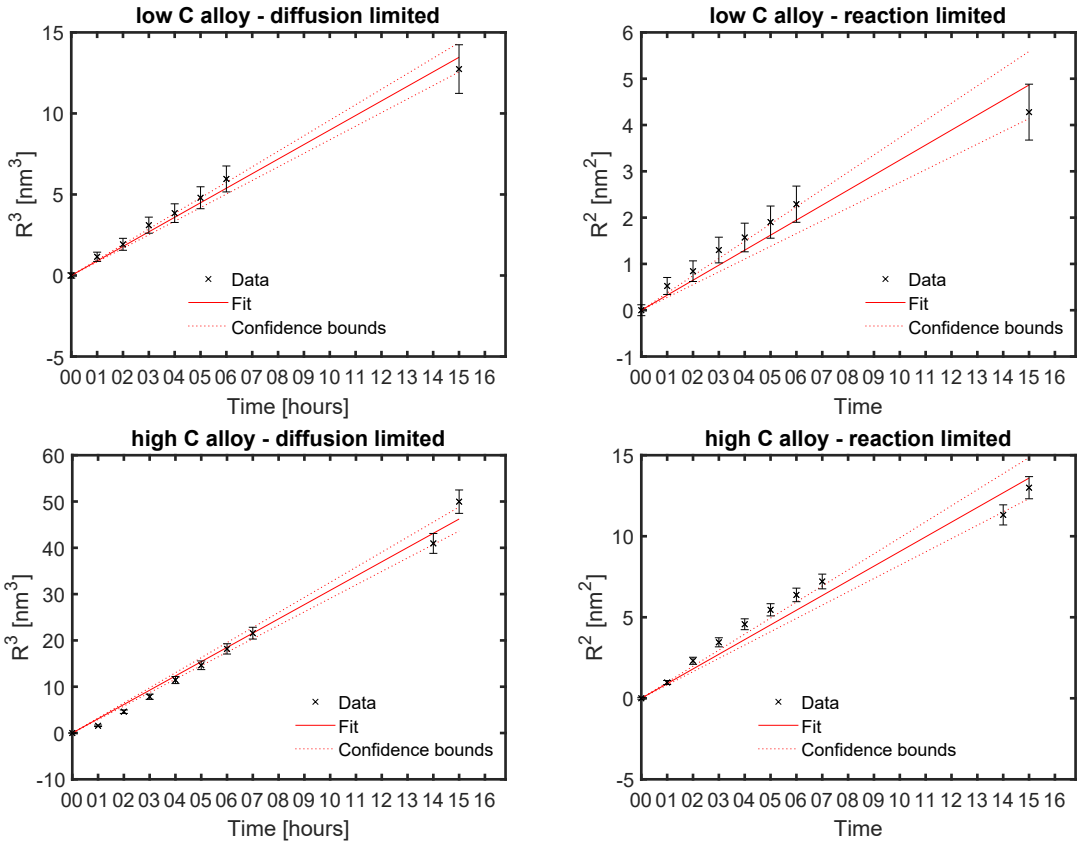

FIGURE 7.1.2: (left) Diffusion limited coarsening, (right) surface reaction limited coarsening for a low C content alloys TaC05 (top) and high C content alloy TaC09 (bottom).

the decreasing rates is the impingement of the diffusion gradients between growing particles. Since the particle sizes and coarsening rates are considerably smaller at 1173 K the effect is not visible at this temperature. At 1473 K, there are insufficient data points to conclude if the coarsening rates are also decelerating.

In the 15 Cr alloy, however, the mean particle size is even decreasing at 1173 K. This can be explained by the evaluation of the TaC volume fractions from the SANS curves (cf. Fig. 6.1.11). They show that there is a continuous minor nucleation of new very small TaC precipitates over time in this alloy during aging at HT. The coarsening of these particles is slower than the nucleation of smaller particles. Thus, within this alloy a lower amount of TaC precipitates did precipitate during its homogenization heat treatment before the in-situ SANS measurements. As a consequence, the classic LSW theory is invalid, since the particle concentration is not in equilibrium in the matrix.

For diffusion limited growth, the activation energy Q is identified with the activation energy for diffusion $Q = Q_D$ of Ta at the respective temperature in Co-Re. Since carbon is an interstitial element in the metallic matrix, its diffusion is fast and can be neglected in comparison to the much larger atom Ta. Taking an Arrhenius-type temperature dependence for the diffusion coefficient D, the rate constant K of coarsening eq. (3.65) is rewritten according to

$$K = \frac{8\Gamma v_\beta^2 D C_{\alpha,\mathrm{eq}}}{9 C_\beta^2 RT} = A \frac{C_{\alpha,\mathrm{eq}}}{T} \exp(-Q_D/RT), \tag{7.1}$$

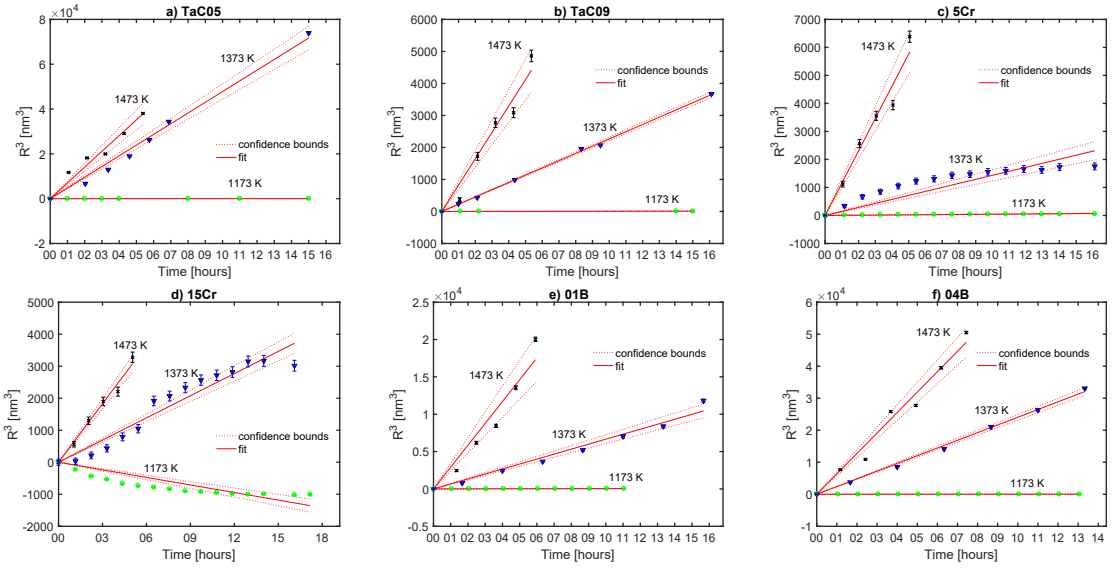

FIGURE 7.1.3: Evolution of coarsening rates, depending on alloy type and temperature. (a) TaC05, (b) TaC09, (c) 5Cr, (d) 15Cr, (e) 01B, (f) 04B alloys. The holding time at HT vs. the cubed mean radius R^3 is plotted. The LSW theory predicts straight lines for diffusion limited coarsening.

with the interfacial tension of the particle Γ, its molar volume v_β, the equilibrium solute concentration in the matrix, the gas constant R, activation energy for coarsening Q_D and all temperature independent values are condensed in the constant A. For the solute concentration in the TaC phase at RT, atom probe measurement showed $C_\beta = 0.93$ [27]. In the following considerations, it is assumed that the value is near temperature independent at $T \leq 1473\,\mathrm{K}$.

7.1.2 Solute concentration of TaC in Co-Re matrix

The solute concentration of Ta in equilibrium $C_{\alpha,\mathrm{eq}}$ in the Co-Re matrix is calculated from the in-situ ND measurements that yield the TaC phase volume fraction (cf. section 5.2) during slow cooling. The evolution of TaC peaks is depicted in Fig. 7.1.4 and the integrated intensity is shown in Fig. 7.1.5. The equilibrium Ta solubility $C_{\alpha,\mathrm{eq}}$ was calculated from the ratio of the measured total TaC volume fraction from ND $w_{\mathrm{TaC}}(T)$ and the maximum TaC peak intensity $w_{\mathrm{TaC}}^{\mathrm{max}}$. It was assumed that the solubilty at RT is $C_{\alpha,\mathrm{eq}} = 0$ for the maximum value $w_{\mathrm{TaC}}^{\mathrm{max}}$. Therefore, the equilibrium content of TaC phase can be determined

$$C_{\alpha,\mathrm{eq}}(T) = C_0 \cdot (1 - w_{\mathrm{TaC}}(T)/w_{\mathrm{TaC}}^{\mathrm{max}}) \quad , \tag{7.2}$$

with the nominal content in the alloy C_0. The resulting curves for alloys of low and high C content, low and high Cr content, and low and high B content alloys are shown in Fig. 7.1.6. In the ND experiments, the samples were cooled and stepwise measured for 20 min. The changes between the respective steps were small $\Delta T = 20\,\mathrm{K}$ and therefore in order to keep the phases near equilibrium. The solubility in dependence of temperature was interpolated with a function of the type $y(T) = a + b(\log(T))$.

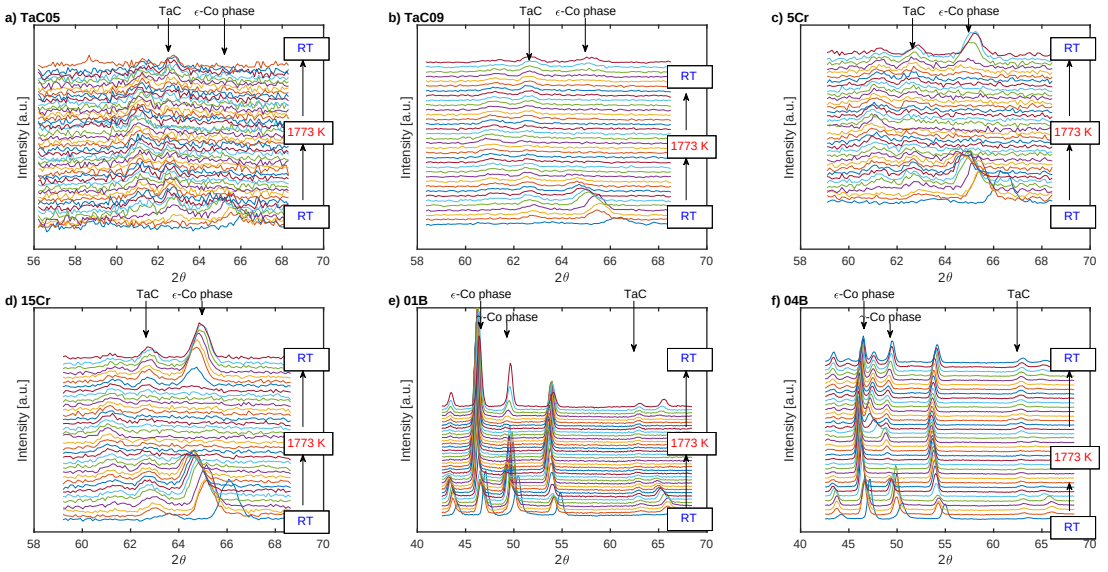

FIGURE 7.1.4: Evolution of ND scattering patterns from the TaC; (a)low C alloy, (b) high C alloy, (c)low Cr alloy, (d) high Cr alloy, (e) low B alloy, (f) high B alloy.

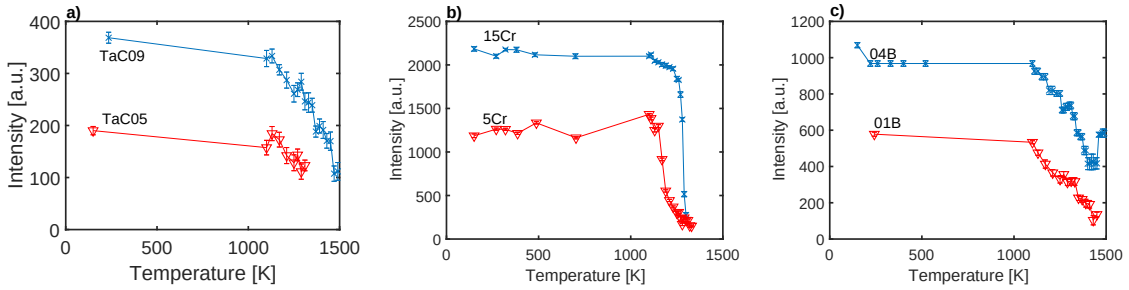

FIGURE 7.1.5: Evolution of TaC phase peak intensities.

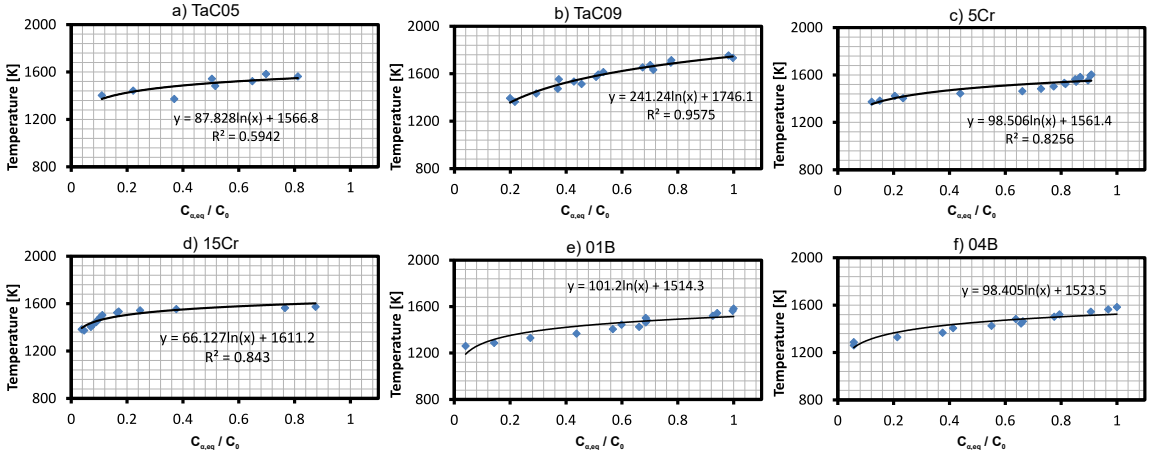

FIGURE 7.1.6: Solubility of TaC phase in Co-Re matrix $C_{\alpha,\mathrm{eq}}$, normalized to 1 by the nominal content of solute in the matrix C_0. $C_{\alpha,\mathrm{eq}}$ is a function of alloy type and temperature. (a) C/Ta = 0.5, (b) C/Ta = 0.9, (c) 5Cr, (d) 15Cr, (e) 0.1B, (f) 0.4B.

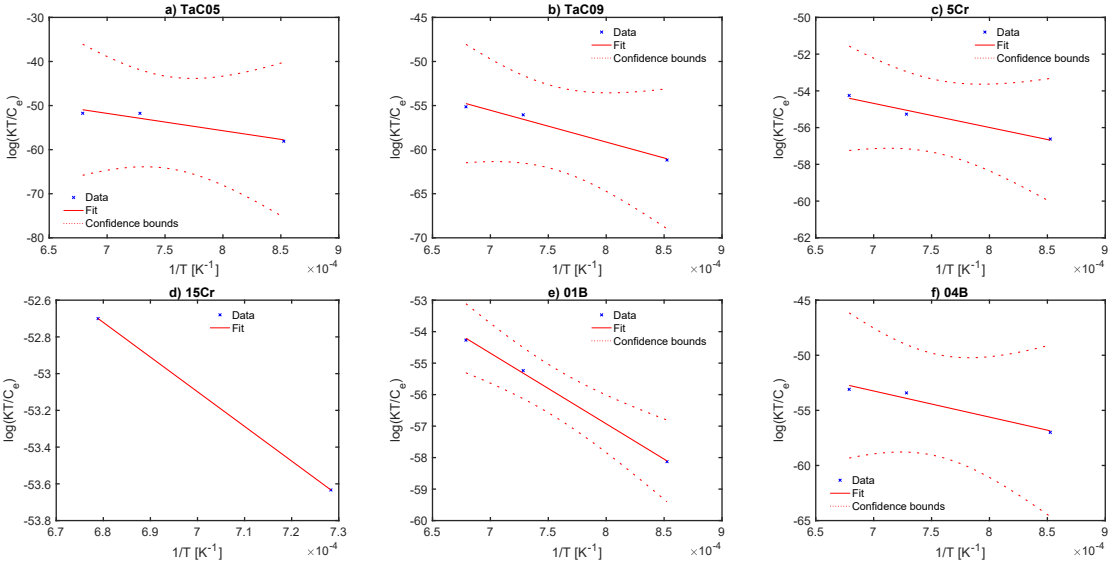

FIGURE 7.1.7: Evaluation of the activation energy of diffusion limited coarsening Q_D, depending on alloy type and temperature. An Arrhenius type dependence of the coarsening rates was assumed. (a) TaC05, (b) TaC09, (c) 5Cr, (d) 15Cr, (e) 01B, (f) 04B. The 15Cr alloy only contains two data points, since a negative coarsening rate was evaluated at 1173 K, due to the constant precipitation of fine TaC during the aging experiment. Due to the low amount of data points, the confidence bounds of the linear fit should be considered.

7.1.3 Activation energies of diffusion limited coarsening

Since the rate constant K was measured for several temperatures, the activation energy for coarsening Q_D can be obtained by a linear regression fit of the function (cf. section 3.2.3)

$$\frac{1}{T} \mapsto -\frac{R}{Q_D}\left(\log\frac{KT}{C_{\alpha,\mathrm{eq}}} + \log A\right) \quad . \tag{7.3}$$

When assuming that Q_D is independent of T, the slope of this function yields

$$Q_D = -R \cdot \frac{\partial \log(KT/C_{\alpha,\mathrm{eq}})}{\partial(1/T)}. \tag{7.4}$$

and therefore the slope of the function $-R\log(KT/C_{\alpha,\mathrm{eq}})/(1/T)$ yields the activation energy for diffusion.

The theory presumes a constant volume fraction during the coarsening process. As shown by SANS, it takes $1-3$ h for the TaC precipitates to reach equilibrium volume fraction in the Co-Re matrix, depending on the exact temperature (cf. sections 5.3, 6.1.4, 6.2.2). Therefore, data points with volume fraction less than 90% of the final volume fraction were omitted in the fit. The fitted values of Q_D in the different alloys are presented in table 7.1.1. The results yield activation energies between $186-336\,\mathrm{kJ\,mol^{-1}}$. However, the error bars are in the range of 20% due to the low amount of evaluated temperatures. Addition of B reduces the activation energy, while Cr addition increases the energy. Alloys with Cr are in single ϵ-Co phase at the investigated temperatures, while the matrix in alloys without Cr consists of a γ/ϵ-Co mixture. As a consequence, the amount of lath boundaries and defects is considerably different and the mode of diffusion can therefore be along the boundaries or be enhanced due to lattice vacancies. Further, the driving force for diffusion is altered for

$D[10^{-16}m^2s^{-1}]$ of Ta in	$D[10^{-16}m^2s^{-1}]$ of Ta in Co at 1273 K	at 1373 K	Q_D kJ mol^{-1}
in pure Co*	10.4*	3.83*	145
in pure fcc Co**			282.5**
low C alloy			326(42)
high C alloy			299(41)
low Cr alloy			336(45)
high Cr alloy			-
low B alloy			197(30)
high B alloy			186(31)

TABLE 7.1.1: Fitted values of activation energy for coarsening Q_D and the corresponding diffusion coefficients D of Ta in pure Co. (*) values from [118]; (**) values from [117].

different elemental concentrations. Addition of Cr also changes the lattice constants of the Co-Re lattice. It has to be noted that the TaC volume fraction is not in equilibrium in the Cr containing alloys (as presumed in classical LSW theory) and the results have therefore be treated as an approximation.

Common values from the literature for Q_D in superalloys are between 250 kJ mol^{-1} and 325 kJ mol^{-1} [115, 116]. The values obtained from the coarsening kinetics measured by SANS are on the top end of this energy range. It is generally desirable to have a large diffusion activation energy within the alloy matrix, in order to limit the particle coarsening rate of precipitates. The Co-Re alloy is therefore a comparably good candidate to ensure HT stability. The strong metallic bonding of the added Re atoms are a likely reason for the slow diffusion in the matrix as was also reported by Neumeier et al. [117]. They argued that Re atoms can form strong directional bonds with neighboring Co atoms. Additionally, the solid solution strengthening effect of the very different atomic radii of Co and Re could influence the atomic diffusion behavior of Ta.

The diffusion coefficients of Ta in pure Co was investigated by Neumeier et al. [117]. They report a value of 282.5kJ mol^{-1} for the activation energy of diffusion, which is in very good agreement with the present results. The diffusion coefficients of Ta in pure Co was investigated by Baheti et al. [118] for the two temperatures 1373 K and 1273 K. From their values, the activation energy of diffusion Q_D can be calculated, assuming an Arrhenius type dependence and temperature independence of Q_D according to

$$Q_D = R\frac{T_1 \cdot T_2}{T_1 - T_2} \cdot \log\frac{D_1}{D_2} = R\frac{1373\,\mathrm{K} \cdot 1273\,\mathrm{K}}{1373\,\mathrm{K} - 1273\,\mathrm{K}} \cdot \log\frac{D_{1373}}{D_{1273}} = 145.17\,\mathrm{kJ\,mol^{-1}} \quad , \qquad (7.5)$$

which is considerably lower than in the present Co-Re alloys. However, it should be noted that this value is also very low in comparison to that of other alloys such as Ni-base. Since it is determined only by two points the calculation is very susceptible for errors.

Remark 7.1 Co-Re alloys have a maximum volume fraction of about $\sim 1.5\%$ of TaC precipitates, which is why the classic LSW is usually valid. However, some other problems arise applying the theory

(i) The LSW theory calculates the coarsening rate according to the mean radius $\langle R \rangle$ of the number weighted particle size distribution. The measured peaks from SANS are very broad and might in fact be consisting of multimodal particle distributions with varying morphology, as suggested by the SEM (cf. Fig. 5.1.2). For such broad log-normal size distributions, the particle weighted mean radius is very sensitive on the log-normal

standard deviation σ, since it depends on the 1^{st} moment of the distribution function

$$\langle R \rangle = \exp(\mu + \sigma^2/2), \tag{7.6}$$

which has a quadratic dependence on σ.

(ii) TaC precipitates can form coherently, but quickly lose their coherence during coarsening due to the large misfit.

(iii) The precipitation is often related with the Co-Re matrix transformation $\epsilon \leftrightarrow \gamma$. Therefore the matrix is a multi-phase system which might require more complex adjustments of the theory. The results have to be considered with some care and be treated as an approximation. However, after $\sim 2\,\mathrm{h}$ of holding at the respective temperatures, the Co-Re matrix state is single phase ϵ-Co in the presented cases

7.2 The Nucleation kinetics of nano scaled TaC precipitates

The nucleation of TaC precipitates during heating and cooling from HT was studied with in-situ SANS. It turns out that the Co-Re matrix transformation $\gamma \leftrightarrow \epsilon$ has a strong influence on the precipitation and dissolution of the TaC phase in form of fine particles. In the first part, the general behavior of TaC precipitation is studied as a function of the C and the Cr content in the alloy. In the second part, a kinetic model for precipitation is fitted to data from in-situ SANS measurements of the alloy TaC09 and 15Cr, i.e. for a fixed C/Ta ratio $y = 0.9$ without and with addition of 15 at.% of Cr.

7.2.1 Evaluation procedure

The nucleation kinetics were measured by means of fast in-situ classical and TOF SANS experiments at a fixed instrument geometry in series of 10 s measurements. In these experiments, only a limited Q-range was covered, since the instrument geometry cannot be changed in time between the fast in-situ SANS measurements. The results from these measurements are twofold: (a) statistical evaluation of the integral intensity in case of classical SANS measurements due to smaller Q-range. The scattering invariant and radius of gyration were determined from these measurements to evaluate their precipitated volume fraction and size. And (b) evaluation of Q vs. intensity in terms of Kratky plots depending on temperature vs Q, derived from the TOF-SANS method that covered a larger Q-range during the fast in-situ SANS measurements. Especially, the large detector area towards larger Q-values were important for sufficient count statistics. Fig. 7.2.1 depicts a scheme on the general procedure of the experiments and their evaluation. The recorded Q-resolved SANS patterns are corrected for Porod scattering and then transformed to Kratky functions $Q \mapsto Q^2 \times I(Q)$ and then serially plotted in a contour representation for varying temperature. In the following, this representation is denoted Kratky surface (cf. eq. (3.40)).

At certain temperatures, the temperature ramps were held in order to measure the full available Q-range with SANS. These measurements were used to get exact values of TaC volume fraction and particle size at the respective steps. A spherical form factor (cf. eq. (B.1)) was assumed for the precipitates with a log-normal distributed particle size. Interparticle interference effects were considered during the evaluation, but a structure factor

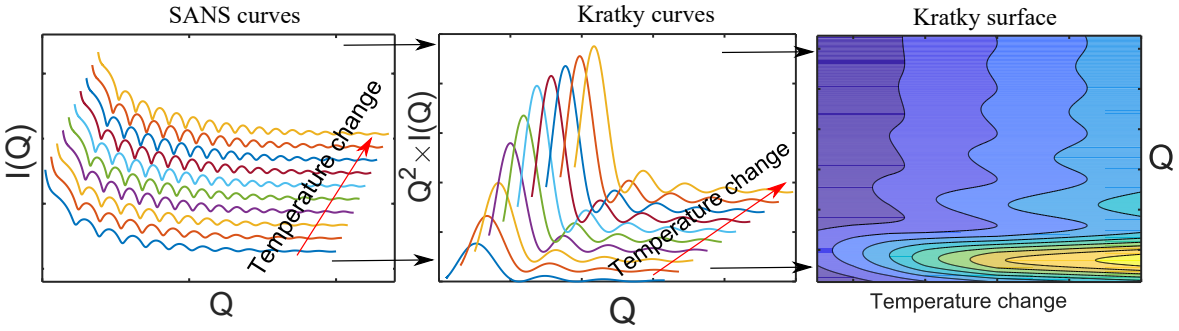

Figure 7.2.1: The recorded Q-resolved SANS patterns are transformed to Kratky functions $Q \mapsto Q^2 \times I(Q)$ and then serially plotted in a contour representation for varying temperature. This representation is denoted Kratky surface. Its intensity is proportional to the precipitate volume fraction resolved by Q and T.

(e.g. hard sphere) did not influence the results, since the TaC volume fraction was low. In addition, the measurements from full available SANS Q-range were used to evaluated the background signal due to Porod scattering from large scale structures and incoherent scattering (eq. (3.39)) in the form

$$P(Q,T) = A(T)\ Q^{-4} + B(T) \quad . \tag{7.7}$$

The parameters A, B from Porod and incoherent background depend on the temperature T. The parameter A was essentially constant throughout temperature ramps up to 1770 K, since large scale structures like large facetted TaC precipitates are constant in volume during the heat treatments. The parameter B from the incoherent background changed slightly during in-situ heat ramps due to the diffuse contribution from inelastic scattering, accounted for by the Debye-Waller factor (cf. section 3.1.1.2). Therefore, the function $B(T)$ was linearly interpolated in between the temperature steps as a function of the temperature T. With this procedure, the Porod surface $P(Q,T)$ was determined and subtracted from the fast in-situ SANS measurements, in order to obtain the coherent signal from the form factor of the fine TaC precipitates, as a function of T.

For the measurements by means of classical SANS, the quick measurements were evaluated in reciprocal space, extracting several integral parameters from the scattering curves. The acquired Q-range is limited to roughly one order of magnitude for the fixed instrument geometry and it is important that the precipitates have their main scattering contribution in this range. The selection of an appropriate Q-range is discussed in appendix B.4. The instruments were set up with a sample to detector distance $d_0 = 8\,\mathrm{m}$ and neutron wavelength $\lambda = 0.6\,\mathrm{nm}$. In the TOF-SANS measurements, a larger Q-range is covered. The instrument was set up with $d_0 = 7.2\,\mathrm{m}$ and the used neutron spectrum was $\lambda \in [0.31 - 1.52]\mathrm{nm}$.

All raw data were treated for instrumental background and absolute calibration (cf. sections A.2, A.3).

7.2.2 TaC precipitation during slow heating and cooling ramps in TaC09 and 15Cr alloy

The evolution of all phases within Co-Re alloys was measured by ND and discussed in section 5.2. However, these measurements monitor the signal from TaC phase in all existing

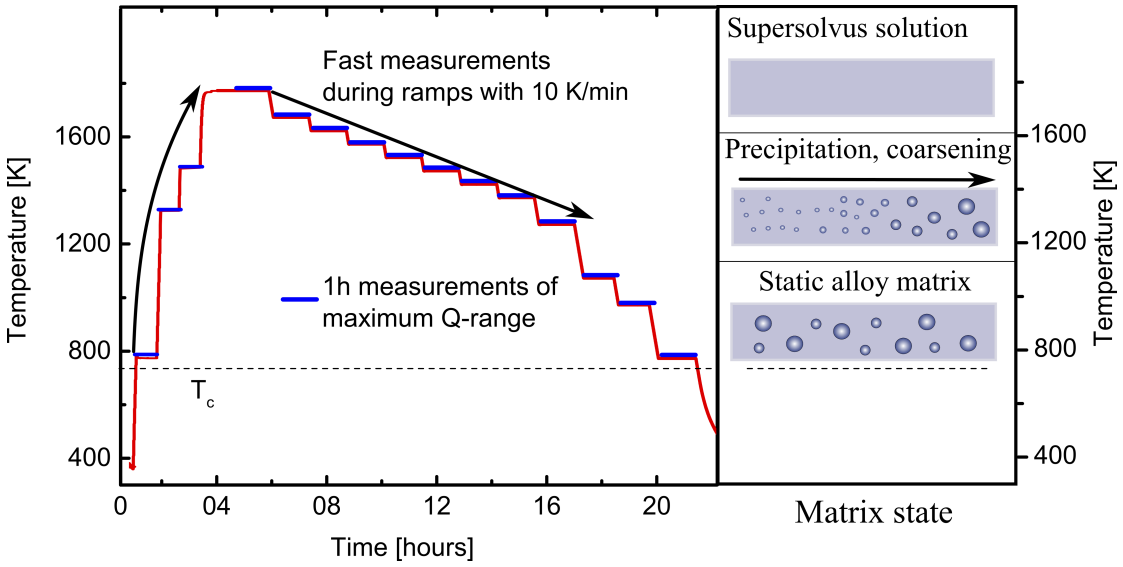

FIGURE 7.2.2: Temperature history of SANS experiments in order to determine nucleation and dissolution temperature of nano scaled TaC precipitates. During the temperature ramps, the SANS intensity was measured by means of the fast measurement technique. At certain steps, the temperature was held in order to record large Q-range patterns to determine exact values of precipitate volume fraction and size. At the highest temperatures the matrix is in supersolvus solution. During cooling, TaC particles precipitate and grow due to the activated diffusion at HT. Below a certain temperature, the kinetics becomes very slow and the alloy microstucture remains essentially static.

forms, namely the nano scaled strengthening TaC, the large facetted TaC within the matrix and blocky TaC at the grain boundaries. In order to get information about the nucleation of the nano scaled TaC precipitates during cooling, in-situ SANS measurements were performed with a slow heating and cooling ramp of $\pm 10\,\mathrm{K\,min^{-1}}$ (Fig. 7.2.2). The ramps were kept slow in order to accurately determine the onset temperatures of nucleation and dissolution of nano scaled TaC phase, respectively. SEM shows that the only scattering structures in the monitored Q-range are nano scaled TaC precipitates (Fig. 5.1.2).

Measurements of the full Q range were performed at the depicted holding temperatures in order to characterize the samples in a larger Q-range. In-situ SANS curves from two representative alloys, TaC09 and 15Cr, are shown in Fig. 7.2.3 during heating and Fig. 7.2.4 during cooling. The corresponding fitted volume fraction and size of nano scaled TaC precipitates from the SANS measurements during cooling is presented in Fig. 7.2.5. The SANS curves during heating show intensity up to a temperature of 1573 K. However, a clear scattering peak in the SANS resolution range is only visible up to 1473 K. Therefore, the nano scaled TaC precipitates have coarsened to sizes $> 300\,\mathrm{nm}$ at 1573 K. At the even higher temperature 1773 K, no SANS signal is observed and the remaining signal only originates from incoherent and Porod scattering. Therefore, the matrix is in supersolvus solution, i.e. in the form of the single HT γ-Co phase and the TaC precipitates are dissolved in the matrix. This is confirmed by the in-situ ND results (cf. section 5.2).

Upon cooling, a small-angle scattering signal first returns at the onset temperature of nucleation 1473 K, but the amount is below 0.1 vol.% during the measurement. Upon cooling further to the onset temperature of precipitation $T_{\mathrm{on}}^{\downarrow} = 1423\,\mathrm{K}$, a larger amount of 0.76 vol.% has precipitated. This signal only slightly increases during further cooling to RT.

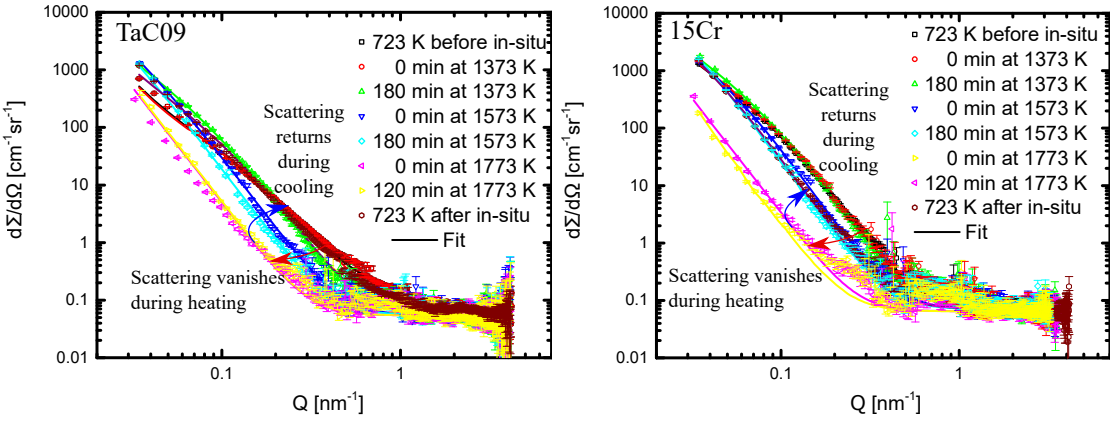

Figure 7.2.3: SANS curves from TaC09 and 15Cr alloy at selected steps during heat to supersolvus solution at 1773 K. The TaC09 alloy has a burst of precipitation at 1173 K. At 1573 K, the precipitates rapidly coarsen, and the scattering peak is out of the SANS resolution range. Upon further heating, the alloy goes to supersolvus solution and no scattering signal from fine TaC precipitates is present at the highest temperature. 15Cr alloy has a similar behavior, but there is no burst upon reaching 1173 K, since TaC precipitates are already present.

Only in the interval 973 K → 723 K, the TaC09 alloy shows a secondary scattering peak at $Q = 0.1 - 2.0$ nm from a secondary precipitation of very fine TaC precipitates (cf. section 5.1.1).

The whole cooling cycle took ∼ 8 h. During this cycle, the TaC precipitates coarsen to a mean size of 111 nm, due to the diffusion limited coarsening at temperatures > 1173 K. The second precipitation in the interval 973 K → 723 K leads to very fine precipitates of ∼ 3 nm.

Cr addition to the alloy changes this behavior. The 15Cr already has a considerable amount of TaC precipitates at RT and their volume fraction is essentially unchanged during heating up to 1573 K around ∼ 1 vol.%. At higher temperatures, the TaC phase in form of nano scaled precipitates dissolves. During cooling, the re-precipitation of TaC occurs at higher temperature of $T_{\text{on}}^{\downarrow} = 1523$ K in small vol.% and at 1473 K the precipitation is almost completed. The coarsening is generally slower in the Cr containing alloy and the TaC particles have a final size of 97 nm after cooling back to RT (due to the higher activation energies of coarsening, cf. table 7.1.1).

During the temperature ramps, the SANS intensity was monitored by the fast measurement technique in the medium Q-range $Q \in [0.15 - 0.82]\text{nm}^{-1}$ and the TaC vol.% was evaluated for their integral parameters with a time resolution of 10 s (cf. section 3.1.2.7). Fig. 7.2.6a depicts the temperature ramp during heating, underlain with a changing color representing the matrix transformation. The total intensity, as well as the scattering invariant and radius of gyration in TaC09 alloy are depicted. The scattering invariant is proportional to the TaC volume fraction (cf. section 3.36). By means of the fits from the large Q-range (Fig. 7.2.5), at several holding temperatures, the exact value of nano-sized TaC volume fraction and size between the ramps was determined (cf. Fig. 7.2.5). The results show a burst of nano scaled TaC precipitation, starting at ∼ 1200 K. This temperature coincides with the matrix transformation $\gamma_m \rightarrow \epsilon$-Co phase and was already observed in the aging in-situ SANS experiments (cf. section 5.3), where the burst started upon reaching and holding at 1173 K, when there is enough activation energy for the matrix to transform the metastable γ_m-Co phase to thermodynamically equilibrium of mainly ϵ-Co phase. Upon heating to the onset temperature

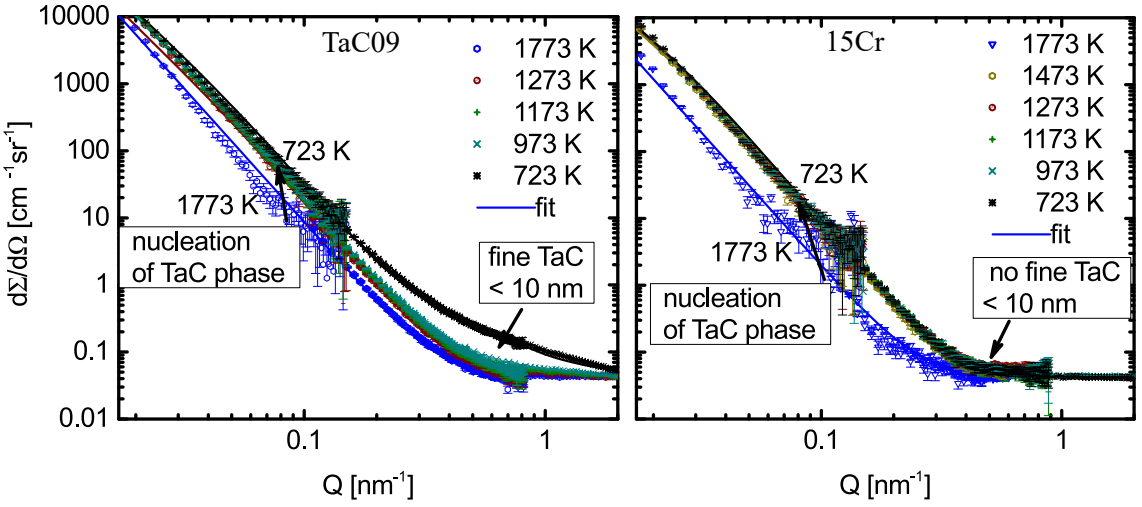

FIGURE 7.2.4: SANS curves from TaC09 and 15Cr alloy at selected steps during slow cooling from supersolvus solution at 1773 K. No scattering signal from fine TaC precipitates is present at the highest temperature. Scattering from nano scaled TaC precipitates appears during cooling. The TaC09 alloy shows a secondary size distribution of very fine TaC, evolving during cooling from 973 K → 723 K. This contribution is not present in 15Cr alloy.

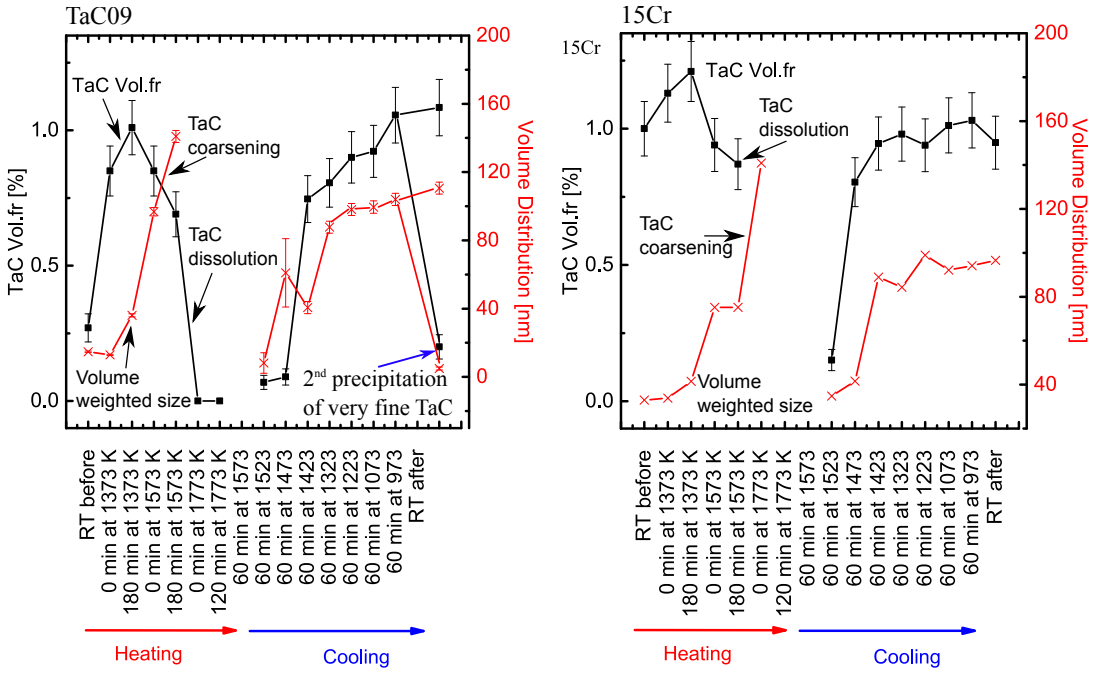

FIGURE 7.2.5: TaC volume fractions and size distributions during heating to 1770 K and during cooling back to RT in TaC09 and 15Cr alloy. The data points are acquired from large Q-range measurements. In TaC09 alloy (left), the nano scaled TaC phase precipitates during heating to 1373 K and starts dissolving at $T_{on}^{\uparrow} = 1573$ K. During cooling, the TaC particles re-precipitate at $T_{on}^{\downarrow} = 1423$ K with considerable volume fraction. In 15Cr alloy (right), the nano scaled TaC precipitates are already present in initial ST condition and start dissolving at $T_{on}^{\uparrow} > 1573$ K. During cooling, the TaC particles re-precipitate at $T_{on}^{\downarrow} = 1473$ K with considerable volume fraction. In addition, the evolution of the TaC particle size is depicted.

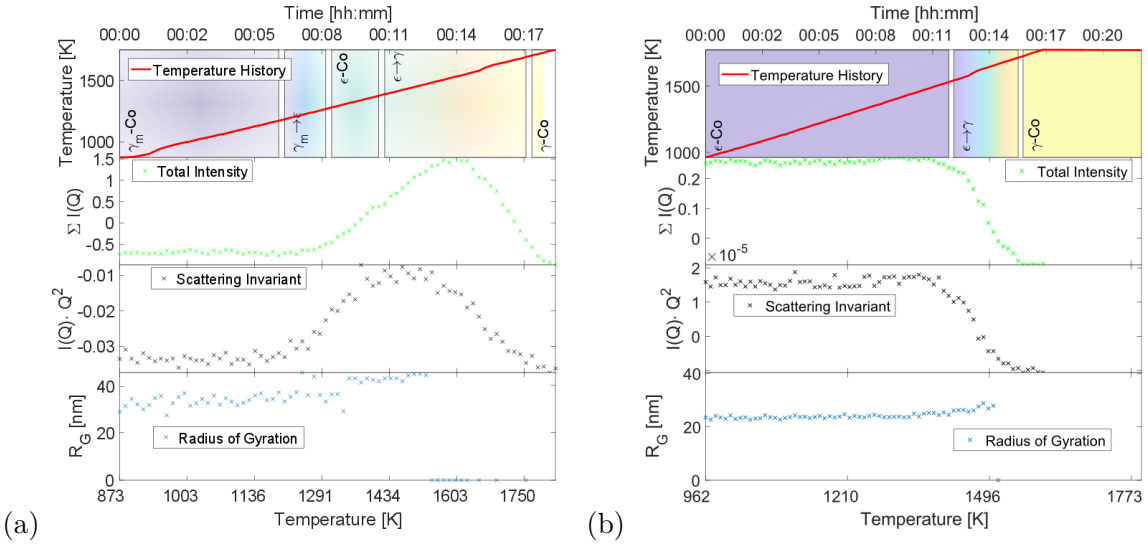

Figure 7.2.6: TaC kinetics during heating of TaC09 (left) and 15Cr alloy (right). The heat ramp is depicted on the top and underlain with the Co-Re phase transformation determined by in-situ neutron diffraction. The total SANS intensity, scattering invariant and radius of gyration during the temperature ramps were evaluated with the fast measurements and are shown in the plot. In TaC09 alloy the SANS scattering invariant increases at 1200 K during heating and decreases at 1500 K. In 15Cr alloy the SANS scattering invariant is constant during heating and decreases at 1620 K from already present precipitates. The particle size is evaluated by a fit of the radius of gyration and yields values of 8 nm in TaC09 alloy for the nucleated precipitates during heating and $\sim$ 23 nm in 15Cr alloy for the already present precipitates.

$T_{\text{on}}^{\uparrow} \sim 1500\,\text{K}$, the TaC phase, in form of nano scaled precipitates, starts to dissolve, whereby the temperature coincides with the allotropic Co-Re matrix transformation to the HT phase $\epsilon \rightarrow \gamma$.

The results from 15Cr alloys are presented in Fig. 7.2.6b. As a consequence of the addition of hcp stabilizer Cr (cf.Fig. 5.2.5), the matrix is completely present in form of ϵ-Co phase in initial state. No burst of TaC precipitation is observed during heating. The transformation to HT phase $\epsilon \rightarrow \gamma$ starts at little higher temperature. Since the TaC precipitates are always present in considerable amount in the ϵ-Co phase, this experiment shows their high solubility in the γ-Co phase.

When comparing the large Q-range results with the fitted radius of gyration during the fast in-situ SANS measurements during heating, it shows that the value gives a rough measure of particle size during the fast in-situ SANS measurements. Large Q-range measurements give a final precipitate size of 87 nm after the cooling ramp and 97 nm for 15Cr alloy, while the fast in-situ SANS measurements yield values of 76 nm and 83 nm, respectively. The relative accuracy is therefore $\sim$ 15%. However, it has to be noted that the precipitate radius is rather small during this experiment and can therefore be resolved by the limited Q-range in the fast in-situ SANS measurements.

The results of alloys TaC09 and 15Cr during cooling with $-10\,\text{K}\,\text{min}^{-1}$ are presented in Fig. 7.2.7. It can be seen that the temperature of nucleation of TaC precipitates again coincides with the allotropic Co-Re matrix transformation in both alloys. In TaC09 alloy, the transformation is sluggish during slow cooling, resulting in a slow precipitation of TaC precipitates over a large temperature interval $> 300\,\text{K}$. As a consequence of the addition

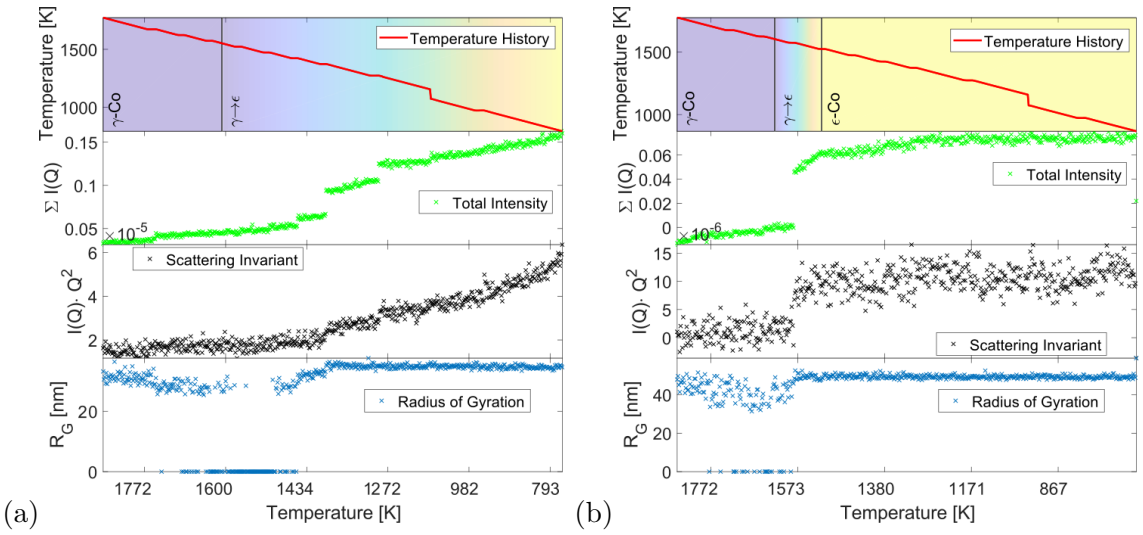

FIGURE 7.2.7: TaC kinetics during cooling in TaC09 (a) and 15 Cr alloy (b). The heat ramp is depicted on the top and underlain with the Co-Re phase transformation determined by in-situ neutron diffraction. The total SANS intensity, scattering invariant and radius of gyration during the temperature ramps were evaluated with the fast measurements and are shown in the plot.

of hcp stabilizer Cr, the $\gamma \rightarrow \epsilon$ transformation starts at higher temperatures in the Cr containing alloys and the TaC volume fraction increases strongly in a short temperature interval of $\Delta T \sim 70$ K. Additionally, this has the effect that the particle size – fitted with the radius of gyration – is larger in Cr containing alloys, due to the larger diffusion coefficient at the higher temperature.

7.2.3 Influence of varying C and Cr content on TaC precipitation

In section 5.3, it was shown that the exact C content has an important influence on the TaC volume fraction and coarsening rate at HT. Further, the addition of Cr for oxidation resistance is vital for the alloy performance. However, it can form parasitic unwanted phases (cf. section 2.1.4). Therefore, it is of interest to study the influence of a varying content of the elements C and Cr on the nucleation behavior of TaC. The experiments were performed with the same temperature ramps as in the previous section, i.e. by fast in-situ SANS measurements during temperature ramps with $-10\,\mathrm{K\,min^{-1}}$ and large Q-range measurements at certain temperature steps (cf. Fig. 7.2.2).

The six alloys TaC05-10 and 5Cr, 15Cr were measured during heating and cooling with the methods described in the previous section 7.2.2. By means of the fast in-situ SANS measurements during ramping the temperature from RT up to 1770 K, the nucleation and dissolution temperatures of nano scaled TaC precipitates were determined. The results are presented in Fig. 7.2.8a. During heating, the low C content (TaC05, TaC07), high C content (TaC09, TaC10) and Cr containing (5Cr, 15Cr) alloys show different features. All four alloys TaC05-10 show the burst of TaC precipitation during heating, coinciding with the transformation of metastable $\gamma_m \rightarrow \epsilon$-Co phase (table 7.2.1). However, in initial state (ST condition at RT), the low C content alloys have a very low volume fraction of TaC. There is already a higher amount of TaC precipitates in high C content alloys. This result is consistent with the fact that low C alloys have a higher amount of metastable γ_m-Co phase

$\epsilon \leftrightarrow \gamma$ transformation temperature	Heating $\epsilon \rightarrow \gamma$		Cooling $\gamma \rightarrow \epsilon$	
	T_{start} [K]	T_{end} [K]	T_{start} [K]	T_{end} [K]
TaC05	1473	1703	1373	γ_m retained
TaC09	1473	1693	1553	γ_m retained
5Cr	1533	1683	1563	1373
15Cr	1533	1713	1603	1523
01B	1473	1673	1493	γ_m retained
04B	1373	1573	1603	γ_m retained

Table 7.2.1: Matrix transformation onset and end temperatures for the $\epsilon \leftrightarrow \gamma$-Co transformation during heating and cooling, measured by in-situ ND (cf. sections 5.2, 6.1.3, 6.2.1). The B containing alloys are added to the table for comparison. TaC05, TaC09, 01B and 04B alloy retain metastable γ_m-Co phase at RT.

TaC formation/dissolution	at heating		at cooling	
Alloy	$T^{\uparrow}_{\text{on}}$ [K]	$T^{\uparrow}_{\text{end}}$ [K]	$T^{\downarrow}_{\text{on}}$ [K]	$T^{\downarrow}_{\text{end}}$ [K]
TaC05	1440	1750	1390	< 800
TaC07	1510	1750	1390	< 800
TaC09	1500	1750	1390	< 800
TaC10	1490	1750	1390	< 800
5Cr	1530	1770	1480	1420
15Cr	1550	1760	1580	1520

Table 7.2.2: Onset and end temperature of TaC dissolution and formation during heating and cooling, measured by in-situ SANS.

in ST condition than high C alloys (cf.table 5.0.2) and the fact that TaC phase shows a lower solubility in ϵ-Co phase. When the matrix transforms to thermodynamically stable ϵ-Co phase at $\sim 1150\,\text{K}$, there is a burst of TaC precipitation. However, the burst is stronger in high C content alloys, due to the higher amount of available C for TaC phase formation. During the transformation to HT phase $\epsilon \rightarrow \gamma$ starting around $\sim 1480\,\text{K}$, the TaC phase in form of nano scaled precipitates dissolves.

Neither of the Cr containing alloys 5Cr and 15Cr does contain metastable γ_m-Co phase at RT (cf. table 6.1.1). As a consequence, there is no burst of nano scaled TaC precipitation during heating, but in contrast, there is already a higher volume fraction in ST condition. By means of the high time resolution measurements, the exact onset and finish temperature of TaC formation could be determined. The results are presented in table 7.2.2. An influence is observed by the addition of Cr, while different C/Ta ratios have essentially no influence on $T^{\uparrow}_{\text{on}}$.

During cooling, the alloys were both measured in the large Q-range at the distinct temperature steps and by the fast in-situ SANS measurement method during the temperature ramps. The exact volume fractions were determined in 100 K temperature steps by large Q-range measurements and the results are compared in Fig. 7.2.9 In the beginning, the alloy is in supersolvus solution at 1770 K. It can be seen that the TaC particles precipitate at higher temperatures in Cr containing alloys 5Cr and 15Cr at $T^{\downarrow}_{\text{on}} \approx 1523\,\text{K}$ within a narrow temperature interval. Their volume fraction remains essentially constant upon further cooling. On the other hand, in alloys without Cr, the precipitation starts at $T^{\downarrow}_{\text{on}} \approx 1423\,\text{K}$ and is much slower. The volume fraction continuously increases over a wider temperature range. When the temperature falls below 973 K, a secondary strong increase of scattering is observed in these alloys.

The results from the fast in-situ SANS measurements during cooling are presented in Fig. 7.2.8b. The curves show several small steps, because the sample was held at specific

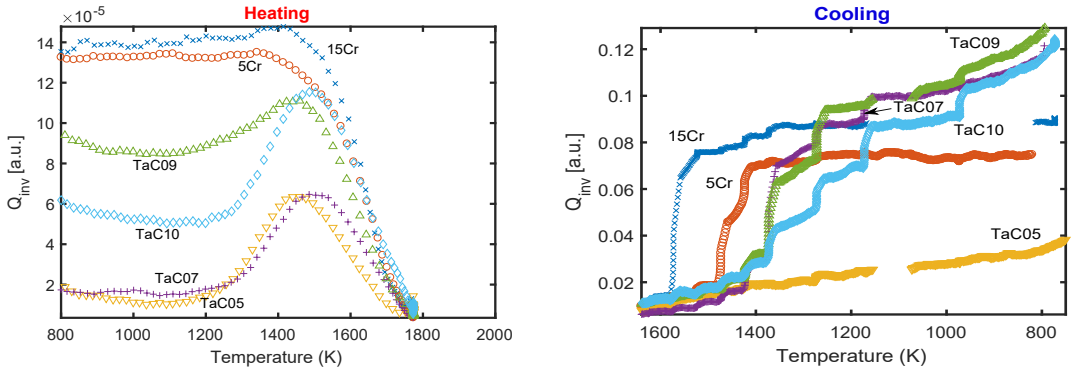

FIGURE 7.2.8: Comparison of the scattering invariant intensity during heating (a) and cooling (b). The cooling curves shows several steps, because the sample was held at specific temperatures during the cooling in order to get an in-situ measurement of the full Q-range. The onset temperature of TaC precipitation can be observed. Alloys without Cr show a burst of precipitation during heating, due to the transformation of metastable $\gamma_m \rightarrow \epsilon$ at $\sim 1200\,\mathrm{K}$. With higher Cr content, TaC precipitation starts at higher temperatures during cooling and is essentially completed at $T^{\uparrow}_{\mathrm{end}} \approx 1450\,\mathrm{K}$. Alloys without Cr show a continuous nucleation during cooling.

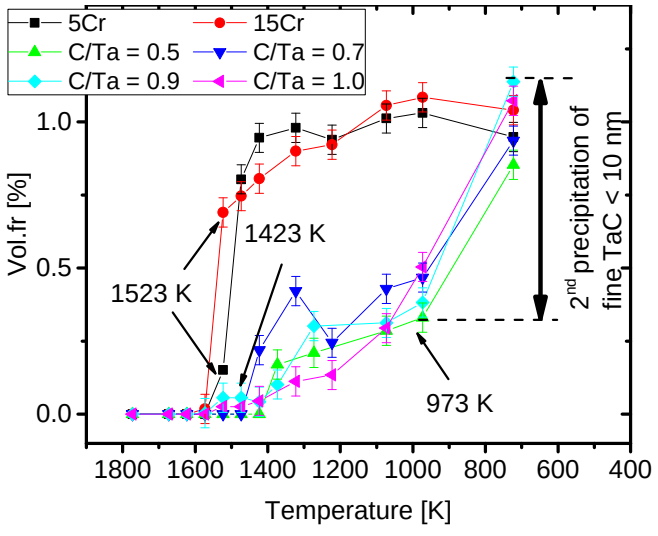

FIGURE 7.2.9: Fit results of the TaC volume fraction from the 1 h SANS measurements over the large Q-range. Cr addition results in a strong burst of TaC precipitation in a narrow temperature interval, while non-Cr containing alloys show a slow continuous precipitation. Higher Cr content results in precipitation at higher temperature. The results coincide with the results from the fast in-situ SANS measurements in Fig. 7.2.8

temperatures in order to get an in-situ measurement of the full Q-range. During holding at these temperatures, the TaC phase fraction often increases by a small amount. The precipitation starts at higher temperatures in alloys with higher Cr content, due to the fact that Cr stabilizes ϵ-Co phase. As a consequence of Cr addition, the precipitation occurs in a small temperature interval of $\sim 50 - 100\,\mathrm{K}$ and is essentially completed at $\sim 1400\,\mathrm{K}$. Unlike Cr containing alloys, all four TaC05-10 without Cr show a continuous increase of TaC vol.% during cooling and the onset temperature $T_{\mathrm{on}}^{\downarrow}$ is at lower temperatures (as is the allotropic matrix transformation). The precipitation is stronger for higher C content, since they retain less metastable γ_m-Co phase at RT.

In addition, the results suggest two precipitation mechanisms. A first precipitation of TaC phase starts when the matrix starts transforming to low temperature phase $\gamma \rightarrow \epsilon$, similarly to the Cr containing alloys. However, the transformation is not complete during cooling as shown by ND. Consequently, there is a continuous TaC precipitation during cooling. A secondary precipitation starts at $\approx 950\,\mathrm{K}$. Looking at the SANS curve from TaC09 alloy (Fig. 7.2.4a), the second increase of scattering can be identified with the very fine TaC precipitates $< 10\,\mathrm{nm}$, producing a Q^{-1} signal.

7.2.4 Activation energies of nucleation and growth by variation of the cooling ramps

For the alloy development, the exact size of TaC precipitates is very important, since the alloy strength is a function of their radius (cf. section 2.2). When quenching the alloy from HT, the cooling ramp ϕ is a crucial parameter, because larger ramps leave less time for the precipitates to grow. It is particularly difficult to determine the crucial parameters for precipitation, such as their interface tension Γ in the matrix, or the activation energies for particle nucleation and growth. For example, there exist parameters for TaC in pure Co for Γ in the literature, ranging from $0.44\,\mathrm{J\,m^{-2}}$ to $2.21\,\mathrm{J\,m^{-2}} \pm 0.2$ [119]. In the following, the precipitation behavior in Co-Re was determined by in-situ SANS measurements and the above mentioned parameters fitted with a developed model. The model is fitted to data from several varying cooling ramps to fit these parameters.

By means of the fast in-situ measurement technique the TaC09 and 15Cr alloys were investigated for the influence of cooling rate on TaC precipitation. However, the $\epsilon \leftrightarrow \gamma$-Co phase transformation of the Co-Re matrix occurs in the same temperature window and might therefore interfere with the precipitation kinetics. Since Cr is a strong hcp stabilizer, the Co-Re matrix is expected to transform at higher temperatures to ϵ-Co phase in Cr containing alloys. In addition, the matrix transformation $\gamma \rightarrow \epsilon$ is not complete during cooling in alloys without Cr. They retain some metastable γ_m-Co phase at RT. This should influence the coarsening kinetics, since the TaC phase in form of fine precipitates showed a different behavior in ϵ- and γ-Co phase.

The TOF-SANS technique (cf. section 4.3.4) was used to maximize the Q-range during in-situ fast measurements while ramping the temperature. The samples were quickly heated to supersolvus solution temperature 1770 K and then cooled with different cooling rates, in order to evaluate the activation energies of precipitation. During the temperature ramps, the Kratky and Guinier surfaces were determined during cooling and heating in order to get Q-resolved information about the nano scaled TaC precipitation (cf. section 3.1.2.8). The

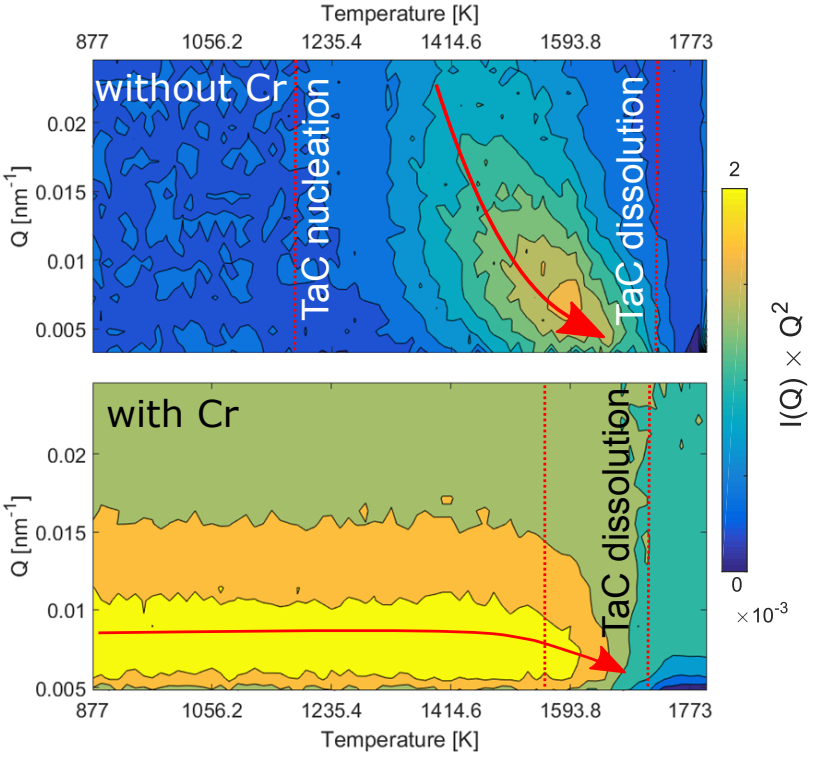

FIGURE 7.2.10: Kratky surfaces during heating. The plot shows the function $(Q,T) \mapsto Q^2 \times I(Q,T)$ which is proportional to the scattering volume fraction at the respective reciprocal Q-value. The TaC kinetics in TaC09 (top) and 15Cr alloy (bottom) during heating can be observed. In TaC09 alloy, precipitates nucleate during heating at $T \approx 1190\,\mathrm{K}$ and start dissolving, at 1520 K. As a consequence of Cr addition the, TaC precipitates are already present in initial state. The Kraty surface shows that they start dissolving at $T \approx 1570\,\mathrm{K}$.

method yields $2D$ functions that contain the scattering intensity of nano scaled precipitates as a function of temperature vs. reciprocal space.

For the TaC09 and 15Cr alloys, Q-resolved Kratky surfaces are depicted in Fig. 7.2.10, measured during heating to supersolvus temperature. In the TaC09 alloy, the Kratky surface shows that the nano scaled TaC precipitates nucleate during heating at $\sim 1190\,\mathrm{K}$. Additionally, the movement of the scattering intensity towards smaller Q can be observed as a result of particles coarsening. Notably, the SANS peak in this $2D$ representation is not connected to the smallest Q-values. Therefore, the nano scaled TaC precipitates do not coarsen towards larger size (implying the SANS peak to move continuously out of the resolved Q-range towards smaller Q), but dissolve into the matrix during heating.

The Kratky surface from high Cr content alloy directly shows the main difference to alloy without Cr: There is already a high volume fraction of fine TaC precipitates in ST condition, that remains stable during heating within ϵ-Co phase. The Cr addition suppresses formation of metastable γ_m-Co phase in ST condition. Upon HT $\epsilon \rightarrow \gamma$-Co transformation, the fine TaC precipitates rapidly vanish in both alloys. The TaC phase is still present in this temperature range as shown by ND (cf. section 6.1.3) and dissolves at higher temperature. This behavior is representative for all investigated Co-Re alloy systems.

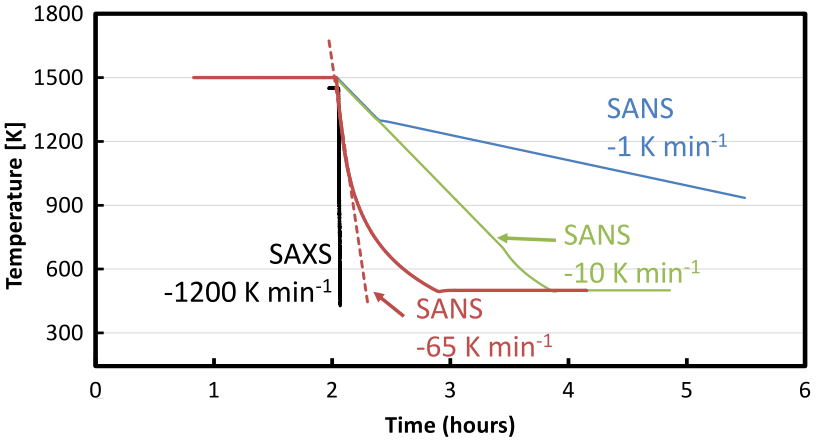

Figure 7.2.11: The applied cooling ramps for in-situ SAS measurements. $\phi = -1, -10\,\mathrm{K\,min^{-1}}$ and $\phi = -65\,\mathrm{K\,min^{-1}}$ were performed with neutron probe with the ILL furnace, while $\phi = -1200\,\mathrm{K\,min^{-1}}$ was performed with photon probe and the in-situ Dilatometer.

TaC vol.fr. [%]	$-1\,\mathrm{K\,min^{-1}}$	$-10\,\mathrm{K\,min^{-1}}$	$-65\,\mathrm{K\,min^{-1}}$	$-1200\,\mathrm{K\,min^{-1}}$
TaC09	0.98	0.97	0.93	0.92
15Cr	1.50	1.51	1.47	

Table 7.2.3: Precipitated TaC volume fraction, in dependence of the applied cooling rate in TaC09 and 15Cr alloy after cooling from 1770 K to RT.

7.2.4.1 Co-Re-Ta-C alloy TaC09

The precipitation kinetics during various cooling ramps was investigated for a fixed C/Ta ratio $y = 0.9$ in the TaC09 alloy. The cooling ramps $\phi = -1\,\mathrm{K\,min^{-1}}, -10\,\mathrm{K\,min^{-1}}$ and $\phi = -65\,\mathrm{K\,min^{-1}}$ from supersolvus solution temperature at 1770 K were applied to three different samples. During cooling, the samples were measured with in-situ SANS. In addition, the alloy was rapidly quenched with a ramp of $\phi = -1200\,\mathrm{K\,min^{-1}}$ and measured by in-situ SAXS. The temperature histories are shown in Fig. 7.2.11. In case of the slowest cooling ramp, the alloy was cooled a bit faster in the beginning – before any phase transformation is expected – to save measurement time.

The SAS curves and corresponding TaC size distributions in the end of the cooling ramps are depicted in Fig. 7.2.12. The applied cooling rate ϕ expectedly influences the shape of TaC precipitates. Higher ϕ results in a SAS curve shifted towards larger Q-values, i.e. smaller particle sizes. The overall scattering intensity, however, is similar in the four curves, suggesting a similar amount of TaC precipitation. The corresponding values of TaC volume fraction are shown in table 7.2.3. It can be seen that the volume fraction is slightly lower for larger cooling ramps.

During the cooling ramp, the SANS signal was measured by a series of fast in-situ measurements. Fig. 7.2.13 presents a comparison of the in-situ measured SANS curves during cooling with $-65\,\mathrm{K\,min^{-1}}$ and the SAXS curves during rapid quenching with $-1200\,\mathrm{K\,min^{-1}}$. The depicted curves are a selection of certain interesting temperature steps and show the increase of scattering as a result of the precipitating nano scaled TaC phase. The curves are rather noisy due to the high time resolution of the experiment. By means of the SANS experiments $120 - 700$ data files were recorded with a time resolution of 10 s during the cooling, while the SAXS experiments recorded 60 files per minute during the rapid quenching.

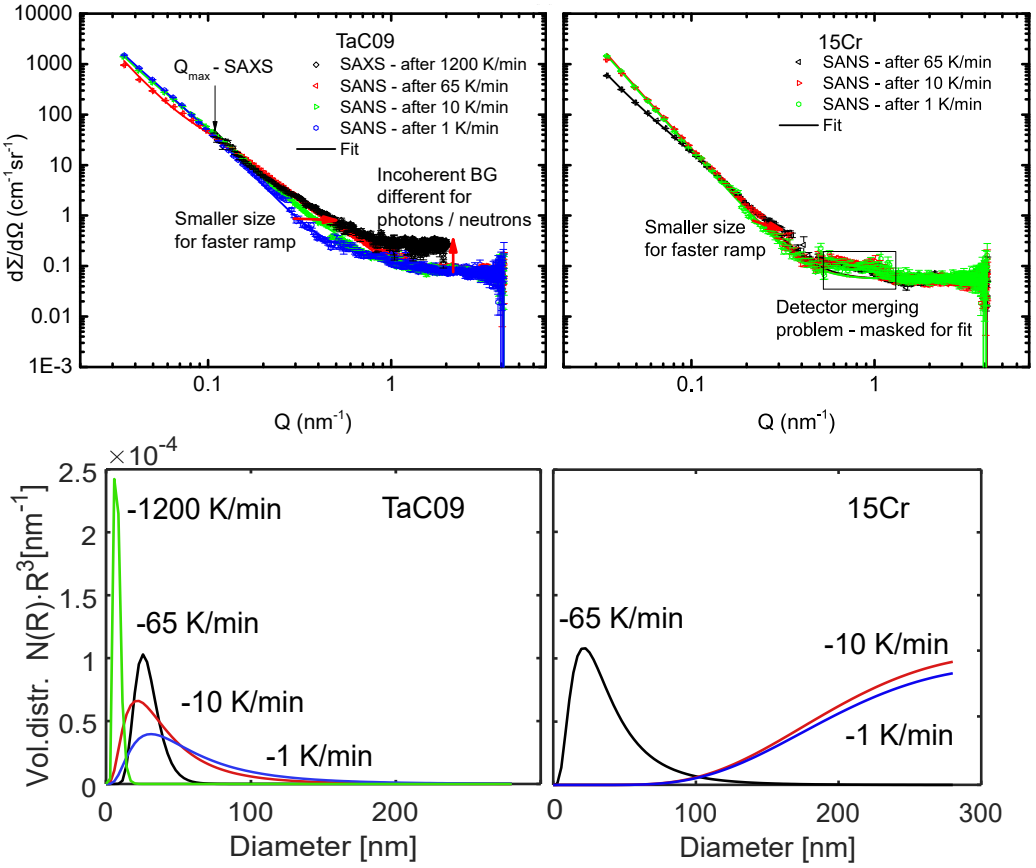

FIGURE 7.2.12: (top) SAS curves after different cooling ramps of TaC09 (left) and 15Cr (right) alloy. Larger cooling ramps result in a shift of the signal towards larger Q, i.e. smaller precipitate sizes. (bottom) Corresponding volume weighted particle size distributions. Since the nucleation occurs at higher temperatures in 15Cr alloy, the particles have grown to considerably larger sizes during the slower cooling ramps.

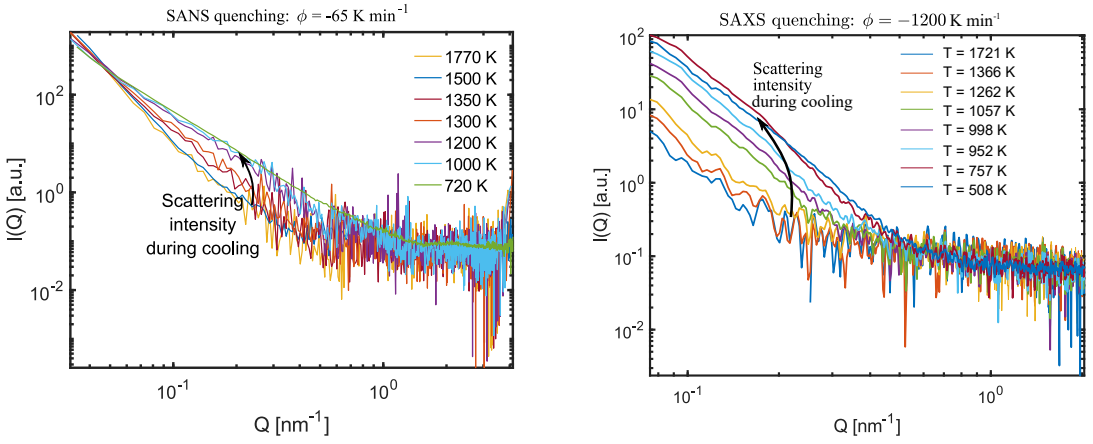

FIGURE 7.2.13: Comparison of the in-situ SANS (left) and SAXS (right) curves during quenching with ramps $\phi = -65, -1200\,\mathrm{K\,min^{-1}}$. The precipitation of nano scaled TaC can be followed by the increasing SAS intensity. The available Q-range of the SAXS measurement is more limited.

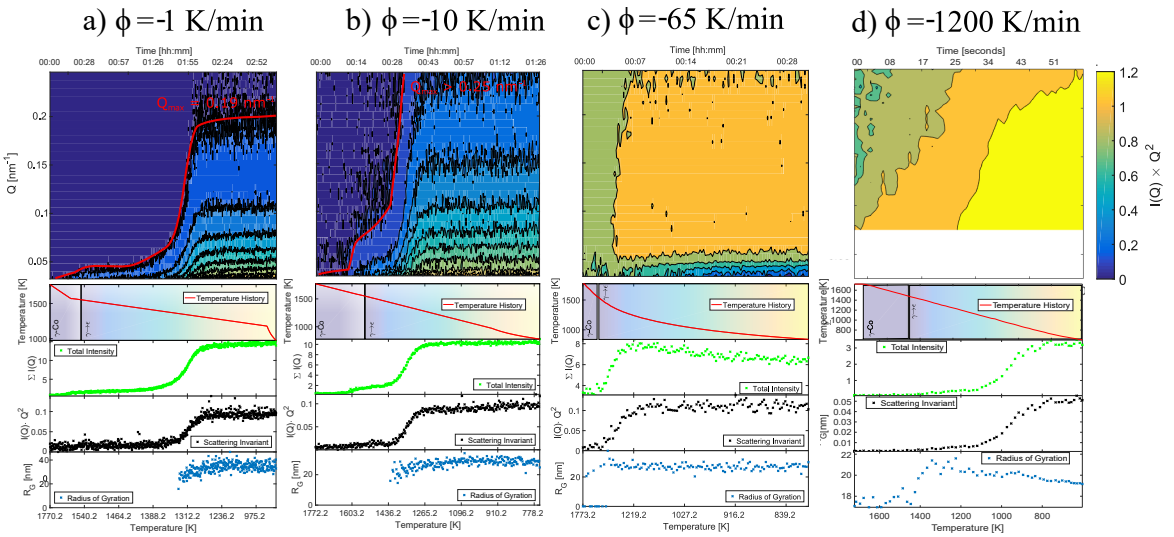

FIGURE 7.2.14: (top) Krakty surfaces $(Q,T) \rightarrow Q^2 I(Q,T)$ of TaC09 alloy during cooling with different cooling rates. The plots show the distribution of small-angle scattering from nano scaled particles in reciprocal space. (a) slow cooling $\phi = -1\,\mathrm{K\,min^{-1}}$; (b) medium $\phi = -10\,\mathrm{K\,min^{-1}}$; (c) fast cooling $\phi = -65\,\mathrm{K\,min^{-1}}$; (d) rapid quenching $\phi = -1200\,\mathrm{K\,min^{-1}}$. The maximum Q-value of scattering intensity corresponds to the minimum precipitate size. Therefore, lower cooling ramps result in larger particles. (bottom) Results from integral parameters of the in-situ fast measurements in TaC09 alloy. The heat ramp is depicted on the top and underlain with the Co-Re phase transformation determined by in-situ ND. The total SANS intensity, scattering invariant and radius of gyration during the temperature ramps were evaluated with the fast measurements and are shown in the plot. The scattering invariant corresponds to the precipitated volume fraction. The size of precipitates increases for slower cooling ramps and are in the range $20 - 40\,\mathrm{nm}$.

The scattering TaC volume fraction as a function of temperature was evaluated by calculating the respective Kratky surfaces of the fast measured SAS curves. The resulting images are presented in Fig. 7.2.14(top). Onset temperature $T^{\downarrow}_{\mathrm{on}}$ and end temperature $T^{\downarrow}_{\mathrm{end}}$ of TaC precipitation can be seen. In addition, the scattered intensity moves towards smaller Q-values as a result of particle growth. For smaller cooling ramps ϕ, this shift of scattering towards smaller Q is stronger, i.e. the particles grow to larger sizes. Unfortunately, the SAXS curve for $\phi = -1200\,\mathrm{K\,s^{-1}}$ monitors only to a minimum of $Q_{\mathrm{min}} = 0.7\,\mathrm{nm^{-1}}$ which limits the validity for particle sizes $> 25\,\mathrm{nm}$.

The Kratky surfaces were evaluated for their integral parameters, in order to calculate volume fraction and radius of gyration of the precipitated TaC phase. The results are presented in Fig. 7.2.14(bottom). This allows a quantification of the phase transformation in terms of volume fraction. The temperature ramp is depicted in the plot on top and was underlain by the amount of Co-Re phase transformation that was determined as a function of temperature by ND. Blue represents high-temperature γ-Co phase and yellow the low temperature ϵ-Co phase. The second plot shows the integral intensity and the third plot the corresponding scattering invariant that is proportional to the precipitated TaC volume fraction. The TaC precipitation starts after the Co-Re $\gamma \rightarrow \epsilon$-Co phase transformation. Especially the slowest ramp with $-1\,\mathrm{K\,min^{-1}}$ shows that the precipitation does not start immediately with the matrix transformation. Since the matrix transformation is very sluggish, larger areas of ϵ-Co phase are seemingly required wherein the TaC phase precipitates. The particle size is determined by a fit to the Guinier surface and the resulting radii of gyration characterize the

particle growth. However, the fitted values are in the order of $20 - 30\,\mathrm{nm}$ and are therefore probably already superimposed by particle coarsening. The 10 s time resolution is apparently too slow to resolve the initial particle growth after nucleation.

7.2.4.2 Co-Re-Cr-Ta-C alloy 15Cr

In addition to the fixed C/Ta ratio of $y = 0.9$, the nucleation kinetics were investigated in an alloy with addition of 15 at.% Cr. The addition of Cr influences the Co-Re phase transformation and might interfere with TaC precipitation due to the affinity of Cr for C. The cooling ramps $\phi = -1\,\mathrm{K\,min^{-1}}, -10\,\mathrm{K\,min^{-1}}$ and $\phi = -65\,\mathrm{K\,min^{-1}}$ from supersolvus solution temperature at 1770 K were applied to three different samples. During cooling the samples were measured with the in-situ SANS temperature technique, shown in Fig. 7.2.11. The corresponding values of TaC volume fraction are shown in table 7.2.3. It can be seen that the volume fraction is essentially independent of cooling ramps.

The scattering TaC volume fraction as a function of temperature was evaluated by calculating the respective Kratky surfaces of the fast measured SAS curves. The resulting images are presented in Fig. 7.2.15(top). Onset temperature $T^{\downarrow}_{\mathrm{on}}$ and end temperature $T^{\downarrow}_{\mathrm{end}}$ of TaC precipitation can be seen. The maximum Q-value where scattering is observed is shown as a guide for the eye. The reciprocal d-value in real space gives an estimate for the size of the smallest precipitates during cooling. In addition, the scattered intensity moves towards smaller Q-values as a result of particle growth. In comparison to alloys without Cr, the scattering is shifted to much smaller Q-values, indicating a stronger particle growth during cooling. For smaller cooling ramps ϕ, this shift of scattering towards smaller Q is stronger, i.e. the particles grow to larger sizes.

The Kratky surfaces from the SANS signal were evaluated for integral parameters, in order to calculate volume fraction and radius of gyration of the precipitated TaC phase as a function of temperature. The results are presented in Fig. 7.2.15(bottom). It can be seen that the transformation starts at higher temperature as a result of the Cr addition. In addition, the particle size is determined by a fit to the Guinier surface and the resulting radii of gyration characterize the particle growth. The fitted values are of the order $30 - 38\,\mathrm{nm}$. The scattering quickly moves towards smaller Q-values due to a stronger particle growth. This is caused by the fact that the diffusion coefficient is larger at the higher transformation temperature. The addition of Cr has the effect that precipitation occurs in a considerably smaller time window, compared to TaC09 alloy without Cr. This is likely caused by the fact that the Co-Re phase transformation occurs in a narrow temperature window. The plot of the scattering invariant shows that the TaC precipitation starts directly after the start of the Co-Re phase transformation.

7.2.4.3 Model implementation for the nucleation kinetics

The classic nucleation theory yields a temperature dependent rate for particle nucleation and growth (cf. section 3.2.1). An adapted KWN multi-class model was developed to fit the TaC precipitate volume fractions, determined by in-situ SANS during isochronal cooling (with constant temperature ramps). The model calculates the number of precipitated particles in a series of time steps and treats their size evolution in separate classes by a numerical integration of the rate equations. Such a model is classified as a mean-field approach, since

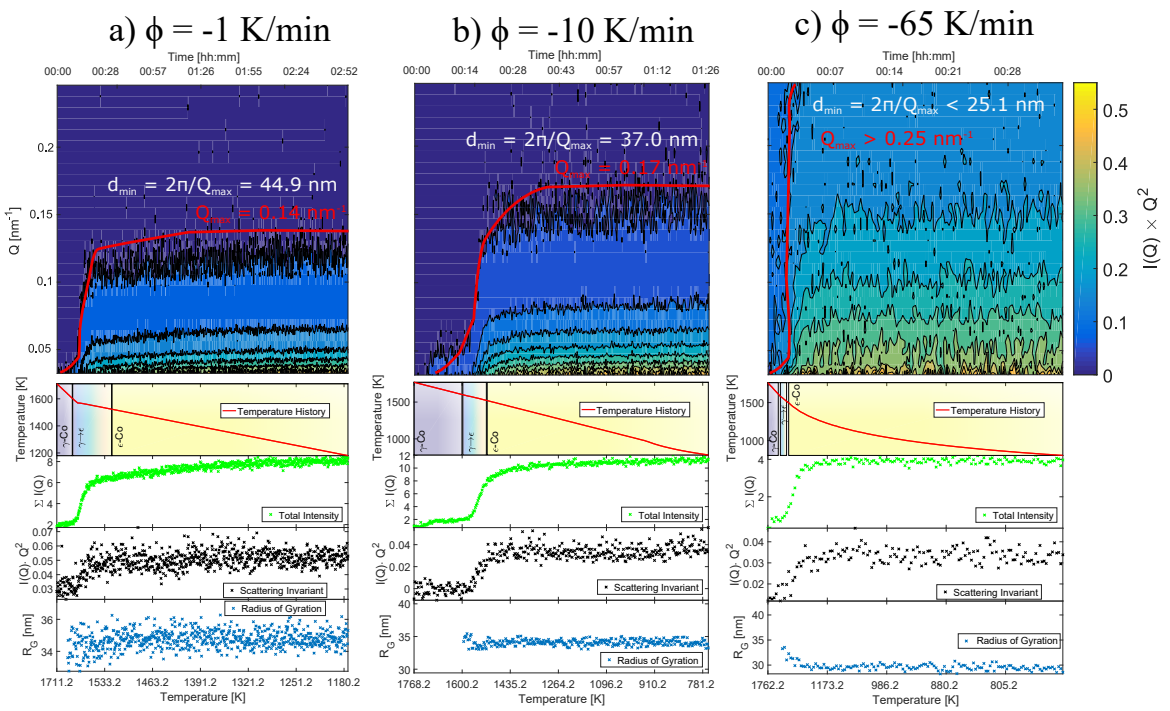

FIGURE 7.2.15: (top) Krakty surfaces $(Q,T) \rightarrow Q^2 I(Q,T)$ of 15Cr alloy during cooling with different cooling rates. The plots show the distribution of small-angle scattering from nano scaled particles in reciprocal space. (a) slow cooling $\phi = -1\,\mathrm{K\,min^{-1}}$; (b) medium $\phi = -10\,\mathrm{K\,min^{-1}}$; (c) fast cooling $\phi = -65\,\mathrm{K\,min^{-1}}$. The maximum Q-value of scattering intensity corresponds to the minimum precipitate size. Therefore, lower cooling ramps result in larger particles. (bottom) Results from statistical evaluation of the in-situ fast measurements in 15Cr alloy. The heat ramp is depicted on the top and underlain with the Co-Re phase transformation determined by in-situ ND. The total SANS intensity, scattering invariant and radius of gyration during the temperature ramps were evaluated with the fast measurements and are shown in the plot. The scattering invariant corresponds to the precipitated volume fraction. The size of precipitates increases for slower cooling ramps and are in the range $30 - 38\,\mathrm{nm}$.

the parent matrix phase is assumed to only change in its amount of supersaturation but otherwise does not interact with the precipitates.

Several approximations have to be applied for the calculation of activation energy of nucleation. For values of the equilibrium solubility of the TaC phase as a function of temperature, the results from ND measurements were used (Fig. 7.1.6). The energy barrier due to elastic strain field distortion of the matrix Δg_{el} depends on the shear modulus μ^α of the matrix and effective bulk modulus K^β of the precipitate. The value was approximated with the approach [120]

$$\Delta g_{el} = 2\mu^\alpha \frac{3K^\beta}{3K^\beta + 4\mu^\alpha} \frac{(v^\alpha - v^\beta)^2}{3v^\beta} \quad . \tag{7.8}$$

This approach assumes isotropic elasticity of matrix and precipitate phase. The bulk modulus of TaC is given by $K^\beta = 308\,\mathrm{GPa}$ [121]. Young's modulus of TaC09 alloy was determined by a tensile stress/strain test [49], yielding a value of $E = 319\,\mathrm{GPa}$. The comparatively large elastic stiffness of the Co-Re alloy is a result of the strong metallic bonding of the added Re atoms. Its shear modulus was calculated by the relationship $\mu^\alpha = \frac{E}{2(1+\nu)} \approx \frac{319\,\mathrm{GPa}}{8/3} = 120\,\mathrm{GPa}$, which approximately holds for metals [122]. It has to be noted, that in real crystals,

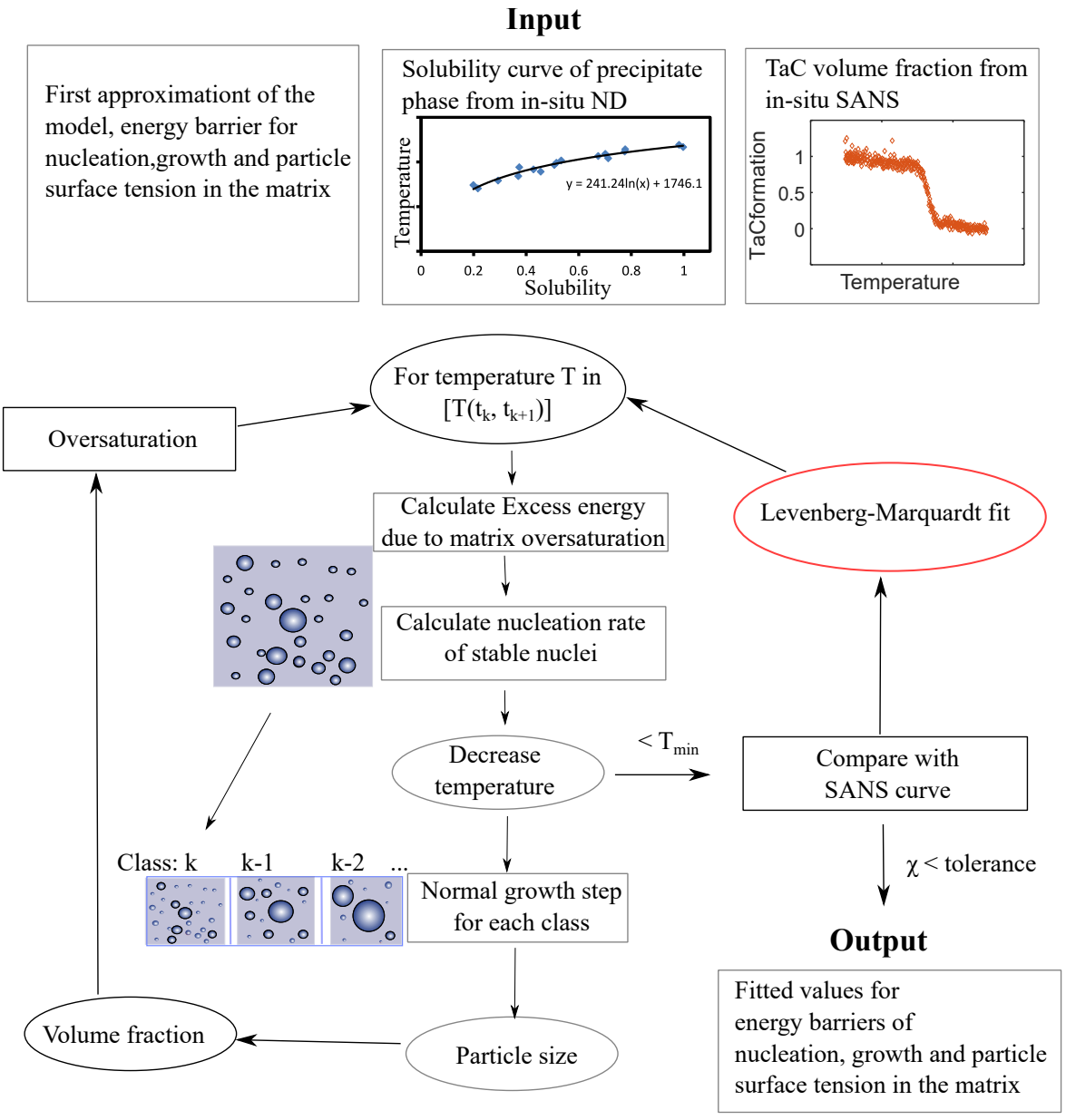

FIGURE 7.2.16: Scheme of the adapted KWN model for TaC nucleation and growth during cooling with constant ramp. In-situ ND data yields the TaC phase solubility at HT and SANS the precipitated volume fraction during cooling. The temperature interval during cooling is separated into several sub-intervals, where the nucleation rate and the growth rate of already present particles is calculated. The procedure can be fitted to SANS curves from several differing cooling rates and yields values for the activation energies of growth and nucleation.

the value might strongly depend on coherence relationships of matrix and precipitate lattice planes. Therefore, the values are sensitive on the exact TaC precipitate coherence to the matrix during nucleation. The coherence relationship is discussed in section 5.4.3, but is neglected in the current approach for calculation of the nucleation energies.

A scheme of the model is depicted in Fig. 7.2.16. The model omits coarsening kinetics at this point, since the isochronal cooling experiments were performed within 2 h. Activation energies for nucleation, growth and surface energy are fitted in the algorithm in the following steps:

() Input data for equilibrium solute concentration is provided from ND. The initial supersaturation C_0 is known from the nominal alloy composition. A step size in form of a temperature interval ΔT is defined. Repeat for each temperature step T^k:

(i) Calculate the amount of remaining dissolved β atoms in the matrix C_α^k and the chemical driving force $g_c^k(T^k, C_\alpha^k)$ and g_{el} for given temperature T^k.

(ii) Calculate the rate equation for nucleation $\dot{N}^k(T^k(t^k))$. Put the nucleated particles in class k.

(iii) For all classes $j \in \{1, \ldots, k\}$ determine the composition $C^j_{\alpha,\mathrm{int}}(r)$ at the particle interface depending on the particle size r^j according to the Gibbs-Thomson equation and the equilibrium solubility C_α, determined by ND.

(iv) For all classes $j \in \{1, \ldots, k\}$ solve the differential rate equation $\dot{r}(T^k, C^j_{\alpha,\mathrm{int}}, \phi)$ for particles nucleated with radius r^* in the current temperature interval $[T_k, T_k + \Delta T]$ and for all already existing particles in the other classes.

(v) Determine the volume fraction of TaC f^k phase at step k depending on the particles in all classes $1, \ldots, k$ by

$$f^k(T^k) = C_0 - \sum_{j=1}^{k} \dot{N}_{k,j}(T^k, g_c, \phi)\frac{4}{3}\pi r_j^3 C_\beta^k \tag{7.9}$$

The model can be fitted to data from SANS of precipitate volume fraction, during isochronal cooling with different cooling rates ϕ.

The adapted Kampmann-Wagner numerical (KWN) model for isochronal cooling was fitted to the results from the cooling experiments. In Co-Re alloys, the formation of nucleation sites at HT – especially defects – has an important influence on the precipitation. They are created during the allotropic $\gamma \rightarrow \epsilon$ Co-Re matrix transformation. Since this is a very complicated mechanism, the following modeling should only be considered as a qualitative proof of principle.

A comparison of the in-situ measured TaC volume fraction in alloys TaC09 and 15Cr is shown in Fig. 7.2.17. The alloys are cooled from supersolvus solution at 1770 K. The formation of nano scaled TaC phase was evaluated in the temperature interval 1700 K−1000 K by the fast measurement SANS method. The faster temperature ramps result in a delayed phase transformation to lower temperatures. The reason for this can be explained by the adapted KWN theory for isochronal cooling and has a twofold explanation: (1) The nucleation rate eq. (3.56) includes a term for the incubation time of nucleation. This term delays the start

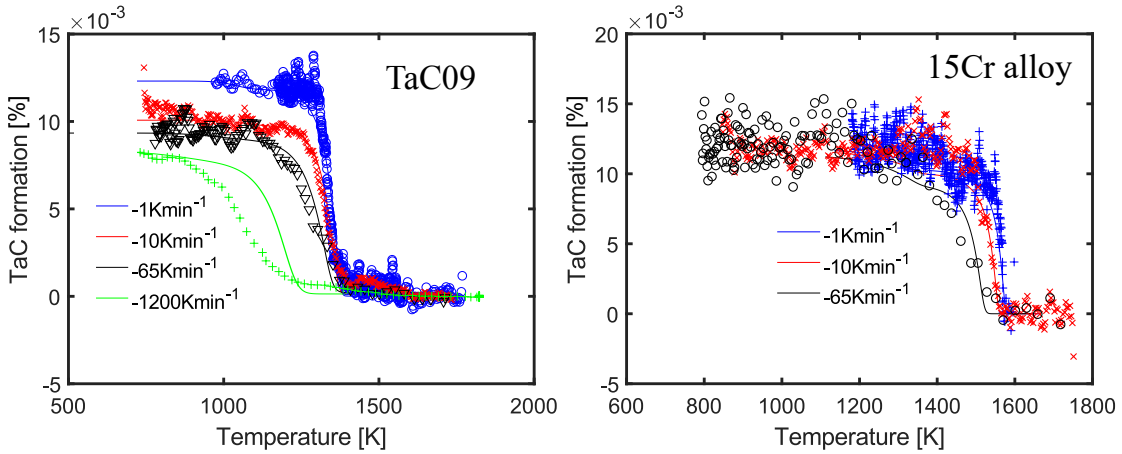

FIGURE 7.2.17: Fits of the adapted KWN model to the measured TaC nucleation in dependence on different cooling ramps from SANS measurements. (a) Non Cr containing alloy TaC09; (b) high Cr content alloy 15Cr. The line for the rapid quenching $-1200\,\mathrm{K\,min^{-1}}$ is the predicted nucleation behavior from the fitted model, but shows some considerable deviations.

	Input parameters			Fitted parameters				
	$v_{\text{Co-Re}}$ $10^{-6}\,\mathrm{g\,cm^{-2}}$	v_{TaC} $10^{-6}\,\mathrm{g\,cm^{-2}}$	g_{el} $10^{9}\,\mathrm{J\,m^{-3}}$	Γ $\mathrm{J\,m^{-2}}$	Q_N $\mathrm{kJ\,mol^{-1}}$	Q_G $\mathrm{kJ\,mol^{-1}}$	D_N $10^{5}\,\mathrm{m^2\,s^{-1}}$	D_G $10^{5}\,\mathrm{m^2\,s^{-1}}$
TaC09	6.96	6.65	736	0.55	270	365	5.0	1.5
15Cr	6.96	6.65	736	0.57	307	296	5.2	2.1

TABLE 7.2.4: Simultaneous fitted values for several cooling rates ϕ of surface tension Γ, activation energy for nucleation Q_N and growth Q_G.

of the phase transformation for high cooling rates ϕ. (2) The phase transformation is limited by the diffusional growth of precipitates. The growth is a function of time and therefore the higher cooling rates result in smaller growth.

Table 7.2.4 shows the fit results for TaC09 and 15Cr alloy from the adapted KWN model. The datasets for each alloy were fitted simultaneously to the data from the respective cooling ramps ϕ. The difference in precipitation behavior is therefore only depending on ϕ, which is a parameter for particle growth and nucleation rate (eqs. (3.61), (3.56)). A larger ϕ results in less time for particle nucleation and growth and therefore the matrix is stronger supersaturated at lower temperatures. Fig. 7.2.18 presents the predicted final precipitate size distributions in both alloys. The mean particle sizes are in the range of $10-200\,\mathrm{nm}$ with larger sizes for slower cooling rates.

The data from rapid quenching $\phi = -1200\,\mathrm{K\,min^{-1}}$ was excluded for the fit, since the model could only qualitatively reproduce its nucleation behavior.

7.2.5 Discussion

The neutron fast measurements were able to determine the onset $T_{on}^{\downarrow}$ and end temperature $T_{end}^{\downarrow}$ of precipitation as a function of the applied cooling rate. The SANS fast measurement results show that the TaC precipitation occurs directly after and during the Co-Re transformation $\gamma \rightarrow \epsilon$. The fact that the Co-Re phase transformation occurs earlier in Cr containing alloys, followed by TaC precipitation at higher temperatures is a strong evidence that the transformation induces the precipitation. Co is known to have a low stacking fault energy

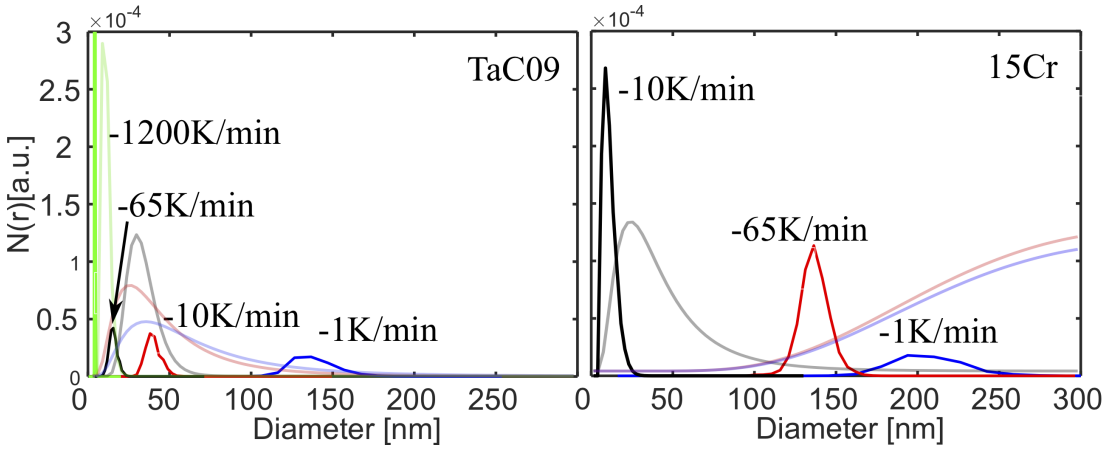

Figure 7.2.18: Predicted size distributions by the adapted KWN model for TaC09 (left) and 15Cr alloy (right). In addition, the measured size distributions from SANS and SAXS (cf. Fig. 7.2.12) are transparently highlighted. The calculated distributions are generally more narrow, but the mean particle size is reproduced for the cooling rates $\phi = -1, -10, -65\,\mathrm{K\,min^{-1}}$. The model yields a very narrow size distribution for the rapid quenching $-1200\,\mathrm{K\,min^{-1}}$.

[123] and therefore the Co-Re phase transformation introduces defects and grain boundaries where the TaC precipitates can nucleate.

The adapted KWN model yields the activation energies for nucleation and growth and reproduces the general behavior that for the smaller cooling ramps the distributions have a higher width and particles grow to larger sizes. This is an expected result, since the slower cooling rates leave more time for particle growth. The model is able to reproduce the creation of precipitating nuclei, which depends on a time lag in eq. (3.56). Therefore, the fast cooling ramps show undercooling before considerable volume fractions are precipitated. Moreover, the growth is diffusion limited and therefore also depending on the time. Therefore, the growth starts at lower temperatures for faster cooling ramps, when the chemical driving force gets larger due to the temperature depending supersaturation of the matrix.

The mean sizes are in the same order as the measured distributions by SAS after the cooling but have a narrower width (Fig. 7.2.18). For the fastest cooling ramp $-1200\,\mathrm{K\,min^{-1}}$, there were some considerable deviations and therefore it was excluded from the fit. Several reasons are possible for this deviation. Firstly, the alloy temperature was measured by a spot-welded thermo couple on the alloy surface. For such high temperature ramps it is, however, likely that there is a strong temperature gradient in the alloy. Moreover, the precipitation is influenced by the kinetics of the alloy matrix transformation $\gamma \rightarrow \epsilon$-Co during cooling, which was not yet studied for such quick ramps.

There are limitations to the model. The TaC precipitate size is also strongly depending on the cooling rate. As shown in section 7.1, the coarsening of nano-sized TaC precipitates occurs on a time scale of $10 - 60\,\mathrm{min}$, depending on the exact temperature and therefore plays a role during the cooling experiments. The slow ramps $-1, -10\,\mathrm{K\,min^{-1}}$ result in considerable coarsening of the precipitates, since the phase transforms at $\sim 1500\,\mathrm{K}$. This was neglected in the current model.

In addition, a coherence relationship of the fine TaC precipitates to the ϵ-Co matrix was proposed in section 5.4.3. Small precipitates are likely to nucleation coherently in order to reduce their surface energy. During the growth of the precipitate, the introduction of misfit

dislocations into the interface is readily observed to reduce the misfit energy. The applied model for the induced elastic strain energy from the particle in the matrix expects fully coherent, spherical precipitates and neglects dislocation effects. In reality, the embedding might be anisotropic, i.e. the particles are semi-coherent to the matrix.

Since the Co-Re phase transformation occurs in the same temperature interval, TaC nucleation and growth might by influenced by the introduction of lattice defects and boundaries. The induced defects can act as nucleation sites in the matrix and the assumption of homogeneous nucleation might be questionable. In this case, the nucleation is heterogeneous which results in smaller nucleation barriers. The matrix transformation is quick and complete in 15Cr alloy (cf. Fig. 7.1.4) and sluggish and incomplete in TaC09 alloy. Therefore, the assumption of homogeneous nucleation is more likely justified in 15Cr alloy than in TaC09 alloy. The activation energies for growth, however, are in a similar size range as the determine activation energies for diffusion (table 7.1.1), supporting the assumption of diffusion limited growth.Moreover, the fits are very sensitive to the experimentally determined equilibrium solubility of TaC phase in the Co-Re matrix. Therefore, the results have to be considered within the accuracy limits of ND for a peak from volume fraction in the order of $\sim 2\%$.

Chapter 8

High Temperature Creep Performance in Co-Re-Ta-C Alloys

Important factors for HT creep resistance in Co-Re alloys include (1) precipitation hardening by semi-coherent and incoherent TaC precipitates (cf. chapter 5), (2) solid solution strengthening due to the Co-Re matrix, (3) second phase (composite) hardening by σ-phase, depending on its extent of refinement and (4) grain boundary strengthening by B addition. Factor (2) is a given from the different radii of the Co and Re atoms in the Co-Re matrix. It might be depending on the degree of Co-Re matrix transformation in ϵ- and γ-Co phase, since they can exhibit elemental partitioning into Re-rich and poor areas. (3) and (4) were investigated in [35, 36].

In this chapter, the influence of carbon content and subsequent creep resistance due to the Orowan strengthening effect by nano-scaled TaC precipitation is investigated in the Co-Re-Ta-C system. Such precipitates generally have a strong effect on the alloy dislocation creep strength at elevated temperatures. The experiments were performed with an in-situ dilatometer during a synchrotron diffraction experiment (cf. section 4.4.4) at 1373 K at constant stress of 50 MPa (Fig. 8.0.1). The TaC alloys TaC05, TaC09, TaC10 were studied. Such experiments simultaneously yield the creep curve and phase fractions within the alloy. Therefore, one gets valuable information on the amount of strengthening TaC precipitates at HT and the evolution of other present phases in the alloy. The experiments were performed with hard synchrotron radiation with an energy of $E = 100$ keV for a sufficient penetration depth of the alloy and a high time resolution in the 1 s range. The samples had a cylindric geometry with 4 mm diameter and 8 mm length.

From ND experiments, it is known that the Co-Re matrix is present as a mixture of γ_m/ϵ-Co phase with metastable γ_m-Co phase in initial ST condition (cf. section 5.2). Upon heating to 1373 K, the matrix transforms $\gamma_m \rightarrow \epsilon$ over time. The transformation is quicker and more complete for higher C/Ta ratio. The SANS results showed a stable population of nano-scale TaC precipitates of $0.67 - 1.24$ vol.% during holding the temperature for 15 h at 1373 K. The TaC volume fraction is highest for TaC10 and lowest for TaC05 alloy and therefore depending on the C content in the alloy. In order to avoid interfering effects, the alloys were deliberately kept free of Cr to avoid second phase (Cr-carbides and σ) formation.

The following results are partly published in [124].

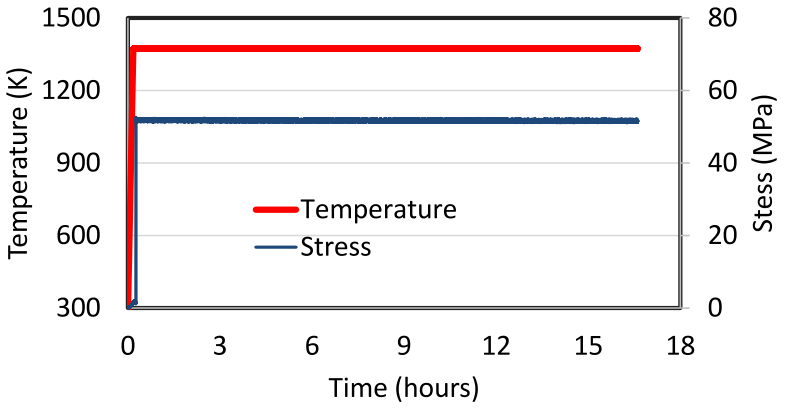

Figure 8.0.1: The samples were heated to 1373 K and a stress of 50 MPa was applied for the creep experiment. During the treatment, in-situ diffraction measurements with synchrotron radiation probed the phase evolution in the samples.

8.1 Fundamentals of a Creep Experiment

Upon applying load on a sample, there is an elastic, instantaneous response, followed by a time-dependent period of thermally activated plastic deformation, the *creep* deformation [38, 125]. For materials that are utilized at HT and under high load, a good creep resistance is vital in order to guarantee a sufficient life time and to prevent failure.

Experimentally, the creep behavior can either be investigated by measuring the material's strain ε at constant load F or constant stress σ over time t. For certain time intervals, ε often follows a relation according to

$$\varepsilon \sim t^m \quad . \tag{8.1}$$

Usually, the creep can be separated into several regions with changed behavior over time, the primary, secondary and tertiary creep. During the primary and secondary creep zone, dislocations glide within the matrix phase. The dislocations are accumulated within the matrix and deposited at grain and precipitate boundaries. The exponent of eq. (8.1) is usually $m < 1$ in the primary region and strain hardening predominates in the alloy. In the end of this region, the creep rate comes to a minimum and the secondary region begins. Dislocation glide and climb processes occur in the matrix and their generation and annealing is near equilibrium. In this so called steady-state creep region, the material strength is nearly conserved and $m \approx 1$. Over time, crystal defects such as voids and cracks begin to accumulate at grain boundaries or within the grains. In this period, the tertiary creep zone, the deformation towards rupture is accelerated and the rate of creep rapidly increases. The exponent of eq. (8.1) can become $m > 1$ and finally the material fails. Fig. 8.1.1 displays a typical creep curve and the associated stages of deformation.

The time derivative of the strain curve, $d/\mathrm{d}t\ \varepsilon(t) = \dot{\varepsilon}$, yields the creep rate. It is usually assumed that the creep is a consequence of the atomic mobility and related to their diffusion. Therefore, the creep rate is assumed to be driven by an Arrhenius type activation energy in the steady-state region. The Norton creep law [39, 126] yields

$$\dot{\varepsilon} = A\ L \left(\frac{\sigma}{E(T)}\right)^n \exp\left(\frac{-Q}{RT}\right) \quad , \tag{8.2}$$

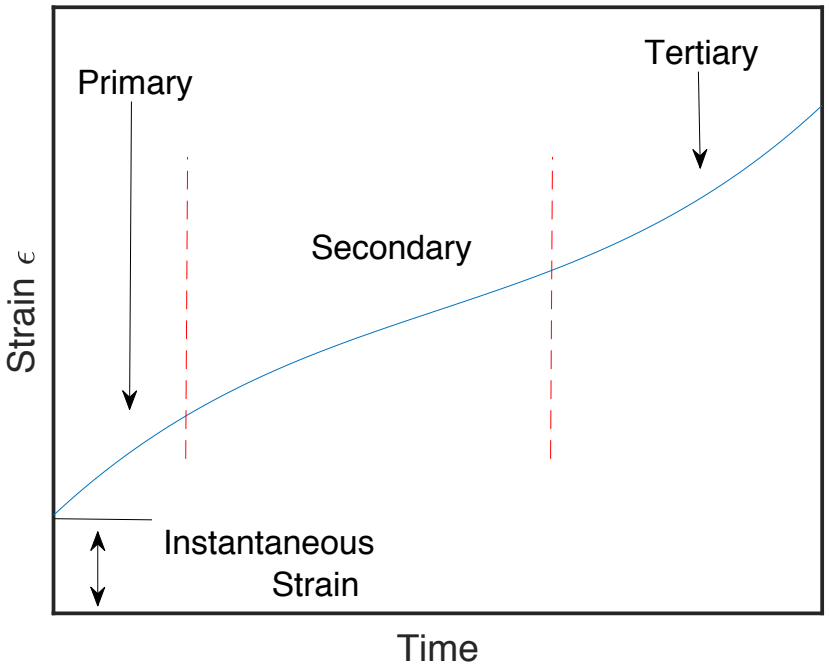

Figure 8.1.1: Schematic of a creep curve vs. time. The different creep regions are depicted.

where $\dot{\varepsilon}, A, \sigma, n, Q$ are creep rate, a material dependent constant, the applied stress, the creep stress exponent and the activation energy of creep. $E(T)$ is the temperature dependent Young's modulus. Depending on the strengthening mechanism, L is related to the precipitate distance or the inverse grain size. The stress exponent n yields information on the type of creep. If the stress is high, creep is usually controlled by the movement of defects and dislocations. A previously investigated Co-Re-Cr alloy showed a creep exponent of $n = 2.7$ at 1373 K [35]. For Ni- and Co-base superalloys with a γ/γ' microstructure, a power-law creep regime with exponents of $n \geq 4$ is readily reported [1, 125, 127–129]. For stresses $\sigma \leq 10^{-3}G$ dislocation creep is active. Dislocations and defects reorder and climb by a diffusion activated mechanism in order to reduce strain and activate recovery of the crystal structure. If strengthening precipitates coarsen at HT, their distance L increases as well. This results in an acceleration of the creep rate. Therefore, small precipitate coarsening rates and high volume fractions are important for creep resistance.

The strain-rate has a minimum value of $\dot{\varepsilon}_{\mathrm{min}}$ in the beginning of the steady-state region

$$\dot{\varepsilon}_{\mathrm{ss}} = \dot{\varepsilon}_{\mathrm{min}} \quad . \tag{8.3}$$

Applying the logarithm to eq. (8.2) yields

$$\log \dot{\varepsilon}_{ss} = \log A + \log L + n(\log \sigma - \log E(T)) - \frac{Q}{RT} \quad . \tag{8.4}$$

Therefore, iso-stress tests at varying temperatures can be applied to determine the activation energy of coarsening Q (i.e. multiple tests with constant σ and varying T) [130]

$$Q = -R\left(\frac{\partial \log \dot{\epsilon}_{ss}}{\partial(1/T)}\right) - nR\frac{\mathrm{d}\log E(T)}{\mathrm{d}(1/T)} = -R\left(\frac{\partial \log \dot{\epsilon}_{ss}}{\partial(1/T)}\right) - nR\frac{T^2}{E}\frac{\mathrm{d}E}{\mathrm{d}T} \quad . \tag{8.5}$$

Alloy	C at.%	ε at $15h$ [%]	Time to 1%	$\dot{\varepsilon}_{ss}[10^{-6}s^{-1}]$
$y = 0.5$	0.6	0.269	10:54 h	2.14
$y = 0.9$	1.04	0.253	7:21 h	3.42
$y = 1.0$	1.2	0.035	12:43 h	1.74

TABLE 8.2.1: Effect of different carbon content on creep behavior.

Log-linear plots of $\dot{\varepsilon}_{ss}$ vs. $\frac{1}{T}$ from multiple experiments with varying T yield the activation energy for creep Q.

8.2 High temperature creep behavior of Co-Re-Ta-C alloys

Previous studies showed that Co-Re alloys containing Cr and B have reasonable creep resistance [35, 36]. For effective strengthening, the C/Ta ratio is a crucial parameter, since it influences size and volume fraction of fine TaC precipitates (cf. section 5.3) and therefore changes the Orowan stress.

Creep curves were recorded during the in-situ synchrotron experiment for varying C/Ta ratio alloys TaC05-TaC10 with the in-situ dilatometer (cf. section 4.2). The creep strain $\varepsilon(t) - \varepsilon_0$ curves after the elastic response from the sample ε_0 and strain-rates $\dot{\varepsilon}(t)$ at 1373 K with 50 MPa are shown in Fig. 8.2.1. A primary and secondary creep region can be observed. The secondary region shows a nearly linear increase of the logarithmic strain-rate in the interval $\sim$ 5 h to 15 h of the experiment. Afterwards, there is a stronger increase of the strain-rate and the beginning of the tertiary creep region. The experiments were stopped at strains of $\sim 20\%$.

Fig. 8.2.2 presents the creep deformation behavior during loading at HT in the representation $\dot{\varepsilon}$ vs. true creep strain ε. The curves have a minimum at ε and $\dot{\varepsilon}$ that approximately corresponds to the creep strain in the end of the primary creep regime. ε varies with the C/Ta ratio in the three investigated alloys. TaC05 alloy has a minimum $\dot{\varepsilon}$ for $\varepsilon = 0.06$, while TaC09 and TaC10 have $\varepsilon = 0.22$. The minimum values of $\dot{\varepsilon}$ are in the range of $\dot{\varepsilon} \in [1.74, 3.42]$ and are compared in table 8.2.1. The time to 1 % deformation is longest for the TaC10 alloy and shortest for the TaC09 alloy. Interestingly, there is no obvious (i.e. linear) dependence on the C content.

The steady-state creep rate ε_{ss} was compared with an ex-situ creep test at 1273 K at the same stress $\sigma = 50$ MPa in TaC05 alloy [49]. By means of eq. (8.5), the activation energy of creep was roughly approximated. The temperature dependence of Young's modulus $\mathrm{d}E/\mathrm{d}T$ was approximated with a data set from the Ni-base superalloy CMSX-4 in [131] that yields $\mathrm{d}E/\mathrm{d}T = -48.6\,\mathrm{MPa\,K^{-1}}$. The activation energy of creep is then approximated with

$$Q = -R\left(\frac{\partial \log \dot{\epsilon}_{ss}}{\partial(1/T)}\right) - 2.7 \cdot R\,\frac{T^2}{E(300\,\mathrm{K}) + \Delta T \mathrm{d}E/\mathrm{d}T} 48.6\,\mathrm{MPa} = \begin{cases} 470\,\mathrm{kJ\,mol^{-1}} - 7.4\,\mathrm{kJ\,mol^{-1}}, & T = 1273\,\mathrm{K} \\ 470\,\mathrm{kJ\,mol^{-1}} - 8.8\,\mathrm{kJ\,mol^{-1}}, & T = 1373\,\mathrm{K} \end{cases} \tag{8.6}$$

for the TaC05 alloy. The Arrhenius-type plot for the determination of the first term is depicted in Fig. 8.2.3. The derived value for the activation energy of creep $Q \approx 462\,\mathrm{kJ\,mol^{-1}}$ are in a realistic range. However, its determination by only two data sites denotes it to large

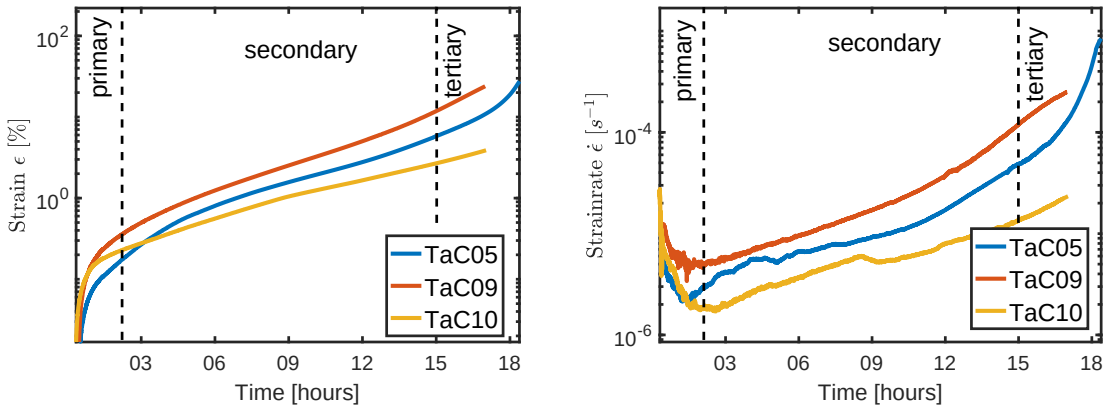

FIGURE 8.2.1: Creep strain (left) and strain-rate over time (right) of the three alloys. The primary region, followed by a secondary region with near constant increase of the strain-rate can be seen. The transition to tertiary region is different in the three alloys an starts after $\sim 15\,\mathrm{h}$, where the strain-rate is starting to exponentially increase.

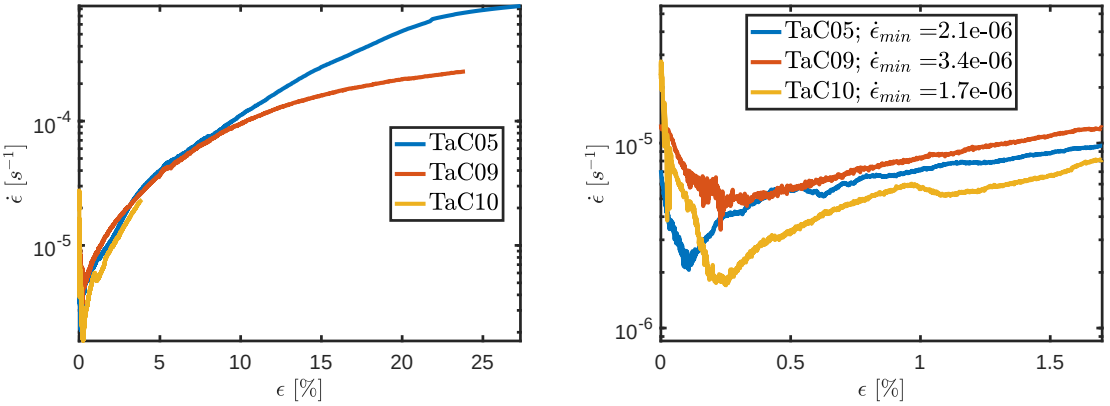

FIGURE 8.2.2: Strain-rate vs. strain. (left) strain-rate during the whole experiment up to very high strains $\varepsilon > 5\%$; (right) zoom of the primary and secondary region.

errors. In addition, a more accurate value for the temperature dependent Young's modulus $E(T)$ would be beneficial. Therefore, it has to be considered within this limitation.

8.3 Phase evolution during the experiment

Fig. 8.3.1 shows the $2D$ diffraction patterns from TaC05, TaC09 and TaC10 alloys during the in-situ creep experiment at the HEMS synchrotron beamline at Petra III (cf. section 4.3.5). In initial ST condition, the intensity pattern is quite spotty. The reason for this type of pattern is twofold: Firstly, the low crystal statistics recorded by the small synchrotron beam cross section. Due the high X-ray absorption of Re only a part of the outer side of the sample cylinder with smaller thickness was irradiated. Therefore, only a very small volume was probed. Secondly, the strong spots are mostly present on Debye-Scherrer rings related to γ-Co phase. This represents the nature of the Co-Re matrix observed by microscopy (cf. section 5.1). The matrix consists of ϵ-Co laths in sub micron size range and large areas of untransformed γ_m-Co phase, i.e. the metastable γ-Co phase at RT.

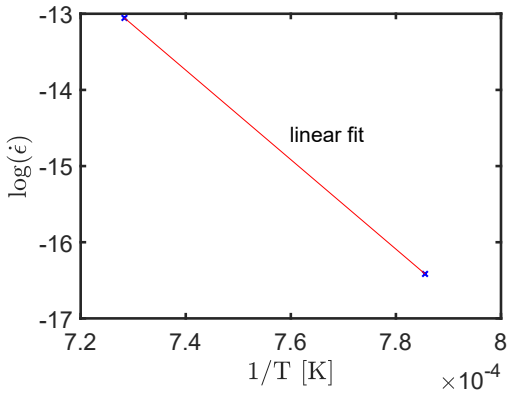

Figure 8.2.3: Comparison of steady-state creep rate ε_{ss} in an Arrhenius type plot. The slope yields the activation energy of creep.

It can be seen that over the course of holding at 1373 K under load, the spots from γ-Co phase start to decrease. From the ND experiments (cf. section 5.2), it is known that the γ-Co phase should almost completely transform to the thermodynamically stable ϵ-Co phase after few hours at this temperature. However, in the alloys under load, such a behavior is not observed. Although the intensity of the phases varies, the most prominent change is a refinement of the γ-Co crystallites (i.e. the strong spots decrease) over the course of the creep experiment. The diffraction signal from γ-Co phase is always present with considerable strength in all three samples.

The evolution of phases in the alloys has been evaluated from the in-situ recorded diffractograms. The strongest spots on the $2D$ patterns were masked because they only represent a small amount of the sample and overshoot the pattern with their very high intensity. Then, the data was azimuthally averaged. Fig. 8.3.2 shows the 2700 $1D$ diffractograms from TaC10 alloy in a $3D$ representation of 2θ and time t. It can be seen that all initially present phases, γ, ϵ and TaC, produce Bragg reflections. During heating and directly after applying load – at the beginning of the experiment – there are some stronger changes of the peaks. The γ-Co phase is almost constantly present throughout the 16 h of holding at HT. This is a completely different result from in-situ ND, where the matrix almost completely transformed into ϵ-Co phase at 1373 K without load (cf. section 5.2).

In order to further quantify the results from the three investigated alloys, they are depicted as a contour plot time t vs. scattering angle 2θ in Fig. 8.3.3(left). The ratio of γ/ϵ-Co phase differs in the three alloys and slightly varies over the course of the experiment. In addition, the TaC (111) peak is visible in the zoom, presented in Fig. 8.3.3(right). A correction treatment was applied to account for the changing sample volume in the beam due to the creep deformation for these patterns. The cylindrical Co-Re samples expand in diameter over time due to the applied compression and sample deformation. However, this results in an increase of Co fluorescence, which expands towards the first peak of the diffractogram from TaC, which cannot be corrected for.

It can be seen, that the TaC phase has some strong changes at the beginning of HT hold. After reaching HT, a strong increase of the TaC peak as a result of precipitation is observed. This was also observed by SANS (cf. section 5.3). It could not be deduced for certain if the strong decrease of TaC phase afterwards is a real effect or a result of the applied correction

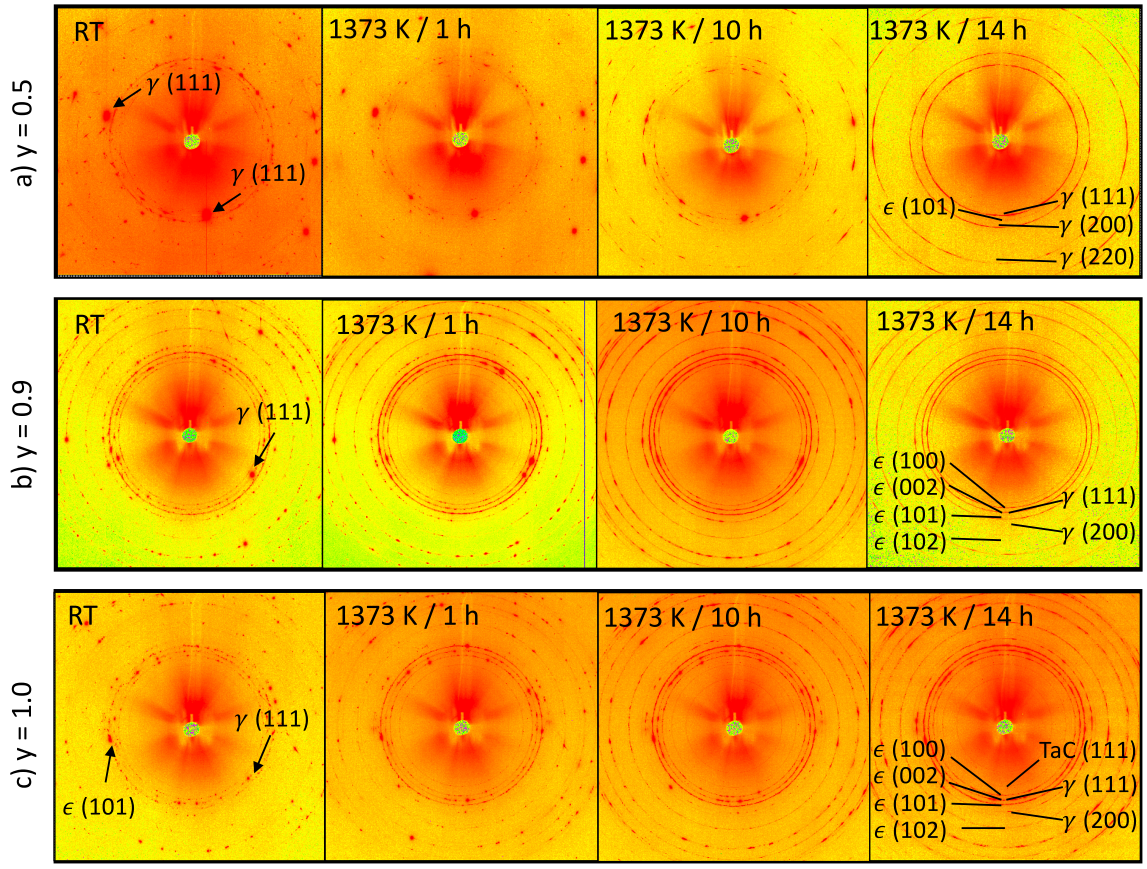

Figure 8.3.1: Evolution of 2D diffraction patterns from (a) TaC05, (b) TaC09 and (c) TaC10 alloys during the in-situ experiment. Due to the limited grain statistics of the method, the patterns are spotty in the beginning. The refinement of grains during the experiment improves the number of grains in the synchrotron beam.

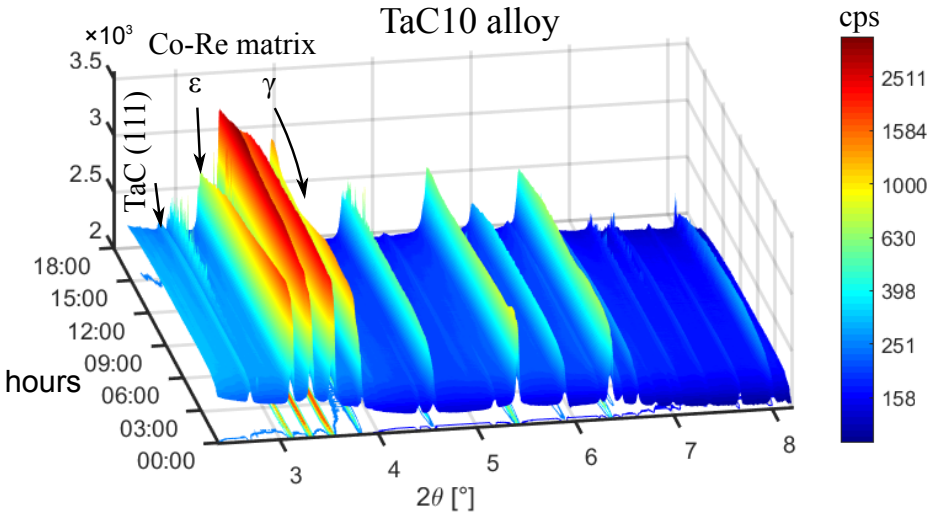

Figure 8.3.2: Diffraction patterns during the $18h$ in-situ creep experiment in TaC10 alloy. It can be seen that the ϵ-Co reflections slightly change in relative intensity. The TaC peak is visible at $\sim 2.7°$.

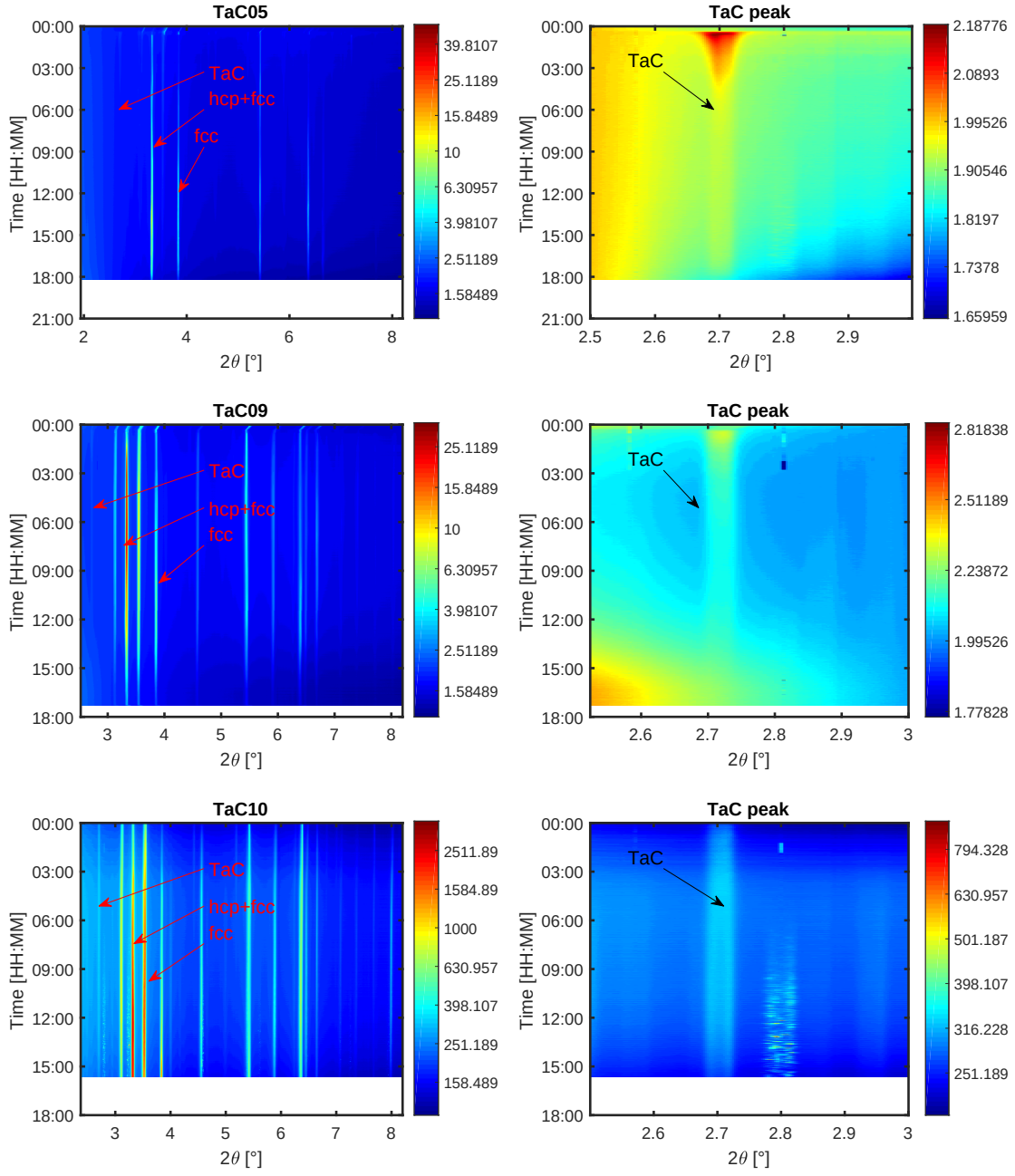

Figure 8.3.3: (left) Contour plots of the total diffracted intensity of TaC05, TaC09 and TaC10 alloy. Several peaks of hcp and fcc Co phase are visible and the strongest were marked by arrows. It can be directly seen that the phase content of fcc is stronger for lower C content alloys. (right) Zoom in the low angle range where the strongest TaC peak is situated. The TaC peak intensity strongly increases during heating and then slowly drops in TaC05 and TaC09 alloy in the first 5 h of the experiment. Next to the TaC peak, the TaC10 alloy contains a parasitic (unknown) reflection that was masked for the Rietveld refinement.

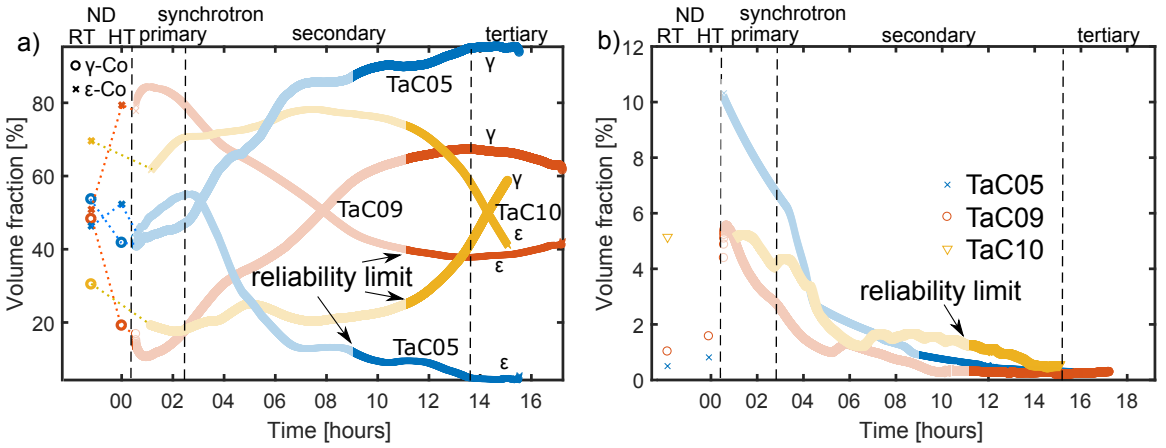

FIGURE 8.3.4: Results from Rietveld refinement of the synchrotron diffraction patterns of TaC05, TaC09 and TaC10 alloy. Phase fractions of ϵ-Co and γ-Co phase (left) and TaC (right) are shown. The first two data points at RT and HT without load were taken from the ND measurements (cf. section 5.2) because they are considered more reliable. Synchrotron data is considered fully reliable after ~10 h. The approximate transition area of the primary and secondary creep regions in the different alloys are marked by vertical lines. All alloys contain a higher amount of ϵ-Co phase that transforms towards γ-Co phase during the heat treatment. Lower C content alloys transform faster. The TaC content is not reliable in the first ~10 h, because the masking of ϵ/γ-Co spots overestimates the TaC contents in the beginning.

treatment. Since the Co-Re peaks are very spotty in the beginning, not all of their intensity is recorded, which results in a biased relative peak intensity. Additionally, less intensity is transmitted due to increasing sample volume in the beam, lowering the visibility of weak peaks such as from the TaC phase. Due to these limitations, the phase fractions in TaC05 alloy are reliable only after $\sim$ 10 h of holding.

The evolution of the phase fractions from the three phases ϵ, γ-Co and TaC phase is presented in Fig. 8.3.4(left). The values were obtained by a sequential Rietveld refinement of the $\sim$ 2700 recorded data files. The first data point originates from the measurement in initial ST condition at RT. The following points are taken directly after application of the load 50 MPa at 1373 K The occasionally observed fluctuations of the data points arise from numerical instabilities in the fit due to the changing spots in the $2D$ patterns. The strong, masked spots sometimes slightly move out of the mask during the creep experiment.

All samples have a higher amount of ϵ-Co phase in ST condition. However, the amount is higher for higher C content. During the experiment, the amount of ϵ-Co phase first increases at HT, but decreases after some time again until finally the amount of γ-Co phase exceeds the one of ϵ-Co. The higher the amount of C, the later increases the amount of γ-Co phase. This result is consistent with the fact that unbound Ta in the matrix is a fcc stabilizer and therefore stabilizes γ-Co phase (cf. section 5.4.1).

The refined TaC volume fractions constantly drop during the experiment and are very large in the beginning of the experiment. After 14 h the refined volume fraction is essentially zero in all of the alloys.

8.4 Discussion

There are two main effects, that influence the creep rates in the secondary region. The $2D$ diffractograms show that granularity of the Co-Re matrix is very different in the three alloys. The pattern from the TaC05 alloy shows strong spots in the γ-Co phase from large grains. These spots are present in all three alloys, but fewer in the TaC10 alloy and even less pronounced in the TaC09 alloy. In diffusion creep processes, the grain size has a strong influence on the creep strength. Secondly, the XRD and SANS experiments have shown that a higher amount of γ-Co phase results in a lower amount of strengthening TaC precipitates (cf. section 5.2, 5.3). These precipitates are important for the dislocation creep strength.

According to SANS the alloy with the highest amount of nano-scale precipitates is the TaC10 alloy, which shows the best creep strength in the present study. On the other hand, the TaC09 alloy has almost the same amount of precipitates but is apparently the weakest alloy. Here, the $2D$ diffractograms show that the matrix grains are the most refined in initial state, suggesting a dependence thereof.

Remarkably, the diffraction experiments show that the γ-Co phase content is higher in the end of the creep experiments than in the beginning, which is not the case if the alloy is not under stress. Therefore, the applied load seemingly changes the equilibrium state of the Co-Re matrix phase. During the primary and steady-state creep period, dislocations typically glide within the ϵ/γ-Co-Re matrix. The strain stores a large amount of energy in the matrix which can activate the Co-Re $\epsilon \leftrightarrow \gamma$ phase transformation. As a consequence, the formation of subgrains in the form of laths has been reported in the ϵ-Co phase [132]. In addition, the vanishing of strong spots on the diffraction pattern suggest a grain refinement mechanism. This result shows that the microstructure of the Co-Re-Ta-C alloys constantly changes during the creep experiment and is inherently unstable under load. Possible reasons for this behavior are discussed in the following.

In ST condition, the microstructure in Co-Re-Ta-C alloys consists of a lath structure of ϵ-Co phase and larger areas of untransformed γ/-Co grains (cf. section 5.1). This finding is similar to pure Co alloys and the lath structure is caused by the very low stacking fault energy of the Co matrix ($27 \pm 4\,\mathrm{mJ\,m^{-2}}$) [123]. The transformation $\gamma \rightarrow \epsilon$ is achieved by shear transformation by partial dislocations [133]. This transformation is quite sluggish and metastable γ_m-Co phase is easily retained at RT. Due to the transformation, Shockley partials and stacking faults are introduced inside the ϵ-Co phase [134]. The reported dislocation slip systems in pure Co are [25, 125, 133]

$$\begin{aligned} \gamma : \frac{a}{2}\langle 1\bar{1}0\rangle\{111\} \quad & \text{with partial slip} \quad \frac{1}{6}\langle 112\rangle \quad , \\ \epsilon : \text{basal slip}\langle 11\bar{2}0\rangle\{0001\} \quad & \text{and prism slip} \quad \langle 11\bar{2}0\rangle\{10\bar{1}0\} \quad . \end{aligned} \tag{8.7}$$

Especially the prism slip is reported to cause subgrain and lath formation and a subsequent increase in misorientation of the subgrains. Under strain, fcc grains can experience a {111} deformation twinning, as an important plastic deformation mechanism [133].

Additionally, Wu et al. [133] reported that larger strain of the matrix can cause a martensitic $\gamma \rightarrow \epsilon$ transformation. They found that this transformation can contribute to a grain

refinement, since the ϵ-Co forms as refined platelets or laths, that introduce grain boundaries in the γ-Co phase and the slip in γ-Co phase is accompanied with a martensitic phase transformation $\gamma \rightarrow \epsilon$.

Similar transformation mechanisms are suggested by the current diffraction results and from microscopy for Co-Re-Ta-C alloys (cf. Fig. 5.1.1). The lath structure of the matrix is likely induced by a martensitic transformation. On the one hand, there is a refinement of matrix grains as a result of the transformation. On the other hand, the subdivision of grains into ϵ-Co laths introduces grain boundaries and new orientations, since the transformation can occur along the four close packed planes in the γ-Co (fcc) structure. In addition, ϵ-Co martensite and twin boundaries can significantly block dislocation slipping, enhancing strain hardening and ductility of Co-alloys [25]. It is likely that the initial strength of the investigated Co-Re-Ta-C alloys benefits from a similar effect.

The strong spots on the $2D$ diffractograms show that the grains are rather coarse in the beginning of the creep test. The Rietveld results reveal that the amount of ϵ-Co phase is still increasing in this stage (Fig. 8.3.4). In the secondary region, the strain-rate linearly increases on the logarithmic scale, showing that the microstructure is changing. The increasing strain-rate shows that there is a microstructural instability in this region. A similar creep behavior is known from Ni-base superalloys, where the stress can form anti-phase boundaries in the γ/γ' microstructure and dislocation structures are constantly evolving. As a result, the creep strength changes over time resulting in a power law creep with $n > 3$ [135, 136].

In the present alloys, the microstructural instability is most likely caused by the precipitate coarsening at 1373 K (cf. section 7.1), which reduces the creep strength over time and by the decreasing TaC content. The phase content decrease is likely a result of the lower TaC stability in the transforming γ-Co phase (cf. section 5.4.1). In addition, the diffraction results show that the amount of γ-Co phase starts increasing in the secondary creep region. The diffusional climb of dislocations is already quite high at 1373 K and is seemingly accelerating with the amount of γ-Co phase in the matrix.

After 14 h the refined TaC content is essentially zero which coincides with the strong acceleration of the creep rate (Fig. 8.2.2). The results agree with the previous SANS experiments in the sense that it was shown that nano-scaled TaC precipitates are unstable in γ-Co phase at temperatures $\geq$1373 K (cf. section 5.3).

After $10 - 14$ h of holding strain and temperature, the crystal structure has significantly refined and continuous Debye-Scherrer rings are observed, instead of the initially spotty patterns (Fig. 8.3.1). This stage can be correlated with an acceleration of the creep rate. The formation of stacking faults and microtwins due to the matrix transformation induces a high amount of SFs and partials and store a high amount of energy in the matrix and the matrix easily transforms fine grains $\epsilon \rightarrow \gamma$. In addition, materials with low SF energy (such as Co) can favor the process of dynamic recrystallization (DRX). Paul et al. [137], Kapoor et al. [138] observed DRX in pure Co in the HT γ-Co phase. They reported that DRX initiates after a certain amount of work W_c was done on the matrix up to a critical strain ε_c. They performed tests up to temperatures 1373 K, where DRX was found for stresses as low as $\sigma = 60$ MPa. Therefore, DRX might also be present in the Co-Re-Ta-C matrix, initiated at $\sigma = 50$ MPa at 1373 K. The accumulated dislocations could start healing within the γ-Co phase and cause a considerable softening of the alloy in the end of the creep test.

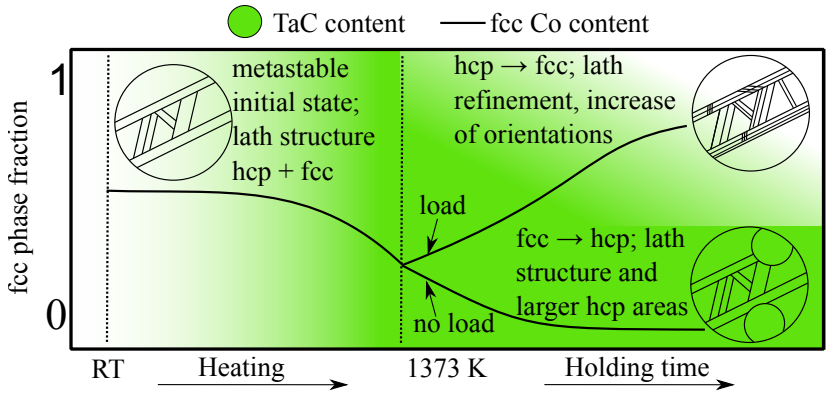

FIGURE 8.4.1: Behavior of Co-Re-Ta-C alloy during heating and compression creep experiment. During heating metastable γ-Co phase (fcc) transforms to ϵ-Co phase. A strain induced transformation of the Co-Re matrix at HT introduces boundaries from transformed laths. This results in a grain refinement.

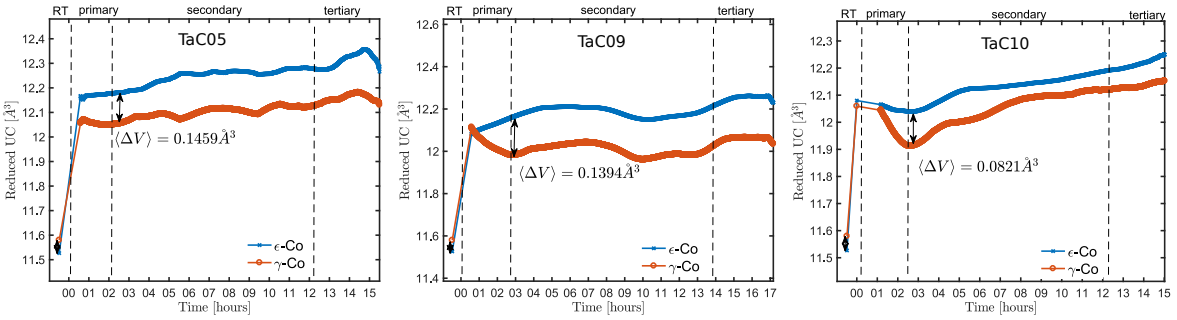

FIGURE 8.4.2: Volume of the ϵ- and γ-Co unit cell per number of atoms. The first data point represents ST condition at RT. The stress $\sigma = 50\,\mathrm{MPa}$ is applied after heating. The mean UC volume change due to the transformation is marked.

The different stages of microstructural changes during creep are schematically depicted in Fig. 8.4.1.

The fact that the γ/ϵ-Co phase fraction strongly differs from ND experiments without load might be explained by the different unit cell (UC) volumes of the two phases. The UC volume was evaluated from the measured lattice constants in the experiment and is presented in Fig. 8.4.2. AT RT, the UC of γ-Co phase is slightly larger than the ϵ-Co UC. During the HT creep experiment, however, the UC of ϵ-Co increases and exceeds the γ-Co UC by $\Delta V \approx 0.1\,\mathrm{Å}^3$. This happens already in the beginning of the primary creep region. Although there are fluctuations in the UC volume, the distances between the volumina of both phases $\langle \Delta V \rangle$ are nearly constant after they reach their maximum. The enthalpy change ΔH from the volume work W due to the phase transformation induced mean shift of UC volumes is calculated for the alloys TaC05, TaC09 and TaC10 according to

$$\begin{aligned} \Delta H &= \int_{V_1}^{V_2} \sigma \cdot \mathrm{d}V = \Delta V \sigma \quad , \\ \Delta H_{05} &= 0.014\,59\,\mathrm{nm}^3 \times 50\,\mathrm{MPa} = 12.114\,\mathrm{kJ\,mol}^{-1} \\ \Delta H_{09} &= 0.013\,94\,\mathrm{nm}^3 \times 50\,\mathrm{MPa} = 11.574\,\mathrm{kJ\,mol}^{-1} \\ \Delta H_{10} &= 0.008\,21\,\mathrm{nm}^3 \times 50\,\mathrm{MPa} = 6.8167\,\mathrm{kJ\,mol}^{-1} \quad . \end{aligned} \tag{8.8}$$

These values might realistically be in the range to energetically favor the γ-Co phase over the ϵ-Co phase at 1373 K and add to the fact, that the TaC05 alloy transforms faster than the others. However, the transformation $\epsilon \rightarrow \gamma$ is usually accompanied by an elemental partitioning of Co and Re in the different phases due to diffusion. It is known that ϵ-Co laths enrich in Re [20], which causes the lattice constant to increase due to the large Re atoms. Subsequently, there is an influence on the ϵ/γ-Co equilibrium under strain due to the increasing molar volume of ϵ-Co phase, in favor of γ-Co phase. Therefore, the given enthalpy values are likely overestimated. The effect could result in a peak splitting of the XRD patterns, but due to the very spotty patterns, the peak resolution is not sufficient to conclude on this hypothesis.

Chapter 9

Summary and Conclusions

This thesis comprehensively characterizes the TaC precipitate kinetics in Co-Re alloys for applications at temperatures $> 1400\,\mathrm{K}$. The TaC precipitates are present in form of finely dispersed particles with a size $< 100\,\mathrm{nm}$ and are used as a main strengthening mechanism in the alloy. SANS and ND were applied to investigate their high temperature stability *in-situ*. Moreover, the influence of Cr and B additives on the Co-Re matrix and TaC precipitates was studied. Complementary results were obtained by microscopy and XRD.

9.1 Summary of the main results

(i) The Co-Re matrix phase exhibits an allotropic transformation $\gamma \leftrightarrow \epsilon$-Co phase at temperature $> 1400\,\mathrm{K}$ and shows a hysteresis of $\sim 100\,\mathrm{K}$ when cooling. Depending on the Cr content in the matrix, metastable γ-Co phase is retained at RT.

(ii) The interplay between the allotropic Co-Re phase transformation and TaC precipitation was investigated. An effective strengthening of the Co-Re matrix by TaC precipitates is only possible if the matrix is present in form of ϵ-Co phase. A lower C content in the matrix results in a higher amount of freely dissolved Ta in the matrix, which stabilizes the γ-Co phase.

(iii) The available C content influences the maximum volume fraction and the size distribution of TaC precipitates at high temperatures. A higher C content results in a higher TaC precipitate volume fraction and a smaller inter-particle distance of the particles.

(iv) A coherence relationship between TaC precipitates and ϵ-Co matrix was deduced from diffraction experiments A lattice misfit of < 2.73 % was found. Therewith, an elongated morphology and their orientation relationship to the Co-Re matrix of some TaC precipitates could be explained.

(v) The addition of B lowers the $\epsilon \rightarrow \gamma$-Co phase transformation temperature. In addition, it has a negative influence on the TaC coarsening rate and their volume fraction in the matrix.

(vi) The addition of Cr to the Co-Re matrix stabilizes the ϵ-Co phase to temperatures $> 1500\,\mathrm{K}$ and suppresses formation of metastable γ-Co phase at room temperature. This also lowers the TaC precipitate coarsening rates.

(vii) The activation energies of coarsening were evaluated in the system Co-Re-Ta-C for varying C/Ta ratio and under the influence of Cr and B addition. This allows the determination of the diffusion coefficients of Ta in the Co-Re matrix and the influence of minor additives. It was found that Cr lowers the coarsening rates, while they slightly increase when adding B.

(viii) The TaC precipitation during cooling from supersolvus solution was characterized by in-situ SANS. A kinetic model was created and fitted to the model and was capable to evaluate the nucleation and growth activation energies of TaC in the Co-Re matrix.

(ix) A creep experiment at 1373 K during in-situ synchrotron diffraction showed that the phase equilibrium of γ-Co and ϵ-Co phases is changed in the Co-Re-Ta-C system under load. This causes a phase transformation and grain refinement and results in an inherent instability of the alloy matrix.

(x) The calibration of a SANS instrument was comprehensively demonstrated. A novel calibration technique for ^{3}He counter tube detectors was introduced.

(xi) A software package with a large variety for fits of $3D$ models to $2D$ SANS data was developed.

(xii) A model-free reconstruction technique of multidimensional scattering particles from $2D$ SANS data was developed. The method uses a mixed Tikhonov and L_1 regularization technique and is therefore related to elastic net regularization.

9.2 Summary of the chapters and conclusions

Chapter 2 summarizes the main features of Co-Re alloys that were studied in previous publications. The important phases ϵ- and γ-Co, TaC, $Cr_{23}C_6$ and σ phase are described, together with their microstructural features. The TaC phase is present in form of nano scaled precipitates that effectively strengthen the alloy The high and low temperature phases γ- and ϵ-Co and their transformation mechanism is described.

In Chapter 3, the theoretical fundamentals of neutron scattering, in particular ND and SAS and the thermodynamics of high temperature alloys is treated. Several methods for the evaluation of in-situ data from SAS are developed and described. Tools for the evaluation of large amounts of SAS datasets (> 1000) are presented. This includes Guinier based fits and innovative interpretations of Kratky curves.
The data from SAS measurements was evaluated in reciprocal space to extract precipitated volume fractions with high time resolution. A Kampmann-Wagner numerical multi-class model is adapted for the case of isochronal cooling, in order to model the kinetics of precipitation from a supersaturated matrix. Rate equations for the nucleation, growth and coarsening of particles are deduced that can be fitted to the SAS data.

Chapter 4 gives an overview over the used in-situ and ex-situ experimental methods and instruments. SANS, SAXS, ND, laboratory and synchrotron XRD, SEM, EDX and EBSD were applied to study the Co-Re microstructure.

In Chapter 5, the main features of the nano scaled TaC phase is discussed. Their evolution at high temperatures up to 1473 K is studied. In particular, the influence of the allotropic

$\epsilon \leftrightarrow \gamma$-Co-Re matrix transformation on TaC precipitates is treated. It is shown that the available C content influences the maximum volume fraction and the size distribution of TaC precipitates (within 24 h of holding) at HT. The higher C content alloys have the higher TaC precipitate volume fraction and a smaller inter-particle distance. There is a small influence on the coarsening rate of the TaC precipitates. The influence of C content on the coarsening rate of the TaC precipitates is small.
The interplay between the allotropic Co-Re phase transformation and TaC precipitation has a considerable influence on the materials high temperature stability and effective strengthening of the Co-Re matrix by TaC precipitates is only possible if the matrix is present in form of the low temperature ϵ-Co phase.
Moreover, a coherence relationship between TaC precipitates and ϵ-Co matrix with lattice misfit $\delta < 2.73$ % was found. Therewith, the elongated TaC morphology of some TaC precipitates as observed in microscopy could be explained.

Chapter 6 discusses the effect of addition of B and Cr on the Co-Re matrix and the TaC precipitation. It is shown that they influence the temperature of the allotropic Co-Re matrix transformation, that has an influence on the stability of the TaC precipitates. Cr addition pushes the allotropic Co-Re phase transformation to higher temperatures and suppresses retaining metastable γ_m-Co phase at room temperature. This is beneficial for the alloy, since the nano scaled TaC precipitates are only stable in the ϵ-Co phase and a it is vital to prevent any matrix phase transformation during operating the alloy at high temperatures. In addition, no negative influence on the nano scaled TaC precipitates was observed but the precipitate sizes are generally a little larger for higher Cr content alloys. Importantly for the alloy development, neither of the alloys with ≤ 15 at.% show any evidence of unwanted Cr-carbides or σ-phase, in contrast to previously studied alloys with 23at. % Cr content.
On the other hand, the addition of B lowers the Co-Re phase transformation temperature. While the evolution of TaC precipitates at temperatures ≤ 1373 K is almost unaltered, their volume fraction considerably lowers at ≤ 1473 K, due to a partial transformation of the matrix. Therefore, it is crucial to carefully tune the B content in the matrix and to compensate its negative effect on the transformation temperature by adding other ϵ-Co stabilizers (such as Cr).

In Chapter 7, the kinetics of TaC precipitates in Co-Re alloys is studied. The rate constants of coarsening of TaC precipitates in the Co-Re matrix are determined by in-situ SANS measurements at HT. The corresponding activation energies of diffusion limited coarsening are determined, and the required equilibrium solubility of TaC phase in Co-Re is determined by in-situ ND. To the best knowledge of the author, these methods were combined for the first time and they allow the determination of the diffusion coefficients of Ta in the Co-Re matrix and the influence of minor additives. The activation energies for coarsening showed to be comparatively large, which ensures slow coarsening kinetics during high temperature applications.
The nucleation kinetics of TaC in the Co-Re matrix is investigated by means of series of fast in-situ SANS with high time resolution (~ 10 s). It is shown that precipitation of nano scaled TaC precipitates starts directly after or during the Co-Re matrix transformation $\gamma \rightarrow \epsilon$. A kinetic model, based on Kampmann-Wagner theory was adjusted for isochronal cooling and fitted to the measured SANS data. The activation energies for nucleation and precipitate growth were determined by fits of the model to in-situ SANS measurements with varying

cooling ramps. With this method the precipitate nucleation kinetics was directly observed during cooling and theoretically described for the first time.
The kinetics of the nano scaled TaC precipitate phase are therefore widely quantified, allowing to develop effective heat treatments for the alloy and knowledge about the limits of the strengthening TaC phase.

Chapter 8 treats the creep properties of Co-Re-Ta-C alloys, measured with an in-situ dilatometer. The experiments were performed during probing the alloys with synchrotron radiation. Debye-Scherrer rings were recorded from the diffracted synchrotron beam in order to quantify the Co-Re phase content. In initial state, the Co-Re alloys are in a mixed state of γ/ϵ-Co phase. At 1373 K under stress, the matrix grains are refining and start transform to γ-Co phase after $6-12$ h, depending on the C/Ta ratio. This differs from the alloy behavior in thermodynamic equilibrium under zero stress, where the alloy transforms to single ϵ-Co phase. This behavior is attributed to the differing unit cell volumes of both phases, which is slightly smaller in γ-Co phase at 1373 K. Therefore, the phase transformation releases volume work.
Primary, secondary and tertiary creep stages are found in the alloys. However, the mixed γ/ϵ-Co phase state results in several unwanted effects, such as grain refinement and dynamical recrystallization due to the induced strain energy in the matrix. Therefore, it is concluded that the addition of ϵ-Co phase stabilizers are crucial to prevent the matrix transformation and for the creep resistance of Co-Re alloys.

Appendix A explains the used methods to calibrate data from SANS to absolute units. A novel and profound method for calibration of ^{3}He counter tube detectors is presented. The method can deal with pixel shadowing and parallax effects at larger incident angles on the detector by a numerical correction. It is shown that the detector pixel efficiencies can be separated from effects arising from the used instrument geometry. This makes it possible to record an efficiency map at one, well-known geometry and then transforming it to any other geometry.

Appendix B summarizes the used models to fit the present SANS data. A tool for the evaluation of $2D$ and $3D$ models denoted to particle size distributions was developed. In order to get thorough information from the SANS data, an innovative model-free image reconstruction technique for SANS data was presented, based on kernel interpolation in frequency space and B-spline interpolation in real space. Fits of the ill-posed problem were done with L_1 and L_2 Tikhonov-regularization in order to reconstruct the particle size distribution.

9.3 Outlook

Interesting problems arose during the development of this thesis. Due to the involved nature of complexity, their elaboration has not been possible.

(i) The coherence relationship of precipitate to matrix was studied by the indirect method of diffraction. The studies would greatly benefit of a thorough investigation with transmission electron microscopy in order to resolve and confirm the results.

(ii) The precipitation was modeled with a log-normal size distribution of particles. Recent studies successfully incorporated the Ostwald size distribution for SAS measurements

and the modeling, which would be better supported by the theory. A comparison of the results with that kind of size distribution would be interesting.

(iii) The adapted KWN-type model for isochronal cooling was not yet tested for any other problems and could greatly benefit from continuing studies. For example, the step sizes for numerical integration during cooling are the main limiting factor for performance on the one hand but also for accuracy of the model on the other hand. At the moment they are chosen heuristically.

(iv) The influence of B on TaC stability at high temperature was measured and is significant. However, the reason for the measured effects are not thoroughly understood. It is possible that B segregates to the TaC phase boundary and therefore influence the phase stability.

Appendix A

Calibration of a Small-Angle Neutron Scattering Instrument

In this chapter, the procedures of data reduction and calibration of the SANS instruments are discussed. The connection between measured data $I(\vec{Q})$, overlapped from scattering of the instrument and smeared by the instrument resolution and the coherent differential cross section $\left(\frac{\mathrm{d}\sigma}{\mathrm{d}\Omega}\right)_c$ of the sample is presented. In addition, the procedure of absolute scaling is discussed and a novel, comprehensible way for the solid angle and detector correction is presented. These resolution considerations were applied for the presented SANS data in the previous chapters and are part of the developed Matlab evaluation software. Some of the results are published in [139].

There is a wide range of publications about correcting SANS data from an experiment with the goal to obtain a sample depending scattering cross-section [93, 140–146]. Determining the background signal produced from the instrument is relatively easy by characterizing the empty beam. However, all methods rely on one common step, namely the calibration of the measured sample scattering signal by the signal of a well-characterized isotropic scatterer, such as water, plexiglass, or vanadium, measured at the same instrumental settings as the sample. This calibration measurement serves three purposes: (1) correction of geometric effects of the instrumental setup, (2) correction of different detection sensitivities of different pixels, and (3) calibration of the measured signal to absolute units.

Unfortunately, several problems arise when performing a calibration measurement: It is basically impossible to find a sample that scatters completely isotropic, even if it is incoherent, due to inelastic [147, 148] or multiple [149, 150] scattering. Additionally, large detector distances require unfeasibly long measurements to achieve reasonable statistics. Therefore, the measurements are usually performed at short and medium detector distances and used for large detector distances as well, or not correcting the measurements at large detector distances at all.

It is therefore advantageous to create a detector efficiency file at an optimal geometry for the respective standard and to transform it to the actually used geometry afterwards. To do so, an accurate solid angle correction has to be performed and possible anisotropic effects of the detector system must be understood very well. Particularly, for nowadays widely used detectors made up from an array of position-sensitive ^{3}He proportional counter tubes, such as SANS-1 at the Heinz Maier-Leibnitz Zentrum (MLZ) in Garching near Munich, Germany [88, 89], KWS-1 at MLZ [151], D22 at ILL [152], SANS-I at PSI [91], LOQ at ISIS [153, 154],

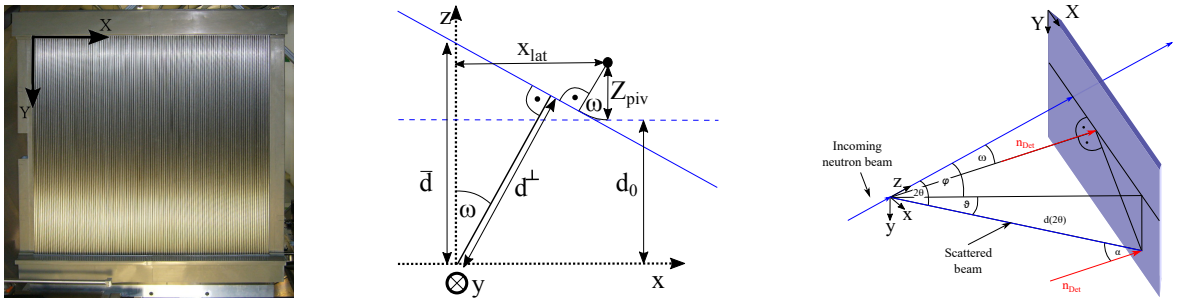

Figure A.1.1: Left: photography of the SANS-1 tube detector as seen from the sample together with a sketch of the coordinate system in detector-based coordinates. Middle: sketch of sample and detector (blue) as seen from above, highlighting some of the quantities used in this contribution; the detector is shown unturned (dashed line) and turned (solid line). Right: same, seen from a different point in space; the detector plane is shown in light blue, detector normals as red vectors, and neutron flight paths as dark blue vectors. Image adapted from [139].

EQ-SANS at SNS [155] or QUOKKA at OPAL [156], several non-trivial effects have to be taken into account which are subject of this contribution.

A.1 Geometry of the instrument

The required geometry setting for the correct calibration of a SANS instrument was shown in Karge et al. [139]. The following paragraph summarizes these results.

SANS data are usually given by an intensity matrix $I \in \mathbb{R}^{a\times b}$, where (a, b) is the detector size (for SANS-1 at MLZ $a = b = 128$). Throughout this chapter, two coordinate systems are used. Coordinates in the detector-based coordinate system will be denoted with uppercase vectors $\vec{R} = (X, Y, Z)$, cf. Fig. A.1.1. Its origin is set to the top-left pixel as seen from the sample position, X, Y is the detector plane and Z is the direction of the detector normal vector – all measured in pixels (px) and enumerated by i, j with $i \in [1, a]$ and $j \in [1, b]$. At SANS-1 at MLZ, each pixel has a size of $p^x = p^y = p^z = 8\,\mathrm{mm/px}$. The center of the direct beam is recorded at position $\vec{C} = (C^x, C^y, C^z)$.

The coordinates of all pixels can also be given in a sample-based coordinate system, denoted by lowercase vectors $\vec{r} = (x, y, z)$, cf. Fig. A.1.1. Its origin is the center of the illuminated sample volume, z is the direction of the incident neutron beam, x and y are in the horizontal and vertical direction, respectively, and are measured in meters. If the detector is not turned ($\omega = 0$), the two coordinate systems have parallel directions $\vec{r} \parallel \vec{R}$. It is customary for the detector to be able to move along the z-direction in order to resolve a wide range of neutron scattering angles 2θ. In more flexible setups, such as the one of SANS-1 at MLZ, the detector can also be moved sideways by a lateral displacement x_{lat} and turned by an angle ω. For this purpose, it is mounted on a hinge that has a rotation axis parallel to y, located in the detector system at $X_{\mathrm{piv}} = 63.5\,\mathrm{px}$ and $Z_{\mathrm{piv}} = 73.1\,\mathrm{mm}/p^z = 9.14\,\mathrm{px}$.

The affine transformation between the two coordinate systems is

$$\begin{pmatrix} x \\ y \\ z \end{pmatrix} = \hat{p}\left(\hat{R}\left(\begin{pmatrix} X \\ Y \\ Z \end{pmatrix} - \vec{T}_1\right) + \vec{T}_2\right) \tag{A.1}$$

with the dimension matrix

$$\hat{p} = \begin{pmatrix} p^x & 0 & 0 \\ 0 & p^y & 0 \\ 0 & 0 & p^z \end{pmatrix} \quad , \tag{A.2}$$

rotation matrix around the y-axis

$$\hat{R} = \begin{pmatrix} \cos(\omega) & 0 & \sin(\omega) \\ 0 & 1 & 0 \\ -\sin(\omega) & 0 & \cos(\omega) \end{pmatrix} \quad , \tag{A.3}$$

and translation vectors

$$\vec{T}_1 = \begin{pmatrix} X_{\text{piv}} \\ 0 \\ Z_{\text{piv}} \end{pmatrix} \qquad \vec{T}_2 = \begin{pmatrix} X_{\text{piv}} - C^x \\ -C^y \\ Z_{\text{piv}} + d_0/p^z \end{pmatrix} \quad . \tag{A.4}$$

The set of pixels in the sample system is defined by their center coordinates $\vec{d}_{i,j} = (x_{i,j}, y_{i,j}, z_{i,j}) \in \mathbb{R}^3$ and the set of pixels in the detector system by their number $\vec{D}_{i,j} = (X_{i,j}, Y_{i,j}, 0) \in \mathbb{N}^3$. With the above transformations, the pixels can be converted from one system into the other. Gravity effects are taken into account in the vector $\vec{T}_2$ trough translation of the system's Y-coordinate by the measured value C^y.

Pixel $p_{i,j}$ has a distance

$$d_{i,j} = \|\vec{d}_{i,j}\| = \sqrt{x_{i,j}^2 + y_{i,j}^2 + z_{i,j}^2} \tag{A.5}$$

from the sample and the shortest distance between the sample and the corresponding detector tube is at $y_{i,j} = 0$, i. e.

$$d_{i,j}^{xz} = \sqrt{x_{i,j}^2 + z_{i,j}^2} \quad . \tag{A.6}$$

A neutron that is detected in pixel $p_{i,j}$ was scattered by the sample under a scattering angle

$$\begin{aligned} 2\theta_{i,j} &= \arccos\left(\frac{\vec{e}_z \cdot \vec{d}_{i,j}}{\|\vec{e}_z\|\|\vec{d}_{i,j}\|}\right) \\ &= \arccos(z_{i,j}/d_{i,j}) \quad . \end{aligned} \tag{A.7}$$

The incident angle with which the neutrons impinge on the detector can thus be calculated using the detector normal $\vec{n}_{\text{Det}} = (-\sin(\omega), 0, \cos(\omega))$ to

$$\begin{aligned} \alpha_{i,j} &= \arccos\left(\frac{\vec{n}_{\text{Det}} \cdot \vec{d}_{i,j}}{\|\vec{n}_{\text{Det}}\|\|\vec{d}_{i,j}\|}\right) \\ &= \arccos\left(\frac{x_{i,j}\sin(\omega) + z_{i,j}\cos(\omega)}{d_{i,j}}\right) \quad . \end{aligned} \tag{A.8}$$

Due to the geometry of the problem, it is beneficial to use spherical coordinates in which pixel $p_{i,j}$ has an azimuthal angle of

$$\begin{aligned}\varphi_{i,j} =& \text{sign}(x_{i,j}) \arccos\left(\frac{\hat{e_z} \cdot \vec{d}_{i,j}|_{y=0}}{\|\vec{d}_{i,j}|_{y=0}\|}\right) \\ =& \arccos\left(z_{i,j} d^{xz}_{i,j}\right)\end{aligned} \tag{A.9}$$

and polar angle

$$\begin{aligned}\vartheta_{i,j} =& \text{sign}(y_{i,j}) \arccos\left(\frac{\vec{d}_{i,j} \cdot \vec{d}_{i,j}|_{y=0}}{\|\vec{d_{i,j}}\| \|\vec{d}_{i,j}|_{y=0}\|}\right) \\ =& \arccos\left(\frac{x^2_{i,j} + z^2_{i,j}}{d_{i,j} d^{xz}_{i,j}}\right) = \arccos\left(\frac{d^{xz}_{i,j}}{d_{i,j}}\right) \quad .\end{aligned} \tag{A.10}$$

The *signum* function is used to orient the angles in positive or negative direction, i.e. for negative y eq. (A.10) yields a negative angle.

The sample to detector distance d_0 conventionally assumes that the detector is perpendicular to the direct beam direction. For detectors that can be moved laterally and rotated by an angle ω around a pivot point which is not necessarily in the detector plane, a different definition is needed. The distance $\bar{d}$ for the primary beam detected in pixel $\vec{C}$ is therefore

$$\begin{aligned}\bar{d} = d(2\theta = 0) = \\ d_0 + \sin(\omega) \cdot (X_{\text{piv}} - C^x) \cdot p^x \\ + Z_{\text{piv}} \cdot p^z \cdot (1 - \cos(\omega))\end{aligned} \tag{A.11}$$

and the shortest distance from sample to detector plane $d^\perp$ is

$$\begin{aligned}d^\perp = d(\alpha = 0) = \\ \cos(\omega) \cdot \left(d_0 + \sin(\omega) \cdot (X_{\text{piv}} - C^x) \cdot p^x\right) \\ + Z_{\text{piv}} \cdot p^z \cdot (1 - \cos(\omega)) \quad .\end{aligned} \tag{A.12}$$

A.2 Data reduction

Two types of background were corrected in the process of data reduction: (1) The background from neutrons scattered by the instrument optics or air molecules I_{EB} and (2) the electronic background arising in the course of electronic processing I_{Cd}.

In order to correct for the background arising from the instrument, an empty beam measurement is performed in addition to the sample measurement. This measurement is subtracted from the sample intensity. Since the neutron beam is attenuated from the sample due to scattered and absorption of neutrons, the background has to be correctly scaled. This is done by measuring the sample transmission τ_{S} at $Q = 0$. The electronic background is determined by performing a measurement with blocked neutron beam.

Both effects are subtracted from the measured intensity I_S according to get the corrected neutron intensity I_{corr} [141]

$$I_{corr} = \frac{I_S - I_{Cd}}{\tau_S} - (I_{EB} - I_{Cd}) \quad . \tag{A.13}$$

A.3 Absolute scaling of SANS data

Absolute scaling is important to get absolute values on scattering volume fractions. The measured intensity $I(\vec{Q})$ depends on the sample's microstructure and the scattering length b of the scattering atoms. In addition, neutrons can be absorbed and scattered incoherently. In general, it is impossible to exactly calculate these factors for a real sample. Instead the calibration is performed with a standard sample.

The corrected scattering intensity $I(\vec{Q})$ from the sample is either compared with the scattering from the standard $I_S(\vec{Q})$. The scattering from the standard is corrected by the same procedure as for the sample itself eq. (A.13). The normalization is done by [141]

$$I_\chi^{abs} = \frac{\frac{I_S - I_{Cd}}{\tau_S} - (I_{EB} - I_{Cd})}{\frac{I_S}{\tau(S)}} \cdot \frac{\text{ScalingFactor}(W)}{\text{ScalingFactor}(S)} \quad , \tag{A.14}$$

where the scaling factors are determined by the incoming neutron flux and an intensity correction for the illuminated solid angle due to varying detector distances. Classically, the standard $I_S(\vec{Q})$ is measured for each used geometry. Section A.5 shows a novel procedure on how to create a detector efficiency file for every geometry on a SANS instrument with $_3$He detector counter tubes such as SANS-1 at MLZ (cf. section 4.3.1) with only one standard measurement at a well defined geometry.

A.4 Treatment of SANS resolution functions

The resolution effects smear the measured form factor with a similar Gaussian function, i.e. they might themselves look like a size distribution. Therefore, it is inevitable to apply a correction for the instrumental resolution function, when operating with size distributions. Their effect is schematically shown in Fig. A.4.1. The neutron beam has only a limitedly defined incoming wave vector k due to the finite collimation and wavelength smearing $\Delta\lambda$ of the instrument. Additionally the certainty of the scattered wave vector $\Delta k'$ is confined by the detector and its distance from the sample. These effects yield a smearing in the solid angle $\Delta\Omega$. While the detector resolution and collimation can be improved by increasing its path length to the sample, the wavelength is usually fixed in a SANS experiment.

The analytical expressions for the smearing functions were applied for the evaluation of data in this thesis, following the paper of Pedersen et al. [157]. They are assumed to have the form of a Gaussian that is convoluted with the ideal scattering-cross section $\left(\frac{d\sigma}{d\Omega}\right)$

$$I(\langle\vec{Q}\rangle) = \int T(\vec{Q}, \langle\vec{Q}\rangle, t) \left(\frac{d\sigma}{d\Omega}\right)(\vec{Q})\, dQ, \qquad t = (\Delta\lambda, \Delta k, \Delta k', \Delta\Omega) \quad . \tag{A.15}$$

The vector t contains the instrumental parameters due to collimation, detector distance, wavelength spread and detector resolution of the resolution function T. The ideal intensity

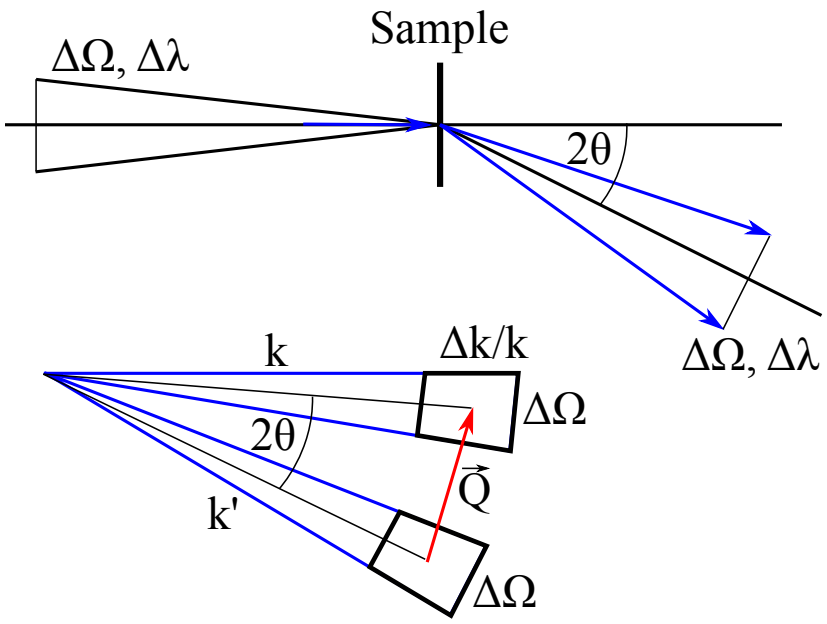

Figure A.4.1: The certainty of the wavevector $\vec{Q}$ is confined by the accuracy of $\Delta k/k$ and $\Delta\lambda/\lambda$. $\vec{Q}$ might have any value of the red arrow between the two boxes.

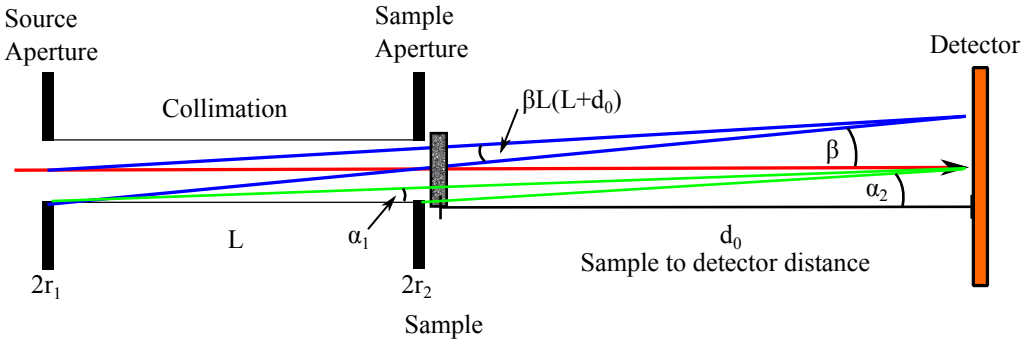

Figure A.4.2: Scheme of a classic SANS experiment. The resolution of the experiment depends on the chosen aperture sizes r_1 and r_2, collimation length L and sample to detector distance l.

$\left(\frac{d\sigma}{d\Omega}\right)$ depends on the average scattering vector $\langle\vec{Q}\rangle$ that arises due to the smearing of the vector $\vec{Q}$. T is calculated by a convolution of the following contributions, as described in [157].

A.4.1 The Resolution Function due to Wavelength Spread

Usually, the distribution of wavelengths $F(\lambda, \Delta\lambda)$ is well known for an instrument. Assuming that the wavelength is normally distributed with mean value $\langle\lambda\rangle$ and a standard deviation σ_λ, its distribution is given by

$$F(\lambda, \langle\lambda\rangle) = \frac{1}{\sqrt{2\pi}\sigma_\lambda} e^{-\frac{(\lambda-\langle\lambda\rangle)^2}{2\sigma_\lambda^2}} \quad . \tag{A.16}$$

The distribution of $\vec{Q}$-vectors is assumed to be isotropic and therefore only depends on its modulus Q. A first order Taylor expansion yields

$$Q - \langle Q\rangle = -(\langle Q\rangle)/\langle\lambda\rangle)(\lambda - \langle\lambda\rangle) \quad . \tag{A.17}$$

This is plugged into eq. (A.16) and yields

$$R_w(Q, \langle Q\rangle) = \frac{1}{\sqrt{2\pi}\sigma_w} e^{-\frac{(Q-\langle Q\rangle)^2}{2\sigma_w^2}} \quad , \tag{A.18}$$

with

$$\sigma_w = \sigma_\lambda \frac{\langle Q\rangle}{\langle\lambda\rangle} \quad . \tag{A.19}$$

Taking these smearing effects into account gives the resolution functional for wavelength spread

$$T_\lambda\left(\frac{\mathrm{d}\sigma}{\mathrm{d}\Omega}\right)(Q) = \int_{\mathbb{R}^3} R_w(Q(\lambda, \Delta\lambda, \langle\lambda\rangle)) \left(\left(\frac{d\sigma}{d\Omega}\right)(Q, \lambda, \Delta\lambda, \langle\lambda\rangle)\right) d\lambda \quad . \tag{A.20}$$

In practice, rather small integration limits are sufficient, since usually $\Delta\lambda/\lambda \approx 0.1$.

A.4.2 Resolution due to Finite Collimation

The fact that the collimation is of finite length, i.e. the incoming neutrons are not a perfect parallel wave, causes a smearing parallel to $\langle Q\rangle$. The geometrical derivation of the influence of this effect is quite extensive and is executed in [157]. The situation is depicted in Fig. A.4.2. The collimation is ultimately defined by two apertures, one in front of the neutron source and one in front of the sample. For the following considerations, both are considered of circular shape with radius r_1 and r_2. The length of the collimation between source aperture and the defining aperture is L and the distance between the latter and the detector is d_0. In the small-angle approximation, the half angular extent from one point of the detector to the source aperture is $\alpha_1 = r_1/(L + d_0)$ and to the sample aperture $\alpha_2 = r_2/d_0$.

Two cases are distinguished. First, for scattering at $\vec{Q} \approx 0$, the resolution function of the unscattered, direct beam can be directly measured. The direct beam should have the intensity function $I(\vec{Q}) = \delta(Q)$. Therefore, the resolution function can be written as

$$R_{\mathrm{col}}(\vec{Q}, \langle\vec{Q}\rangle) = R^0_{\mathrm{col}}(|\vec{Q} - \langle\vec{Q}\rangle|) \quad . \tag{A.21}$$

Secondly, for $\vec{Q} \neq 0$, the angular distribution perpendicular to the scattering plane is given by the two cases

$$\begin{cases} \Delta\beta_1 = \frac{2r_1}{L} - \frac{1}{2}\frac{r_2^2}{r_1}\frac{\cos^4 2\theta}{d_0^2 L} & \alpha_1 \geq \alpha_2 \quad , \\ \Delta\beta_1 = 2r_1\left(\frac{1}{L}\frac{\cos^2 2\theta}{d_0}\right) - \frac{1}{2}\frac{r_1^2}{r_2}\frac{d_0}{L}\frac{1}{L\cos^2 2\theta(L + d_0/\cos^2 2\theta)} & \alpha_1 < \alpha_2 \quad , \end{cases} \tag{A.22}$$

and the distribution in the scattering plane is given by

$$\begin{cases} \Delta\beta_2 = \frac{2r_1}{L} - \frac{1}{2}\frac{r_2^2}{r_1}\frac{\cos^2 2\theta}{d_0}\langle(L + \frac{d_0}{\cos 2\theta}\rangle)^2 & \alpha_1 \geq \alpha_2 \quad , \\ \Delta\beta_2 = 2r_1\left(\frac{1}{L}\frac{\cos^2 2\theta}{d_0}\right) - \frac{1}{2}\frac{r_1^2}{r_2}\frac{d_0}{L}\frac{1}{L\cos 2\theta(L + d_0/\cos 2\theta)} & \alpha_1 < \alpha_2 \quad . \end{cases} \tag{A.23}$$

Finally, the resolution function due to finite collimation is split into a component parallel and perpendicular to the scattering vector $Q = Q_{\parallel} + \vec{Q}_{\perp}$. Expressed by these contributions, the resolution function reads

$$R_{\mathrm{col}}(Q, \langle Q \rangle) = \frac{1}{2\pi\sigma_{C1}\sigma_{C2}} \exp\left(-\frac{(Q_{\parallel} - \langle Q \rangle)^2}{2\sigma_{C1}^2} - \frac{Q_{\perp}^2}{2\sigma_{C2}^2} \right) \quad , \tag{A.24}$$

where

$$\sigma_{C1} = \langle k \rangle \cos\langle \theta \rangle \Delta\beta_1 / 2\sqrt{2\log 2} \tag{A.25}$$

$$\sigma_{C2} = \langle k \rangle \Delta\beta_2 / 2\sqrt{2\log 2} \tag{A.26}$$

This yields the resolution functional due to finite collimation

$$T_{\mathrm{col}}\left(\frac{\mathrm{d}\sigma}{\mathrm{d}\Omega}\right)(Q) = \lim_{Q' \to \infty} \int_{-Q'}^{Q'} R_{\mathrm{col}}(Q', \sigma_{C1}, \sigma_{C2}) \left(\frac{\mathrm{d}\sigma}{\mathrm{d}\Omega}\right)(Q') dQ' \quad . \tag{A.27}$$

A.4.3 Dependence on detector resolution

The detector resolution is determined by the pixel size and the sample to detector distance. A larger distance yields a finer solid angle resolution. Since the detector is usually a planar 2D object, one has to consider a projection of the $\vec{Q}$-vector onto the detector plane. Therefore, there is a parallel and perpendicular contribution to the scattering vector $\vec{Q}$. The resolution function is given by

$$R_{\mathrm{det}}(\vec{Q}, \langle \vec{Q} \rangle) = \frac{1}{2\pi\sigma_{D1}\sigma_{D2}} \exp\left(-\frac{(Q_{\parallel} - \langle Q \rangle)^2}{2\sigma_{D1}^2} - \frac{Q_{\perp}^2}{2\sigma_{D2}^2} \right) \quad , \tag{A.28}$$

with

$$\begin{aligned} \sigma_{D1} &= \langle k \rangle \cos\theta \cos^2 \Delta(l\sqrt{(2\log 2)})^{-1} \\ \sigma_{D2} &= \langle k \rangle \cos 2\theta \Delta(l\sqrt{(2\log 2)})^{-1} \quad . \end{aligned} \tag{A.29}$$

This yields the resolution functional due to detector resolution

$$T_{\mathrm{det}}\left(\frac{\mathrm{d}\sigma}{\mathrm{d}\Omega}\right)(\vec{Q}) = \lim_{Q' \to \infty} \int_{-Q'}^{Q'} R_{\mathrm{det}}(Q', \sigma_{D1}, \sigma_{D2}) \left(\frac{\mathrm{d}\sigma}{\mathrm{d}\Omega}\right)(\vec{Q}') dQ' \tag{A.30}$$

In addition to the smearing of wavelength and finite instrument dimensions, the detector causes a smearing itself. This is due to the applied neutron detection, which prevents the exact determination of the position of incoming neutrons. As a result there arise shadowing and parallax effects. These are treated in detail in section A.5.

A.4.4 Characterization of instrument resolution, using a Latex round robin standard

A latex round robin standard was measured in order to characterize the instrumental resolution. The sample consists of polysterene latex, dissolved in D_2O with nearly perfect spherical morphology and unimodal size distribution.Figure A.4.3 presents the measured

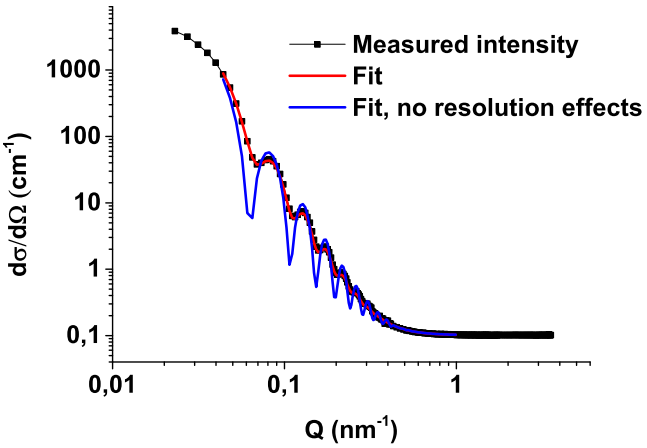

Figure A.4.3: Radial averaged scattering curve of the latex sample. Two fits with the proposed function for homogeneous spheres eq. (B.1).

intensity, fitted both, neglecting the resolution effects and using the resolution function from eqs. (A.20), (A.27) and A.30. The spherical shape of the particles causes the Bessel-shaped behavior from the spherical form factor (eq. (B.1)). The fit was only performed down to a minimum $Q = 0.04\,\mathrm{nm}^{-1}$, because multiple scattering becomes relevant for smaller Q. This effect is not considered in the resolution function.

A.5 Calibration procedure for a detector consisting of an array of ^{3}He tubes

The results and graphs in the following section are published in [139].

The solid-angle correction differs from a standard $\cos^3$ dependence, since the cylindrical detector tubes have an anisotropic geometry. The situation is schematically depicted in Fig. A.5.1. In addition, shadowing effects arise at large angles, since multiple detection voxels intersect the trajectory of a scattered neutron. The neutron might even pass a first detector tube and be recorded in the neighboring one. Since the transmission of ^{3}He depends on the neutron wavelength, this effect has to be understood for the whole neutron spectrum of the source. Recent SANS instruments support even more extreme geometries, such as a sideways movable detector to reach scattering angles 2θ of $\sim 45°$ (SANS-1 at MLZ) and rotations of the detector system which amplifies these effects.

In the following, a procedure is proposed which solves several of the above-mentioned problems for position sensitive ^{3}He proportional counter tubes. The tools for transforming a calibration measurement to arbitrary SANS geometries are provided. This includes all available wavelengths from a cold neutron source and large scattering angles, tested up to $\sim 40°$. In addition, the pixel sensitivity is corrected by comparing two individual measurements of the same scatterer, measured with a small lateral offset.

This procedure is separated into five parts: (1) the solid angle covered by the pixels, (2) an idealized detector efficiency including shadowing effects, (3) determination of different pixel sensitivities, and (4) the sample transmission for scattering at large angles. Finally, (5) the effect of these corrections will be demonstrated on the scattering pattern of vanadium.

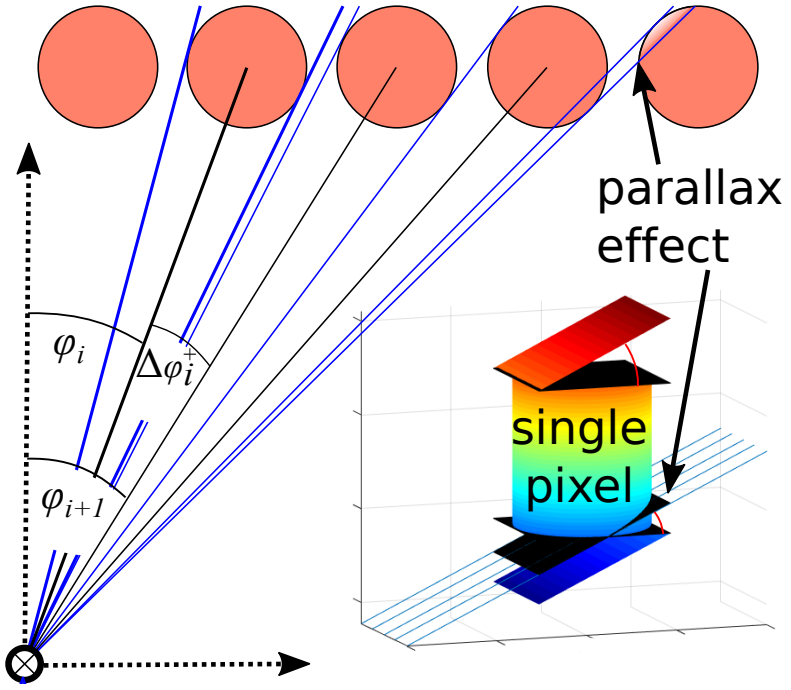

Figure A.5.1: Scheme of the applied procedure. The incoming neutrons are scattered to the detector pixels. Due to their geometry, there is a shadowing effect in x-direction between the pixels that leads to a parallax effect since neutrons are recorded in the wrong pixel. In addition there is a parallax effect in y-direction since the detection volume of a single pixel is a cylinder (inset). Therefore, neutrons can pass the above or below neighboring pixel before being recorded. The incident angles on the detector are determined by the positioning of the detector and therefore the effects differ with the instrument's geometry.

A.5.1 Solid angle corrections for a flat 2D detector

It is instructive to look at the case of an "isotropic" detector (e. g. a wire chamber) first which is normally treated as if it were a completely flat 2D structure. In this case, the only effect that has to be accounted for is the variation of the solid angle element of the different pixels. This yields the well-known solid angle correction [158, 159]

$$\Delta\Omega(2\theta) = \frac{p^x p^y}{\bar{d}} \cdot \cos^2(2\theta) \cdot \cos(2\theta) \tag{A.31}$$

where $\bar{d}$ is the distance from sample to detector and p^x, p^y the pixel size in x and y direction. The first term represents a scaling factor taking in account that a pixel of a given size covers a smaller solid angle element when the detector is further away from the sample. The second term, $\cos^2(2\theta)$, takes into account that the detector is not a spherical shell and therefore pixels with $2\theta > 0$ are even further away from the sample. The third term, $\cos(2\theta)$, accounts for the decrease in solid angle coverage because of the angle between pixel surface and scattered neutron beam.

For a detector consisting of cylindrical tubes, the $\cos(2\theta)$ correction has to be adjusted because a cylinder seen from the side still looks like a cylinder. He et al. [159] suggest a correction for the tube geometry according to

$$\Delta\Omega(2\theta) = \frac{p^x p^y}{\bar{d}} \cdot \cos^2(2\theta) \cdot \cos(\theta^y) \tag{A.32}$$

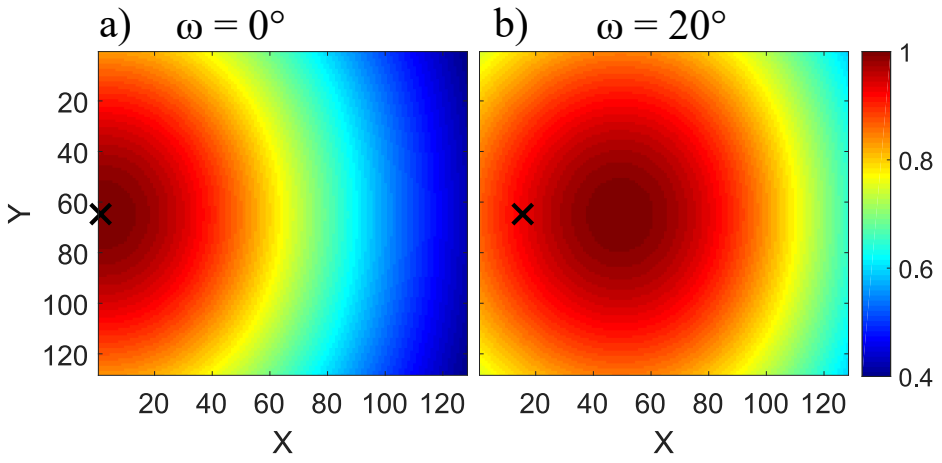

Figure A.5.2: Colour plot of equation A.33 for SANS-1 at MLZ specs $p^x = p^y = 8mm$, $d^\perp = 1111$ mm normalized to 1. The beam center is marked with a black cross. (a) detector plane perpendicular to the incoming neutron beam ($\omega = 0$), (b) detector rotated to $\omega = 20°$. Image adapted from [139].

where θ^y is the "y-component" (i. e. the polar angle) of the scattering angle 2θ, e. g. $\theta^y = \tan(d_{i,j}/\bar{d})$.

This formula can be adjusted to a detector system rotated by an angle ω by introducing the incident detector angle from eq. (A.8) and (A.10) (Fig. A.1.1). Therewith, $\bar{d}$ is replaced by $d^\perp$, further $\cos(2\theta)$ by $\cos(\alpha)$ and $\cos(\theta^y)$ by the polar angle $\cos(\vartheta)$:

$$\boxed{\Delta\Omega(\alpha,\vartheta) = \frac{p^x p^y}{d^\perp} \cdot \cos^2(\alpha) \cdot \cos(\vartheta)} \tag{A.33}$$

This correction is shown in Fig. A.5.2 and is indeed the most important term of all the corrections discussed in this contribution. However, for d below ∼2.5 m, it becomes apparent that this treatment of a tube detector as flat 2D structure with a few modifications to somehow account for the tube structure is not enough and some effects caused by the 3D nature of the tubes are not accounted for. These additional corrections will be discussed in the following.

A.5.2 Idealized detector efficiency and shadowing effects in a 3D detector

At large scattering angles the detection volumes partly shadow each other, effectively reducing the illumination intensity. In x-direction, there is a certain critical angle at which the shadowing effect starts. In y-direction, shadowing is present for any $\vartheta \neq 0$. To correct for these effects, the idealized efficiency $\eta_{i,j}$ of pixel $p_{i,j}$ (not taking into account manufacturing differences or effects like dead time) is calculated by a numerical integration of a function of the form

$$\eta_{i,j} = \tau_0^n \iint_{\Delta\Omega_{i,j}} E \cdot T \, \mathrm{d}\Omega \tag{A.34}$$

where E and T are the absorption and the transmission probability functions of a neutron with its flight trajectory through the detecting infinitesimal element $\mathrm{d}\Omega$. The function E describes the probability that a neutron is absorbed within a given pixel and the probability that neighboring pixels have not absorbed the neutron on its way T. $\Delta\Omega_{i,j}$ denotes the solid

angle element covered by pixel $p_{i,j}$. τ_0^n arises from the absorption function of the tube wall material. n is the number of walls that the neutron intersects between sample and ^{3}He, i. e. normally $n = 1$ and $n \geq 2$ if several tubes are intersected, i. e. shadowing occurs.

In order to calculate E and T, the functions are parametrized in spherical coordinates (Fig. A.1.1 right)

$$\mathrm{d}\Omega = d^2 \cos(\vartheta)\ \mathrm{d}\vartheta\ \mathrm{d}\varphi \quad \text{with } \vartheta \in [0, \pi],\ \varphi \in [0, 2\pi[\tag{A.35}$$

$$\eta_{i,j} = \tau_0^n \iint_{\Delta\Omega_{i,j}} E \cdot T\ d^2 \cos(\vartheta)\ \mathrm{d}\vartheta\ \mathrm{d}\varphi \quad . \tag{A.36}$$

Note that d and $\cos(\vartheta)$ are essentially constant over a single solid angle element $\Delta\Omega_{i,j}$, i. e. it is possible to write $d_{i,j}^2 \cos(\vartheta_{i,j})$ for the Jacobian determinant in the integral. A cos instead of the usual sin function is due to the definition of the coordinate system.

The transmission of ^{3}He depends on gas pressure p, neutron wavelength λ, and the flight path length s that the neutron has to pass within the gas [160]

$$\tau(s) = \exp(-0.0732 \cdot p \cdot \lambda \cdot s) \quad . \tag{A.37}$$

The absorption accounts for the neutrons which were not transmitted according to

$$E(s) = 1 - \tau(s) \quad . \tag{A.38}$$

The distance s is a function of the exact position and angle of the incoming neutron and will be parametrized in the following.

A.5.2.1 Absorption probability *E* in *x*-direction (y=0, no shadowing)

At this point let ($y = 0$, $\vartheta = 0$), i. e. the neutron flight trajectory is within the horizontal plane from the sample position. Hence, neutrons within this plane see a horizontal cut of the cylindrical tube, which is a circle with radius r. The *azimuthal opening angle* from sample position to this circle is

$$\psi_{i,j} = 2 \arcsin(r / d_{i,j}^{xz}) \quad . \tag{A.39}$$

With $h \in [-r, r]$ the distance from the centre of a tube (r is the tube radius), the path length function s of the neutron depends on h according to (see Fig. A.5.3)

$$s(h) = 2 \cdot \sqrt{\max(r^2 - h^2, 0)} \quad . \tag{A.40}$$

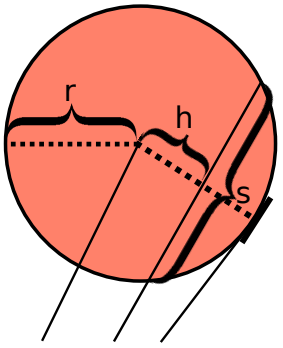

FIGURE A.5.3: Cross section of a single detector tube with radius r and neutron path distance s at distance h from midpoint. Image adapted from [139].

The distance h further depends on the azimuthal opening angle $\psi_{i,j}$ and the pixel distance $d_{i,j}^{xz}$ from the sample

$$h(\psi, d_{i,j}^{xz}) = d_{i,j}^{xz} \cdot \sin(\psi) \quad \psi \in [-\psi_{i,j}, \psi_{i,j}] \quad . \tag{A.41}$$

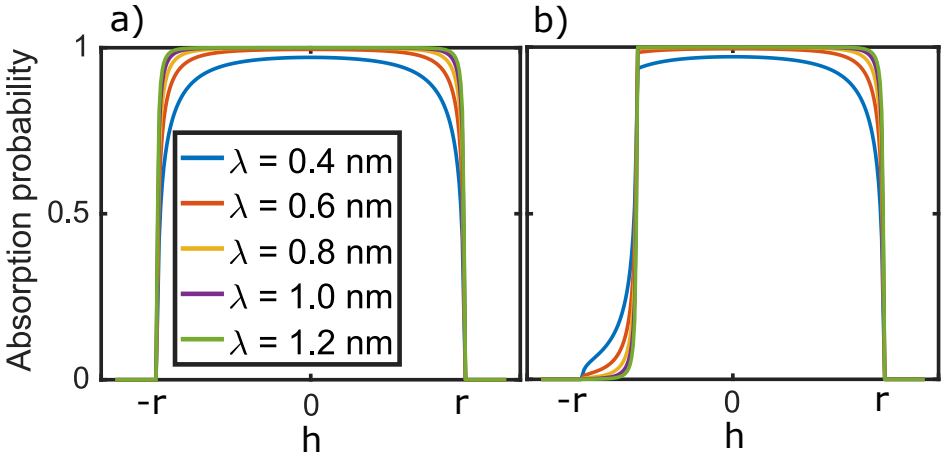

Figure A.5.4: Neutron absorption probability for neutrons with several wavelengths λ impinging at a distance h from the center of a detector tube with radius r. (a) without shadowing effects the absorption probability drops close to the ends due to the shorter path length in the tube (eq. (A.43). (b) partially shadowed tube, eqs. (A.43) and (A.45). Image adapted from [139].

By definition of the sample to pixel distance $d_{i,j}$ in eq. (A.5), these opening angles are also valid for a detector system rotated by an angle ω. For pixel $p_{i,j}$, the azimuthal angle φ of the spherical coordinate system is related to the angle ψ by the relation

$$\begin{aligned} \varphi &= \varphi_{i,j} + \psi \\ \mathrm{d}\varphi &= \mathrm{d}\psi \\ d^2 \cos(\vartheta)\ \mathrm{d}\vartheta\ \mathrm{d}\varphi &= d^2 \cos(\vartheta)\ \mathrm{d}\vartheta\ \mathrm{d}\psi \quad . \end{aligned} \tag{A.42}$$

Using this substitution, the integrand of function (A.36) for non-shadowed pixels along the $y = 0$ plane is a function of the azimuthal angle of pixel $p_{i,j}$

$$E\Big(s\big(d_{i,j} \cdot \sin(\psi)\big)\Big) \quad . \tag{A.43}$$

The effect is shown in Fig. A.5.4a for different neutron wavelengths. It can be seen that the absorption probability decreases close to the left and right ends of the tube because the neutron travels through less ^{3}He.

A.5.2.2 Including the shadowing effect T in x-direction (y=0)

Since the neutrons can hit the detector under an angle, they can cross other detector voxels before they are recorded. From Fig. A.5.5, it can be seen that the corresponding shadowing effect in x-direction occurs for

$$|\varphi_{i,j}| > \varphi_{\mathrm{crit}} := \arccos(2r/p) + \omega \quad . \tag{A.44}$$

For the SANS-1 at MLZ detector, $\varphi_{\mathrm{crit}} \approx 21° + \omega$. In order to take this effect into account for pixel $p_{i,j}$ at azimuthal angle $\varphi_{i,j}$, the transmission function T in the integrand of eq. (A.36) is determined by the neutron flight path length through the neighboring tubes $p_{i\pm1,j}$, that overshadow the same solid angle element $\Delta\Omega_{i,j}$ (Fig. A.5.5). For $y = 0$, $\vartheta = 0$, the path length through the neighboring tubes can be determined as function of the azimuthal angle

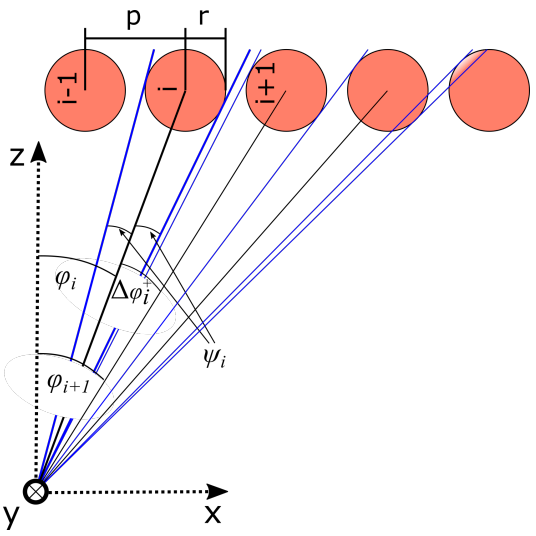

FIGURE A.5.5: The angles $\varphi_{i,j}$ and $\psi_{i,j}$. The index j is skipped for readability. The tube on the right is partially shadowed by its neighbor. Image adapted from [139].

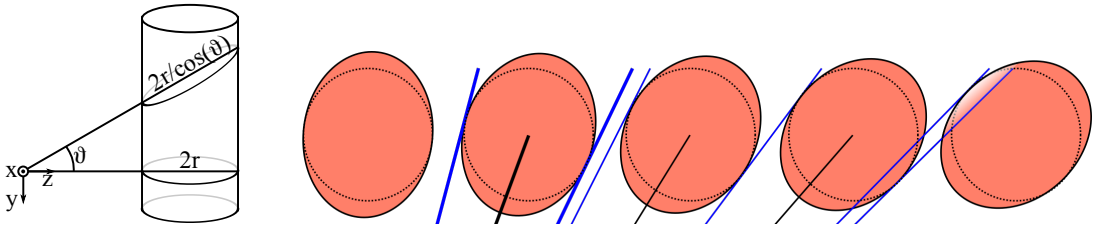

FIGURE A.5.6: (left) When neutrons are scattered up- or downwards, the cylinder cut is no longer a circle but an ellipse. (right) For increasing y, the cuts through the cylindrical tubes are ellipses. Image adapted from [139].

φ shifted by the offset of the neighboring tube's azimuthal angle $\Delta\varphi_{i,j}^{\pm} = \varphi_{i,j} - \varphi_{i\pm1,j}$. "+" denotes the case when the tube is shadowed on the right side and "−" the case on the left side

$$\begin{aligned} T &= \tau\Big(s\big(d_{i\pm1,j}\sin(\varphi - \varphi_{i,j} - \Delta\varphi_{i,j}^{\pm})\big)\Big) \\ &= \tau\Big(s\big(d_{i\pm1,j}\sin(\psi - \Delta\varphi_{i,j}^{\pm})\big)\Big) \end{aligned} \tag{A.45}$$

where the substitution eq. (A.42) was used for the azimuthal angle φ in the second step. An additional factor of the tube material transmission τ_0^2 is required, since the neutrons cross the material again when leaving the shadowing tube. The damped neutron flux by the neighboring tubes is depicted in Fig. A.5.4b.

A.5.2.3 Absorption probability E in x- and y-direction (no shadowing)

The cylindric section of the horizontal plane $y = 0$ and the detector tubes are circles with radius r. The situation changes if the neutrons are scattered up- or downwards and impinge under a non-zero angle ϑ in y-direction on the detector: the mean path length is increased because the neutrons *see* a skewed cut through the cylinder, which is in fact an ellipse (Fig. A.5.6(left)). Hence, there is a higher probability for them to be detected. For pixel $p_{i,j}$, the circular cross section is deformed to an ellipse with minor axis r and major axis

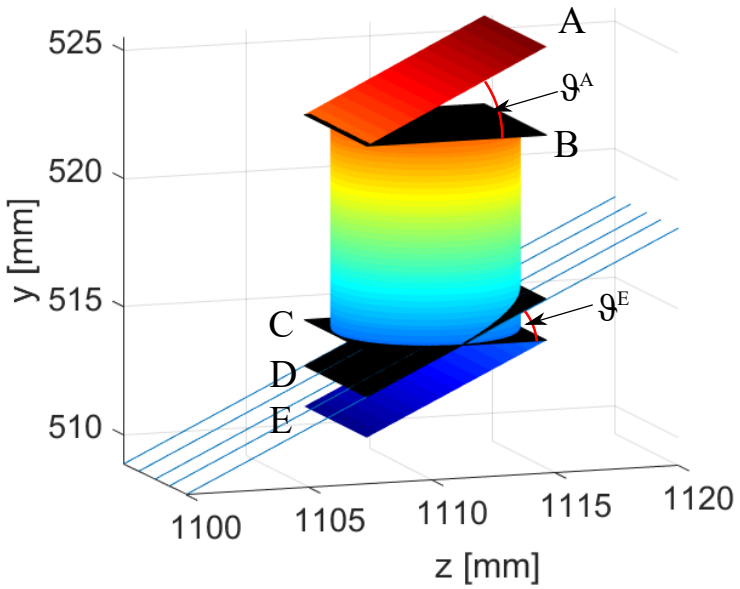

Figure A.5.7: Geometry of a single voxel for $\vartheta = 25°$. Neutrons can be partly detected in the voxel below or above as shown in the situation with a neutron trajectory within plane D that intersects plane C. Image adapted from [139].

$r/\cos(\vartheta)$ (Fig. A.5.6(right)) and hence s is increased by a factor $1/\cos(\vartheta)$ in the integrand of eq. (A.43)

$$E\Big(s(d_{i,j} \cdot \sin(\psi))/\cos(\vartheta)\Big) \tag{A.46}$$

Note that $\cos(\vartheta)$ is essentially constant over the solid angle element and it is therefore possible to use $\cos(\vartheta_{i,j})$.

A.5.2.4 Including the shadowing effect T in x- and y-direction

As can be readily seen in Fig. A.5.6(bottom), the shadowing in x-direction occurs for $y \neq 0$ at exactly the same positions as for $y = 0$, i. e. the considerations from above are also valid in this case.

In y-direction, shadowing occurs for any polar angle $\vartheta \neq 0$. The path length function s has to be considered within each respective detection voxel separately. Its intersection with the upper and lower end plane of the voxel (Fig. A.5.7) has to be calculated.

If the neutron intersects the upper or lower plane, the path length function is subdivided in $s = s_{\text{in}} + s_{\text{out}}$ with path length within the voxel s_{in} and outside of it s_{out} (Fig. A.5.7). Without neglecting useful cases, it can be assumed that the neutron trajectory intersects not more than one of the confining horizontal planes. This subdivision can be calculated analytically by geometric considerations.

In the following, the geometric considerations for the intersection of the voxel's upper or lower confining plane with the trajectory of a neutron are presented (Fig. A.5.8). Using equations (A.40) and (A.41), the function s reads for different ψ

$$s(\psi, \vartheta) = 2 \cdot \frac{\sqrt{r^2 - \left(d \sin(\psi)\right)^2}}{\cos(\vartheta)} \quad . \tag{A.47}$$

The condition that plane D from Fig. A.5.7 cuts plane B or C at the boundaries of a voxel with distance d in a tube with distance d^{xz} from the sample position is fulfilled if

$$|i^{\pm}(\vartheta)| \leq r \quad \text{with} \tag{A.48}$$

$$i^{\pm}(\vartheta) = \frac{d\ \sin(\vartheta) \pm p^y/2}{\tan(\vartheta)} - d^{xz} \quad , \tag{A.49}$$

where "+" is the condition for plane B and "−" the condition for plane D.

The split $s(\psi, \vartheta) = s_{\text{in}}(\psi, \vartheta) + s_{\text{out}}(\psi, \vartheta)$ is performed by the following set of equations for the case $D \cap C$ and $\vartheta > 0$ (Fig. A.5.8).

$$\delta^{\pm}(\vartheta) = r + i^{\pm}(\vartheta), \tag{A.50}$$

$$t^{\pm}(\psi, \vartheta) = \frac{r - \delta^{\pm}(\vartheta)}{\cos(\psi)}, \tag{A.51}$$

$$h(\psi) = d \sin(\psi), \tag{A.52}$$

$$o(\psi) = \frac{d}{\cos(\psi)} - (d^2 - h(\psi)^2)$$

$$= \frac{d}{\cos(\psi)} - d\ \cos(\psi), \tag{A.53}$$

$$l^{\pm}(\psi, \vartheta) = \min\left(\frac{s(\psi, \vartheta)}{2} \cdot \cos(\vartheta), t^{\pm}(\psi, \vartheta) - o(\psi)\right), \tag{A.54}$$

$$s_1(\psi, \vartheta) = \frac{s(\psi, \vartheta)}{2} - l^{\pm}(\psi, \vartheta), \tag{A.55}$$

$$s_2(\psi, \vartheta) = s(\psi, \vartheta) - s_1(\psi, \vartheta) \quad . \tag{A.56}$$

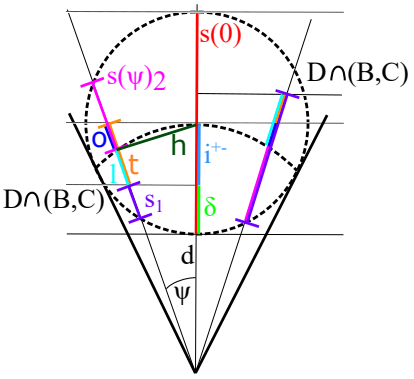

FIGURE A.5.8: $D \cap C$ and $D \cap B$ for cases that the intersection of planes is before or after the midpoint. For the line segment $s_1 = s_{\text{out}}$ if $\vartheta > 0$ and $D \cap C$ and vice versa. Image adapted from [139].

The other cases work analogously. $s_{\text{out/in}}$ is decided by the angle cases $\vartheta > 0$ or $\vartheta < 0$ and if one looks at plane B or C. Subsequently, similarly as in x-direction, the transmission function T for pixel $p_{i,j}$ eq. (A.45) is further extended by the transmission function of neutron flight path s_{out} in the voxel above ($\vartheta^A < 0$) or below ($\vartheta^E > 0$)

$$T_{i,j} = \tau\Big(s\big(d_{i\pm1,j} \sin(\psi - \Delta\vartheta^{\pm}_{i,j})\big)\Big) \cdot \tau\big(s_{\text{out}}(\vartheta, \psi)\big) \quad . \tag{A.57}$$

The idealized efficiency is therefore determined by an integration over the azimuthal opening angle ψ and the polar angle ϑ. The integration limits of the polar angles are determined by the confining planes A, E according to

$$\vartheta^A_{i,j} = \max_{x \in \pm r}\left\{\arctan\left(\frac{d_{i,j}\ \sin(\vartheta_{i,j}) + p^y/2}{d^{xz}_{i,j} + x}\right)\right\} \tag{A.58}$$

$$\vartheta^E_{i,j} = \min_{x \in \pm r}\left\{\arctan\left(\frac{d_{i,j}\ \sin(\vartheta_{i,j}) - p^y/2}{d^{xz}_{i,j} + x}\right)\right\} \quad . \tag{A.59}$$

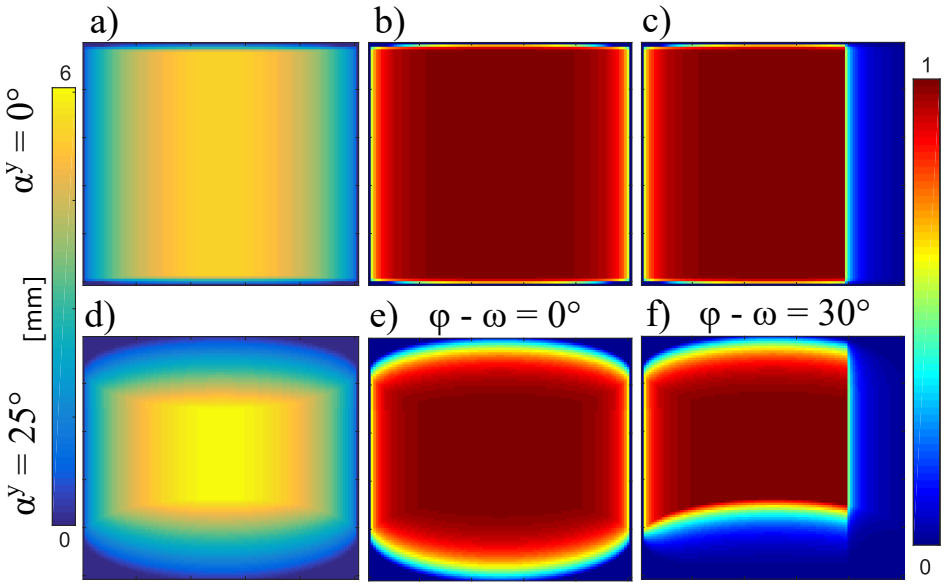

Figure A.5.9: Idealized efficiency, eq. (A.60), of single voxels. The detector is positioned with a distance $d_0 = 1.111\,\mathrm{m}$ from the sample. (top) $\vartheta = 0$. (a) Single voxel as seen from the sample position. The color is related to the neutron flight path distance in the voxel (b) idealized efficiency of a non-shadowed voxel. (c) idealized efficiency of a shadowed voxel with $|\varphi| > \varphi_{\mathrm{crit}}$. (bottom) $\vartheta = 25°$. (d) Single voxel as seen from the sample position. (e) idealized efficiency of a non-shadowed voxel. (f) For $\vartheta > 0$, the neutron path length is truncated at the lower plane of the neighbor voxel within the same tube. Additionally the voxel is shadowed by the neighboring tube for $|\varphi| > \varphi_{\mathrm{crit}}$. Image adapted from [139].

Finally the idealized efficiency of pixel $p_{i,j}$ is calculated by

$$\begin{aligned}\eta_{i,j} = \tau_0^n \int_{\vartheta^E_{i,j}}^{\vartheta^A_{i,j}} \int_{-\psi^x_{i,j}}^{\psi^x_{i,j}} & E\big(s_{\mathrm{in}}(\vartheta,\psi)\big) \\ & \cdot \tau\Big(s\big(d_{i,j}\sin(\psi - \Delta\vartheta^{\pm}_{i,j})\big)\Big) \\ & \cdot \tau\big(s_{\mathrm{out}}(\vartheta,\psi)\big) \\ & \cdot d^2\cos(\vartheta)\,\mathrm{d}\vartheta\,\mathrm{d}\psi \quad .\end{aligned} \tag{A.60}$$

The integration can be performed numerically, for example by Gauss-Tschebyschow Quadrature [161] with reasonable speed and very good accuracy.

The effect of a shadowing neighbor tube on the right for a single pixel is shown in Fig. A.5.9c,f. The effect of a shadowing neighbor voxel below in the same tube can be seen in Fig. A.5.9f.

Fig. A.5.10a,b depict the idealized efficiency function due to the shadowing effects and changed neutron path length s in the tubes for neutron wavelengths $\lambda = 0.49\,\mathrm{nm}$ and $\lambda = 1.2\,\mathrm{nm}$ without any solid angle effects. The detector is positioned with $d_0 = 1.111\,\mathrm{m}$ and $x_{\mathrm{lat}} = 0.5\,\mathrm{m}$. The shadowing effect is strongly visible, as well as a weak efficiency increase in Y-direction due to the increase of neutron flight path s within the tube. Fig. A.5.10c shows the same situation but with a turned detector system $\omega = 20°$. The visible effect is purely the efficiency change due to increased s. With this geometry the shadowing is only present for the left 4 tubes and not visible in the 2D image.

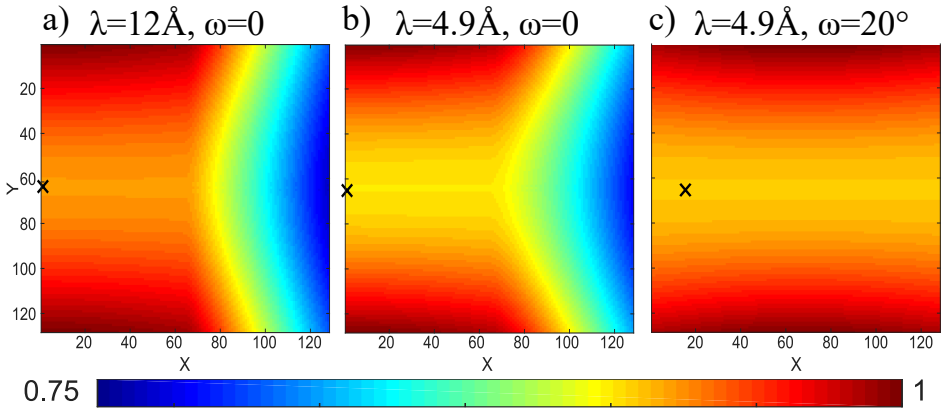

FIGURE A.5.10: Idealized detector efficiency, eq. (A.60), taking into account shadowing and efficiency change due to neutron path length within the cylindrical tube. The detector is positioned with a distance $d_0 = 1.111\,\mathrm{m}$ from the sample. (a) $\lambda = 1.2\,\mathrm{nm}, \omega = 0$, (b) $\lambda = 0.49\,\mathrm{nm}, \omega = 0$, (c) $\lambda = 0.49\,\mathrm{nm}, \omega = 20°$ all with lateral movement of the detector $x_{\mathrm{lat}} = 0.5\,\mathrm{m}$. The beamcenter is marked with a cross. Intensities were normalized to 1. Image adapted from [139].

A.5.3 Pixel sensitivity

So far, only geometric effects were dealt with – it was implicitly assumed that every neutron absorbed by ^{3}He corresponded to a detection event. Due to factors like manufacturing irregularities, this is not the case and every pixel has a sensitivity ε. The task of determining these sensitivities is often performed by using an incoherent scatterer (vanadium, plexiglass, water) which is assumed to scatter isotropically. Due to the reasons mentioned above – direction dependence of the probability for multiple scattering and a Q-dependence of inelastic scattering – even a purely incoherent scatterer cannot be expected to result in a flat intensity distribution on the detector after all geometrical corrections. In the following, a procedure is presented which does not require the sample to scatter isotropically, but instead uses two measurements of the same arbitrary sample with displaced detector to determine the pixel sensitivity, inspired by procedures used for X-rays [162].

For this procedure to work, it is essential to have measurements in which the intensity fluctuations due to counting statistics are much smaller than the systematic effects that are to be corrected. In the current case of sensitivity differences on the order of 10^{-2}, one would aim for a relative counting error on the order of 10^{-3} or better, corresponding to at least 10^6 neutrons per pixel. A strongly scattering sample is therefore beneficial – in the present work, Glassy Carbon was used [145].

Two measurements of the scattering of Glassy Carbon were performed, one with the detector further left (denoted l, at $x = 4\,\mathrm{mm}$) and one with the detector shifted one pixel distance of 8 mm to the right (denoted r, at $x = 12\,\mathrm{mm}$). The pixel number i in a given row increases from left to right. If a pixel is illuminated with a true intensity I_i, it will register c_i counts with statistical error $\sqrt{c_i}$ due to its sensitivity ε_i. When displacing the detector, the intensity that arrived at pixel i when the detector was on the right hits pixel $i+1$ when the detector is on the left

$$c_i^r = \varepsilon_i \cdot I_i \quad \text{and} \quad c_{i+1}^l = \varepsilon_{i+1} \cdot I_i, \quad \forall i \in [1, a-1] \tag{A.61}$$

which can be combined and rearranged to

$$\frac{\varepsilon_{i+1}}{\varepsilon_i} = \frac{c^l_{i+1}}{c^r_i} =: r_i \pm \sigma_i, \quad \forall i \in [1, a-1] \tag{A.62}$$

where r_i is a shorthand notation for the ratio of measured counts and σ is the propagated statistical error of the counts. In reality, the ratio of the sensitivity and the ratio of the measured counts are not identical for all pixels but should be as similar as possible, i. e. the aim is to minimize the quantity

$$\chi^2(\varepsilon) = \sum_{i=1}^{a-1} \left(\frac{\varepsilon_{i+1}/\varepsilon_i - r_i}{\sigma_i} \right)^2 \quad . \tag{A.63}$$

The whole set of pixel efficiencies is the solution to

$$\boxed{\min_{\varepsilon \in \mathbb{R}^{a-1}} \left(\chi^2(\varepsilon) \right)} \quad . \tag{A.64}$$

The gradient vector $\partial\chi^2/\partial\varepsilon_i$ of this function can be calculated analytically which speeds up the fit process considerably.

A.5.4 Sample effects

There are some effects with which the sample itself influences the detected intensity so that it is not proportional to the scattering function. They have been described in detail elsewhere and are summarized in the following.

A.5.4.1 Transmission of the sample

When neutrons are scattered to large angle (e.g. $2\theta > 5°$), the sample transmission is a function of the scattering angle 2θ and an angle dependent transmission has to be applied. This effect scales with $1/\cos(2\theta)$ and can therefore be neglected at very small angles. However, it has to be taken into account when larger scattering angles are considered.

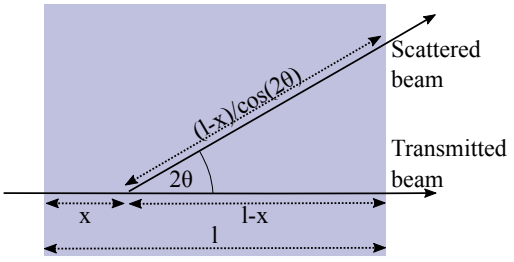

FIGURE A.5.11: Transmission change at large angles due to the increased path length within the sample. Image adapted from [139].

The neutron absorption from a sample with thickness l is a function of the sample thickness and a material constant μ. Experimentally, the constant μ is usually approximated by a measurement of the sample transmission T_s at $2\theta = 0$ [163]

$$T_s(2\theta = 0) = \exp(-\mu\, l) \quad . \tag{A.65}$$

In this measurement, the beam is attenuated by absorption and additionally by coherently and incoherently scattered neutrons to large angles. For weak scatterers such as vanadium, this is a very good approximation.

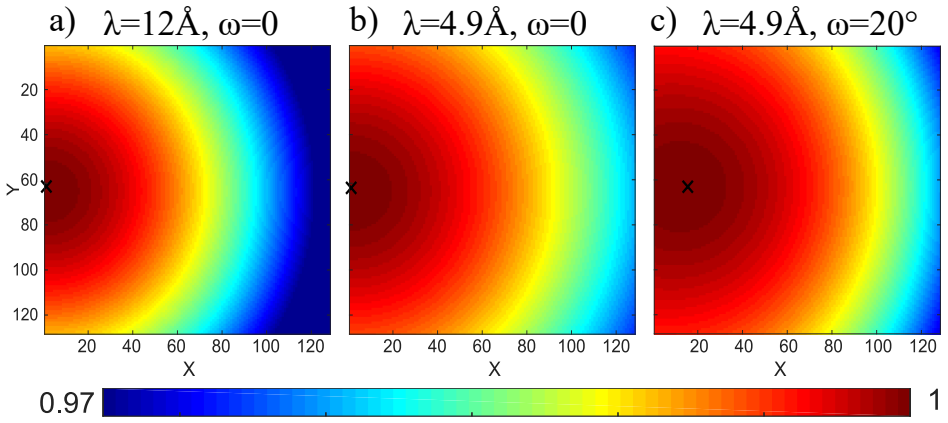

FIGURE A.5.12: Transmission change from vanadium sample at large angles, eq. (A.68). (a) $\lambda = 1.2\,\text{nm}, \omega = 0$, (b) $\lambda = 0.49\,\text{nm}, \omega = 0$, (c) $\lambda = 0.49\,\text{nm}, \omega = 20°$ all with lateral movement of the detector $x_{\text{lat}} = 0.5\,\text{m}$. Image adapted from [139].

However, the distance that scattered neutrons travel through a sample also depends on the scattering angle (cf. Fig. A.5.11).

As the scattering angle increases, the flight distance increases. A neutron that is scattered after the distance x after entering the sample by a scattering angle 2θ traverses a distance of [164]

$$x + \frac{l - x}{\cos(2\theta)} \quad . \tag{A.66}$$

For scattering events that occur after passing a distance of x within the sample, the neutron amplitude is attenuated by a factor $\exp(-\mu x)$ with the material dependent value μ. The neutron amplitude that is scattered at x to an angle of 2θ is attenuated by an additional factor $\exp\left(-\mu(e - x)/\cos(2\theta)\right)$. Then, the angle dependent transmission is calculated analytically according to [144, 158]

$$T_{\text{s}}(2\theta) = \frac{1}{l}\int_0^l \exp\left(-\mu\left(x + \frac{l - x}{\cos(2\theta)}\right)\right)\,\mathrm{d}x \tag{A.67}$$

$$T_{\text{s}}(2\theta) = \frac{\exp(-l\mu)(1 - \exp(-l\mu\ f(2\theta))}{l\mu\ f(2\theta)} \quad , \tag{A.68}$$

with $f(2\theta) = -1 + 1/\cos(2\theta)$. The effect is depicted in Fig. A.5.12.

A.5.4.2 Inelastic scattering

An energy transfer between neutron and sample causes two problems: first, the momentum transfer Q is calculated wrongly, and second, the detected intensity depends on the energy-dependent detection probability of the detector and a flux normalisation factor. This affects both, the total number of neutrons recorded by the detector and the Q-dependence of the scattering signal, since the amount of inelastic scattering increases with Q. On spectrometers, the connected Debye-Waller-factor can be accounted for; there are also correction procedures for diffractometers [165] but they are less well defined.

It has been shown [142, 166] that an energy transfer between sample and neutron is noticeable for many standards normally used in neutron scattering (in descending order: water,

plexiglass, vanadium, glassy carbon) and has the systematic effect of increasing the neutron energy towards that of thermal wavelengths ∼2 Å.

An energy transfer from the sample to the neutron requires both, thermal motion in the sample and a scattering process that can transfer its energy to the neutron. Incoherent scattering probes single particle motions and is therefore particularly susceptible to such an energy transfer. The coherent scatterer Glassy Carbon causes orders of magnitude less inelastic scattering than the other standards mentioned above [146], which makes it particularly suitable for calibration purposes. Its only drawback is that the scattered intensity is markedly not 4π while the other, incoherent, standards scatter in zeroth approximation with 4π. However, this does not pose a problem for the determination of the absolute scattering intensity and also the voxel sensitivities can be calibrated with such an non-4π scatterer as shown in section A.5.3.

A.5.4.3 Multiple scattering

Multiple scattering distorts the scattered intensity [167]. The calibration methods presented in this contribution are valid independently of the amount of multiple scattering in the calibration standard but do not correct for multiple scattering in the sample.

A.6 Results of the novel method for Detector calibration and absolute scaling

All measurements were carried out on the instrument SANS-1 at the Heinz Maier-Leibnitz Zentrum (MLZ) in Garching near Munich, Germany [89]. The instrument is equipped with an array of 128 position sensitive ^{3}He detectors of type Reuter-Stokes P4-0341-201 installed with a pitch of 8 mm. They have an active length of slightly more than 1 m, an inner diameter of 7.324 mm and a gas pressure p_{He} of 15 bar. The detector system can be moved sideways for up to 570 mm and rotated by angles up to 21°.

The determination of pixel sensitivities ε via eq. (A.64), was performed with an established reference sample of Glassy Carbon [145]. Its fabrication procedure is described in [168]. The sample had a thickness of 1 mm was measured with a neutron wavelength of $\lambda = 0.49$ nm, a collimation of 4 m and a detector distance of $d_0 = 4.0$ m two times: once with a lateral displacement of the detector of $x_{\mathrm{lat}} = 4$ mm and once with $x_{\mathrm{lat}} = 12$ mm. The resulting sensitivity matrix is shown in fig. A.6.1 by itself and in combination with the idealized detector efficiency and shadowing eq. (A.60).

It can be seen that the procedure works very well for local sensitivity fluctuations without distorting or smearing the general shape. In particular, there is no drift across the detector from top to bottom which could have happened since the detector can only be moved sideways and not lifted. Some features that are most probably not in the true scattering pattern have not been removed completely, in particular a vertical line of lower sensitivity around $X = 30$ and a slight distortion of the otherwise azimuthally symmetric pattern around the beamstop. However, it was decided to not enforce azimuthal symmetry and not correct for these small effects in order to not introduce artefacts.

Using this sensitivity matrix, the rest of the procedure is demonstrated on the scattering of a vanadium sample which is a nearly perfect incoherent scatterer [106]. For the vanadium

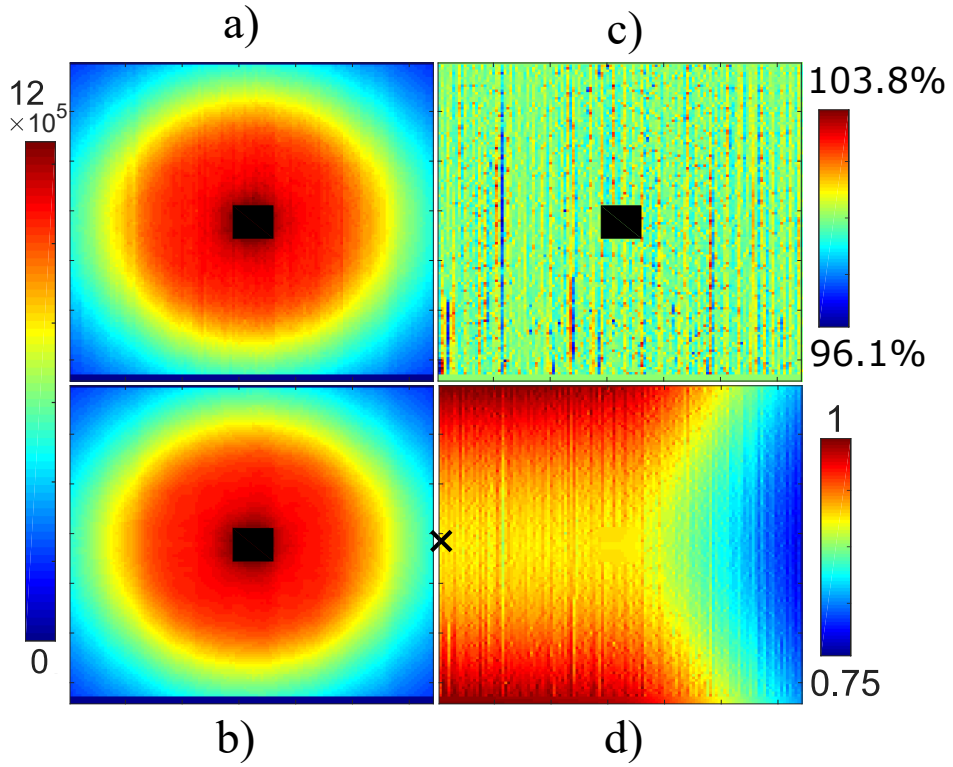

Figure A.6.1: (a) Measurement of Glassy Carbon as taken by the instrument SANS-1 at MLZ. (b) Glassy Carbon after pixel efficiency correction. (c) Corresponding pixel sensitivities. Note that a total count number of $\sim 10^6$ per pixel was obtained. (d) Pixel efficiency for the geometry $\lambda = 0.49\,\text{nm}, \omega = 0$, including the idealized detector efficiency and shadowing eq. (A.60) and pixel sensitivities eq. (A.64). Image adapted from [139].

measurements, a neutron wavelength of $\lambda = 0.49\,\text{nm}$, a collimation of 6 m and a detector distance of $d_0 = 1.111\,\text{m}$, were used. Additionally, an offset of x_{lat} =500 mm with two distinct rotation angles ω of 0 and 20° were chosen to obtain different tube shadowing conditions. The measurement time was always 30 min.

The efficiency maps for these measurement conditions were calculated by multiplying the effects from solid angle corrections $\Delta\Omega$ eq. (A.33), idealized detector efficiency and shadowing η eq. (A.60), non-ideal detection probability ε eq. (A.64) and sample transmission correction T_s eq. (A.68). Fig. A.6.2 shows the efficiency maps for two detector angles ω. Comparison with Fig. A.5.2 shows that the solid angle effect is the leading order correction but the other effects introduced in this contribution have a clearly visible influence.

These efficiency maps have been applied to the scattering of a vanadium sample. Figure A.6.3a,c show the results of vanadium raw data for $\omega = 0$ and $\omega = 20°$. Around $2\theta = 0$ (marked by a cross), the area of the beamstop is masked. In addition, the detector is partly overshadowed from the nose system towards the detector at the right side of the pattern, which was masked as well.

With the detector orthogonal to the incoming neutron beam $\omega = 0$, the scattering intensity decreases by $\sim 50\%$ towards the largest scattering angles due to the solid angle and detector effects. The rotated detector has its shortest distance to the sample nearly in its center. For that reason, the scattering intensity decreases around that point by 10% towards the sides of the detector. Fig. A.6.3b,d depict the respective scattering patterns divided by the predicted efficiencies in Fig. A.6.2. The corrections reproduce constant scattering patterns,

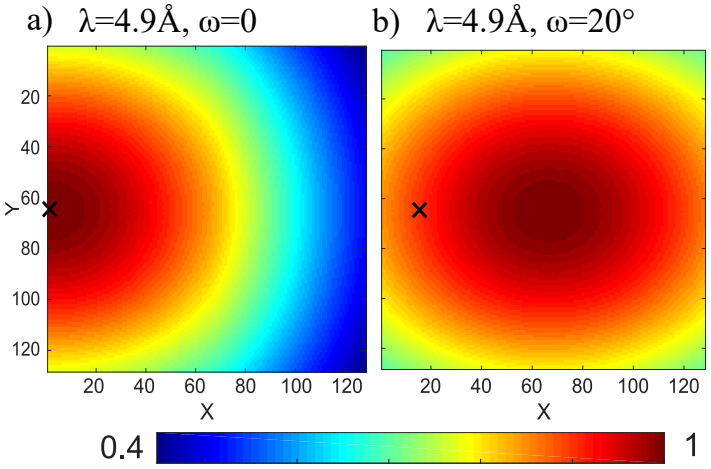

FIGURE A.6.2: Predicted detector efficiency, including the effects from solid angle corrections eq. (A.33), idealized detector efficiency and shadowing eq. (A.60), non-ideal detection probability ε eq. (A.64) and sample transmission correction eq. (A.68). (a) $\lambda = 0.49\,\text{nm}, \omega = 0$, (b) $\lambda = 0.49\,\text{nm}, \omega = 20°$ all with lateral movement of the detector $x_{\text{lat}} = 0.5\,\text{m}$. Image adapted from [139].

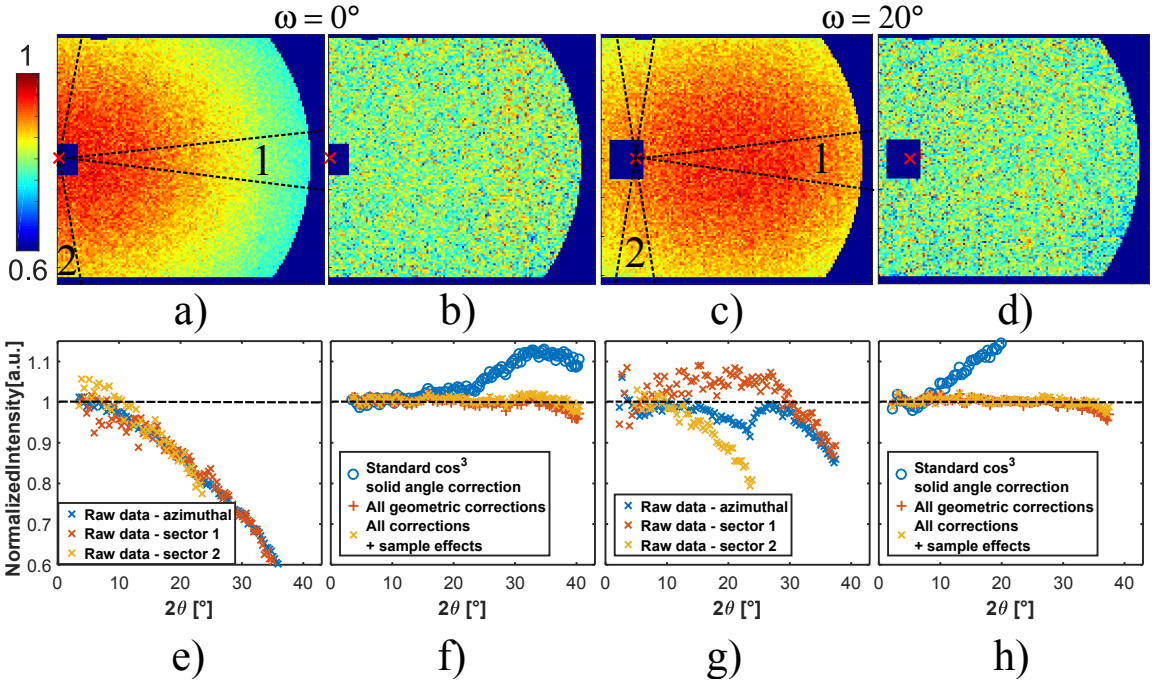

FIGURE A.6.3: Measurement of vanadium with $\lambda = 0.49\,\text{nm}, d = 1.111\,\text{m}$ (left) with $\omega = 0$ and (right) with rotated detector $\omega = 20°$. Top: 2D data before (a,c) and after (b,d) applying the geometric corrections. Bottom: Corresponding azimuthally averaged data, before (e,g) and after (f,h) applying corrections. Intensities were normalized by eye to 1. The raw data were additionally evaluated in sectors as indicated in the figure. For $\omega = 0$, the normalized curve has a range of $I_{\text{max}} - I_{\text{min}} = 1.0159 - 0.9716 = 4.4\%$. For $\omega = 20°$, the range is $I_{\text{max}} - I_{\text{min}} = 1.0232 - 0.9697 = 5.4\%$. Image adapted from [139].

superimposed with statistical noise, as expected from a vanadium sample. The measurement time of the sample was not enough to resolve the sensitivity fluctuations (Fig. A.6.1) between the pixels, but it is clear that there are no distinct systematic features visible on the $2D$ image after the correction.

The azimuthally averaged scattering cross-sections are depicted A.6.3e,f. Even at the largest 2θ-values of $\sim 40°$, the procedure reproduces basically a constant. The intensity shows a very small decrease to very large 2θ-values, which might be induced from inelastic scattering effects from vanadium. At $\omega = 20°$, the averaged raw data show a kink at $2\theta \approx 23°$ which originates from the superimposed effects in vertical and horizontal direction: As soon as the scattering angle 2θ reaches the upper and lower boundary of the detector, the effects in horizontal direction become suddenly more prominent, which shows the necessity of the applied anisotropic correction procedure. For $\omega = 0$, the normalized curve has a range of $I_{\max} - I_{\min} = 1.0159 - 0.9716 = 4.4\%$. For $\omega = 20°$, the range is $I_{\max} - I_{\min} = 1.0232 - 0.9697 = 5.4\%$. These statistical fluctuations are to be expected for the employed measurement time (30 min).

Appendix B

Models for Small-Angle Scattering

There exist various approaches for the evaluation of SAS data [61, 94, 169–171]. Depending on the quality of the data and knowledge about the scattering sample, the evaluation can be done in real or reciprocal space. Model independent fits in reciprocal space is the more general approach, since universally valid laws of scattering can be used. In order to create a real space model, a more profound knowledge about the scattering sample is required and for more complicated systems the mathematical tools for the fits often have to be developed for each problem individually. Since the instrument resolution functions have to be considered as well (cf. appendix A), these mathematical problems quickly get quite involved.

In the following, an overview of the tools for evaluation of SAS data from materials science is presented. A Matlab program for the evaluation of SANS data was developed as part of this work. The package allows fits of $3D$ models from the most common form and structure and form factors B.1 together with size distributions. Additionally, model-free fits based on a grid B-spline interpolation B.5 is implemented. Common integral parameters from big data sets (e.g. $>$ 1000 files) can be evaluated simultaneously (cf. section 3.1.2.7).

B.1 Form factors and structure factors

In the following, the most important form factors for materials science are discussed. These form factors are supported by the developed Matlab software program and can be fitted to measured data.

Sphere For an isotropic particle such as a single sphere, the SAS intensity eq. (3.23) only depends on the modulus of the scattering vector $Q = |\vec{Q}|$. Therefore, the azimuthally averaged scattering intensity contains all information about the scatterer. The form factor of a sphere with radius R is obtained by integrating over the Fourier transform of a function of the form $f(x) = 1, x \leq R, f(x) = 0, x > R$. This yields

$$I_{sp}(Q;R) = \Delta\rho^2 \left(\frac{4}{3}\pi R^3\right)^2 \left(\frac{3(\sin QR - QR\cos QR)}{(QR)^3}\right)^2. \tag{B.1}$$

This form factor is essentially the square of the Bessel function of the first kind with order $3/2, J_{3/2}(QR)$. Fig. B.1.1 depicts the $2D$ and azimuthal averaged result.

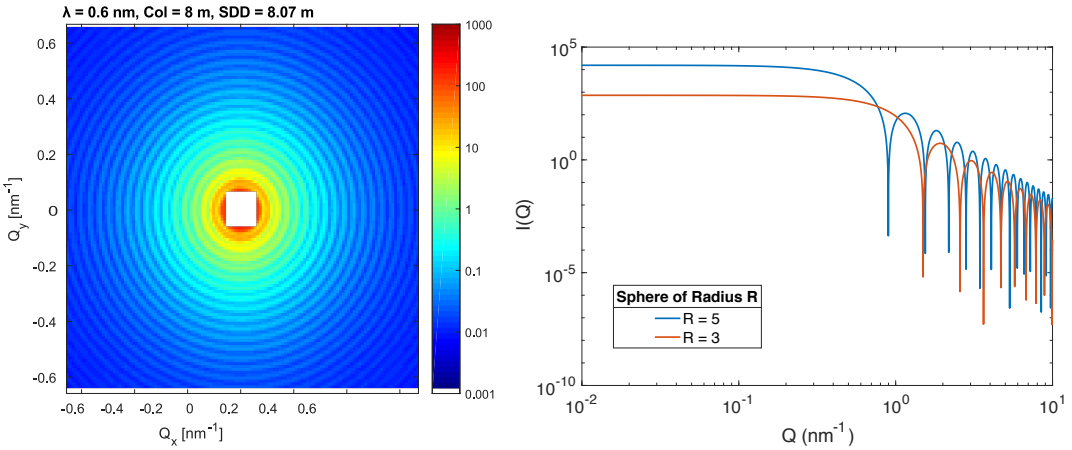

Figure B.1.1: (left) Simulated 2D scattering signal of a sphere with radius 70 nm. (right) 1D scattering signal of a sphere.

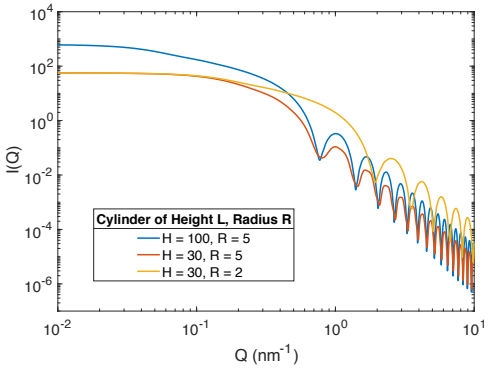

Figure B.1.2: Simulated 1D scattering signal of a cylinder.

Cylinder The form factor of a cylinder only depends on the modulus Q and the angle φ defined by $Q_z = Q\cos\varphi$

$$I_{Cy}(Q;\epsilon,R,\varphi) = \Delta\rho^2 V^2 \left|\frac{\sin(Q\cos\varphi\epsilon/2)}{Q\cos\varphi\epsilon/2}\right|^2 \left|\frac{2J_1(Q\sin\varphi R)}{Q\sin\varphi R}\right|^2, \tag{B.2}$$

where J_1 is the Bessel function of first kind and order 1. Varying φ corresponds to a rotation of the cylinder around the incoming neutron beam trajectory. If the cylinders have no distinct preferential orientation, the detector image records the azimuthally averaged signal of the form factor. The azimuthal averaging results in a loss of information, since the cylinder is not a symmetric structure. The resulting 1D SANS curve is shown in Figure B.1.1 right.

If there is a spatial orientation relationship, the detector will record an anisotropic image. Within this work, a method to fit $3D$ form factors was developed and demonstrated [172]. The scattering arises from a sintered molybdenum-hafnium-carbon alloy, with a strongly textured matrix. Hf-carbides precipitate in the alloy, that coherently align to the textured matrix and, therefore, show an orientation relationship. The streaks correspond to the smaller dimension of the cylindric form factor. In addition, the texture gives rise to an anisotropic Porod like signal (cf. section B.2) that had to be considered in the fits. The two dimensional scattering cross section arising from such an arrangement of platelets is shown in Fig. B.1.3a. The

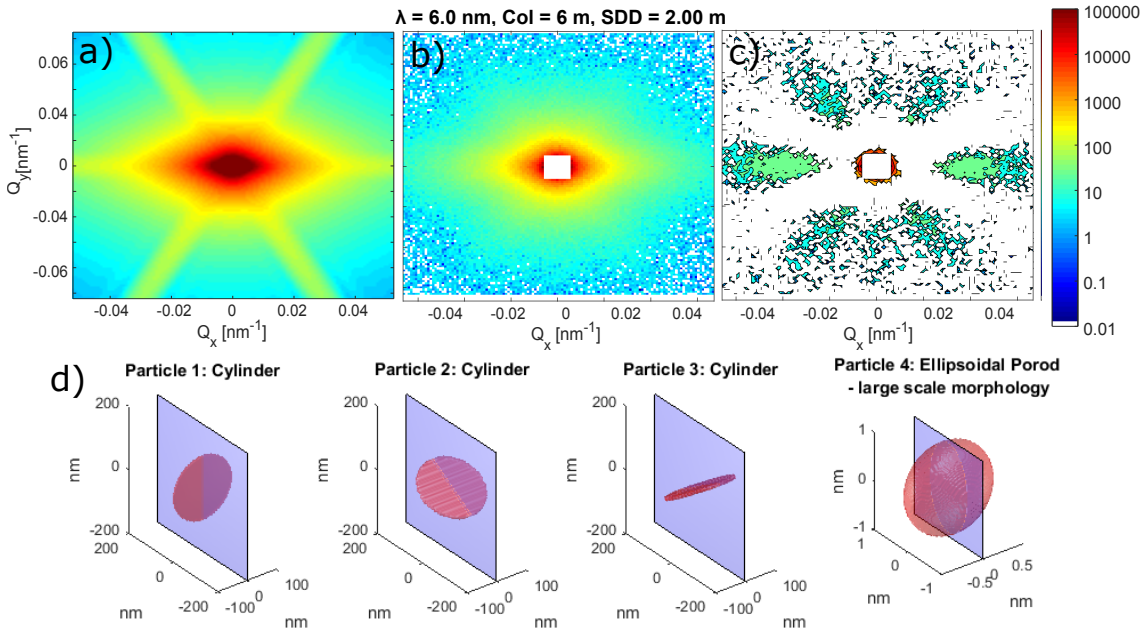

FIGURE B.1.3: (a) Model of three thin cylinders, superimposed by a generalized Porod like background; (b) scattering signal of an MHC sample; (c) signal from the MHC sample, corrected for the generalized Porod like background, i.e. only from the form factor of the thin cylinders. The fitted platelets are aligned to the matrix (d) due to its strong texture.

scattering signal from the HfC streaks and the residual signal after subtracting the fitted Porod like background from the scattering cross-section is presented in Figure B.1.3b and c. The fitted platelets and a representation for the Porod like background are presented in Figure B.1.3d.

Ellipsoid The 3D form factor of an ellipsoid can be calculated by a coordinate transform of the reciprocal $\vec{Q}$-space

$$\vec{Q}' = SR\vec{Q} \tag{B.3}$$

with a rotation matrix R and a diagonal matrix S that has the values of the semi-principal axes of the ellipsoid on its diagonal. Then, its Fourier transform is calculated by the spherical form factor of the transformed $\vec{Q}'$-space.

$$I_{El}(\vec{Q}) = I_{sp}(Q') = I_sp(|SR\vec{Q}|) \quad . \tag{B.4}$$

The resulting image in reciprocal space is depicted in Fig. B.1.4. The image strongly varies with the particle orientation in proportion to the incoming neutron beam.

Cube The 3D form factor of a cube can be decomposed into the $1D$-Fourier transforms along the edges of the cube. The cube's orientation is defined by a rotation matrix R that defines the coordinate transformation $Q' = RQ$. Then, the scattering signal is given by

$$I_{cu}(\vec{Q}) = \left(\frac{\sin Q'_x a}{Q'_x a}\right)^2 \left(\frac{\sin Q'_y b}{Q'_y b}\right)^2 \left(\frac{\sin Q'_z b}{Q'_z b}\right)^2 \tag{B.5}$$

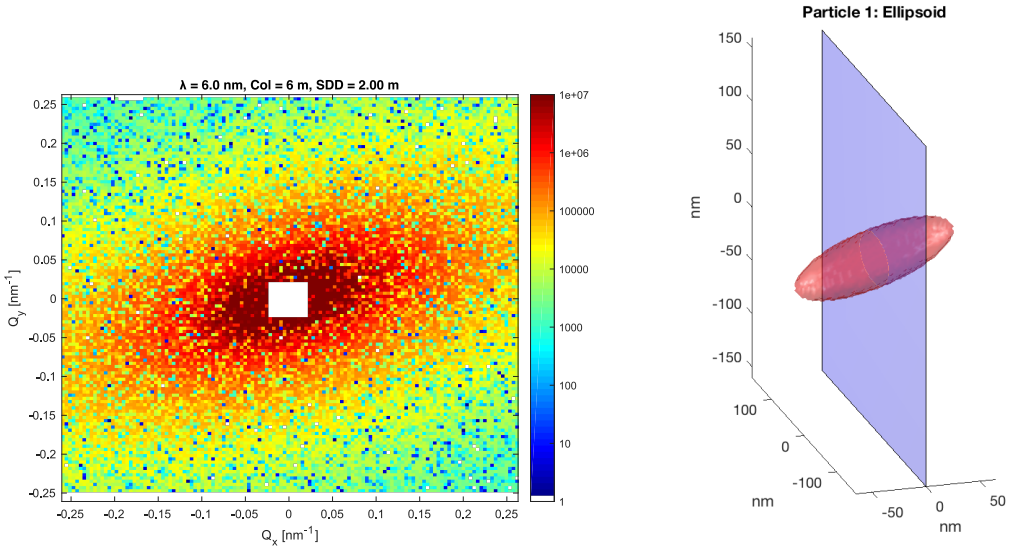

FIGURE B.1.4: Simulated scattering signal of a single ellipsoid with the depicted orientation to the sample plane in blue.

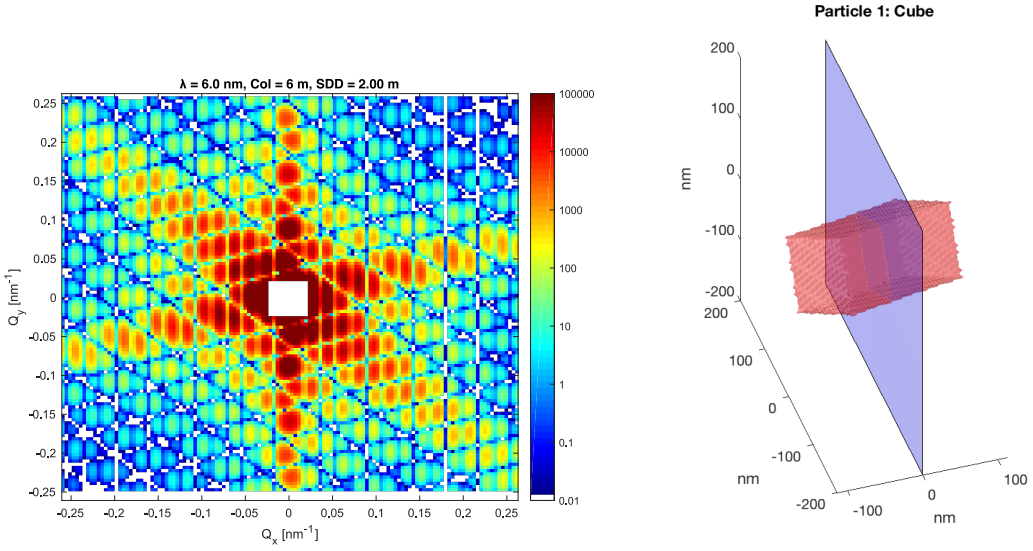

FIGURE B.1.5: Simulated scattering signal of a single cube with the depicted orientation to the sample plane in blue.

The resulting image in reciprocal space is depicted in Fig. B.1.5. The image strongly varies with the particle orientation in proportion to the incoming neutron beam.

B.2 Generalization of Porod scattering

If there exists a preferred orientation relationship of non-spherical large scale structures, their scattering produces an anisotropic background signal. Such behavior was observed in a sintered Mo-Hf-C material [172]. The raw, as-sintered material showed an isotropic Q^{-4} Porod background due to large sintering pores as depicted in Fig. B.2.1a. However, after compression of the sintered material, the background signal obtained an anisotropic

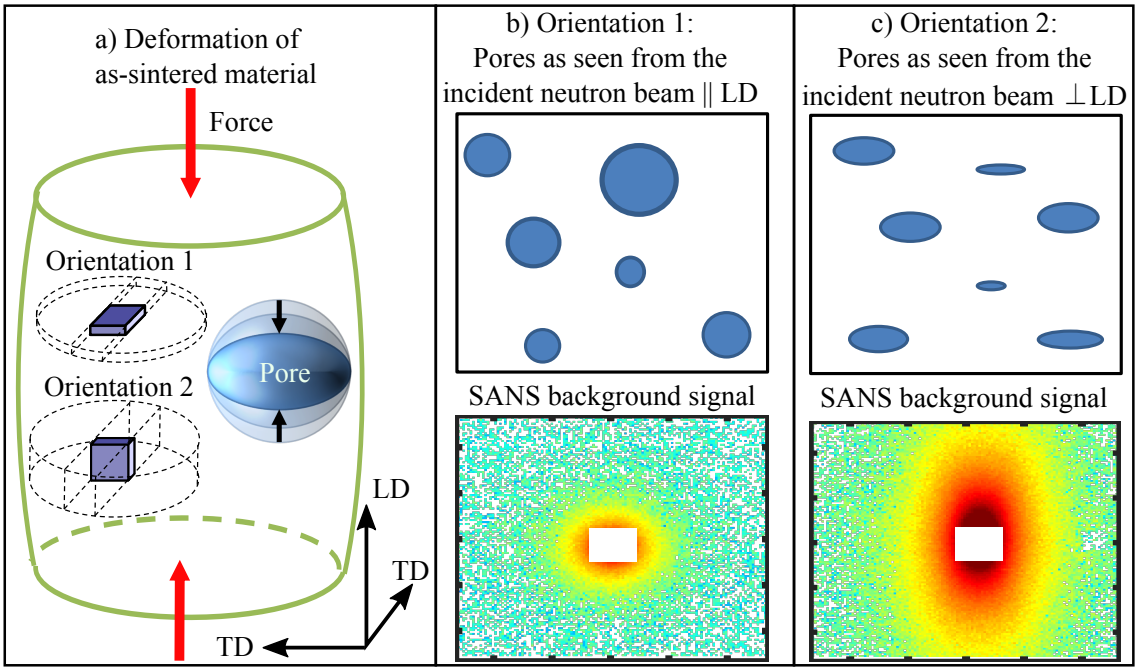

Figure B.2.1: (a) Scheme of the as-sintered and (b) the as-compressed material. The deformation of large-scale pores results in an anisotropic SANS signal.

shape (Fig. B.2.1b). Even after an recrystallization treatment at 1873 K, this behavior was observed. SANS could therefore yield evidence, that such large pores do not heal from the material.

In order to quantify such type of signal for considering it in the fit, a generalized, $\vec{Q}$-depending Porod background signal can be derived according to [173]

$$I(\vec{Q}) = \frac{4\pi\Delta\rho^2}{Q^4} \sum_j^N \frac{1}{\kappa_{G,j}(\pm\vec{Q})} \quad , \tag{B.6}$$

where $\kappa_{G,j}$ is the Gaussian curvature of the j-th particle. Therefore, the Q^{-4} decrease is more or less strong in a direction of the vector $\vec{Q}$, depending on the Gaussian curvature of all particle surfaces.

Assuming that the radii of curvature $R = 1/\kappa_G$ of all N large-scale structures are symmetrically distributed (e.g. by a Gaussian), the sum can be replaced by the mean value of all radii of curvature of all N particles, i.e. by $N\bar{R}$.

In the present case, the large scale structure's interfaces are modeled by the inverse image $f^{-1}(0)$ of the function

$$f(x,y,z) = \left(\frac{x}{a}\right)^2 + \left(\frac{y}{b}\right)^{2/\beta} + \left(\frac{z}{c}\right)^{2/\beta} - 1 \quad , \tag{B.7}$$

i.e. by $\{(\bar{x},\bar{y},\bar{z}) \in \mathbb{R} : f(\bar{x},\bar{y},\bar{z}) = 0\}$. This shape is denoted β-ellipsoid. For $\beta = 1$, $f^{-1}(0)$ yields an ellipsoid with half-axis vector (a,b,c). The parameter β is introduced to allow more *blocky* shapes (Figure B.2.2(top)). In order to avoid a numerical singularity, β is not used for the term $(x/a)^2$, which is only a small restriction as shown later. The Gaussian curvature of

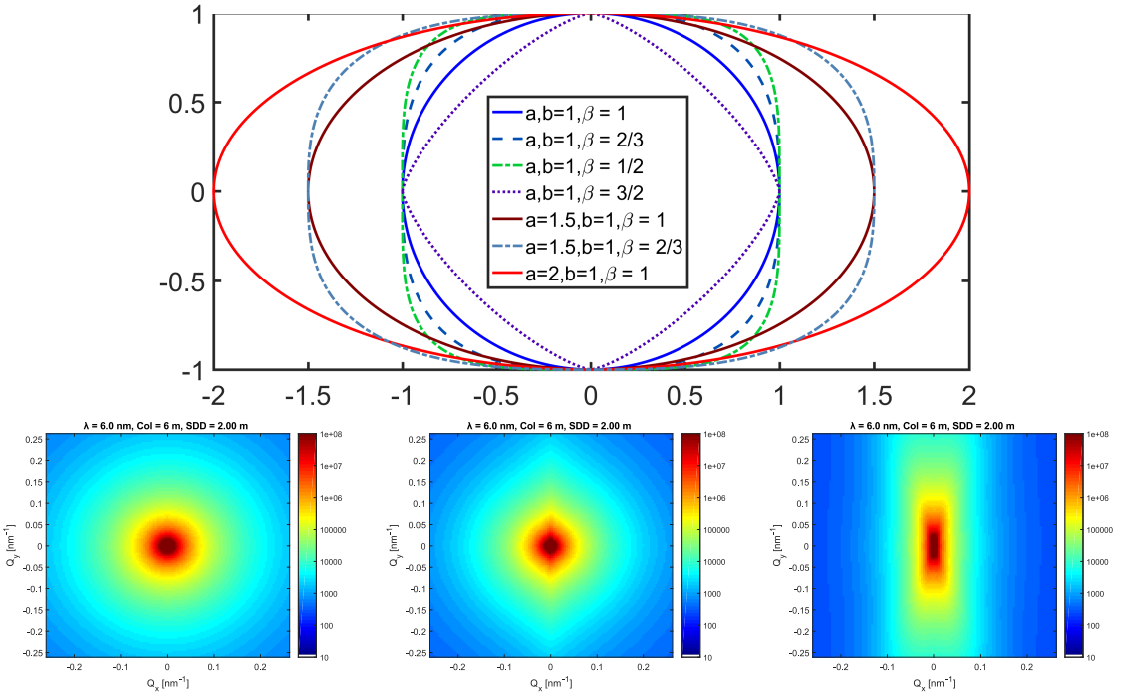

FIGURE B.2.2: (top) Possible large scale shapes that can be obtained with the model of the β-ellipsoid. (bottom) Simulated SAS patterns from β-cuboidal Porod background. (left) $a = b = \beta = 1$; (middle) $a/b = 1.3, \beta = 3/2$; (right) $a/b = 1.3, \beta = 2/3$.

this object can be calculated according to [174]

$$\kappa_\beta = \frac{\nabla f^T \cdot \mathrm{adj}(H_f) \cdot \nabla f}{|\nabla f|^4}, \tag{B.8}$$

with the gradient ∇f and the adjoint matrix of the Hessian $\mathrm{adj}(H_f)$ of the function f. For $\beta \to 0$, the shape gets more cuboidal, while for $\beta \geq 2$ the shape is no longer convex. For $\beta \geq 2$, κ_β is set to 1 at $x, y = 0$, since the Gaussian curvature is not defined at these points.

The calculation can be simplified in the case of $\beta = 1$, where [174]

$$\kappa_G = \frac{1}{a^2 b^2 c^2} \frac{1}{g^4}, \tag{B.9}$$

with

$$g = g(x, y, z) = \sqrt{\frac{x^2}{a^4} + \frac{y^2}{b^4} + \frac{z^2}{c^4}}. \tag{B.10}$$

Only the contribution of the curvature perpendicular to the neutron beam is *seen* in the measurement, since in small-angle scattering the scattering vector $\vec{Q}$ in the argument of κ is parallel to the detector plane. With this formula, the degree of deformation a/b of large scale structures can be fitted. Fig. B.2.2 shows examples of simulated SAS signals.

The method was applied in [172], where a strongly deformed and textured Mo-Hf-C sample contained ellipsoidal pores that were oriented according to the matrix texture (Fig. B.1.3). As a result, the SANS signal from precipitates was strongly overshadowed by an anisotropic Porod-like signal.

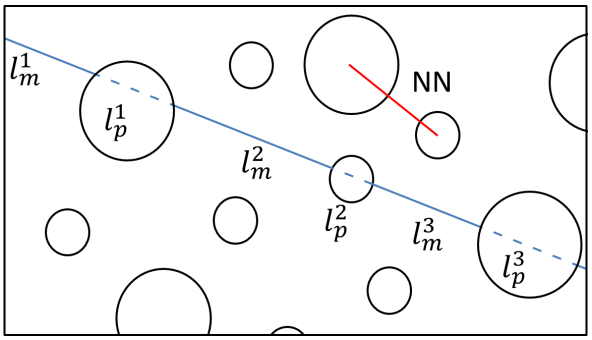

Figure B.3.1: The particle size distribution derived from SANS gives experimentally access to $\langle l_p \rangle$ of the dilute phase. From that, the mean line intersection length $\langle l_m \rangle = 1/N \sum_j^N l_m^j$ can be calculated. The nearest neighbor distance (NN) is marked with a red bar.

B.3 Moments of the size distribution

If the scattering particles are denoted to a size distribution in the modeling (cf. section 3.1.2.4), various physical parameters can be obtained from the moments of order p of the particle size distributions [59, 85]

$$\langle R^p \rangle = \frac{\int_0^\infty \mathcal{N}(R) R^p \, \mathrm{d}R}{\int_0^\infty \mathcal{N}(R) \, \mathrm{d}R} \quad . \tag{B.11}$$

If the scattering structures are N spheres with a particle size distribution, some important structural parameters can be automatically derived with the provided Matlab package from the moments of the size distribution

$$\text{Mean particle radius} \quad r = \langle R \rangle \quad , \tag{B.12}$$

$$\text{Volume weighted radius} \quad r_v = \langle R^3 \rangle \quad , \tag{B.13}$$

$$\text{Volume fraction} \quad w_p = N \frac{4}{3} \pi \langle R^3 \rangle \quad , \tag{B.14}$$

$$\text{Correlation length} \quad l_c = \frac{\langle R^4 \rangle}{\langle R^3 \rangle} \quad , \tag{B.15}$$

$$\text{Mean intersection length} \quad l_m = \frac{\langle R^3 \rangle}{\langle R^2 \rangle} \quad . \tag{B.16}$$

If the volume fraction w_p of a particle distribution in a two-phase system is known, the mean intersection length can be used to calculate the inter-particle distance between the particles l_p [10]

$$l_p / l_m = w_p / w_m \quad , \tag{B.17}$$

where w_m is the volume fraction of the matrix $w_m = 1 - w_p$. The inter-particle distance derived from this eq. (B.17) is depicted in Fig. B.3.1. This value can be used to obtain statistical information about the environment of a particle in a matrix. By definition, the value is always larger than the nearest neighbor distance (NN) between two particles. In Co-Re alloys, it usually attains values around 500 nm, while SEM suggests an NN in the range of 50 nm. Similar calculations can be derived for non-spherical common particle geometries.

B.4 Error estimates for integral parameters

In order to measure the scattering volume fraction in an in-situ SANS experiment with high time resolution, one can use the scattering invariant Q_{inv}. However, the measured accuracy of $Q_{\mathrm{inv}} = \int_0^\infty \mathrm{d}Q\ Q^2 I(Q)$ is limited since it is defined as integral over $\mathbb{R}^+ = [0, \infty]$. Such a measurement is not possible in a true experiment as can directly be seen on the definition of $Q = 4\pi/\lambda\ \sin(2\theta/2) \leq 4\pi/\lambda < \infty$. In the limit $Q \to 0$, the detector pixel resolution limits the accuracy. Especially in a SANS measurement, only small values of 2θ are considered. Hence, it is important to chose an appropriate Q-interval $[Q_{\mathrm{min}}, Q_{\mathrm{max}}]$ for an accurate estimate of Q_{inv}. In the following, an error approximation is given for Q, depending on the scattering particle size.

The case of the spherical form factor is treated. Other form factors can be calculated similarly. Let

$$Q_{\mathrm{inv}} = \underbrace{\int_0^{Q_{\mathrm{min}}} dQ\ Q^2 I(Q)}_{A} + \underbrace{\int_{Q_{\mathrm{min}}}^{Q_{\mathrm{max}}} dQ\ Q^2 I(Q)}_{B} + \underbrace{\int_{Q_{\mathrm{max}}}^{\infty} dQ\ Q^2 I(Q)}_{C} \quad , \tag{B.18}$$

where the interval $[Q_{\mathrm{min}}, Q_{\mathrm{max}}]$ defines the accessible Q-range in the measurement. In order to achieve a good accuracy, the goal is to maximize B or minimize A and C. Using the form factor of a sphere $I(Q) = I_{\mathrm{sp}}(Q; R)$ with radius R (eq. (B.1)), an indefinite integral of eq. (B.18) can be calculated

$$\begin{aligned} &\int dQ\ Q^2 I_{\mathrm{sp}}(Q; R) \\ &= \frac{2R^3x^3\mathrm{Si}(2Rx) - 3R^2x^2 + (R^2x^2 + 1)\cos(2Rx) + 2Rx\sin(2Rx) - 1}{6x^3} + \mathrm{const.} \quad , \end{aligned} \tag{B.19}$$

with the sine integral function $\mathrm{Si}(x) = \int_0^x \sin(t)/t \mathrm{d}t$. Constant pre-factors of $I_{\mathrm{sp}}(Q; R)$ were neglected for this calculation. The scattering invariant can therefore be calculated explicitly

$$\begin{aligned} Q_{\mathrm{inv}} &= \lim_{x \to \infty} \frac{2R^3x^3\mathrm{Si}(2Rx) - 3R^2x^2 + (R^2x^2 + 1)\cos(2Rx) + 2Rx\sin(2Rx) - 1}{6x^3} \\ &= \frac{R^3\pi}{6} \quad . \end{aligned} \tag{B.20}$$

A numerical assessment yields

$$A = 0.05 \cdot Q_{\mathrm{inv}} \qquad \text{for } Q^R_{\mathrm{min}} = 0.92/R \quad , \tag{B.21}$$

$$C = 0.05 \cdot Q_{\mathrm{inv}} \qquad \text{for } Q^R_{\mathrm{max}} = 18.97/R \quad , \tag{B.22}$$

and therefore $B = 0.9 \cdot Q_{\mathrm{inv}}$ with the settings $[Q^R_{\mathrm{min}}, Q^R_{\mathrm{max}}]$. This demonstrates the importance of a large accessible Q-range per instrument setting to quantify the scattering volume fraction with only one geometry. At the SANS-1 instrument, the order of magnitude of accessible Q-values per geometry is almost exactly equal to the necessary ratio $Q_{\mathrm{min}}/Q_{\mathrm{max}} = 0.0485$ to detect 90% of the scattering volume. The fast experiments with only one instrument geometry were optimized for these settings and the respective expected scattering precipitate size R.

B.5 Model-free fits of SAS Data

Based on the *indirect Fourier transformation method* from Glatter and Kratky [175] and the *regularization method* from Svergun et al. [176], a method for model-free fits of Data from SAS was developed. Their classic papers yield very powerful tools for the model-free reconstruction of a scattering pattern. However, they are confined to $1D$ problems and their regularization approaches are rather heuristic. In the following, they are extended to higher dimensional problems and combined with modern regularization tools. The elastic net [177], a combination of L_1 and L_2 regularization was applied. The methods are nowadays widely used in image processing, as they combines the advantages of classic Tikhonov L^2 regularization and feature selection in sparse feature spaces by L^1 regularization.

Such a procedure is useful if the scattering pattern of a SAS experiment is anisotropic and the form factor of the scatterer is unknown. If a function $\Delta\rho$ represents an unknown scattering length density of a scattering sample, then the *SANS operator* $\mathcal{I}$ describes the scattering data obtained as the output of the experiment. Hence, the inverse of the SAS operator $\mathcal{I}^{-1}$ is required to reconstruct the original scattering length density from the scattering data. The operator has the structure of a squared Fourier transform $\mathcal{F}$, smeared with the SAS resolution function $T = T_{\text{det}} \circ T_{\text{col}} \circ T_{\lambda}$ (cf. section A.4)

$$\mathcal{I}(\rho) = T \circ |\mathcal{F}(\rho)|^2 \quad . \tag{B.23}$$

Two strategies for a model-free solution of this equations are used in the literature: (1) A two-step solution that uses the identity $|\mathcal{F}(\rho)|^2 = (\mathcal{F})(\rho \hat{*} \rho)$ (cf. eq. (3.31)). First, the autocorrelation function $\rho \hat{*} \rho$ is reconstructed and then a deconvolution algorithm is applied [170, 178]. (2) A direct solution of the problem $\mathcal{I}^{-1}$ by means of an optimization algorithm that fits a real space function to the data [176].

The solution of this problem is called an ill-posed inverse problem, since the goal is to find the not necessarily continuous inverse $\mathcal{I}^{-1}$ of a smoothing operator. Not continuous means, that the solution is not stable with respect to measurement errors and small deviations in the given data might result in completely different solutions. A smoothing operator has non-unique solutions. The latter is a consequence of the resolution functionals, applied to the SAS data and the phase problem in scattering, i.e. the loss of phase information during detection of a the scattered radiation. For such a problem, a regularization method of the interpolated function is crucial for the reconstruction. The regularization integrates *a priori* information about the unknown scattering length density function $\Delta\rho$ of the scattering sample into the problem.

The results from the presented procedures are interpreted as multi-dimensional size distributions of precipitates in *superalloys*. A full data set of the detector with $n \times m$ pixels can be used, without premature azimuthal integration. A trust region Levenberg-Marquardt method with several regularization methods is used to solve the problem. L_2-regularization can be applied in order to prefer continuously differentiable functions – such as size distributions – or L_1-regularization to prefer locally constant step-functions – such as sharp boundaries of single particles. The program is written in Matlab.

B.5.1 Two-step method: Reconstruction of the autocorrelation function and convolution square root

B.5.1.1 Reconstruction of the autocorrelation

The inverse Fourier transform of the unsmeared SANS signal I yields the autocorrelation function

$$\mathcal{F}^{-1}I = \rho \hat{*} \rho = \gamma(\rho) \quad . \tag{B.24}$$

However, the Fourier transform is smeared with the resolution functional $\mathcal{T}$ and the experimental data is only given for discrete values. The idea is to reformulate the problem as a generalized interpolation problem that can be applied on an interpolation function space.

Suppose the data matrix $g_\chi \in \mathbb{R}^K$ of an experiment is given. Then a generalized interpolant is a function $\gamma \in H(\Omega)$, satisfying

$$\lambda_k(\gamma) = g_k, \quad \forall\ 1 \leq k \leq K \quad , \tag{B.25}$$

with $(\lambda_1, \ldots, \lambda_k)^T \in \mathbb{R}^K$ the set of real-valued, linear *information functionals*, that contain the *experimental results* on γ. For the discrete data matrix g_χ, they have to satisfy $\mathcal{I}(\gamma)(\vec{Q}^k) = \lambda_k(\gamma)$. The information functionals are given by

$$\lambda_k = \Delta\Omega_k \circ (\mathcal{T} \circ \mathcal{F}) \quad . \tag{B.26}$$

with point evaluation functionals $\Delta\Omega_k$ for single discrete scattering vectors $\vec{Q}^k$, pointing on a detector pixel. Additionally, the $\Delta\Omega_k$ contain the solid angle correction for this pixel. These λ_k are continuous functionals on the space of band-limited functions (due to the component wise continuity of the convolution and Fourier Transform on $L^2(\Omega)$ for band-limited functions).

The solution to this problem is determined in the finite dimensional recovery space

$$\mathcal{V}_K := \mathrm{span}\{\lambda_k(\phi(\|\cdot - y\|)) | 1 \leq k \leq K\}, \tag{B.27}$$

generated by a positive definite interpolation kernel ϕ. The recovery space is therefore created by applying the information functional to an interpolating function from a recovery space $H(\Omega)$. The recovery space can be chosen as the set of B-splines of order p, which are recursively defined for $1D$ by

$$N^1 = \frac{1}{h}\mathbf{1}_{x_{j+1}-x_j} \quad , \tag{B.28}$$

$$N^p(x) = (N^{p-1} * N^1)(x) = \int_{x_j}^{x_{j+1}} N^{p-1}(x-t) \cdot \mathrm{d}t \quad , \tag{B.29}$$

where h is the distance between the grid points x_j. In the present approach, the d-dimensional B-spline interpolant for a vector $\vec{x} = (x_1, x_2, \ldots, x_D)$ is defined by $N^p(\|\vec{x}\|)$.

Another choice is the set of Gaussians kernels with standard deviation as a parameter σ (Fig. B.5.1c,e)

$$\phi(x) = \exp(-\frac{\sigma^2}{2}||x - x_j||^2) \quad . \tag{B.30}$$

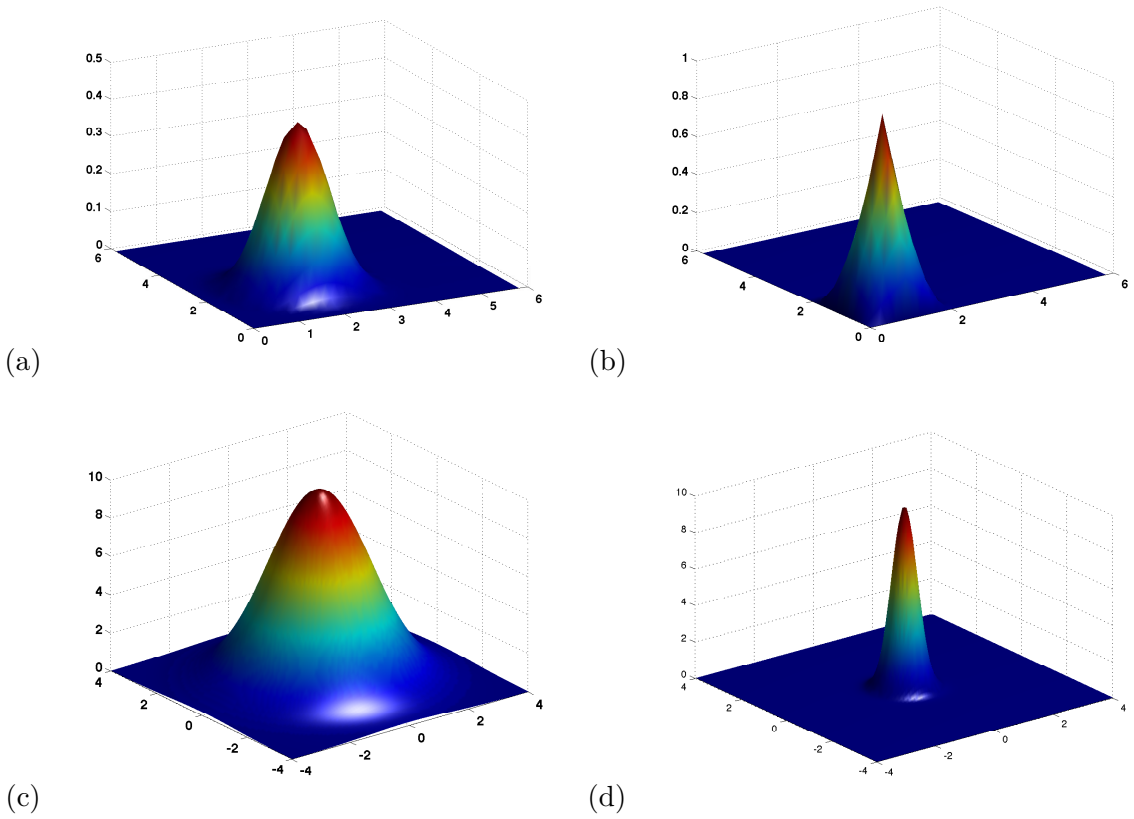

Figure B.5.1: Different interpolation kernels. (a) cubic and (b) linear B-spline. (c,d) Gaussians with varying widths. The width should be chosen according to the density of the interpolation mesh.

This approach is motivated by the fact that the space, generated by Gaussians, interpolates the band-limited functions – i.e. the functions whose Fourier transform has a bound support and is therefore resolution limited to certain Q-values – arbitrarily well [179]. Hence, this is a *natural* space to seek for band-limited solutions of the autocorrelation. In order to guarantee performance, one should select an interpolant that has an analytical Fourier transform, which is a given for B-splines or Gaussians. Therefore, the space $H(\Omega)$ is a *reprodcuing kernel hilbert space*. In such a space the optimality of the recovered solution can be shown [180]. Optimality means, that there exists a norm-minimal, unique solution in the interpolation space. The goal is inverting the linear operator

$$\mathcal{M} : H(\Omega) \to \mathbb{R}^{K\times L}, \qquad \mathcal{M} = \mathcal{T} \circ \mathcal{F} \quad . \tag{B.31}$$

with the Fourier Transform $\mathcal{F}$ and an appropriate function space H.

Given the set of information functionals $\Lambda = \{\lambda_1, \ldots, \lambda_K\}$, the norm-minimal solution of the autocorrelation function f^* to the problem $\mathcal{M}_\chi(f) = g_\chi$ can be reconstruction by the following algorithm

Algorithm 1

Assume linear independency of Λ. Let $\tilde{f}$ be the solution of the continuous operator equation $T \circ \mathcal{F}(f) = g$ with the resolution functional

$Ts(x) = \int_\Omega \Pi_j k_j(x,y)s(y)\mathrm{d}y, \qquad k_j(x,y) = \frac{1}{\sigma_j\sqrt{2\pi}} e^{-\frac{1}{2}(\frac{y}{\sigma_j})^2}.$

1: **Input**: Data from detector $g_\chi \in \mathbb{R}^K$, $\chi = \{Q^k : 1 < k < K\}$ discrete pixel positions, interpolation kernel ϕ.

2: Generate the SANS matrix on a $K^{'} \times L^{'}$ grid in real space

$(\mathcal{M}_{\Lambda,\phi})_k^{k',l'} = \sum_{k',l'} \lambda_k \phi(\|x^{k'} - x^{l'}\|) \in \mathbb{R}^K \times (K'L')$

3: Solve the linear system

$(\mathcal{M}_{\Lambda,\phi})\alpha = g_\chi.$

4: Generate the basis functions

$v_{kl}(x) = \mathcal{M}_\chi(\phi(\cdot - x)) = \Delta\Omega_k T \int_\Omega e^{-ix^T\vec{Q}}\phi(\cdot - x)\,\mathrm{d}x$

5: **Output**:

$f^* = \sum_{k=1}^K \alpha_k v_k \ \in \mathcal{V}_K$

which is the unique norm-minimal solution of $\mathcal{M}_\chi(f) = g_\chi$ and satisfies

$\mathcal{M}_\chi(f^*)(\vec{Q}_k) = \mathcal{M}_\chi(\tilde{f})(\vec{Q}), \qquad$ for every $1 \le k \le K$.

The numerical complexity of the problem is therefore depending on the SANS matrix dimension $(\mathcal{M}_{\Lambda,\phi})_k^{k',l'} \in \mathbb{R}^K \times (K'L')$. Note that the application of the information functionals λ_k on B-splines equals a Fourier transform and a convolution, which can be calculated efficiently, since the analytical Fourier transform of the B-spline basis exists [181]

$$\mathcal{F}(N^p)(Q) = e^{-ipQ/2}\left(\frac{\sin Q/2}{Q/2}\right)^p \quad , (p \ge 1, Q \in \mathbb{R}) \quad . \tag{B.32}$$

B.5.1.2 Deconvolution of the autocorrelation

In order to deconvolve the reconstructed autocorrelation function $\gamma := \rho\hat{*}\rho$, a generalized interpolant has to be found in the recovery space

$$\mathcal{V}_\chi := \mathrm{span}\{\phi^p(\cdot, y_k)|y_k \in \mathcal{Y}\} \quad . \tag{B.33}$$

In the following the cardinal B-spline basis of order p is applied to the problem

$$\phi^p(x,y) = N^p(x-y), \tag{B.34}$$

on an equidistant grid $\mathcal{Y} = (y_1, \ldots y_{K'})$, $y_k \in A$, $1 \le k \le K^{'}$, $A \subset \mathbb{R}^2$. The recovered interpolation functions have the form

$$\rho_a^p = \sum_{j=1}^{K^{'}} c_j N^p(\cdot - y_j), \qquad y_j \in \mathcal{Y}, \tag{B.35}$$

with coefficients c_j to be determined with two-dimensional B-splines of order p.

For the autocorrelation of two B-spline basis functions an explicit formula can be calculated. Since $N^p \in S(\mathbb{R})$ is contained in the Schwartz space for all p, the B-splines can be represented

in the Fourier basis. Using the representation for their Fourier transform $\hat{N}$, one gets

$$\begin{aligned}(N^p(x-y_k)\hat{*}N^p(x-y_j))\,(q) =& \frac{1}{2\pi}\int_{-\infty}^{\infty} |\hat{N}^p(q)|^2 e^{iq^T x} e^{iq^T(y_k-y_j)} dq \\ =& \frac{1}{2\pi}\int_{-\infty}^{\infty} |\hat{N}^{2p}(q)| e^{iq^T p} e^{iq^T x} e^{iq^T(y_k-y_j)} dq \\ =& N^{2p}(x+y_k-y_j+p).\end{aligned} \tag{B.36}$$

W.l.o.g., assume $y_1 = (0,0)^T$, $y_2 = (1,0)^T$, $y_{(K'+1)} = (0,1)^T, \ldots$. For the interpolant ρ_a^p with coefficient vector $c \in \mathbb{R}^N$, the DIM matrix $A_p \in \mathbb{R}^{N\times N}$ is defined by

$$A_p(x) = \begin{pmatrix} N^{2p}(x+p) & N^{2p}(x+p+1) & \ldots & N^{2p}(x+p+N-1) \\ N^{2p}(x+p-1) & N^{2p}(x+p) & & N^{2p}(x+p+N-2) \\ \vdots & & \ddots & \vdots \\ N^{2p}(x+p-N+1) & N^{2p}(x+p-N+2) & \ldots & N^{2p}(x+p) \end{pmatrix} . \tag{B.37}$$

With this matrix, the autocorrelation of the interpolant ρ_a is given by

$$(\rho_a^p \hat{*} \rho_a^p)(x) = c^T A_p(x) c \quad . \tag{B.38}$$

The solution to this problem simplifies to determining the right sign to the coefficients c_j. This is strongly depending on the applied regularization technique (cf. section B.5.4).

B.5.2 Inverse Fourier Transform Method

Instead of recovering the autocorrelation function, the inverse Fourier Transform method (IFT) seeks to invert the full SANS operator in reciprocal space. The coefficients c_j of the interpolant eq. (B.35) have to be determined for the B-spline basis of order p. The evaluation operators λ_k are nonlinear for this problem, since the SANS operator eq. (B.23) is nonlinear. The SANS operator with resolution smearing

$$T \circ \mathcal{I}(f) = g \tag{B.39}$$

is applied on the generalized interpolation function on the real space grid $\{y_j, 1\}$

$$(\lambda_k \circ \rho_a^p)(x) = \Delta\Omega_k \circ T \circ \left| \mathcal{F}\left(\sum_{j=1}^{K'} c_i N^p(x-y_j) \right)(\vec{Q}^k) \right|^2 = g_k. \tag{B.40}$$

The operation $\mathcal{I}(\rho)$ in eq. (B.39) can be calculated explicitly, since the Fourier transform of the B-spline of order p is given by $\hat{N}^p(Q) = e^{-ipQ/2}\,\mathrm{sinc}^p(Q/2)$

$$\begin{aligned}
\mathcal{I}(\rho_a^p) = |\hat{\rho}_a^p|^2 &= \left|\sum_{j=1}^{K'} \widehat{c_j\phi_j}\right|^2 = \left|\sum_{j=1}^{K'} c_j\hat{\phi}_j\right|^2 \\
&= \sum_{j=1}^{K'} c_j\hat{\phi}_j \sum_{k}^{K'} c_k\overline{\hat{\phi}_k} = \sum_{j,k\leq K',} c_jc_k\widehat{\phi_j}\overline{\widehat{\phi_k}} \\
&= \sum_{j,k\leq K'} c_jc_ke^{-i(y_j-y_k)^T(\cdot)}\hat{N}^p\overline{\widehat{N^p}} = \sum_{j,k\leq K',L'} c_jc_ke^{-i(y_j-y_k)^T(\cdot)}|\hat{N}^p|^2 \\
&= \sum_{j,k\leq K'} c_jc_ke^{-i(y_j-y_k)^T(\cdot)}\mathrm{sinc}^{2p}(\cdot/2) \\
&= c^T\hat{A}(\cdot)c,
\end{aligned} \tag{B.41}$$

with the CIM matrix $\hat{A}(q) = e^{-i(y_j-y_k)^T(q)}\,\mathrm{sinc}^{2p}(q/2) \in \mathbb{R}^{K'}$. This matrix has to be calculated for each detector position $q = (q_y, q_z) \in \chi$. The coefficient vectors c are determined by a least squares minimization technique (c.f. section B.5.3).

The performance of a fit hugely benefits from analytical derivatives of the interpolation function. The operator $\mathcal{I}$ in eq. (B.39) is fitted by an interpolant with the coefficients c_j and the derivative of the discrete with respect to c_j can be explicitly calculated

$$\begin{aligned}
\frac{\partial\mathcal{F}(\rho_a^p(c))}{\partial c_l} &= \frac{\partial}{\partial c_l}\left(\sum_{j=1}^{N} c_j\hat{\phi}_j \sum_{k=1}^{N} c_k\overline{\hat{\phi}_k}\right) \\
&= \hat{\phi}_l\sum_{k=1}^{N} c_k\overline{\hat{\phi}_k} + \overline{\hat{\phi}_l}\sum_{j=1}^{N} c_j\hat{\phi}_j \\
&= e^{-ix_l^T(\cdot)}\hat{\phi}\sum_{k=1}^{N} c_ke^{ix_k^T(\cdot)}\overline{\hat{\phi}} + \overline{\hat{\phi}}e^{ix_l^T(\cdot)}\sum_{j=1}^{N} c_j\hat{\phi}e^{-ix_j^T(\cdot)} \quad .
\end{aligned} \tag{B.42}$$

This linearization is used in each step of the evaluation model. The derivative to eq. (B.39) is then easily calculated using the chain rule and the analytic representation from eq. (B.41) for $\mathcal{I}(\rho)$.

B.5.3 Optimization and Regularization

Solving eq. (B.23), is a problem of the form

$$\mathcal{I}(u) = \lambda \quad , \tag{B.43}$$

where u is the unknown solution, λ the data and J, the SANS operator. Such an equation is called well posed if (1) the solution is unique and (2) the solution is stable with respect to errors. Therefore, $\mathcal{I}^{-1}$ has to be continuous. Neither of these preconditions is necessarily fulfilled. Due to the quadratic structure of $\mathcal{I}$, the imaginary information of the Fourier transform is lost and the SANS operator is smoothing due to the resolution functionals (section A.4) [176].

In such a setting, a unique solution can only be found in a constrained setting, where several regularization assumptions have to be implemented. A solution is searched by a minimizing procedure in a control space. This yields a problem of the form

$$\begin{cases} \min \mathcal{J}(u,\rho) = \frac{1}{2}\|u-u_d\|^2_{L^2} + \pi(\rho) \\ \text{subject to } \mathcal{I}(\rho) = u \quad \text{in } \Omega, \quad a \le \rho \le b \quad , \end{cases} \tag{B.44}$$

with data $u_d \in L^2(\Omega)$, $a \le b$, $\Omega \in \mathbb{R}^n$ bound, convex and closed and a control function $\pi : Q \to \mathbb{R}^+ \cup \{0\}$. The control π is an appropriate semi-norm acting as a penalty function. If the function ρ is chosen from and interpolation space with the form $\rho_a = \sum c_j \phi_j$, then π acts as a control on the function space parameters c_j. For example, the penalty function π might restrict the differences between c_j and therefore gets large if parameters c_j deviate strongly.

The optimization algorithm uses a linear approximation of ρ in each step, i.e. the target function is approximated by the gradient $J = \nabla\mathcal{I} = \left(\frac{\partial\mathcal{I}_i}{\partial c_j}\right)$ and therefore, the problem transforms into the form

$$\begin{cases} \min \mathcal{J}(u,\rho) = \frac{1}{2}\|Jc-u_d\|^2_{L^2} + \pi(c) \\ a \le c \le b \quad . \end{cases} \tag{B.45}$$

The fits with were implemented in Matlab and the minimization was performed with a Trust-Region Levenberg-Marquardt algorithm [182–184]. In order to chose efficient steps during the minimization, an analytic gradient of the target function $\mathcal{J}$ is given by eq. (B.42). The second derivate – the Hess matrix – was approximated by $\mathcal{J}^T\mathcal{J}$.

B.5.4 Regularization for the inverse problem of SANS

In the following L^1, L^2 and *elastic net* regularization are discussed.

L^1 and L^2 regularization An appropriate regularization for the DIM and the deconvolution of an autocorrelation function as part of the CIM might come from the assumption that the solution to the problem eq. (B.45) has sparse features. The scattering particles are contained at local positions with locally constant scattering length density ρ. Such solutions can be found with L^1 regularization [185]

$$L_1 : \pi_1(c) = ||c||_1 = \sum_{j=1}^{N} |c_j| \quad . \tag{B.46}$$

The vector c consists of the B-spline coefficients. The optimality conditions for minimization of such regularization terms are discussed elsewhere [185]. For numerical stability, the L_1 norm is replaced with a continuously, differentiable approximation (Huber-loss function)

$$\|c\|_{1,\beta} = \begin{cases} c - \frac{\beta}{2} & \text{if } c \ge \beta, \\ -c - \frac{\beta}{2} & \text{if } c \le -\beta, \\ \frac{1}{2\beta}c^2, & \text{if } |c| < \beta \quad . \end{cases} \tag{B.47}$$

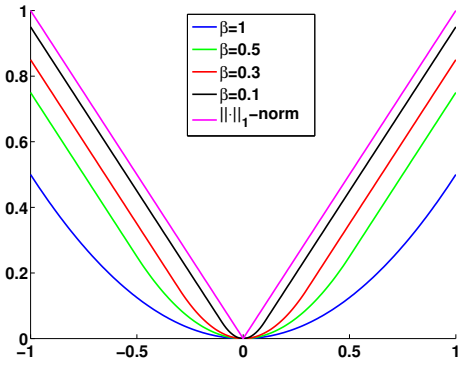

FIGURE B.5.2: Huber-loss function for varying β parameter.

For $\beta \to 0$, function converges to the L_1 norm, but it is continuously differentiable for any $\beta > 0$. The function is depicted in Fig. B.5.2.

The L^2 regularization penalty function has the form

$$L^2 : \pi_2(c) = ||Lc||^2 = \sum_{i=1}^{N} \sum_{j=1}^{N} ||l_{j,i} c_j||^2 \quad , \tag{B.48}$$

for N coefficients. This corresponds to the classic Tikhonov regularization [186]. If the parameter β is sufficiently large and the matrix L is positive definite, the problem eq. (B.44) will become convex and is therefore well defined. Common choices for the matrix L are the identity (L^2 regularization) or can consist terms that approximate the derivative, such as Glatter's method [178] in $1D$

$$\begin{pmatrix} 1 & -1 & 0 & & & \dots & 0 \\ -1 & 2 & -1 & 0 & & \dots & 0 \\ 0 & -1 & 2 & -1 & & \dots & 0 \\ \vdots & & & \ddots & & & \vdots \\ \vdots & & & & \ddots & & \vdots \\ 0 & & \cdots & & -1 & 2 & -1 \\ 0 & & \cdots & & 0 & 2 & -1 \end{pmatrix} \quad . \tag{B.49}$$

In higher dimensions, the matrix is extended to a tensor, that implies the regularization terms in each dimension, so that in $2D$:

$$||Lc||^2 = \sum_{j=1}^{K-1} \sum_{I=1}^{L-1} (c_{j+1,k} - c_{j,k})^2 + (c_{j,k+1} - c_{j,k})^2 \quad , \tag{B.50}$$

for $K \times L$ coefficients. This approach is strongly related to the total variation denoising theory in image processing [187].

Elastic Net Regularization The elastic net regularization performs a convex combination of both techniques eq. (B.47) and (B.48) [177]. The penalty function has the form

$$\pi = \lambda||Lc||_2^2 + \mu||\beta||_{1,c} \quad . \tag{B.51}$$

For the matrix L, Glatter's matrix was used eq. (B.49).

With these regularization techniques, the target function in eq. (B.45) reads

$$\|Jc - u_d\|_2^2 + \lambda\|Lc\|_2^2 + \mu\|c\|_1 \tag{B.52}$$

Rules for choosing the μ and λ parameters is given by the point of inflexion method, discussed by Glatter [170]. The basic idea is to calculate eq. (B.52) for several selections of μ and λ and find optimal values before a strong mean deviation of the B-spline coefficients c_j is observed. A strong deviation usually corresponds to an over-stabilization.

The minimization was performed by a trust region semi-smooth newton algorithm with regularization for minimizing a function f with gradient ∇f, μ_0 penalty parameters for L_1 regularization, λ_0 penalty parameter for L_2 regularization, r_{hi} and r_{lo} maximum and minimum step size parameters for the descending step in order to confine the step-size to reasonable values, β_0 the smoothness of the Huber-loss function, TOL, $N_{\max}$ the exit conditions for accuracy and number of steps. The algorithm is described in [188] and the optimality conditions for the elastic net are taken from [189]. The algorithm follows the scheme:

Algorithm 2

CIM/DIM Levenberg-Marquard with trust region and elastic net

Input: $f, \nabla f, \lambda_0, \beta_0 > 0,\ r_{\text{lo}} > 0,\ r_{\text{hi}} > r_{\text{lo}}, \mu_0,\ N_{\max}$, TOL
Set $n = 0,\ (c, \mu, \lambda) = (c_0,\ \mu_0,\ \lambda_0)$
repeat ▷ for decreasing μ, improve L_1-regularization
    Set $r = f(c),\ J = \nabla f(c),\ P = \nabla \| \cdot \|_{1,\ \beta_0},\ S = r^T r + \mu \|c\|_{1,\beta_0}$,
        $H = J^T J, v = J^T r, L = \text{diag}(H))$ or Glatter's matrix
    repeat ▷ Levenberg-Marquardt for different trust regions
        Solve optimality system for p,

$$p = (H + \lambda L + \mu P)^{-1} v$$

        Set $n \leftarrow n + 1,\ c^{'} = c - p,\ r^{'} = f(c^{'}),\ S^{'} = (r^{'})^T r^{'} + \mu \|c^{'}\|_{1,\beta_0}$,
            $dS = p^T(2 * v - H)p,\ \rho = \frac{S - S^{'}}{dS}$ ▷ predicted reduction by Taylor
        if $\rho > r_{\text{hi}}$ ▷ check size of reduction and adjust L_2 regularization
            $\lambda \leftarrow \lambda/2$, ▷ for high reduction decrease gradient step
        elseif $\rho < r_{\text{lo}}$
            $\lambda \leftarrow \lambda\nu$ ▷ $\nu \in [2, 10]$, depending on ρ
        end
        if $S^{'} < S$
            Set $S \leftarrow S^{'},\ c \leftarrow c^{'},\ r \leftarrow r^{'},\ J \leftarrow \nabla f(c),\ H \leftarrow J^T J$,
                $L \leftarrow$ update, $v \leftarrow J^T r,\ P \leftarrow \nabla \| \cdot \|_{1,\beta_0}$
        end
    until $n > N_{\max}$ or $f(c) < \mu$Tol
    Set $\mu = \mu/2$
until $f(c) <$ Tol or $n > N_{\max}$
Output: Coefficients for the B-spline basis functions. Calculate solution
    $\rho_a(x) = \sum c_j \phi_j(x)$.

B.5.5 Implementation

With the previously presented regularization tools, an algorithm for a model-free solution of the SANS problem B.43 looks as follows

B.5.6 Results with Artificial Data

In the following, the scattering from artificially created structures is simulated to test the multidimensional reconstruction techniques.

Example B.1 *Single cube with edge size 20 nm* (Figure 7.2.1).
The scattering from a single cube was simulated. As starting parameters, a sphere with radius 10 nm was created on a real space grid of 10×10 points. As exit condition, a relative tolerance of $\chi^2 = 1\%$ was chosen. Fig. B.5.4 shows the artificially created cube, its simulated scattering pattern and the reconstruction. The shape quickly converges to that of a cube and the fit terminated after a total of 101 steps. For this test, the regularization parameters were chosen beforehand $\lambda = \mu = 1$. In table B.5.1 shows the fit results with the CIM technique. Fig. B.5.4

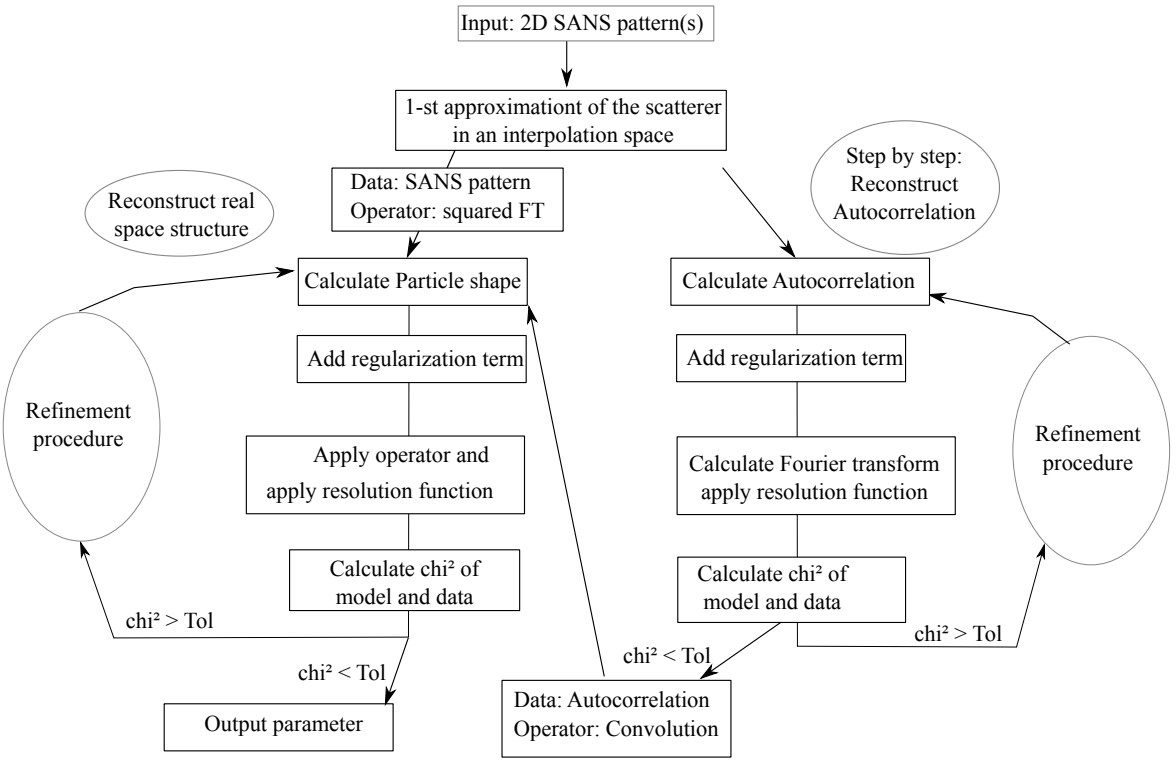

Figure B.5.3: Scheme of the different steps of the two presented techniques for model-free reconstruction of SAS data.

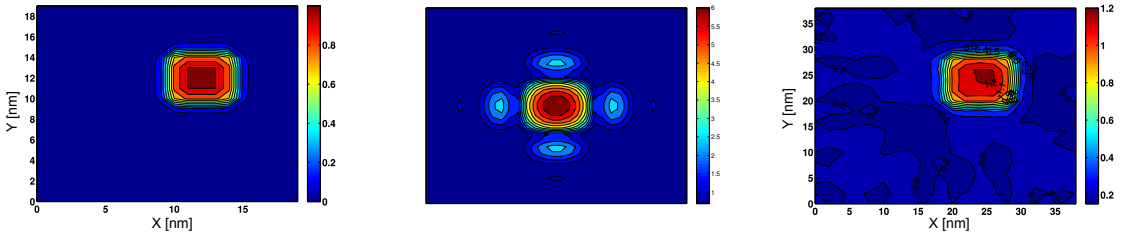

Figure B.5.4: (left) Artificially created cube. (middle) simulated SANS signal. (right) Reconstruction.

Basis functions	B-spline order	Newton Steps	Regularization steps	Exit condition
10×10	3	101	5	reduced $\chi^2/100 < 1\%$
20×20	3	205	5	reduced $\chi^2/400 < 1\%$

Table B.5.1: Fit results with CIM technique for a cube.

Example B.2 *Single plate with size* $15 \times 70\,\mathrm{nm}^2$

As starting parameters, a sphere with radius 10 nm was simulated. As exit condition, a relative tolerance of $\chi^2 = 1\%$ was chosen. Fig. B.5.4 shows the artificially created cube, its simulated scattering pattern and the reconstruction. The shape quickly converges to that of a cube and the fit terminated after a total of 160 newton steps. For this test, the regularization parameters were chosen beforehand $\lambda = \mu = 1$. Table B.5.2 shows the fit results with the CIM technique. The Fig. B.5.5

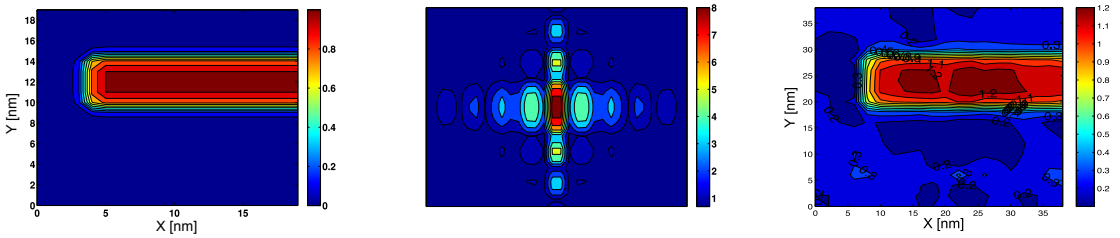

FIGURE B.5.5: (left) Artificially created plate. (middle) simulated SANS signal. (right) Reconstruction.

Basis functions	B-spline order	Newton Steps	Regularization steps	Exit condition
10×10	3	160	5	reduced $\chi^2/100 < 1\%$
20×20	3	313	5	reduced $\chi^2/400 < 1\%$

TABLE B.5.2: Fit results with CIM technique for a plate.

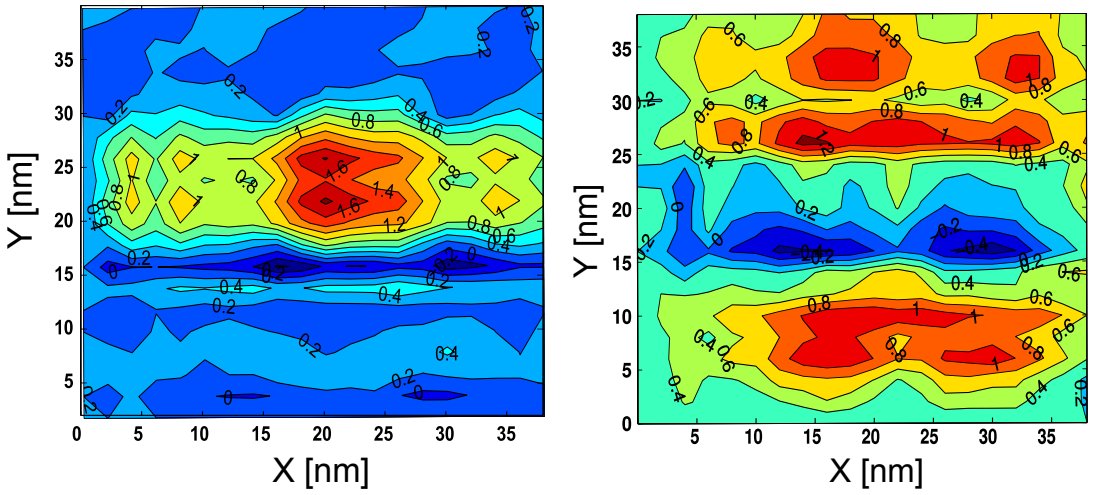

FIGURE B.5.6: (left) Reconstruction without sparse feature regularization L^1. (right) without any regularization.

Example B.3 *Importance of regularization* The regularization is crucial for the fits. Images of fits only with the Tikhonov L_2 regularization term and without any regularization are presented in Fig. B.5.6. The fit still converges with Tikhonov regularization only (Fig. B.5.6 left). Without any regularization, the fit does not yield a useful result (Fig. B.5.6 right).

B.5.7 The Application on a Latex Standard Sample

The DIM method is applied to the round robin latex standard sample (cf. Fig. A.4.3). In the first step, the autocorrelation is reconstructed, taking into account the instrument resolution functions. A B-spline basis grid of size 25×25 was used for the reconstruction and the cubic B-spline interpolation with elastic net regularization was applied.

The fit with DIM is depicted in Fig. B.5.7. The reconstructed autocorrelation function is expectedly smooth, due to the smoothing cubic spline regularization. The parameter λ was chosen by $1 - 1/(1 + h^3/6)$, where $h = x_{i,jj+1} - xi, jj$ is the distance between two grid points. The cubic splines were deconvoluted with the elastic net regularization. The fit yields

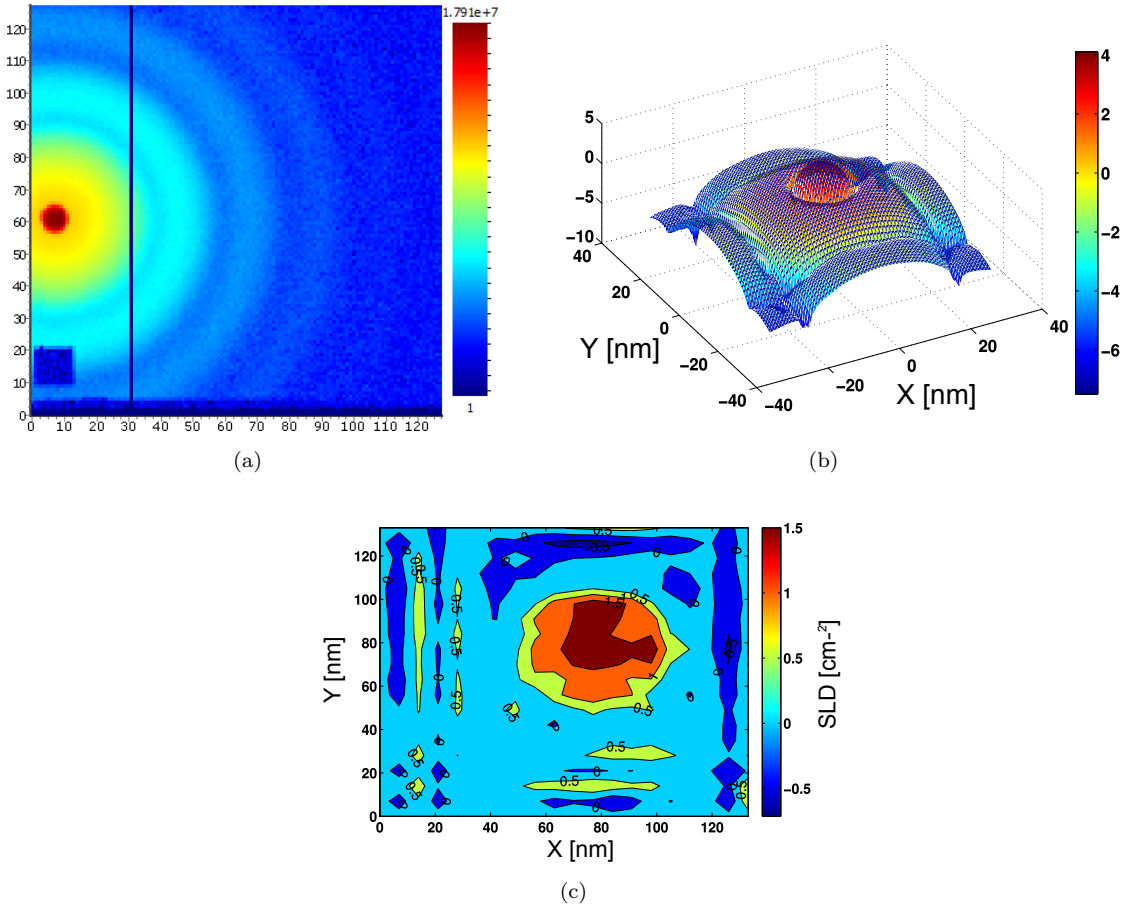

Figure B.5.7: (a) SANS pattern from latex polystyrene sample. (b) reconstructed autocorrelation function. (c) Deconvolution of particle shape, using the elastic net for regularization.

a particle size of $\sim 63\,\text{nm}$, which is within 10% of the reported size value of $\sim 72\,\text{nm}$ [190]. The fit converged with the exit condition reduced $\chi^2 < 0.01$.

B.5.8 Results from a superalloy

The CIM method is applied to a Co-Re superalloy sample containing nano-scale TaC precipitates. Fig. B.5.9a, b shows the high resolution pattern, measured with collimation $= 20\,\text{m}$, sample-detector distance $d_0 = 20\,\text{m}$ and a neutron wavelength $\lambda = 1.2\,\text{nm}$ before and after a 6 h heat treatment at 1473 K. A standard evaluation from the azimuthal averaged $1D$ curves is shown in Fig. B.5.8.

As starting parameters a sphere with radius $R0 = 15\,\text{nm}$ is created with the Spline basis. Larger structures are neglected, by choosing the recovery space of size $70 \times 70\,\text{nm}$. The fit is performed to $K \times L = 128 \times 128$ detector data. For the real space reconstruction grid a resolution with 25×25 cubic B-spline basis functions was chosen. In addition, the model is superimposed by a Porod fit to large scale structures (cf. eq. (3.39)).

The fit results from the CIM method are presented in Fig. B.5.9c, d. The fits terminated with a weighted $\chi^2 < 1\%$. The fits show the expected behavior from TaC precipitates. It can be seen that the reconstructed structures continuously decrease from their center to the edges. Due to the applied elastic net regularization with Glatter's matrix L and the L^1 term,

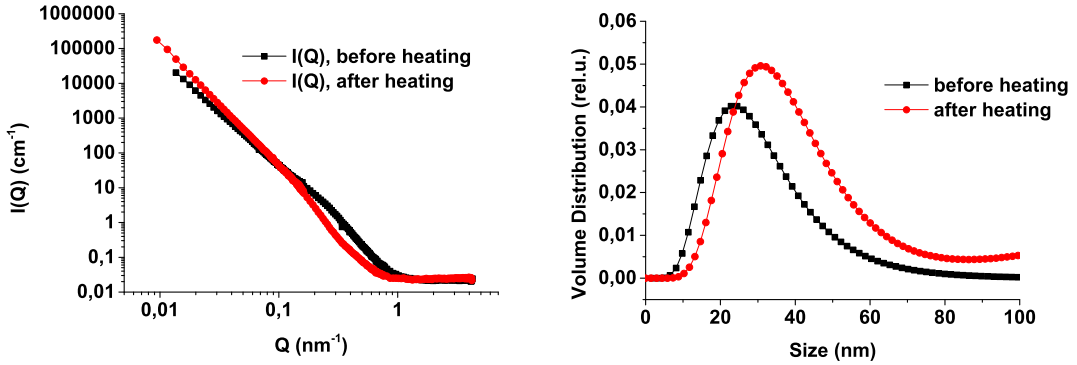

FIGURE B.5.8: (left) 1*D* SANS patterns of a Co-Re alloy before and after a heat treatment at 1200 K. (right) Corresponding volume distributions.

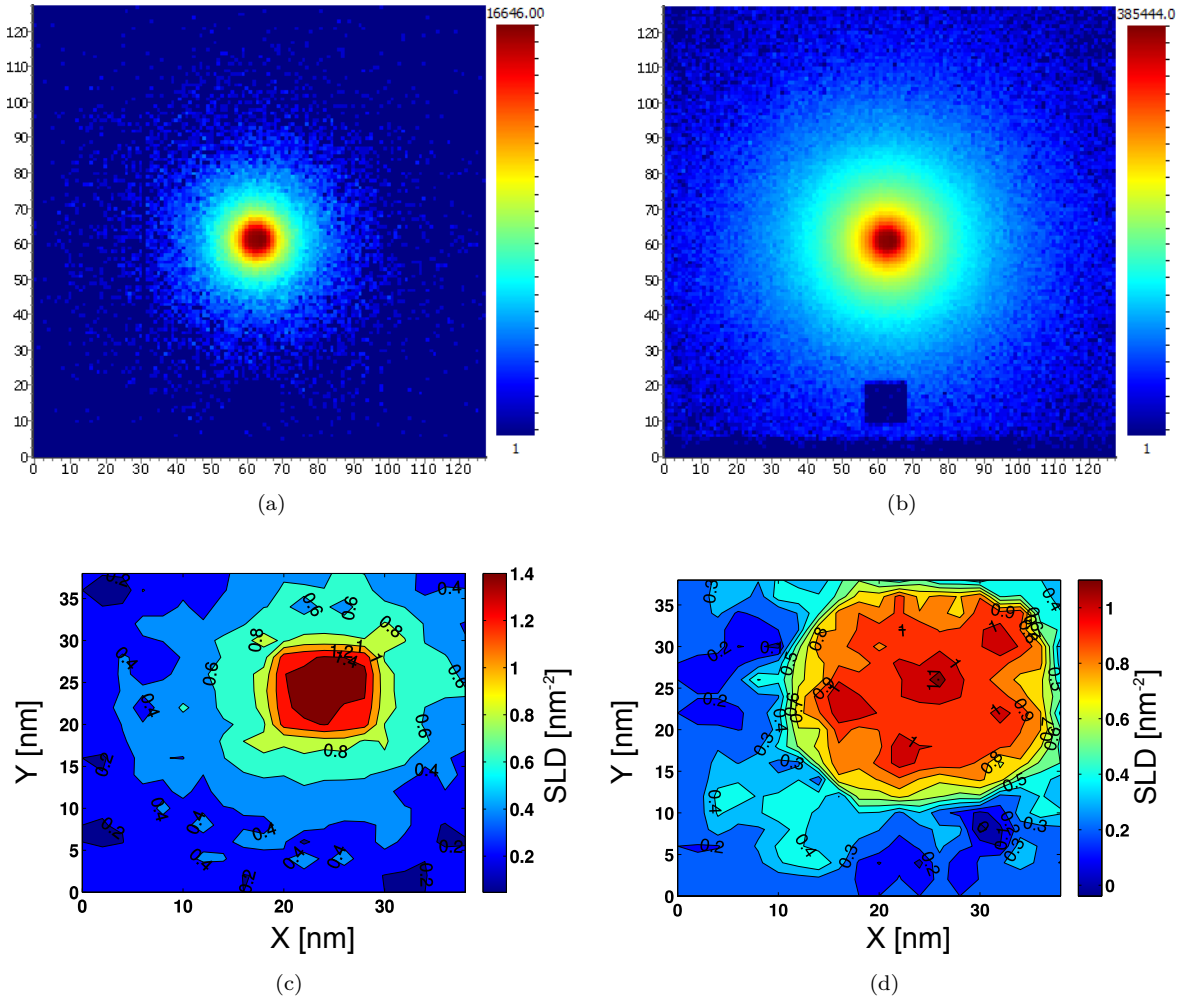

FIGURE B.5.9: Two-dimensional SANS patterns before (a) and after (b) heat treatment. (c) and (d) show the respective fitted particles on a nm scale. The scattering contrast is given in relative units.

smooth functions with sparse features are preferred. The results are therefore interpreted as size distributions. The particles coarsen as a result of the heat treatment from 22 nm to 40 nm. These results are comparable with the fitted size distributions in Fig. B.5.9.

Acknowledgements

Allen voran bei Prof. Winfried Petry, dass ich diese Arbeit in den letzten dreieinhalb Jahren bei Ihnen durchführen konnte. Vielen Dank, dass ich ein Teil zu der großartigen wissenschaftlichen Arbeit des Heinz Maier-Leibnitz Zentrum beitragen durfte.
Besonderer Dank gilt Ralph Gilles, der das MLZ ursprünglich in der Entwicklung and Co-Re Legierungen eingebunden hat und diese Arbeit hauptsächlich betreut hat. Danke für die großen Freiheiten, die du mir für meine wissenschaftliche Arbeit gewährt hast.
Bei Debashis Mukherji möchte ich mich für die mittlerweile sechsjährige Zusammenarbeit und sein stets offenes Ohr zu Fragen rund um die Materialphysik bedanken. Große Teile dieser Arbeit wären ohne diese Zusammenarbeit nicht möglich gewesen.
Bei Pavel Strunz bedanke ich mich für die Einführung in die Geheimnisse der Neutronenkleinwinkelstreuung. Viele verwendete Auswertemethoden basieren auf seinen Ideen und Anregungen.
Dem gesamten SANS-1 Team: Sebastian Mühlbauer, Andre Heinemann, Sebastian Busch, Andreas Wilhelm, Svato Semecky für die großartige Zusammenarbeit am Instrument und die stets vorhande Unterstützung bei jeglicher Art von Fragen.
Vielen Dank an Prof. Joachim Rösler, dessen konstruktive Anregungen diese Arbeit auf ein höheres Niveau gehoben haben.
Bei allen Kollegen am MLZ und der TUM möchte ich mich bedanken. Insbesondere bei Armin Kriele für die große Unterstützung im Labor, Stefan Seidlmayer für die zahlreichen Diskussionen und ganz besonders bei der Probenumgebung um Jürgen Peters und Milan Antic, ohne die die Hochtemperaturexperimente undenkbar gewesen wären.

Vielen Dank an meine Freunde auf die ich mich immer verlassen konnte und ohne die letzten Jahre nicht halb so schön geweswen wären: Felix, Leonie, Tobi, Saskia, Paddo, Karin, Manu, Fritz, Richard, Andre, Alex, Markus, Tina, Ellen, Sebastian, Sebastian Konrad, Jusuf, Irina, Mary, Chrischi, Seeger, Thomas. Danke Pascal, meine Gedanken sind weiterhin sehr häufig bei deiner Familie und dir.

Ganz besonderer Dank gilt meiner Familie: Anne, Eva, Manfred, Gerd, Nok, Niels, Gertrud, Klaus, Susanne, Hanna und Theo, Erich, Janna, Lena, Marcel, Anna und Paula.

Der deutschen Forschungsgemeinschaft danke ich herzlich für die finanzielle und ideelle Förderung meiner Arbeit (Projekt GI 242/4-1).

Meike, danke dass du mir in den letzten Jahren immer zur Seite gestanden bist und mir immer unheimlich viel Kraft gegeben hast. Dir ist diese Arbeit gewidmet. Ich freue mich riesig auf unsere weitere gemeinsame Zukunft.

Abbreviations & Symbols

Abbreviations

CIM	**C**omplete **I**nversion **M**ethod
DIM	**D**econvolution **I**nversion **M**ethod
EBSD	**E**lectron **B**ack**S**catter **D**iffraction
EDS	**E**nergy-**D**ispersive X-ray **S**pectroscopy
fcc	**f**ace-**c**entered **c**ubic
gb	**g**rain **b**oundary
hcp	**h**exagonal **c**lose-**p**acked
HT	**H**igh **T**emperature(s)
IPF	**I**nverse **P**ole **F**igure
IQ	**I**mage **Q**uality
KWN	**K**ampmann-**W**agner **N**umerical model
LM	**L**evenberg **M**arquardt
LSW	**L**ifshitz-**S**lyozov-**W**agner theory of Ostwald ripening
MLSW	**M**odified **L**ifshitz-**S**lyozov-**W**agner theory of Ostwald ripening
ND	**N**eutron **D**iffraction
RT	**R**oom **T**emperature
SEM	**S**canning **E**lectron **M**icroscopy
SLD	**S**cattering **L**ength **D**ensity
SE	**S**econdary **E**lectron image
SANS	**S**mall **A**ngle **N**eutron **S**cattering
SAS	**S**mall **A**ngle **S**cattering
SAXS	**S**mall **A**ngle **X**-ray **S**cattering
ST	**S**tandard homogenization **T**reatment
SX	**S**ingle crystal
TEM	**T**ransmission **E**lectron **M**icroscopy
TCP	**T**opologically **C**lose **P**acked

XRD **X-R**ay **D**iffraction

Symbols

a_j	Lattice constant of phase j
C_0	Initial concentration of solute in the matrix
C_α	Solute concentration in the matrix
$C_{\alpha,\mathrm{eq}}$	Equilibrium solute concentration of phase α
$C_{\alpha,\mathrm{int}}$	Equ. solute concentration of phase α at interface
C_β	Solute concentration in the secondary phase
l_p	Inter-particle distance
$\vec{Q}$	Scattering vector
Q	Modulus of the scattering vector
Q_C	Activation energy for coarsening
Q_G	Activation energy for growth
Q_N	Activation energy for nucleation
Q_D	Activation energy for diffusion
v_j	Molar volume of phase j
$\left(\frac{d\sigma}{d\Omega}\right)$	Differential scattering cross section
$\left(\frac{\mathrm{d}\sigma}{\mathrm{d}\Omega}\right)_c$	Coherent scattering cross section
$\left(\frac{\mathrm{d}\sigma}{\mathrm{d}\Omega}\right)_i$	Incoherent scattering cross section
$\left(\frac{\mathrm{d}\Sigma}{\mathrm{d}\Omega}\right)$	Azimuthally averaged scattering cross section
ε	Strain
Γ	Surface tension
ρ	Scattering length density
$\Delta\rho$	Scattering contrast
σ	Stress
2θ	Scattering angle

Physical Constants

Boltzmann constant	k_B	$=$	$1.380\,648\,52(79) \times 10^{-23}\,\mathrm{J\,K^{-1}}$
Gas constant	R	$=$	$8.314\,459\,8(48)\,\mathrm{J\,K^{-1}\,mol^{-1}}$
Neutron mass	m_n	$=$	$1.009\,\mathrm{u} = 1.675 \times 10^{-27}\,\mathrm{kg}$
Planck's constant	$\hbar$	$=$	$1.054\,571\,726 \times 10^{-34}\,\mathrm{J\,s\,rad^{-1}}$

Publication List

(i) L. Karge, R. Gilles, D. Mukherji, P. Strunz, P. Beran, M. Hofmann, J. Gavilano, U. Keiderling, O. Dolotko, A. Kriele, A. Neubert, J. Rösler, and W. Petry. The influence of C/Ta ratio on TaC precipitates in Co-Re base alloys investigated by small-angle neutron scattering. *Acta Materialia*, 132:354–366, 2017. doi: 10.1016/j.actamat.2017.04.029.

(ii) L. Karge, R. Gilles, and S. Busch. Calibrating SANS data for instrument geometry and pixel sensitivity effects: access to an extended Q range. *Journal of applied crystallography*, 50(5):1382–1394, 2017. doi: 10.1107/s1600576717011463.

(iii) L. Karge, R. Gilles, D. Mukherji, P. Beran, P. Strunz, H. Markus, and R. Joachim. Beyond Ni-base superalloys: Influence of Cr addition on Co-Re base alloys strengthened by nanosized TaC precipitates. *Physica B: Condensed Matter*, in press, 2017. doi: 10.1016/j.physb.2017.11.059.

(iv) L. Karge, R. Gilles, D. Mukherji, B. Přemysl, P. Strunz, A. Stark, N. Schell, M. Hofmann, J. Häusler, and J. Rösler. Creep behavior of Co-Re-Ta-C alloys with varying C content – investigated in-situ by simultaneous synchrotron radiation diffraction. *Material Science and Engineering A*, 719:124–131, 2018. doi: 10.1016/j.msea.2018.02.009.

(v) P. Strunz, D. Mukherji, P. Beran, R. Gilles, L. Karge, M. Hofmann, M. Hoelzel, J. Rösler, and G. Farkas. Matrix Transformation in Boron Containing High-Temperature Co-Re-Cr Alloys. *Metals and Materials International*, in press, 2018. doi: 10.1007/s12540-018-0121-8.

(vi) D. Lang, L. Karge, J. Schatte, R. Gilles, R. Dallinger, I. Weißensteiner, P. Staron, W. Knabl, S. Primig, and H. Clemens. Evolution of strain-induced hafnium carbides in a molybdenum base Mo–Hf–C alloy studied by small-angle neutron scattering and complementary methods. *Journal of Alloys and Compounds*, 688:619–631, 2016. doi: 10.1016/j.jallcom.2016.06.282.

(vii) S. Mühlbauer, A. Heinemann, A. Wilhelm, L. Karge, A. Ostermann, I. Defendi, A. Schreyer, W. Petry, and R. Gilles. The new small-angle neutron scattering instrument SANS-1 at MLZ – characterization and first results. Nuclear Instruments & Methods

in Physics Research Section a – Accelerators Spectrometers Detectors and Associated Equipment, 832: 297-305, 2016. doi: 10.1016/j.nima.2016.06.105.

(viii) R. Gilles, D. Mukherji, L. Karge, P. Strunz, P. Beran, B. Barbier, A. Kriele, M. Hofmann, H. Eckerlebe, and J. Rösler. Stability of TaC precipitates in a Co-Re-based alloy being developed for ultra-high-temperature applications. *Journal of Applied Crystallography*, 49(4):1253–1265, 2016. doi: 10.1107/S1600576716009006.

(ix) P. Beran, D. Mukherji, P. Strunz, R. Gilles, M. Hofmann, L. Karge, O. Dolotko, and J. Rosler. Effect of composition on the matrix transformation of the Co-Re-Cr-Ta-C alloys. *Metals and Materials International*, 22(4):562–571, 2016. doi: 10.1007/s12540-016-5697-2.

(x) P. Strunz, D. Mukherji, R. Gilles, U. Gasser, P. Beran, G. Farkas, M. Hofmann, L. Karge, and J. Rösler. In Situ Neutron Diffraction Characterization of Phases in Co-Re-Based Alloys at High Temperatures. *Acta Physica Polonica A*, 128(4):684–688, 2015. doi: 10.12693/APhysPolA.128.684.

(xi) D. Mukherji, P. Strunz, R. Gilles, L. Karge, and J. Rösler. Current status of Co-Re-based alloys being developed to supplement Ni-based superalloys for ultra-high temperature applications in gas turbines. *Kovove Materialy-Metallic Materials*, 53(4):287–294, 2015. doi: 10.4149/km_2015_4_287.

(xii) S. Seidlmayer, J. Hattendorff, I. Buchberger, L. Karge, H. A. Gasteiger, and R. Gilles. In operando small-angle neutron scattering (SANS) on Li-ion batteries. *Journal of The Electrochemical Society*, 162(2):A3116–A3125, 2015. doi: 10.1149/2.0181502jes.

(xiii) R. Gilles, D. Mukherji, H. Eckerlebe, L. Karge, P. Staron, P. Strunz, and T. Lippmann. Investigations of early stage precipitation in a tungsten-rich nickel-base superalloy using SAXS and SANS. *Journal of Alloys and Compounds*, 612(0):90–97, 2014. doi: 10.1016/j.jallcom.2014.05.154.

(xiv) D. Mukherji, R. Gilles, L. Karge, P. Strunz, P. Beran, H. Eckerlebe, A. Stark, L. Szentmiklosi, Z. Macsik, G. Schumacher, I. Zizak, M. Hofmann, M. Hoelzel, and J. Rosler. Neutron and synchrotron probes in the development of Co-Re-based alloys for next generation gas turbines with an emphasis on the influence of boron additives. *Journal of Applied Crystallography*, 47(4):1417–1430, 2014. doi: 10.1107/S1600576714013624.

References

[1] R. Reed. *The superalloys [electronic resource]: fundamentals and applications*. Cambridge University Press, 2006. ISBN 9780521859042.

[2] J. H. Perepezko. The hotter the engine, the better. *Science*, 326(5956):1068–1069, 2009.

[3] R. E. Sonntag and C. Borgnakke. *Introduction to engineering thermodynamics*, volume 2. Wiley New York, 2001.

[4] N. P. Padture, M. Gell, and E. H. Jordan. Thermal barrier coatings for gas-turbine engine applications. *Science*, 296(5566):280–4, 2002. doi: 10.1126/science.1068609.

[5] M. Donachie. *Superalloys: A Technical Guide*. ASM International, 2002. ISBN 9781615030644.

[6] J. Sato, T. Omori, K. Oikawa, I. Ohnuma, R. Kainuma, and K. Ishida. Cobalt-base high-temperature alloys. *Science*, 312(5770):90–91, 2006.

[7] J. Rösler, D. Mukherji, and T. Baranski. Co-Re-based Alloys: A New Class of High Temperature Materials? *Advanced Engineering Materials*, 9(10):876–881, 2007. doi: 10.1002/adem.200700132.

[8] D. Mukherji, R. Gilles, L. Karge, P. Strunz, P. Beran, H. Eckerlebe, A. Stark, L. Szentmiklosi, Z. Macsik, G. Schumacher, I. Zizak, M. Hofmann, M. Hoelzel, and J. Rosler. Neutron and synchrotron probes in the development of Co-Re-based alloys for next generation gas turbines with an emphasis on the influence of boron additives. *Journal of Applied Crystallography*, 47(4):1417–1430, 2014. doi: 10.1107/S1600576714013624.

[9] R. Gilles, D. Mukherji, L. Karge, P. Strunz, P. Beran, B. Barbier, A. Kriele, M. Hofmann, H. Eckerlebe, and J. Rösler. Stability of TaC precipitates in a Co-Re-based alloy being developed for ultra-high-temperature applications. *Journal of Applied Crystallography*, 49(4):1253–1265, 2016. doi: 10.1107/S1600576716009006.

[10] L. Karge, R. Gilles, D. Mukherji, P. Strunz, P. Beran, M. Hofmann, J. Gavilano, U. Keiderling, O. Dolotko, A. Kriele, A. Neubert, J. Rösler, and W. Petry. The influence of C/Ta ratio on TaC precipitates in Co-Re base alloys investigated by small-angle neutron scattering. *Acta Materialia*, 132:354–366, 2017. doi: 10.1016/j.actamat.2017.04.029.

[11] S. Paranjpe. Small angle neutron scattering. Technical report, IAEA, 2006.

[12] B. Hammouda. Small-Angle Neutron Scattering (SANS), 05 2012. URL `http://www.ncnr.nist.gov/programs/sans/`.

[13] A. Bauer, S. Neumeier, F. Pyczak, and M. Göken. Microstructure and creep strength of different γ/γ'-strengthened Co-base superalloy variants. *Scripta Materialia*, 63(12):1197–1200, 2010.

[14] A. Suzuki, G. C. DeNolf, and T. M. Pollock. Flow stress anomalies in γ/γ' two-phase Co-Al-W-base alloys. *Scripta Materialia*, 56(5):385–388, 2007.

[15] D. Mukherji and J. Rösler. Design Considerations and Strengthening Mechanisms in Developing Co-Re-Based Alloys for Applications at $+100°C$ above Ni-Superalloys. *Advanced Materials Research*, 278:539–544, 2011. doi: 10.4028/www.scientific.net/AMR.278.539.

[16] T. Depka, C. Somsen, G. Eggeler, D. Mukherji, J. Rösler, M. Krüger, H. Saage, and M. Heilmaier. Microstructures of Co-Re-Cr, Mo-Si and Mo-Si-B high-temperature alloys. *Materials Science and Engineering: A*, 510-511:337–341, 2009. doi: 10.1016/j.msea.2008.06.054.

[17] D. Mukherji, P. Strunz, R. Gilles, M. Hofmann, F. Schmitz, and J. Rösler. Investigation of phase transformations by in-situ neutron diffraction in a Co-Re-based high temperature alloy. *Materials Letters*, 64(23):2608–2611, 2010. doi: 10.1016/j.matlet.2010.08.066.

[18] D. Mukherji, J. Rösler, P. Strunz, R. Gilles, G. Schumacher, and S. Piegert. Beyond Ni-based superalloys: Development of CoRe-based alloys for gas turbine applications at very high temperatures. *International Journal of Materials Research*, 102(9):1125–1132, 2011. doi: 10.3139/146.110563.

[19] D. Mukherji, P. Strunz, S. Piegert, R. Gilles, M. Hofmann, M. Hölzel, and J. Rösler. The Hexagonal Close-Packed (HCP) $\leftrightarrows$ Face-Centered Cubic (FCC) Transition in Co-Re-Based Experimental Alloys Investigated by Neutron Scattering. *Metallurgical and Materials Transactions A*, 43(6):1834–1844, 2012. doi: 10.1007/s11661-011-1058-4.

[20] P. Beran, D. Mukherji, P. Strunz, R. Gilles, M. Hofmann, L. Karge, O. Dolotko, and J. Rosler. Effect of composition on the matrix transformation of the Co-Re-Cr-Ta-C alloys. *Metals and Materials International*, 22(4):562–571, 2016. doi: 10.1007/s12540-016-5697-2.

[21] M.-X. Zhang, S.-Q. Chen, H.-P. Ren, and P. Kelly. Crystallography of the simple HCP/FCC system. *Metallurgical and Materials Transactions A*, 39(5):1077–1086, 2008.

[22] A. L. Bowman, G. P. Arnold, E. K. Storms, and N. G. Nereson. The crystal structure of Cr23C6. *Acta Crystallographica Section B*, 28(10):3102–3103, 1972. doi: doi:10.1107/S0567740872007526.

[23] J. W. Christian. *The theory of transformations in metals and alloys*. Pergamon Press, 1965. ISBN 978-0-08-044019-4.

[24] B. Strauss, F. Frey, W. Petry, J. Trampenau, K. Nicolaus, S. M. Shapiro, and J. Bossy. Martensitic phase transformation and lattice dynamics of fcc cobalt. *Physical Review B*, 54(9):6035–6038, 1996.

[25] X. Wu, N. Tao, Y. Hong, J. Lu, and K. Lu. $\gamma \rightarrow \epsilon$ martensite transformation and twinning deformation in fcc cobalt during surface mechanical attrition treatment. *Scripta Materialia*, 52(7):547–551, 2005. doi: 10.1016/j.scriptamat.2004.12.004.

[26] D. Mukherji, M. Klauke, P. Strunz, I. Zizak, G. Schumacher, A. Wiedenmann, and J. Rösler. High temperature stability of Cr-carbides in an experimental Co-Re-based alloy. *International Journal of Materials Research*, 101(3):340–348, 2010.

[27] N. Wanderka, M. S. Mousa, P. Henke, O. Korchuganova, D. Mukherji, J. Rösler, and J. Banhart. Carbides in Co-Re-Cr-based high-temperature alloys. *Journal of Materials Science*, 51(15):7145–7155, 2016. doi: 10.1007/s10853-016-9995-3.

[28] A. I. Gusev, A. S. Kurlov, and V. N. Lipatnikov. Atomic and vacancy ordering in carbide ζ-Ta4C3-x ($0.28 \leq x \leq 0.40$) and phase equilibria in the Ta-C system. *Journal of Solid State Chemistry*, 180(11):3234–3246, 2007. doi: 10.1016/j.jssc.2007.09.015.

[29] D. Mukherji and J. Rösler. Co-Re-based alloys for high temperature applications: Design considerations and strengthening mechanisms. *Journal of Physics: Conference Series*, 240:012066, 2010. doi: 10.1088/1742-6596/240/1/012066.

[30] D. Mukherji, J. Rösler, M. Krüger, M. Heilmaier, M.-C. Bölitz, R. Völkl, U. Glatzel, and L. Szentmiklósi. The effects of boron addition on the microstructure and mechanical properties of Co–Re-based high-temperature alloys. *Scripta Materialia*, 66(1):60 – 63, 2012. doi: 10.1016/j.scriptamat.2011.10.007.

[31] D. Mukherji, J. Rösler, J. Wehrs, H. Eckerlebe, and R. Gilles. Co-Re-based alloys a new class of material for gas turbine applications at very high temperatures. *Advanced in Materials Research*, Vol. 1, No.3:205–219, 2012. doi: 10.1002/adem.200700132.

[32] D. Mukherji, P. Strunz, R. Gilles, L. Karge, and J. Rösler. Current status of Co-Re-based alloys being developed to supplement Ni-based superalloys for ultra-high temperature applications in gas turbines. *Kovove Materialy-Metallic Materials*, 53(4): 287–294, 2015. doi: 10.4149/km_2015_4_287.

[33] M. Heilmaier, M. Krüger, H. Saage, J. Rösler, D. Mukherji, U. Glatzel, R. Völkl, R. Hüttner, G. Eggeler, and C. Somsen. Metallic materials for structural applications beyond nickel-based superalloys. *JOM Journal of the Minerals, Metals and Materials Society*, 61(7):61–67, 2009.

[34] K. Adams, J. DuPont, and A. Marder. The influence of centerline sigma (σ) phase on the through-thickness toughness and tensile properties of alloy AL-6XN. *Journal of materials engineering and performance*, 16(1):123–130, 2007.

[35] M. Brunner, R. Hülttner, M.-C. Bölitz, R. Völkl, D. Mukherji, J. Rösler, T. Depka, C. Somsen, G. Eggeler, and U. Glatzel. Creep properties beyond 1100°C and microstructure of Co-Re-Cr alloys. *Materials Science and Engineering: A*, 528(2):650–656, 2010. doi: 10.1016/j.msea.2010.09.035.

[36] T. Depka, C. Somsen, G. Eggeler, D. Mukherji, and J. Rösler. Sigma phase evolution in Co-Re-Cr-based alloys at 1100°C. *Intermetallics*, 48:54–61, 2014. doi: 10.1016/j.intermet.2013.11.003.

[37] K. Janghorban, J. Kirkaldy, and G. Weatherly. The Hume-Rothery size rule and double-well microstructures in gold-nickel. *Journal of Physics: Condensed Matter*, 13 (38):8661, 2001.

[38] E. Hornbogen. *Werkstoffe: Aufbau und Eigenschaften von Keramik-, Metall-, Polymer- und Verbundwerkstoffen*. Springer-Verlag, 2007. ISBN 3540307249.

[39] C. Sims and W. Hagel. *The superalloys*. Wiley series on the science and technology of materials. Wiley-Interscience, 1972. ISBN 9780471792079.

[40] D. Mukherji, J. Rösler, J. Wehrs, P. Strunz, P. Beran, R. Gilles, M. Hofmann, M. Hoelzel, H. Eckerlebe, L. Szentmiklósi, and Z. Mácsik. Application of In Situ Neutron and X-Ray Measurements at High Temperatures in the Development of Co-Re-Based Alloys for Gas Turbines. *Metallurgical and Materials Transactions A*, 44(1): 22–30, 2012. doi: 10.1007/s11661-012-1363-6.

[41] L. Wang, B. Gorr, H.-J. Christ, D. Mukherji, and J. Rösler. Optimization of Cr-Content for High-Temperature Oxidation Behavior of Co-Re-Si-Base Alloys. *Oxidation of Metals*, 80(1-2):49–59, 2013. doi: 10.1007/s11085-013-9369-z.

[42] D. Jones and J. Stringer. The effect of small amounts of silicon on the oxidation of high-purity Co-25 wt.% Cr at elevated temperatures. *Oxidation of Metals*, 9(5):409–413, 1975.

[43] P. Hou and J. Stringer. Effect of internal oxidation pretreatments and Si contamination on oxide-scale growth and spalling. *Oxidation of Metals*, 33(5-6):357–369, 1990.

[44] R. Durham, B. Gleeson, and D. Young. Silicon contamination effects in the oxidation of carbide-containing cobalt-chromium alloys. *Materials and Corrosion*, 49(12):855–863, 1998.

[45] B. Gorr, V. Trindade, S. Burk, H. J. Christ, M. Klauke, D. Mukherji, and J. Rösler. Oxidation Behaviour of Model Cobalt-Rhenium Alloys During Short-Term Exposure to Laboratory Air at Elevated Temperature. *Oxidation of Metals*, 71(3-4):157–172, 2009. doi: 10.1007/s11085-008-9133-y.

[46] S. Zaefferer and N.-N. Elhami. Theory and application of electron channelling contrast imaging under controlled diffraction conditions. *Acta Materialia*, 75:20–50, 2014.

[47] B. Gorr, S. Burk, T. Depka, C. Somsen, H. Abu-Samra, H.-J. Christ, and G. Eggeler. Effect of Si addition on the oxidation resistance of Co-Re-Cr-alloys: Recent attainments in the development of novel alloys. *International Journal of Materials Research*, 103 (1):24–30, 2012. doi: 10.3139/146.110626.

[48] H. Okamoto. Co-Cr (cobalt-chromium). *Journal of phase equilibria*, 24(4):377–378, 2003.

[49] D. Mukherji and J. Rösler. Private Communications. 2017.

[50] T. Mayer-Kuckuk. *Kernphysik: Eine Einführung.* Teubner Studienbücher. Vieweg+teubner Verlag, 2002.

[51] A. Furrer, J. Mesot, and T. Straässle. *Neutron scattering in condensed matter physics.* World Scientific, 2009. ISBN 9789810248307.

[52] G. L. Squires. *Introduction to the theory of thermal neutron scattering.* Cambridge university press, 2012. ISBN 1107644062.

[53] H. M.-L. Zentrum, 2017. URL `http://www.mlz-garching.de/instrumente-und-labore/struktur/stress-spec.html`.

[54] P. Debye. Interferenz von Röntgenstrahlen und Wärmebewegung. *Annalen der Physik*, 348(1):49–92, 1913.

[55] R. Gross and A. Marx. *Festkörperphysik*. Oldenbourg Wissenschaftsverlag, 2012. ISBN 9783486712940.

[56] J. S. Pedersen. Determination of size distribution from small-angle scattering data for systems with effective hard-sphere interactions. *Journal of applied crystallography*, 27 (4):595–608, 1994.

[57] M. Kotlarchyk and S.-H. Chen. Analysis of small angle neutron scattering spectra from polydisperse interacting colloids. *The Journal of chemical physics*, 79(5):2461–2469, 1983.

[58] J. K. Percus and G. J. Yevick. Analysis of Classical Statistical Mechanics by Means of Collective Coordinates. *Physical Review*, 110:1–13, April 1958. doi: 10.1103/PhysRev.110.1.

[59] E. Limpert, W. A. Stahel, and M. Abbt. Log-normal distributions across the sciences: Keys and clues on the charms of statistics, and how mechanical models resembling gambling machines offer a link to a handy way to characterize log-normal distributions, which can provide deeper insight into variability and probability-normal or log-normal: That is the question. *BioScience*, 51(5):341–352, 2001.

[60] A. Khintchine. Korrelationstheorie der stationären Korrelationstheorie der stationären stochastischen Prozesse. *Mathematische Annalen*, 1869.

[61] J. Kohlbrecher. SASfit: A program for fitting simple structural models to small angle scattering data. *Paul Scherrer Institut, Laboratory for Neutron Scattering*, 2012.

[62] A. Guinier and G. Fournet. *Small-angle scattering of X-rays*. Structure of matter series. Wiley, 1955.

[63] A. Guinier. "La diffraction des rayons X aux tres petits angles; application a l'etude de phenomenes ultramicroscopiques.". *Ann. phys.*, 12:161–237, 1939.

[64] R. Wagner, R. Kampmann, and P. W. Voorhees. Homogeneous second-phase precipitation. *Phase transformations in materials. Weinheim: Wiley-VCH*, pages 309–409, 2001.

[65] O. R. Myhr and Ø. Grong. Modelling of non-isothermal transformations in alloys containing a particle distribution. *Acta Materialia*, 48(7):1605–1615, 2000. doi: 10.1016/S1359-6454(99)00435-8.

[66] B. Rheingans and E. J. Mittemeijer. Analysis of Precipitation Kinetics on the Basis of Particle-Size Distributions. *Metallurgical and Materials Transactions A*, 46(8):3423–3439, 2015. doi: 10.1007/s11661-015-2937-x.

[67] I. M. Lifshitz and V. V. Slyozov. The kinetics of precipitation from supersaturated solid solutions. *Journal of physics and chemistry of solids*, 19(1-2):35–50, 1961.

[68] C. Wagner. Theorie der alterung von niederschlägen durch umlösen (Ostwald-reifung). *Berichte der Bunsengesellschaft für physikalische Chemie*, 65(7-8):581–591, 1961.

[69] A. Baldan. Review progress in Ostwald ripening theories and their applications to nickel-base superalloys Part I: Ostwald ripening theories. *Journal of materials science*, 37(11):2171–2202, 2002.

[70] D. Porter and K. Easterling. Phase Transformations in Metals and Alloys. *Chapman & Hall, New York, 1993) p*, 44(116):314, 1981.

[71] S. Semiatin, F. Zhang, R. Larsen, L. Chapman, and D. Furrer. Precipitation in powder-metallurgy, nickel-base superalloys: review of modeling approach and formulation of engineering methods to determine input data. *Integrating Materials and Manufacturing Innovation*, 5(1):1, 2016.

[72] J. Mao. *Gamma Prime Precipitation Modeling and Strength Responses in Powder Metallurgy Superalloys*. Thesis, West Virginia University, 2002.

[73] J. W. Mullin. *Crystallization*. Butterworth-Heinemann, 2001.

[74] J. W. Gibbs. Influence of surfaces of discontinuity upon the equilibrium of heterogeneous masses-Theory of capillarity. *The collected works*, 1:219, 1948.

[75] M. Volmer. *Kinetik der Phasenbildung*. Steinkopff, 1939.

[76] S. Arrhenius. On the reaction velocity of the inversion of cane sugar by acids. *Zeitschrift für physikalische Chemie*, 4(226-248):24, 1889.

[77] R. Kampmann and R. Wagner. Decomposition of alloys: the early stages. In *Proc. 2nd Acta-Scripta Metall. Conf., Pergamon, Oxford*, pages 91–103, 1984.

[78] J. Feder, K. Russell, J. Lothe, and G. Pound. Nucleation and Growth in Homogeneous Vapors. *Adv. Phys*, 15:111, 1966.

[79] W. Püschl. Phasenübergänge in Festkörpern, 2010. URL `https://www.univie.ac.at/physikwiki/images/4/48/Skript_Phasen%C3%BCberg%C3%A4ngeWS10.pdf`.

[80] J. Crank. *The Mathematics of Diffusion: 2d Ed*. Clarendon Press, 1975.

[81] K. Fan, F. Liu, W. Yang, G. Yang, and Y. Zhou. Analysis of soft impingement in nonisothermal precipitation. *Journal of Materials Research*, 24(12):3664–3673, 2011. doi: 10.1557/jmr.2009.0434.

[82] C. Zener. Theory of growth of spherical precipitates from solid solution. *Journal of Applied Physics*, 20(10):950–953, 1949.

[83] J. E. McDonald. Homogeneous nucleation of supercooled water drops. *Journal of Meteorology*, 10(6):416–433, 1953.

[84] F. S. Ham. Theory of diffusion-limited precipitation. *Journal of Physics and Chemistry of Solids*, 6(4):335–351, 1958.

[85] J. Möller, R. Kranold, J. Schmelzer, and U. Lembke. Small-angle X-ray scattering size parameters and higher moments of the particle-size distribution function in the asymptotic stage of ostwald ripening. *Journal of applied crystallography*, 28(5):553–560, 1995.

[86] A. Ardell. The effect of volume fraction on particle coarsening: theoretical considerations. *Acta metallurgica*, 20(1):61–71, 1972.

[87] N. Schell, A. King, F. Beckmann, T. Fischer, M. Müller, and A. Schreyer. The high energy materials science beamline (HEMS) at PETRA III. In *Materials Science Forum*, volume 772, pages 57–61. Trans Tech Publ, 2014. ISBN 3037859113.

[88] R. Gilles, A. Ostermann, C. Schanzer, B. Krimmer, and W. Petry. The concept of the new small-angle scattering instrument SANS-1 at the FRM-II. *Physica B: Condensed Matter*, 385:1174–1176, 2006.

[89] S. Mühlbauer, A. Heinemann, A. Wilhelm, L. Karge, A. Ostermann, I. Defendi, A. Schreyer, W. Petry, and R. Gilles. The new small-angle neutron scattering instrument SANS-1 at MLZ-characterization and first results. *Nuclear Instruments & Methods in Physics Research Section a-Accelerators Spectrometers Detectors and Associated Equipment*, 832:297–305, 2016. doi: 10.1016/j.nima.2016.06.105.

[90] U. Keiderling and A. Wiedenmann. New SANS instrument at the BER II reactor in Berlin, Germany. *Physica B: Condensed Matter*, 213:895–897, 1995.

[91] J. Kohlbrecher and W. Wagner. The new SANS instrument at the Swiss spallation source SINQ. *Journal of applied crystallography*, 33(3):804–806, 2000.

[92] C. Dewhurst. D33 – a third small-angle neutron scattering instrument at the Institut Laue Langevin. *Measurement Science and Technology*, 19(3):034007, 2008.

[93] U. Keiderling. The new 'BerSANS-PC' software for reduction and treatment of small angle neutron scattering data. *Applied Physics A: Materials Science & Processing*, 74: 1455–1457, 2002.

[94] P. Butler, M. Doucet, A. Jackson, and S. King, 2017. URL `http://www.sasview.org/`.

[95] A. Hammersley. FIT2D: an introduction and overview. *European Synchrotron Radiation Facility Internal Report ESRF97HA02T*, 68, 1997.

[96] M. Hofmann, G. A. Seidl, J. Rebelo-Kornmeier, U. Garbe, R. Schneider, R. C. Wimpory, U. Wasmuth, and U. Noster. The new materials science diffractometer STRESS-SPEC at FRM-II. In *Materials science forum*, volume 524, pages 211–216. Trans Tech Publ, 2006. ISBN 0878494146.

[97] M. Hoelzel, A. Senyshyn, N. Juenke, H. Boysen, W. Schmahl, and H. Fuess. High-resolution neutron powder diffractometer SPODI at research reactor FRM II. *Nuclear Instruments and Methods in Physics Research Section A: Accelerators, Spectrometers, Detectors and Associated Equipment*, 667:32–37, 2012.

[98] L. Finger, D. Cox, and A. Jephcoat. A correction for powder diffraction peak asymmetry due to axial divergence. *Journal of Applied Crystallography*, 27(6):892–900, 1994.

[99] H. M. Rietveld. A Profile Refinement Method for Nuclear and Magnetic Structures. *Journal of Applied Crystallography*, 2:65–71, 1969. doi: 10.1107/S0021889869006558.

[100] J. Rodríguez-Carvajal. Recent advances in magnetic structure determination by neutron powder diffraction. *Physica B: Condensed Matter*, 192(1-2):55–69, 1993. doi: 10.1016/0921-4526(93)90108-I.

[101] K. Momma and F. Izumi. VESTA 3 for three-dimensional visualization of crystal, volumetric and morphology data. *Journal of Applied Crystallography*, 44(6):1272–1276, 2011. doi: 10.1107/S0021889811038970.

[102] T. Degen, M. Sadki, E. Bron, U. König, and G. Nénert. The HighScore suite. *Powder Diffraction*, 29(S2):S13–S18, 2014. doi: 10.1017/s0885715614000840.

[103] S. Pennycook. Z-contrast STEM for materials science. *Ultramicroscopy*, 30(1-2):58–69, 1989.

[104] A. I. Gusev, A. A. Rempel, and A. J. Magerl. *Disorder and order in strongly nonstoichiometric compounds: transition metal carbides, nitrides and oxides*, volume 47. Springer Science & Business Media, 2013. ISBN 3662045826.

[105] T. B. Massalski, H. Okamoto, P. Subramanian, L. Kacprzak, and W. W. Scott. *Binary alloy phase diagrams*, volume 1. American Society for Metals Metals Park, OH, 1986.

[106] V. F. Sears. Neutron scattering lengths and cross sections. *Neutron News*, 3(3):29–37, 1992.

[107] C. Sims, N. Stoloff, and W. Hagel. *Superalloys II*. Wiley-Interscience publication. Wiley, 1987. ISBN 9780471011477.

[108] G. Beaucage. Approximations Leading to a Unified Exponential/Power-Law Approach to Small-Angle Scattering. *Journal of Applied Crystallography*, 28(6):717–728, 1995.

[109] M. Hansen, K. Anderko, and H. W. Salzberg. Constitution of binary alloys. *Journal of the Electrochemical Society*, 105(12):260C–261C, 1958.

[110] K. Shinagawa, H. Chinen, T. Omori, K. Oikawa, I. Ohnuma, K. Ishida, and R. Kainuma. Phase equilibria and thermodynamic calculation of the Co-Ta binary system. *Intermetallics*, 49:87–97, 2014.

[111] F. S. Varley. Neutron scattering lengths and cross sections. *Neutron News*, 3(3):29–37, 1992.

[112] M. Klauke, D. Mukherji, B. Gorr, V. B. da Trindade Filho, J. Rösler, and H.-J. Christ. Oxidation behaviour of experimental Co-Re-base alloys in laboratory air at 1000°C. *International Journal of Materials Research*, 100(1):104–111, 2009. doi: 10.3139/146.101792.

[113] L. Karge, R. Gilles, D. Mukherji, P. Beran, P. Strunz, H. Markus, and R. Joachim. Beyond Ni-base superalloys: Influence of Cr addition on Co-Re base alloys strengthened by nanosized TaC precipitates. *Physica B: Condensed Matter*, in press, 2017. doi: 10.1016/j.physb.2017.11.059.

[114] P. Strunz, D. Mukherji, P. Beran, R. Gilles, L. Karge, M. Hofmann, M. Hoelzel, J. Rösler, and G. Farkas. Matrix Transformation in Boron Containing High-Temperature Co-Re-Cr Alloys. *Metals and Materials International*, in press, 2018. doi: 10.1007/s12540-018-0121-8.

[115] R. MacKay and M. Nathal. γ' coarsening in high volume fraction nickel-base alloys. *Acta Metallurgica et Materialia*, 38(6):993–1005, 1990.

[116] D. McLean. Predicting growth of γ' in nickel alloys. *Metal science*, 18(5):249–256, 1984.

[117] S. Neumeier, H. Rehman, J. Neuner, C. Zenk, S. Michel, S. Schuwalow, J. Rogal, R. Drautz, and M. Göken. Diffusion of solutes in fcc Cobalt investigated by diffusion couples and first principles kinetic Monte Carlo. *Acta Materialia*, 106:304–312, 2016.

[118] V. A. Baheti, S. Santra, S. Roy, K. Perumalsamy, S. Prasad, R. Ravi, and A. Paul. Phase evolutions, growth kinetics and diffusion parameters in the Co-Ni-Ta system. *Journal of Alloys and Compounds*, 622:1033–1040, 2015. doi: 10.1016/j.jallcom.2014.10.112.

[119] V. Sarin. *Comprehensive hard materials*. Newnes, 2014. ISBN 0080965288.

[120] J. Eshelby. The continuum theory of lattice defects. *Solid state physics*, 3:79–144, 1956.

[121] matweb.com, 2017. URL `http://www.matweb.com/search/datasheet.aspx?matguid=9b8f8c69fe92446491de3c3dff2ef3e6&ckck=1`.

[122] K.-H. Grote and J. Feldhusen. *Dubbel–Taschenbuch für den Maschinenbau (24. Aufl.)*. Springer-Vieweg, Berlin, Heidelberg, New York, 2014.

[123] A. Korner and H. Karnthaler. Weak-beam study of glide dislocations in hcp cobalt. *Philosophical Magazine A*, 48(3):469–477, 1983.

[124] L. Karge, R. Gilles, D. Mukherji, B. Přemysl, P. Strunz, A. Stark, N. Schell, M. Hofmann, J. Häusler, and J. Rösler. Creep behavior of Co-Re-Ta-C alloys with varying C content – investigated in-situ by simultaneous synchrotron radiation diffraction. *Material Science and Engineering A*, 719:124–131, 2018. doi: 10.1016/j.msea.2018.02.009.

[125] J. S. Van Sluytman. *Microstructure and high temperature creep of platinum group metal modified nickel base superalloys*. Thesis, The University of Michigan, 2010.

[126] F. H. Norton. *The creep of steel at high temperatures*. McGraw-Hill Book Company, Incorporated, 1929.

[127] A. Bauer, S. Neumeier, F. Pyczak, R. Singer, and M. Göken. Creep properties of different γ'-strengthened Co-base superalloys. *Materials Science and Engineering: A*, 550:333–341, 2012.

[128] J. Tong, S. Dalby, J. Byrne, M. Henderson, and M. Hardy. Creep, fatigue and oxidation in crack growth in advanced nickel base superalloys. *International Journal of Fatigue*, 23(10):897–902, 2001.

[129] C. T. Liu, A. Taub, N. Stoloff, and C. Koch. High-Temperature Ordered Intermetallic Alloys III. Report, Pittsburgh, PA (USA); Materials Research Society, 1989.

[130] R. Lund and W. Nlx. On high creep activation energies for dispersion strengthened metals. *Metallurgical Transactions A*, 6(7):1329–1333, 1975.

[131] A. Sawant and S. Tin. High temperature nanoindentation of a Re-bearing single crystal Ni-base superalloy. *Scripta materialia*, 58(4):275–278, 2008.

[132] J. C. Zhao and M. R. Notis. Kinetics of the Fcc to Hcp Phase-Transformation and the Formation of Martensite in Pure Cobalt. *Scripta Metallurgica Et Materialia*, 32(10): 1671–1676, 1995. doi: 10.1016/0956-716x(95)00253-R.

[133] X. Wu, N. Tao, Y. Hong, G. Liu, B. Xu, J. Lu, and K. Lu. Strain-induced grain refinement of cobalt during surface mechanical attrition treatment. *Acta Materialia*, 53(3):681–691, 2005.

[134] C. Hitzenberger, H. P. Karnthaler, and A. Korner. Contrast Analysis of Intrinsic and Extrinsic Stacking Faults in H.C.P. Cobalt. *physica status solidi (a)*, 89(1):133–146, 1985. doi: 10.1002/pssa.2210890113.

[135] C. Carry and J. L. Strudel. Apparent and effective creep parameters in single crystals of a nickel base superalloy-I Incubation period. *Acta Metallurgica*, 25(7):767–777, 1977. doi: 10.1016/0001-6160(77)90092-X.

[136] S. A. Sajjadi and S. Nategh. A high temperature deformation mechanism map for the high performance Ni-base superalloy GTD-111. *Materials Science and Engineering: A*, 307(1-2):158–164, 2001. doi: 10.1016/S0921-5093(00)01822-0.

[137] B. Paul, R. Kapoor, J. Chakravartty, A. Bidaye, I. Sharma, and A. Suri. Hot working characteristics of cobalt in the temperature range $600 - 950°C$. *Scripta Materialia*, 60 (2):104–107, 2009.

[138] R. Kapoor, B. Paul, S. Raveendra, I. Samajdar, and J. K. Chakravartty. Aspects of Dynamic Recrystallization in Cobalt at High Temperatures. *Metallurgical and Materials Transactions A*, 40(4):818–827, 2009. doi: 10.1007/s11661-009-9782-8.

[139] L. Karge, R. Gilles, and S. Busch. Calibrating SANS data for instrument geometry and pixel sensitivity effects: access to an extended Q range. *Journal of applied crystallography*, 50(5):1382–1394, 2017. doi: 10.1107/s1600576717011463.

[140] G. D. Wignall and F. S. Bates. Absolute calibration of small-angle neutron scattering data. *Journal of Applied Crystallography*, 20(1):28–40, 1987. doi: 10.1107/S0021889887087181.

[141] P. Strunz, J. Saroun, U. Keiderling, A. Wiedenmann, and R. Przenioslo. General formula for determination of cross-section from measured SANS intensities. *Journal of Applied Crystallography*, 33(3 Part 1):829–833, 2000. doi: 10.1107/S0021889899013382.

[142] R. E. Ghosh, S. U. Egelhaaf, and A. R. Rennie. *A computing guide for small-angle scattering experiments*. Institut Laue-Langevin, 2000.

[143] T. Zemb and P. Lindner. *Neutrons, X-rays and light: scattering methods applied to soft condensed matter*. North-Holland delta series. Elsevier, 2002.

[144] A. Brûlet, D. Lairez, A. Lapp, and J.-P. Cotton. Improvement of data treatment in small-angle neutron scattering. *Journal of Applied Crystallography*, 40(1):165–177, 2007. doi: 10.1107/s0021889806051442.

[145] F. Zhang, J. Ilavsky, G. G. Long, J. P. G. Quintana, A. J. Allen, and P. R. Jemian. Glassy Carbon as an Absolute Intensity Calibration Standard for Small-Angle Scattering. *Metallurgical and Materials Transactions A*, 41(5):1151–1158, 2010.

[146] J. G. Barker and D. F. R. Mildner. Survey of background scattering from materials found in small-angle neutron scattering. *Journal of Applied Crystallography*, 48(4): 1055–1071, 2015. doi: 10.1107/S1600576715010729.

[147] R. P. May, K. Ibel, and J. Haas. The forward scattering of cold neutrons by mixtures of light and heavy water. *Journal of Applied Crystallography*, 15(1):15–19, 1982. doi: 10.1107/S0021889882011285.

[148] P. Lindner, F. Leclercq, and P. Damay. Analysis of water scattering used for calibration of small-angle neutron scattering (SANS) measurements. *Physica B: Condensed Matter*, 291(1-2):152–158, 2000. doi: 10.1016/S0921-4526(99)01397-6.

[149] J. R. D. Copley. The significance of multiple scattering in the interpretation of small-angle neutron scattering experiments. *Journal of Applied Crystallography*, 21(6):639–644, 1988.

[150] M. Shibayama, M. Nagao, S. Okabe, and T. Karino. Evaluation of incoherent neutron scattering from softmatter. *Journal of the Physical Society of Japan*, 74(10):2728–2736, 2005. doi: 10.1143/JPSJ.74.2728.

[151] A. V. Feoktystov, H. Frielinghaus, Z. Di, S. Jaksch, V. Pipich, M.-S. Appavou, E. Babcock, R. Hanslik, R. Engels, and G. Kemmerling. KWS-1 high-resolution small-angle neutron scattering instrument at JCNS: current state. *Journal of applied crystallography*, 48(1):61–70, 2015.

[152] I. Laue-Langevin, 2017. URL `http://www.ill.eu/instruments-support/instruments-groups/instruments/d22/description/instrument-layout/`.

[153] R. Heenan, J. Penfold, and S. King. SANS at pulsed neutron sources: present and future prospects. *Journal of Applied Crystallography*, 30(6):1140–1147, 1997.

[154] R. Heenan, S. King, D. Turner, and J. Treadgold. SANS2D at the ISIS second target station. *Proc ICANS-XVII*, pages 780–785, 2006.

[155] S. Boukhalfa, L. He, Y. B. Melnichenko, and G. Yushin. Small-angle neutron scattering for in situ probing of ion adsorption inside micropores. *Angewandte Chemie International Edition*, 52(17):4618–22, 2013. doi: 10.1002/anie.201209141.

[156] E. P. Gilbert, J. C. Schulz, and T. J. Noakes. 'Quokka' - the small-angle neutron scattering instrument at OPAL. *Physica B: Condensed Matter*, 385:1180–1182, 2006.

[157] J. S. Pedersen, D. Posselt, and K. Mortensen. Analytical treatment of the resolution function for small-angle scattering. *Journal of Applied Crystallography*, 23(4):321–333, Aug 1990. doi: 10.1107/S0021889890003946.

[158] I. Grillo. *Small-Angle neutron scattering and applications in soft condensed matter*, pages 723–782. Springer, 2008. ISBN 140204464X.

[159] L. He, C. Do, S. Qian, G. D. Wignall, W. T. Heller, K. C. Littrell, and G. S. Smith. Corrections for the geometric distortion of the tube detectors on SANS instruments at ORNL. *Nuclear Instruments and Methods in Physics Research Section A: Accelerators, Spectrometers, Detectors and Associated Equipment*, 775:63–70, 2015. doi: 10.1016/j.nima.2014.11.061.

[160] S. Masalovich. Method to measure neutron beam polarization with 2×1 Neutron Spin Filter. *Nuclear Instruments and Methods in Physics Research Section A: Accelerators, Spectrometers, Detectors and Associated Equipment*, 581(3):791–798, 2007. doi: 10.1016/j.nima.2007.08.150.

[161] M. Abramowitz and I. A. Stegun. *Handbook of mathematical functions: with formulas, graphs, and mathematical tables*, volume 55. Courier Corporation, 1964.

[162] J. Hagemann, A.-L. Robisch, M. Osterhoff, and T. Salditt. Probe reconstruction for holographic X-ray imaging. *Journal of Synchrotron Radiation*, 24:498–505, 2017. doi: 10.1107/S160057751700128X.

[163] P. Calmettes. Diffusion des neutrons aux petits angles : choix de l'échantillon et traitement des données. *J. Phys. IV France*, 9:83–93, 1999. doi: 10.1051/jp4:1999106.

[164] A. J. Guinier. *Théorie et technique de la radiocristallographie*. Dunod Paris, 1964.

[165] G. Placzek. The Scattering of Neutrons by Systems of Heavy Nuclei. *Phys. Rev.*, 86:377–388, 1952. doi: 10.1103/PhysRev.86.377.

[166] R. E. Ghosh and A. R. Rennie. Assessment of detector calibration materials for SANS experiments. *Journal of Applied Crystallography*, 32(6):1157–1163, 1999. doi: 10.1107/s0021889899009991.

[167] J. Schelten and W. Schmatz. Multiple-scattering treatment for small-angle scattering problems. *Journal of Applied Crystallography*, 13(4):385–390, 1980. doi: 10.1107/S0021889880012356.

[168] C. Moreno-Castilla, O. Mahajan, P. Walker, H. Jung, and M. Vannice. Carbon as a support for catalysts-III glassy carbon as a support for iron. *Carbon*, 18(4):271–276, 1980.

[169] B. Hammouda. The SANS Toolbox. *NIST Center for Neutron Research, available at http://tinyurl. com/SANStoolbox*, 2008.

[170] O. Glatter. A new method for the evaluation of small-angle scattering data. *Journal of Applied Crystallography*, 10, 1977.

[171] P. Strunz and A. Wiedenmann. Fully Numerical Procedure for Anisotropic Small-Angle Neutron Scattering Modelling and Data Evaluation. *Journal of Applied Crystallography*, 30(6):1132–1139, Dec 1997. doi: 10.1107/S0021889897001283.

[172] D. Lang, L. Karge, J. Schatte, R. Gilles, R. Dallinger, I. Weißensteiner, P. Staron, W. Knabl, S. Primig, and H. Clemens. Evolution of strain-induced hafnium carbides in a molybdenum base Mo–Hf–C alloy studied by small-angle neutron scattering and complementary methods. *Journal of Alloys and Compounds*, 688:619–631, 2016. doi: 10.1016/j.jallcom.2016.06.282.

[173] S. Ciccariello, J. M. Schneider, B. Schönfeld, and G. Kostorz. Generalization of Porod's law of small-angle scattering to anisotropic samples. *EPL (Europhysics Letters)*, 50(5): 601, 2000.

[174] M. Spivak. *A comprehensive introduction to differential geometry*. Publish or Perish, Texas, 3 edition, 1999. ISBN 0914098705.

[175] O. Glatter and O. Kratky. *Small angle x-ray scattering*. Academic Press, 1982. ISBN 9780122862809.

[176] D. I. Svergun, A. V. Semenyuk, and L. A. Feigin. Small-angle-scattering-data treatment by the regularization method. *Acta Crystallographica Section A*, 44(3):244–250, May 1988. doi: 10.1107/S0108767387011255.

[177] H. Zou and T. Hastie. Regularization and variable selection via the elastic net. *Journal of the Royal Statistical Society: Series B (Statistical Methodology)*, 67(2):301–320, 2005.

[178] O. Glatter. Convolution square root of band-limited symmetrical functions and its application to small-angle scattering data. *Journal of Applied Crystallography*, 14(2): 101–108, Apr 1981. doi: 10.1107/S002188988100887X.

[179] T. Schlumprecht and N. Sivakumar. On the sampling and recovery of bandlimited functions via scattered translates of the Gaussian. *Journal of Approximation Theory*, 159(1):128–153, 2009.

[180] H. Wendland. *Scattered Data Approximation*. Cambridge University Press, 2004. doi: 10.1017/CBO9780511617539.

[181] E. Neuman. Moments and Fourier transforms of B-splines. *Journal of Computational and Applied Mathematics*, 7(1):51–62, 1981.

[182] K. Levenberg. A method for the solution of certain problems in least squares. *Quart. Applied Math.*, 2:164–168, 1944.

[183] D. W. Marquardt. An algorithm for least-squares estimation of nonlinear parameters. *Journal of the society for Industrial and Applied Mathematics*, 11(2):431–441, 1963.

[184] A. Ranganathan. The levenberg-marquardt algorithm. *Tutoral on LM algorithm*, pages 1–5, 2004.

[185] A. Milzarek and M. Ulbrich. A semismooth newton method with multidimensional filter globalization for l_1-optimization. *SIAM Journal on Optimization*, 24(1):298–333, 2014.

[186] A. N. Tikhonov. *Solutions of ill-posed problems*. Winston Distributed solely by Halsted Press, Washington New York, 1977. ISBN 0470991240.

[187] L. I. Rudin, S. Osher, and E. Fatemi. Nonlinear total variation based noise removal algorithms. *Physica D: Nonlinear Phenomena*, 60(1–4):259 – 268, 1992. doi: 10.1016/0167-2789(92)90242-F.

[188] M. Balda. LMFsolve. m: Levenberg-Marquardt-Fletcher algorithm for nonlinear least squares problems. *MathWorks, File Exchange, ID*, 16063, 2007.

[189] C. Yi and J. Huang. Semismooth Newton Coordinate Descent Algorithm for Elastic-Net Penalized Huber Loss Regression and Quantile Regression. *Journal of Computational and Graphical Statistics*, 26(3):547–557, 2017. doi: 10.1080/10618600.2016.1256816.

[190] A. R. Rennie, M. S. Hellsing, K. Wood, E. P. Gilbert, L. Porcar, R. Schweins, C. D. Dewhurst, P. Lindner, R. K. Heenan, S. E. Rogers, P. D. Butler, J. R. Krzywon, R. E. Ghosh, A. J. Jackson, and M. Malfois. Learning about SANS instruments and data reduction from round robin measurements on samples of polystyrene latexThis article will form part of a virtual special issue of the journal, presenting some highlights of the 15th International Small-Angle Scattering Conference (SAS2012). This special issue will be available in late 2013. *Journal of Applied Crystallography*, 46(5):1289–1297, 2013. doi: 10.1107/S0021889813019468.

[191] P. Strunz, D. Mukherji, R. Gilles, U. Gasser, P. Beran, G. Farkas, M. Hofmann, L. Karge, and J. Rösler. In Situ Neutron Diffraction Characterization of Phases in

Co-Re-Based Alloys at High Temperatures. *Acta Physica Polonica A*, 128(4):684–688, 2015. doi: 10.12693/APhysPolA.128.684.

[192] S. Seidlmayer, J. Hattendorff, I. Buchberger, L. Karge, H. A. Gasteiger, and R. Gilles. In operando small-angle neutron scattering (SANS) on Li-ion batteries. *Journal of The Electrochemical Society*, 162(2):A3116–A3125, 2015. doi: 10.1149/2.0181502jes.

[193] R. Gilles, D. Mukherji, H. Eckerlebe, L. Karge, P. Staron, P. Strunz, and T. Lippmann. Investigations of early stage precipitation in a tungsten-rich nickel-base superalloy using SAXS and SANS. *Journal of Alloys and Compounds*, 612(0):90–97, 2014. doi: 10.1016/j.jallcom.2014.05.154.